Turbulent Transport in Tokamak Plasmas: bridging theory and experiment

Clarisse Bourdelle

Aix-Marseille Université

Habilitation à Diriger des Recherches

Turbulent Transport in Tokamak Plasmas: bridging theory and experiment

---

Clarisse Bourdelle

Jury:
Dr. Lorne Horton, EUROfusion, Head of JET Exploitation, *Referee*
Dr. Alberto Loarte, ITER Organization, Section Leader, *Referee*
Dr. Ron Waltz, General Atomics, Senior Technical Advisor, *Referee*
Pr. Peter Beyer, Aix-Marseille University, PIIM, Professor
Dr. Xavier Garbet, CEA/DSM/IRFM, Research Director
Dr. Tuong Hoang, CEA/DSM/IRFM, International Expert

January 16, 2015

Contents

Chapter 1

Introduction

The aim of this report is to provide a pedagogical summary of the knowledge I have acquired since starting my post-graduate work in 1997. The focus is on turbulent transport in tokamak plasmas. A key issue is the achievement of good energy confinement in fusion devices. A numerical tool, bridging theory and experiments, will be introduced. It is based on quasilinear gyrokinetic modeling of turbulence. This document is aimed towards contributing to a more global effort in the education and acclimatization of future students, and to acquaint them with numerous open issues that remain to be addressed in the field of turbulent transport in magnetically confined fusion devices such as tokamaks.

1.1 Brief historical background

In each field of science, a familiarity of its history is vital for placing one's own work into context and perspective. In fusion, a recent book (first published in March 2013), "A piece of the Sun" by Daniel Clery [1] describes the past 70 years of fusion history. The book traverses through both the "small" stories of the researchers, the science managers, their friendships, their political backgrounds, as well as through the history of the science within the context of the race for the atomic bomb and the Cold War. This clear and high quality exposition – written by a knowledgeable and talented journalist – is highly advised to anyone involved in fusion research.
In [1], the discovery of fusion within the framework of understanding the energy source of the Sun by Eddington is recalled. It mentions the first ideas for magnetically confined devices to contain the hydrogen fuel by scientists working on the atomic bomb in the USA during the second World War (Manhattan project). The Cold War with its East/West competition

on the science battlefield also strongly impacted fusion science development. It was finally declassified in 1958. That year, in Geneva, the second "Atom for Peace" United Nations conference took place. For the first time, Soviet and American scientists could exchange their ideas. The proceedings of this historical conference are available on the web [2]. On this website, one can find moreover the Kurchatov speech at Harwell in Great Britain in 1956 as well as the 1958 Geneva conference speeches, in particular the speech of E. Teller, the father of the US H-bomb, reporting on controlled thermonuclear research, a speech by Artsimovich for the USSR, etc. These speeches showed that the tokamak was not far around the corner. Indeed, the pinch machines were suggesting that the addition of an external toroidal magnetic field would lead to increased stability, and that the magnetic mirrors should close their ends... In Daniel Clery's book [1], the atmosphere of the conference is reported. The Americans had shipped 140 tons of material to reconstruct a mirror machine, a stellarator, and a pinch machine. Around 100 000 visitors came and 900 journalists attended the event. In 2008, 50 years later, an IAEA conference on fusion took place in the same United Nation Palace in Geneva. The public interest for the event was not quite the same... A review of the 50 years of research was given by J. Jacquinot [3]. He recalled an essential, central aspect of fusion research: "In fusion devices, engineering and physics are highly integrated. To a large extent the machine itself as a whole is the experiment." This is different from other so called "big science" installations such as the synchrotrons or the particle accelerators where the machines are providing the light or the ion jets needed by the physicists. In fusion, "the machine itself as a whole is the experiment." This is responsible for making fusion a field where each scientist, after a few years, typically wears two hats, either a technician and experimentalist, or experimentalist and diagnostician, or experimentalist and modeler, etc. This makes the daily life more complex but also more interesting. This specific integrated aspect should be an appealing attribute for anyone starting fusion, since this strong interaction is essential for the progress of fusion research.

Among other interesting readings are the 1964 Trieste lectures. In Trieste, Italy, a meeting took place which lasted over almost a year, where scientists from each side of the Iron curtain could work together. It focused on theory [4]. This event is reported in R. Sagdeev's memoirs – "The making of a Soviet scientist: my adventures in nuclear fusion and space from Stalin to Star Wars" – published in 1994 [5] as well as in a transcript of an interview of Marshall Rosenbluth [6].

Over the past 70 years, it was understood that: metallic wall machines had to be avoided to reduce core radiation by heavy ions; the tokamak configuration allowed for drastic reduction in collisional transport and the attainment

of high temperatures; Ohmic heating was not sufficient and additional means of heating must be added, such as Radio Frequency and Neutral Beam Injection; by adding power, the confinement was found to degrade due to increased turbulence; at high power a transition occurs to a high confinement regime called H-mode; the presence of a divertor to extract the heat significantly helps to achieve transition to H-mode. In modern machines, the divertor configuration is a primary characteristic. However, carbon tiles of the plasma facing wall components are now being replaced by metallic elements such as tungsten and beryllium and the control of heavy impurity radiation returns to the forefront. This brief summary illustrates the rise and fall of fusion research. The final word is still far away. Fusion is hoped to provide energy to produce electricity. The hope is to extract as much energy from 1 gram of a mix of deuterium and tritium as from 1 ton of coal. If achieved, such a goal would change the face of the world by relaxing numerous geopolitical and environmental constraints. There is no certainty for a success. The only certainty there is, is that we have to try it.

1.2 Sources for general physics background on tokamak plasma turbulent transport

In the previous section, it was mentioned that the Ohmic heating which occurs in the tokamak configuration was not sufficient. Indeed, it is limited by the temperature it produces, since the resistivity decreases as the temperature increases. Additional external heating power is required to achieve the fusion temperature for the D-T reaction which is of the order of 10 keV (100 000 000 K). See the book "Tokamaks" by Wesson [7] for more detailed information on the tokamak configuration and the various heating systems.
When increasing the power P, it was reported experimentally that the energy confinement time τ_E was reduced: $\tau_E \propto P^{-0.7}$ [8]. The onset of a significant level of turbulence, highly sensitive to the driving pressure gradients, explains this trend. Therefore, in tokamak plasmas, one has to live with turbulent transport.
Tokamak turbulence theory has been long studied. The reader is referred to pioneering work by Kadomstev, Rosenbluth, and to the Trieste lectures [4, 9]. The lecture notes by Yanick Sarazin [10] summarizes the mechanisms behind the main classes of instabilities (drift wave, interchange and Kelvin-Helmholtz), the reader is referred to the references therein for a more complete bibliography. The book by Nicholson, among others, is an excellent pedagogical introduction to turbulence theory [11]. Moreover, numerous

PhD dissertations have very useful introductions on the subject, for example Beers' PhD [12], Casati's PhD [13] and Cottier's PhD [14]. These mechanisms are not reviewed in this manuscript. Many very nice lecture notes and important historical articles are also available from the web, for example [15, 16].
Experimental measurements of density, temperature, electric and magnetic fields fluctuations have been carried out by pioneers such as [17] up to more recent work [18, 19], a nice overlook of such measurements can be found in Roland Sabot's Habilitation [20].
To bridge theory with experiments, codes have been developed. In particular the so-called nonlinear gyrokinetic codes computing the coupled Vlasov and Maxwell equations [21, 22, 23, 24]. Recently, direct comparisons between code output and turbulence measurements have been carried out [25, 26, 27]. But, as R. Sagdeev said during his brilliant Rosenbluth lecture which took place at the "Festival de ThÃľorie" in Aix-en-Provence in July 2013, now two bridges have to be built, one from theory to computing science and another from computing science to experiments.

1.3 The spirit of the present work

The spirit of the work presented in this report is to bridge theory, advanced numerical modeling and experiments thanks to a simplified approach which is quicker than the physically comprehensive advanced numerical tools. Indeed, the rapidity of turbulent transport modeling allows systematic comparisons between the model and experiments as well as predictive work. Heat, particle and angular moment transport are modeled. The simplified model also stimulates the development of the more advanced numerical approaches and theoretical understanding, since its construction relies on a deep understanding of the nonlinear physical mechanisms. Such work is hence at the cross-roads between experimental observations and detailed theoretical investigations.
The trade-off presented here relies on a quasilinear gyrokinetic approach. In the present report, the details of the model will be outlined, the quasilinear fluxes will be compared to nonlinear fluxes and to experiments at a given time slice, and finally they will be used in a time evolving platform to predict temperature, density and rotation profiles. The successes and limits of the quasilinear approach will be reviewed. Perspectives for the future will be given in the discussion section.

1.4 Some "historical" background to the quasi-linear model QuaLiKiz

During my PhD (1997-2000), a linear gyrokinetic code was developed, Kinezero [28]. It was based on the linear Vlasov equation for each species of the plasma and the dispersion relation was derived from the electroneutrality constraint. The idea was to facilitate the comparison between theory and experiment with a fast code for providing qualitative information on the key parameters underlying mode stability. The inputs were based on experimental profiles: temperature, density, current, etc. The outputs of the code were the growth rates and frequencies of the modes. Thanks to this approach it was possible to identify the stabilizing role of the effective charge Z_{eff}, of negative magnetic shear, etc. It also demonstrated that the analytic fluid limit was recovered far from the instability threshold, while closer to the threshold the physics taken into account in the code was not accessible analytically, justifying the need for numerical solutions of the gyrokinetic equations.
Nowadays, thanks to the routine availability of high performance computing systems, more complete gyrokinetic codes such as GENE [22], GKW [29], GS2 [30], and GYRO [23] can be easily used for linear or quasilinear investigations of experimental profiles. For example C. Angioni's Habilitation à Diriger des Recherches [31] is a good illustration of the intensive usage of such tools to interpret experimental data.
Nonetheless, the main issue – predicting temperature, density, rotation in future tokamaks such as ITER – remains highly challenging. This requires the modeling of heat, particle and momentum fluxes, which then need to be integrated with heat, particle and momentum source modeling, together with a self consistent magnetic equilibrium. This system is characterized by numerous nonlinear interactions, e.g., between temperature and current diffusion, and density and radio frequency heating. To reach a stationary state, it is necessary to model these interactions over times on the order of a few confinement times, i.e. on the order of a second, during which the transport model would need to be run an approximate 10^3 times. This sets a constraint on model speed in order not to exceed several days of wall-clock time to model 1 s. Direct numerical nonlinear simulation with gyrokinetic codes such as those mentioned above is much too slow for this purpose, even with massive parallelization, due to the excessive demanded CPU time. Typically, 5 000 to 10 000 CPU hours are required to compute the turbulent fluxes for at one radial position for a given input parameter set. Around 20 radial positions are needed in an integrated framework for profile prediction. This means that, even if using 1000 processors, then around 4 000 to 8 000 days

are needed to model 1 s of plasma with the gyrokinetic nonlinear codes.
To tackle this issue, the turbulent transport model has to be sped up by a factor of, at least, 100 000. Within this framework, based on Kinezero [28], a quasilinear gyrokinetic code has been developed: QuaLiKiz [32, 33, 34]. The quasilinear approximation allows to gain a factor 100 over the nonlinear approach. This is far from being enough. Further approximations are needed. The 4D axisymmetric gyrokinetic problem is further simplified thanks to the use of the lowest order ballooning transform. Some integrals are also reduced by treating separately trapped and passing particles. Finally the eigenfunction is not solved self-consistently together with the eigenvalue, but rather is deduced from the fluid limit of the gyrokinetic equations. More recently, during J. Citrin's post-doc [35], efforts in simplifying the numerical schemes have allowed to optimize the dispersion relation solver and the plasma dispersion functions thanks to the help of O. Gürcan [36]. Thanks to these further approximations, another factor 5 000 is gained. Overall a factor 500 000 to 1 million is gained compared to non-linear gyrokinetic models. With such a tool, 1 s of plasma can be modeled over 10 processors during a day, or using 100 processors over a couple of hours. This has required QuaLiKiz to run in parallel over radial positions and wavenumbers. However, the ultimate goal is not purely to construct a fast code, but a code which is both fast and correct. Hence the limits of an acceptable trade off have to be carefully explored. This means that developing such a code requires one to constantly go back and forth from nonlinear complete modeling to quasilinear approximate modeling in order to validate or invalidate the choices made.
The quasilinear approximation has been tested in great detail during Alessandro Casati's PhD [13, 33], has been further investigated thanks to Jonathan Citrin's efforts during his PhD [37] and to Pierre Cottier's work on momentum transport [14]. Numerous other observations confirm that the quasilinear approximation is valid when compared to nonlinear simulations for Trapped Electron Modes [38], for Electron Temperature Gradient modes [39], and that also it is valid when studying various transport fluxes of heat [33, 40], particles [31] and momentum [41, 42].
The quasilinear approach has also been shown to successfully model various experimental results such as the particle pump out [43], the Ni response to electron temperature gradient [44], the particle transport threshold [45], the angular momentum at JET [41] and more recently the momentum modulation experiments [42]. And when embedded in a time evolving platform which self-consistently models the sources, it was shown to predict the temperature and density within less than 20% rms [40].
The predictive simulations using QuaLiKiz in CRONOS [46] are now starting. Both heat and particle transport have been modeled in JET H mode

pulses [47], thanks to the effort of B. Baiocchi during her post-doc [48, 49]. The manuscript is organized as follows:

- In chapter 2, the linear gyrokinetic equation is derived, and the electrostatic dispersion relation is given.
- In chapter 3, the use of the linear code is introduced and the main parametric dependencies of the linear threshold are presented.
- Chapter 4 is dedicated to the quasilinear fluxes derivation. The validity of the quasilinear approximation is tested thanks to comparison with nonlinear gyrokinetic codes and turbulence measurements.
- In chapter 5, the quasilinear fluxes are compared to experimental results for particle, heat and momentum transport.
- The results are discussed in chapter 6. Perspectives for further work are presented.

Chapter 2

Linear stability analysis

In this chapter, the derivation of the linear dispersion relation for electrostatic instabilities is introduced. At first, the reaction of the plasma to the electromagnetic field is given by the Vlasov equation. Then, the modified distribution of charged particles generates a modification of the electromagnetic field through the Maxwell equations. The coupled equations lead to the dispersion relation. In the following, magnetic perturbations are neglected, as well as the nonlinear terms. The Vlasov equation will then lead to an expression of the form $\delta f_s = R_{lin,s}\delta\phi$, where a perturbed distribution function, δf_s , of a species s responds linearly ($R_{lin,s}$) to the perturbed linear electrostatic potential, $\delta\phi$. In the electrostatic case, the Maxwell equations, for lengths much larger than the Debye length, lead to the electroneutrality constraint. The perturbed electrostatic potential is expressed using a Gaussian trial function derived in the fluid limit, in the lowest order ballooning representation. The perturbation frequency is a solution of the computed dispersion relation, evaluated using a generalized Nyquist's method. The imaginary part of the frequency characterizes the linear instability and is called the growth rate (γ). In sections 2.1 and 2.2, the derivation of the linear dispersion relation is presented in detail. In section 2.3, the linear eigenfunctions are derived in the fluid limit. In section 2.4, the numerical method for searching for eigenvalues is explained. Benchmarks of the derived growth rates are presented in section 2.5. The chapter is concluded in section 2.6.

2.1 Framework of the dispersion relation

In this section, the path used to derive the dispersion relation is reviewed. The perturbed Vlasov equation is introduced as well as the necessary set of

angular and action variables adapted to the tokamak configuration. Indeed, charged particles trajectories in a tokamak are such the system is integrable and the movement quasi-periodic. Such as system can be described using angle and action variables as demonstrated in [50].
The gyrokinetic approximation is introduced as well as the variational form of the electroneutrality. Indeed, the gyroaveraged distribution function produces center guide charge densities and currents which differ from particle charge densities and currents used in Maxwell's equations. To overcome this difficulty, the Lagrangian of the electromagnetic field is used L and its associated functional $S = \int dtL$ is made extremal with respect to field variations, this is called the variational principle [50, 51].
The ballooning transform is explained step by step. This transform takes advantage of the anisotropy of the microinstabilities in a tokamak which tend to be more extended along the field lines than across it [52]. Finally the phase space element used in the following is derived.
Based on these elements, a simplified dispersion relation using at most bidimensional integrals will be derived in section 2.2.

2.1.1 The perturbed Vlasov equation

Individual trajectories in the electromagnetic field of a tokamak are defined by the Hamilton's equations:

$$\begin{cases} \dot{\vartheta}_i = & \frac{\partial H}{\partial J_i} \\ \dot{J}_i = & -\frac{\partial H}{\partial \vartheta_i} \end{cases} \tag{2.1}$$

H is the Hamiltonian, i.e. the sum of the kinetic and potential energies of a particle. J_i are the action variables and ϑ_i the angle variables. The dot stands for the time derivative.
i varies from 1 to 3, in the case of three degrees of freedom. There are thus 6 equations to be solved to determine the trajectory of a particle. If invariants exist, i.e. $\dot{J}_i = 0$, then the system becomes:

$$\begin{cases} \vartheta_i = & \frac{\partial H}{\partial J_i} t + \vartheta_{i0} \\ J_i = & J_{i0} \end{cases} \tag{2.2}$$

In other words, if the actions are conserved, the ratio energy to frequency stays fixed, see Nicholson's book section 2.7 [11]. From the three invariants along the trajectories, J_i, one can define three associated cyclic coordinates, ϑ_i. In this system of 6 coordinates, the trajectories are integrable as demonstrated in [53].
Solving each particle trajectory is not achievable, indeed it would require to

follow 6 times 10^{23} particles. There are two alternatives, the first is to solve the trajectories of a limited number of particles, this is chosen by the Particle In Cell codes, the second is to compute the dynamics of the distribution function. The numerical challenges of the two approaches are discussed in [54].
In the present work, the statistical approach is used. The distribution function $f_s(\vec{\vartheta}, \vec{J}, t)$ of a species s multiplied by a phase space volume element $d\vec{\vartheta}d\vec{J}$ represents the probability that a given particle finds itself in the region of the phase space between $(\vec{\vartheta}, \vec{J})$ and $(\vec{\vartheta} + d\vec{\vartheta}, \vec{J} + d\vec{J})$. If the number of particles in a Debye sphere ($n_s\lambda_D^3 \simeq 3.5 \times 10^{21} \times \frac{T_s^{3/2}}{\sqrt{n_s}}$ with T_s in keV and n_s in $10^{19}m^{-3}$) tends towards infinity and in absence of collisions, it is exact to replace the individual particle trajectory equation with an equation for the distribution function. One then obtains a generalized Hamilton's equation. In a plasma, at the equilibrium, this is called the Vlasov equation:

$$\frac{df}{dt} = \frac{\partial f}{\partial t} + [f, H] = 0 \tag{2.3}$$

[...] are the Poisson brackets, such that : $[f, H] = \frac{\partial f}{\partial \vartheta}\frac{\partial H}{\partial \vec{J}} - \frac{\partial f}{\partial \vec{J}}\frac{\partial H}{\partial \vartheta}$.
Note that the Vlasov equation can also be derived from an ensemble average of the Klimontovich equation, which is an exact equation of the evolution of a plasma, see Nicholson Chapter 3 for more details [11] and also [10]. It can be written as :

$$\frac{\partial f}{\partial t} + [f, H] = \frac{\partial f}{\partial t} + (\dot{\vec{J}}\frac{\partial f}{\partial \vec{\vartheta}} + \dot{\vec{\vartheta}}\frac{\partial f}{\partial \vec{J}}) = 0 \tag{2.4}$$

In the case of an unperturbed Hamiltonian, $H = H_0$, i.e. at the thermodynamical equilibrium, the solution of the equation $[f_0, H_0] = 0$ is an equilibrium distribution function, f_0, which depends only on the invariant action variables. To determine its form, the impact of collisions have to be included. This is the subject of neoclassical theory [55]. In the following a Maxwellian is taken for the equilibrium distribution function such that, for a given species s of density n_s, temperature T_s, mass m_s and charge e_s, one gets:

$$f_{0,s} = n_s \frac{1}{(2\pi m_s T_s)^{3/2}} e^{-E/T_s} \tag{2.5}$$

E is different from H_0. H_0 is the energy of a particle which, by definition, does have any information about the thermodynamical equilibrium. E is the kinetic energy of a particle at the thermodynamical equilibrium. In the case of a plasma rotating at a rigid body velocity $U_\parallel$, and in the electrostatic case: $H_0 = \frac{m_s {v_\parallel}^2}{2} + \frac{m_s {v_\perp}^2}{2} + e_s\phi_0$.

whereas: $E = \frac{m_s(v_\parallel - U_\parallel)^2}{2} + \frac{m_s {v_\perp}^2}{2} = H_0 - e_s\phi_0 + m_s U_\parallel(U_\parallel/2 - v_\parallel)$.
$v_\parallel$ and $v_\perp$ are respectively the velocities parallel and perpendicular to the magnetic field B. ϕ_0 is the equilibrium electrostatic potential.
By integrating the equilibrium distribution function one has to find the equilibrium quantities, among which the rigid body rotation $U_\parallel = \frac{1}{n_s}\left\langle v_\parallel f_{0,s}\right\rangle$ with $< ... >$ the volume average.
In presence of collisions, the Vlasov equation becomes the Boltzmann kinetic equation:

$$\frac{df}{dt} = \frac{\partial f}{\partial t} + [f, H] = C(f) \tag{2.6}$$

where $C(f)$ is a generic collision operator. Depending on the collision operator, this equation is also referred to as the Fokker-Planck equation. This equation can also be derived exactly starting from the Liouville equation using the BBGKY hierarchy accounting for the interactions between two particles, as detailed in Nicholson chapter 4 [11].
To account for the a perturbed part of the Hamiltonian, one writes: $H = H_0 + \delta H$ and $f = f_0 + \delta f$. H and f are always solutions of the Vlasov or Fokker-Planck equation. The equilibrium distribution function f_0 is assumed to remain a Maxwellian despite the fluctuations. This approximation is equivalent to assuming that the perturbed quantities δH and δf are small compared to the equilibrium quantities H_0 and f_0. In the core of tokamak plasmas, i.e. for $r/a < 0.8$ the fluctuations amplitude is typically of a few percents, see for example [26].
Using the angular variables $\vec{\vartheta}$ and the action variables $\vec{J}$, δH and δf can then be developed in Fourier series with respect to the angular variables such that:

$$\begin{aligned}
\delta H(\vec{J}, \vec{\vartheta}, t) &= \sum_{\vec{n}\omega} H_{\vec{n}\omega}(\vec{J}) e^{i(\vec{n}.\vec{\vartheta} - \omega t)} \\
\delta f(\vec{J}, \vec{\vartheta}, t) &= \sum_{\vec{n}\omega} f_{\vec{n}\omega}(\vec{J}) e^{i(\vec{n}.\vec{\vartheta} - \omega t)}
\end{aligned} \tag{2.7}$$

ω is the perturbation frequency. Its imaginary part, if positive, is the so called growth rate characterizing unstable modes.
Now, if one supposes that the growth time (γ^{-1}) and the spatial scales of the perturbations are respectively smaller than the equilibrium evolution time and the gradient lengths of the equilibrium quantities (T_s, n_s, $U_\parallel$), one can account only for the first derivatives of the equilibrium quantities with respect to $\vec{J}$. Moreover, if one neglects the non-linear terms, i.e. the quadratic terms of the fluctuating quantities, then the linearized Vlasov equation can be

written as:

$$f_{\vec{n}\omega}(\vec{J}) = -\vec{n}\cdot\frac{df_0(\vec{J})}{d\vec{J}}\frac{1}{\omega-\vec{n}\cdot\frac{dH_0(\vec{J})}{d\vec{J}}+i0^+}H_{\vec{n}\omega}(\vec{J}) \tag{2.8}$$

In the electrostatic case: $H_{\vec{n}\omega}(\vec{J}) = e_s\phi_{\vec{n}\omega}(\vec{J})$.
And with:

$$f_{0,s}(\vec{J}) = n_s\frac{1}{(2\pi m_s T_s)^{3/2}}e^{-\left(\frac{m_s(v_\parallel-U_\parallel)^2}{2}+\frac{m_s {v_\perp}^2}{2}\right)/T_s} \tag{2.9}$$

One obtains for the linearized Vlasov equation:

$$f_{\vec{n}\omega}(\vec{J}) = -\frac{f_0(\vec{J})}{T_s}(1-\frac{\omega-\vec{n}\cdot\vec{\omega}_s^*-\vec{n}\cdot\vec{\omega}_E}{\omega-\vec{n}\cdot\vec{\Omega}_J+i0^+})e_s\phi_{\vec{n}\omega}(\vec{J}) \tag{2.10}$$

In this form, the adiabatic response is singled out. $\vec{n}\cdot\vec{\Omega}_J = \vec{n}\cdot\frac{dH_0(\vec{J})}{d\vec{J}}$ is the drift frequency representing the forces felt in the tokamak electromagnetic field, $\vec{n}\cdot\vec{\omega}_E = \vec{n}\cdot\frac{e_s d\phi}{T_s d\vec{J}}$ is the $E\times B$ drift and $\vec{\omega}^*$ is the diamagnetic frequency which represents the instability drive term since it expresses the departures from thermodynamical equilibrium of the quantities T_s, n_s and $U_\parallel$ such that:

$$\vec{\omega}_s^* = T_s\left(\frac{1}{n_s}\frac{dn_s}{d\vec{J}}+\left(\mathcal{E}-\frac{3}{2}-\frac{U_\parallel}{v_{T_s}}\left(\frac{2v_\parallel-U_\parallel}{v_{T_s}}\right)\right)\frac{1}{T_s}\frac{dT_s}{d\vec{J}}+2\left(\frac{v_\parallel-U_\parallel}{v_{T_s}}\right)\frac{dU_\parallel}{d\vec{J}}\frac{1}{v_{T_s}}\right) \tag{2.11}$$

with $\mathcal{E} = \frac{\frac{m_s {v_\parallel}^2}{2}+\frac{m_s {v_\perp}^2}{2}}{T_s}$ and v_{T_s} such that $T_s = \frac{1}{2}m_s v_{T_s}^2$.
To express in greater details the linearized Vlasov equation in a tokamak the angular and actions variables need to be defined, this is done in the section below. Then the electroneutrality will be expressed providing a dispersion relation of which $\phi_{\vec{n}\omega}(\vec{J})$ will be the eigenfunctions and ω the eigenvalues. The electroneutrality will be further simplified thanks to the use of the ballooning transform and of a test eigenfunction derived in the fluid limit. All these points are detailed in the following.

2.1.2 Angular and action variables

The three conserved quantities $\vec{J} = (J_1, J_2, J_3)$ along the trajectories of particles in a tokamak have to be identified together with their associated frequencies $\vec{\vartheta} = (\vartheta_1, \vartheta_2, \vartheta_3)$.

Derivation of the 1st invariant, J_1, and its associated frequency, ω_1

The presence of a strong magnetic field implies that the cyclotronic motion is such that its frequency ω_c is much larger than the characteristic frequency of the modes ω. Under the condition $\omega_c >> \omega$, the magnetic moment $\mu = \frac{m_s v_\perp^2}{2B}$ is an adiabatic invariant of the motion as first demonstrated in [56] (see the dedicated section of Y. Sarazin's lectures [10]). Here B is the magnetic field. In order to obtain the angular variable ϑ_1 such that $\frac{d\vartheta_1}{dt} = \frac{dH}{dJ_1} = \omega_c$, J_1 is such that $J_1 = \frac{m_s}{e_s}\mu$.
Taking advantage of the fact that the cyclotronic motion can be decoupled, one gets:

$$\begin{cases} r = r_G + \rho_{cs} cos(\vartheta_1) \\ \theta = \theta_G + \frac{\rho_{cs}}{r} sin(\vartheta_1) \\ \varphi = \varphi_G \end{cases}$$

where $r_G, \theta_G, \vartheta_G$ are the guiding center coordinates. The coordinates have been shifted from the angle-action variables to the more intuitive coordinates of a tokamak, namely the toroidal angle, φ, the poloidal angle, θ, and the radial distance from the magnetic axis, r.

Derivation of the 2nd invariant, J_2, and its associated frequency, ω_2

The exact conservation of the guiding center energy $E = \frac{1}{2} m_s v_\parallel^2 + \mu B$ is associated to J_2. The angular variable ϑ_2 is associated to the frequency characterizing the motion along the field line, neglecting the departures due to the curvature and $\vec{\nabla} B$ drifts. For the trapped particles it will be the bounce frequency, for the passing the transit frequency, ω_2 such that:

$$\omega_2 = \frac{\vartheta_2}{dt} = \frac{2\pi}{T_2} = \frac{2\pi}{\oint d\theta \frac{1}{d\theta/dt}} \tag{2.12}$$

with :

$$d\theta/dt = J(\theta, \psi) v_\parallel \simeq \frac{v_\parallel}{qR} \tag{2.13}$$

where $J(\theta, \psi) = \frac{\vec{B}}{B} \cdot \vec{\nabla}\theta$ is the Jacobian, which in circular geometry is simply $\frac{1}{qR}$. R is the major radius and q – named the safety factor – represents the number of toroidal revolutions performed by a field line for one poloidal revolution. The parallel velocity $v_\parallel$ is expressed as follows:

$$v_\parallel = \sqrt{\frac{2T_s}{m_s}} \epsilon_\parallel \sqrt{\mathcal{E}} \sqrt{1 - \lambda b(r, \theta)} \tag{2.14}$$

With $\mathcal{E} = \frac{E}{T_s}$, $\lambda = \frac{\mu B(r,\theta=0)}{E}$, $\epsilon_\parallel = \pm 1$ and, in the large aspect ratio circular geometry, $b(r,\theta) = \frac{B(r,\theta)}{B(r,0)} \simeq 1 - \frac{r}{R} cos\theta$, since $\frac{r}{R} \ll 1$.
Hence:

$$\omega_2 = \frac{v_{Ts}}{qR} \epsilon_\parallel \sqrt{\mathcal{E}} \bar{\omega_2}(r,\lambda) \tag{2.15}$$

With:

$$\bar{\omega_2}(r,\lambda) = \frac{1}{\oint \frac{d\theta}{2\pi} \frac{1}{\sqrt{1-\lambda b(r,\theta)}}} \tag{2.16}$$

$\oint$ stands for a complete poloidal revolution for passing particles and for a back and forth trajectory for trapped particles.
ω_2 is the average poloidal rotation frequency for passing particles, and the bounce frequency for trapped particles.

Derivation of the 3rd invariant, J_3, and its associated frequency, ω_3

Assuming that the system is invariant with respect to the toroidal direction (i.e. neglecting the toroidal field ripple and other toroidal variations of the field such as Resonant Magnetic Perturbations), then the toroidal angular momentum is an invariant according to Hamilton's equations (see Y. Sarazin's lecture for a more detailed derivation [10]).Therefore, the third quantity which is conserved is the toroidal angular momentum of guiding center, $M = e_s \Psi + m_s R V_\varphi$, where Ψ is the poloidal magnetic flux. In the case of a circular cross section, Ψ at r_0 is : $\int_0^{r_0} 2\pi R B_\theta dr$ where B_θ is the poloidal magnetic field. In the case of uniform B_θ, the angular variable ϑ_3 would be such that $\frac{d\vartheta_3}{dt} = \frac{v_\parallel}{R} = \frac{d\varphi}{dt}$. This is not the case in a tokamak, where B_θ varies across r. Therefore ϑ_3 associated to J_3 is such that:

$$\begin{cases} r_G = \bar{r} + \tilde{r}(H,\mu,\bar{r},\vartheta_2) \\ \theta_G = \bar{\epsilon}\vartheta_2 + \tilde{\theta}(H,\mu,\bar{r},\vartheta_2) \\ \varphi_G = \vartheta_3 + q(\bar{r})\tilde{\theta}(H,\mu,\bar{r},\vartheta_2) + \tilde{\varphi}(H,\mu,\bar{r},\vartheta_2) \end{cases} \tag{2.17}$$

Where $\bar{\epsilon}$ equals 0 for trapped and 1 for passing particles and $q(\bar{r}) = \frac{d\varphi_G}{d\theta_G}$.
$\tilde{\varphi}$ symbolizes the difference between the toroidal precession in a circular equilibrium and the toroidal precession in a more general equilibrium including elongation and triangularity. In the following $\tilde{\varphi}$ is neglected. Therefore by taking $\varphi_G = \vartheta_3 + q(\bar{r})\tilde{\theta}(H,\mu,\bar{r},\vartheta_2)$ a circular equilibrium is assumed.
From the equations above, one sees that the frequency $\omega_3 = \frac{d\vartheta_3}{dt}$ depends on both $\frac{d\varphi_G}{dt}$ and on $\frac{d\theta_G}{dt}$. The equations of motion are needed to express the temporal evolution of the guiding coordinates. The guiding center equations of motion are derived in detail in books such as [57] or [10]. Its projection

on the three directions of interest are:

$$\begin{cases} \frac{dr_G}{dt} = V_{Dr} \\ \frac{d\theta_G}{dt} = \frac{V_\parallel}{qR} + \frac{V_{D\theta}}{r} + \frac{V_{E\theta}}{r} \\ \frac{d\varphi_G}{dt} = \frac{V_\parallel}{R} \end{cases} \tag{2.18}$$

With the drift velocity in a static electromagnetic field:

$$\vec{V}_{Gs\perp} = \vec{V}_{Ds} + \vec{V}_E = \frac{\vec{F}_{Ds} \times \vec{B}}{e_s B^2} + \frac{\vec{E} \times \vec{B}}{B^2} \tag{2.19}$$

Where:

$$\vec{F}_{Ds} = -m_s V_\parallel^2 \frac{\vec{N}}{R} - \mu \vec{\nabla} B \tag{2.20}$$

is the force due to the curvature (centrifugal acceleration) and the gradient of $\vec{B}$. $\vec{N}$ is the unit vector normal to $\vec{B}$.
It is anticipated that tokamak perturbations are very elongated along the field lines such as the parallel wave vectors $k_\parallel$ are much smaller than the perpendicular wave vectors $k_\perp$. Therefore the perpendicular drifts remain smaller than the parallel motion along the field line, i.e. $\frac{V_\parallel}{qR} \gg \frac{V_{Ds}+V_E}{r}$. This has been used to characterize ω_2. On the contrary $\omega_3 = \frac{d\vartheta_3}{dt}$ represents the drift frequency due to the curvature and gradient of $\vec{B}$. Indeed, in circular geometry, $\vartheta_3 = \varphi_G - q(\bar{r})\tilde{\theta}$, with:

$$\frac{d\vartheta_3}{dt} = -\frac{q(V_{D\theta} + V_{E\theta})}{r} - \frac{dq}{dr} V_{Dr} \theta \tag{2.21}$$

Hence :

$$\frac{d\vartheta_3}{dt} \simeq -\frac{qV_{D_s}}{r} \langle cos\theta + (s\theta - \alpha sin\theta) sin\theta \rangle - \frac{q}{r} V_{E\theta} \tag{2.22}$$

where $s = \frac{r}{q}\frac{dq}{dr}$ is called the magnetic shear and $\alpha = q^2\beta\frac{-R\nabla P}{P}$, with $\beta = \frac{P}{B^2/(2\mu_0)}$ the ratio of the kinetic pressure P, to the magnetic pressure. μ_0 is the magnetic permeability. The historical reference for this so called $s-\alpha$ equilibrium is [58]. This equilibrium is valid for large aspect ratio only, its limitations in the gyrokinetic framework are discussed in [59]. When using the $s-\alpha$ equilibrium, for low β cases, the curvature and the ∇B drifts have similar expressions and are both proportional to $(cos\theta + (s\theta - \alpha sin\theta) sin\theta)$ as derived for example in [60].
Therefore, one finally obtains:

$$\omega_3 \simeq \frac{d\vartheta_3}{dt} = -\frac{qV_{Ds}}{r} \bar{\omega}_2(r,\lambda) \oint \frac{d\theta}{2\pi} \frac{1}{\sqrt{1-\lambda b(r,\theta)}} (cos\theta + (s\theta - \alpha sin\theta) sin\theta) + \omega_E \tag{2.23}$$

With $V_{Ds} = \bar{\omega}_{ds}\mathcal{E}\,(2 - \lambda b)$ and $\omega_E = -\frac{q}{r}V_{E\theta}$ with $\bar{\omega}_{ds} = \frac{T_s}{e_s BR}$.
For passing particles, ω_3 is the toroidal rotation frequency. It is the toroidal precession frequency for trapped particles.

2.1.3 The gyrokinetic approximation

In the previous subsection, three invariants of motion associated to three frequencies were outlined. They are associated to three types of quasi-periodic motions: (1) the fast gyromotion around the magnetic field lines, (2) an intermediate bounce motion along the parallel direction due to the parallel gradients and (3) a slow motion across the field lines driven by magnetic curvature and the transverse gradients. The gyrokinetic theory takes advantage of this time scale separation to gyroaverage the fluctuating potential seen by a guiding center particle [61]. To be applicable, and reduce the problem from 6 dimensions down to 5 dimensions, some spatial and temporal ordering must be met. Taking L as a typical macroscopic spatial scale, such as the plasma minor radius a or a gradient length $T/|\nabla T|$, the most relevant relation is:

$$\frac{\rho_c}{L} \ll 1 \tag{2.24}$$

Stating that the Larmor radius ρ_c is negligible compared to the other characteristic lengths of the problem.
Using the modern formalism of gyrokinetic theory [62, 63] (for further details see for example J. Abiteboul PhD thesis part 2.2 [64]) the Hamiltonian can be exactly expressed as:

$$H = \frac{m_s {v_\parallel}_G^2}{2} + \frac{m_s {v_\perp}_G^2}{2} + e_s J \cdot \phi \tag{2.25}$$

H being now the gyrocenter Hamiltonian, with:

$$J \cdot \phi = \int \phi \frac{1}{2\pi} d\vartheta_1 = \int_{-\infty}^{+\infty} \frac{d^3\vec{k}}{(2\pi)^2} J_0(k_\perp \rho_c) \hat{\phi}_{\vec{k}} e^{i\vec{k}\vec{x}} \tag{2.26}$$

Where J_0 is the Bessel function of first order. The general Vlasov equation can be rewritten using a gyroaveraged distribution function.
In addition to this ordering, the fluctuating parts are often assumed to be small compared to the equilibrium ones:

$$\frac{|\delta\vec{B}|}{\vec{B}} \simeq \frac{\delta f}{f_0} \simeq \mathcal{O}(\rho^*) \ll 1 \tag{2.27}$$

From this later ordering, the distribution function and the fields can be split in two parts: a slowly varying (in time and space) equilibrium part, characterizing the background quantities, and a fast varying fluctuating part. In the so-called "full-f" gyrokinetic codes such as GYSELA [65] and GT5D [66], the distribution function f is not split. However, this approximation is carried out in most of the other gyrokinetic codes, in particular in QuaLiKiz and in the codes used later in this report such as GS2, GENE, GYRO or GKW.

2.1.4 Variational formulation of the electroneutrality

The linearized Vlasov equation has been expressed in equation (2.10). It needs to be coupled to the Maxwell equations in the electrostatic case. The gyroaverage leads to distribution functions of guiding centers, whereas Maxwell equations apply to particles. To solve this issue, the Maxwell equations can be expressed with the variational approach (details in [67, 50, 68, 51, 69]). According to the variational principle, the action $\int dt\mathcal{L}$ is extremal for any variation of the vector potential $\vec{A}$ and of the electric potential ϕ, where $\mathcal{L}$ is the electromagnetic Lagrangian defined by:

$$\mathcal{L}(\vec{A},\phi) = \int d^3\vec{x}\left(\frac{\epsilon_0\vec{E}^2}{2} - \frac{\vec{B}}{2\mu_0}\right) + \int d^3\vec{x}\left(\vec{j}\cdot\vec{A} - \rho\phi\right) \tag{2.28}$$

where $\vec{j}$ is the current density, ρ the density of charge and $d^3\vec{x}$ the volume element.
For relevant wavelengths much larger than the Debye length, the Poisson equation leads to the electroneutrality such that $\sum_s n_s e_s = 0$ where n_s is the particle density. The particle density is such that $n_s = n_{G,s} + n_{pol,s}$ where $n_{G,s}$ is an integral in gyro-center phase-space and the polarization density $n_{pol,s}$ is a function of the electric potential and is of order ρ_s^2 (see section 2.2.3 of [64] for more details). In the following, $n_s \simeq n_{G;s}$ is assumed. The relevant Lagrangian becomes:

$$\mathcal{L}(\omega,\vec{n}) = \sum_s \mathcal{L}_s(\omega,\vec{n}) \tag{2.29}$$

where $\mathcal{L}_s$ is the particle Lagrangian defined for each species s by $\mathcal{L}_s(\omega,\vec{n}) = \int d^3\vec{x}\,(-\rho_s(\omega,\vec{n})\phi^*(\omega,\vec{n}))$. ω and $\vec{n}$ are such that, the perturbed distribution function : $\delta f = f_{\vec{n}\omega}e^{i\vec{n}\vec{\vartheta}-\omega t} + cc$. In the electrostatic case considered here, the variational principle states that the solution $\phi_{\vec{n}\omega}$ is an extremum of the Lagrangian for any variation of $\phi^*_{\vec{n}\omega}$. The variational form of the Maxwell

equations is then reduced to:

$$\mathcal{L}_s(\omega,\vec{n}) = -\int d^3\vec{x}\rho_s(\omega,\vec{n})\phi^*_{\vec{n}\omega} \tag{2.30}$$

(Note that for resolving the Resistive Ballooning Modes at the very edge of tokamak plasmas [70], the current contribution to the variational form of the Maxwell equation should not be neglected.) And the electroneutrality condition leads to:

$$\sum_s \frac{\partial\mathcal{L}_s(\omega,\vec{n})}{\partial\phi^*_{\vec{n}\omega}} = -\sum_s \int d^3\vec{x}\rho_s(\omega,\vec{n}) = 0 \tag{2.31}$$

A weak formulation of the variational form of the electroneutrality condition is :

$$\sum_s \mathcal{L}_s(\omega,\vec{n}) = 0 \tag{2.32}$$

This form is exact in the case of a unique eigenfunction [51]. This weak form is the one used in the following.
Combining the weak variational formulation, equation (2.32), to the linearized Vlasov equation (2.10), one obtains the equation driving the electrostatic potential perturbations:

$$\sum_s \frac{e_s^2 f_0^s}{T_s}[\langle\phi_{\vec{n}\omega}\phi^*_{\vec{n}\omega}\rangle - \langle\frac{\omega-\vec{n}\cdot\vec{\omega}^*-\vec{n}\cdot\vec{\omega}_E}{\omega-\vec{n}\cdot\vec{\Omega}+i0^+}\phi_{\vec{n}\omega}\phi^*_{\vec{n}\omega}\rangle] = 0 \tag{2.33}$$

where $\langle ...\rangle = d^3\vec{\vartheta}d^3\vec{J}...$
Here the abiabatic part is summed to the non-adiabatic one. An alternative formulation of the dispersion relation isolates the polarization term and the gyrocenter part [63].
There are 6 dimensions to the problem. Thanks to the gyroaverage the dimensions can be reduced from 6 to 5. The toroidal axisymmetry allow for a further dimensional reduction down to 4. The ballooning transform detailed below will allow simplify further the numerical treatment of equation (2.33).

2.1.5 Ballooning transform

When the Vlasov equation of each species is coupled to the variational form of the electroneutrality, assuming a toroidal symmetry, a 4D dispersion relation is obtained.
In this system, the perturbed electrostatic potential is expressed as:

$$\delta\phi(\vec{\vartheta},\vec{J},t) = \sum_{\vec{n}\omega}\phi_{\vec{n}\omega}(\vec{J})e^{i(\vec{n}\cdot\vec{\vartheta}-\omega t)}$$

The periodicity with respect to the variables $\vec{\vartheta}$ allows writing:

$$\phi_{\vec{n}\omega}(\vec{J}) = \int_0^{2\pi} \frac{d^3\vartheta}{(2\pi)^3} \phi_{n\omega}(r,\theta,\varphi) e^{-i\vec{n}\cdot\vec{\vartheta}} \tag{2.34}$$

By accounting for the toroidal axisymmetry one gets:

$$\phi_{\vec{n}\omega}(r,\theta,\varphi) e^{-i\vec{n}.\vec{\vartheta}} = \tilde{\phi}_1(r,\theta) e^{-in\varphi} \tag{2.35}$$

The poloidal symmetry cannot be used since the magnetic field varies strongly with the poloidal angle: $b(r,\theta) = \frac{B(r,\theta)}{B(r,0)} \simeq 1 - \frac{r}{R} cos\theta$. Since the dynamics along the field line is stronger than the dynamic across the field line $\frac{V_\parallel}{qR} \gg \frac{V_{Ds}+V_E}{r}$, i.e. $k_\parallel \ll k_\perp$, one can assume that the dependence in θ is comprised of a slowly varying envelope on the resonant field line with n (toroidal mode number) and m (poloidal mode number) helicity, and a eikonal part with $n(\phi + q(r)\theta)$ dependence, which is rapidly varying off the resonant surface. This ordering is at the heart of the ballooning transform. $q(r) = q_0 + \frac{x}{nd}$, where $q_0 = m/n$ is the safety factor of the resonant surface, $d = \frac{1}{n\nabla q}$ the distance between resonant surfaces and $x = r - r_0$ is the distance from r_0 labeling the resonant surface. References and inspiring explanations of this transform can be found in annex B of X. Garbet's Habilitation à Diriger des Recherches [51], see also [71] and references therein, the appendix B3 of P. Beyer's Habilitation à Diriger des Recherches [72].
Based on this ordering, $\tilde{\phi}_1$ is expressed as the product of two terms: a resonant part, $e^{im\theta}$ and a part varying slowly with θ, $\tilde{\phi}_2(r,\theta)$:

$$\tilde{\phi}_1(r,\theta) = \tilde{\phi}_2(r,\theta) e^{im\theta} \tag{2.36}$$

Using the field aligned coordinate $\varphi - q(r)\theta$ (see Beer's PhD for more details [12]):

$$\phi_{\vec{n}\omega}(r,\theta,\varphi) e^{-i\vec{n}.\vec{\vartheta}} = \tilde{\phi}_2(r,\theta) e^{-in(\varphi - q(x)\theta)} \tag{2.37}$$

When assuming $q(x) \simeq q_0 + \frac{x}{nd}$, it is supposed that the radial wave length of the turbulence is small compared to $q/\nabla q$. Also assuming a slowly varying part with respect to θ means that the characteristic scale length of the turbulence is also small compared to the gradient length at play, meaning that one can assume to be not far from the thermodynamical equilibrium, such that $\nabla_r(\nabla_r T/T, \nabla_r n/n) \simeq 0$. There is therefore no $\nabla_r(k_r)$ in the equations solved. k_r is hence a parameter. To take advantage of the existence of such a parameter, $\tilde{\phi}_2(r,\theta)$ is rewritten as:

$$\tilde{\phi}_2(r,\theta) = \sum_p \phi_p(\theta,\theta_b) e^{i(\theta_b + 2p\pi)\frac{x}{d}} \tag{2.38}$$

The parameter θ_b is called the ballooning angle. It is linked to k_r, such that $k_r d = \theta - \theta_b$ as will be demonstrated later.
One is free to rewrite $\tilde{\phi}_2(r,\theta)$ such that:

$$\tilde{\phi}_2(r,\theta) = \sum_p \phi_p(\theta,\theta_b) e^{-inq_0(\theta_b+2p\pi)} e^{in(q_0+\frac{x}{nd})(\theta_b+2p\pi)} \tag{2.39}$$

Leading to:

$$\phi_{\vec{n}\omega}(r,\theta,\varphi) e^{-i\vec{n}.\vec{\vartheta}} = \sum_p e^{-in(\varphi - q(x)(\theta-\theta_b-2p\pi))} \phi_p(\theta,\theta_b) e^{-inq_0(\theta_b+2p\pi)} \tag{2.40}$$

In a tokamak, thanks to simulations treating the complete 4D problem (GENE [22], GKW [29], GS2 [30], GYRO [23], etc), it is known that the most unstable modes are localized around $\theta_b = 0$ due to the dominant interchange nature of the instabilities. Hence in the following $\theta_b \simeq 0$ is chosen. In presence of finite rotation $\nabla U_\parallel \neq 0$ and of finite $E \times B$, the ballooning angle if shifted away from zero. The shift remains below 5% of π for finite and rather large values $\nabla U_\parallel$ and γ_E as illustrated later by figures 2.7 and 2.8. Therefore in the following, for all cases, $\theta_b \simeq 0$ is assumed.
It is also known from simulations treating the 4D problem that the linear eigenmodes are usually well localized in $\theta = [-\pi, \pi]$. Some illustrations of this will be given later. In the lowest order ballooning representation, $\phi_p(\theta) = \phi_{n\omega}(\theta)$ is assumed to be identical on all resonant surfaces.

$$\phi_{\vec{n}\omega}(r,\theta,\varphi) e^{-i\vec{n}.\vec{\vartheta}} = \sum_{p=-\infty}^{+\infty} e^{-in(\varphi - q(x)\theta)} \phi_{n\omega}(\theta) \tag{2.41}$$

The eigenfunction to be solved is then the 1D θ function $\phi_{n\omega}(\theta)$.
As promised earlier, the link between k_r and θ is expressed:

$$\partial_r \phi_{n\omega}(\theta) \equiv -\imath k_r \phi_{n\omega}(\theta) \rightarrow -\imath n \frac{\mathrm{d}q}{\mathrm{d}r} \theta \hat{\phi}_{n\omega}(\theta) \tag{2.42a}$$

$$\partial_\theta \phi_{n\omega}(\theta) \equiv -\imath k_\theta r \phi_{n\omega}(\theta) \rightarrow -\imath n q \hat{\phi}_{n\omega}(\theta) \tag{2.42b}$$

Therefore, k_r is such that $\theta = k_r d$ and $k_\theta = nq/r$. Meaning that, in the ballooning representation, ∂_θ can be replaced by ∂_{k_r}/d.
The parallel wave number $k_\parallel = -i\nabla_\parallel$ is such that: $\nabla_\parallel = \partial_\theta/(qR)$, with $\partial_\theta = \partial_{k_r}/d$, and $\partial_{k_r} = -\imath x$. Therefore, $k_\parallel$ is given by:

$$k_\parallel \simeq \dot{k}_\parallel x = \frac{x}{qRd} = \frac{k_\theta s}{qR} x \tag{2.43}$$

These expressions will be used in section 2.2 to simplify the dispersion relation from equation (2.33).

2.1.6 Phase space element

In the following, it will be important to express the phase space element $d^3\vartheta d^3J$ when integrating the distribution function to derive the electroneutrality.

As discussed earlier, the three invariants are respectively the magnetic moment, the guiding center energy and the toroidal angular moment. Three action variables J_1, J_2 and J_3 have been derived. The phase space element $d^3\vec{J}d^3\vartheta$ needed for the integrations in the dispersion relation, is derived in the simplified electrostatic $s-\alpha$ case considered here with:

$$\begin{cases} dJ_1 = -\frac{m_s}{e_s}d\mu \\ dJ_2 = \frac{dE}{\omega_2} \\ dJ_3 = -e_s B_\theta R dr \end{cases}$$

Leading to:

$$d^3\vec{J} = \mid \frac{m_s}{e_s}d\mu\frac{dE}{\omega_2}e_s B_\theta R dr \mid \frac{1}{2}\Sigma_{\epsilon_\parallel} \tag{2.44}$$

or :

$$d^3\vec{J} = rRdr\frac{(m_s T_s)^{3/2}}{\sqrt{2}}\sqrt{\mathcal{E}}d\mathcal{E}\frac{d\lambda}{\bar{\omega}_2}\frac{1}{2}\Sigma_{\epsilon_\parallel} \tag{2.45}$$

The integration in r does not take place in the framework presented. Indeed all quantities are assumed to be independent of the radial location in this local approach where the gradient lengths are all taken fixed.
$d^3\vartheta$ is simplified by the gyroaverage over ϑ_1, the assumed toroidal axisymmetry over ϑ_3, and the ballooning approximation over ϑ_2. The integration will only be carried out over ϑ_2, i.e. either k_r, θ or x since the ballooning transform is used here.
Ultimately a 3D integration remain to be carried out: in energy, in pitch angle and in k_r.

2.2 The final dispersion relation

Within the framework reviewed in the previous section: linearized Vlasov equation, electrostatic fluctuations only, gyroaveraged and using the lowest order ballooning transform, the dispersion relation to be solved can now be expressed. Three dimensions are retained, two in velocity (or action variable): the energy $\mathcal{E}$ and the pitch angle λ, and one in space (or angle variable), the radial direction r which can be related to the angle along the field lines θ through the ballooning transform. The trapped and passing particles will

be treated separately to take advantage of their specific characteristics in reducing the integration dimensions from three to two. One should remember that the goal of the present work is to have a sufficiently fast code for allowing systematic comparison to experiments. The methods used to find the eigenfunctions and the eigenvalues are detailed later and validated against gyrokinetic codes which do not use either the ballooning approximation or the simplified integrals described in this section.

2.2.1 General dispersion relation

When implementing the Maxwellian equilibrium distribution function (equation (2.5)) in the weak variational form of the electroneutrality constraint (equation (2.33)), together with the phase space element from equation (2.44), one obtains:

$$\sum_{p=-\infty}^{+\infty} \sum_s \frac{e_s^2 n_s}{T_s} \int\int\int \frac{2}{\sqrt{\pi}} \sqrt{\mathcal{E}} \mathrm{d}\mathcal{E} \frac{\mathrm{d}\lambda}{4\bar{\omega}_2} \frac{\mathrm{d}k_r}{2\pi} \exp\left(-\frac{U_\parallel^2 - 2v_\parallel U_\parallel}{v_{T_s}^2} - \mathcal{E}\right) \left(1 - \frac{\omega - n\omega_s^* - n\omega_E}{\omega - n\Omega_{Js} + i0^+}\right) J_0^2 \left|\phi_{n\omega}(k_r)\right|^2 = 0 \quad (2.46)$$

Or in short:

$$\sum_s \frac{e_s^2 n_s}{T_s} \left(1 - \mathcal{L}_s(\omega)\right) = 0 \quad (2.47)$$

Where $n\omega_s^*$ is as defined in equation (2.11), where the gradients are taken versus $dJ_3 = -e_s B_\theta R dr$ hence with respect to r and $n\Omega_J = n_2\omega_2 + n_3\omega_3 + n\omega_E$. From the ballooning transform, equation (2.43), $n_2 = \frac{x}{d}$ and $n_3 = n$. ω_2 is expressed thanks to equation (2.15) and ω_3 from equation (2.23). And $n\omega_E = -k_\theta \frac{E_r}{B} = -n\frac{q}{r}\frac{E_r}{B}$.
In the low Mach number limit, relevant for tokamak plasmas, the exponential: $\exp\left(-\frac{U_\parallel^2 - 2v_\parallel U_\parallel}{v_{T_s}^2}\right)$ is approximated by $1 + \frac{2v_\parallel U_\parallel}{v_{T_s}^2} + \frac{U_\parallel^2}{v_{T_s}^2}\left(2\frac{v_\parallel^2}{v_{T_s}^2} - 1\right)$.
The gradient of the bulk rotation $U_\parallel$ is accounted for. Therefore the gradient of E_r is also considered. From the force balance equation, one gets:

$$E_r = U_\phi B_\theta - U_\theta B_\phi + \frac{\nabla_r P_s}{n_s e_s} \quad (2.48)$$

In large aspect ratio tokamaks, $U_\parallel \simeq \frac{U_\phi}{1+\left(\frac{\epsilon}{q}\right)^2}$. From the ballooning approximation, the second derivatives of density or temperature profiles are assumed

negligible, hence the contributions of $\nabla_r U_\theta$ and $\nabla_r(\nabla_r P_s)$, since from neoclassical theory [55] $U_\theta \propto \nabla T_i$. Therefore $\nabla_r E_r \simeq \left(\nabla_r U_\parallel B_\theta + U_\parallel B_\theta \frac{1-s}{r}\right)\left(1+\left(\frac{\epsilon}{q}\right)^2\right)$ and $\varpi = \omega - n\omega_E = \omega - n\omega_{E0} - n\nabla_r\omega_E x = \omega' - n\nabla_r\omega_E x = \omega' - k_\theta\gamma_E x$, with $\gamma_E = -\frac{\nabla E_r}{B}$.
Therefore the functional $\mathcal{L}_s(\omega)$ can be written as:

$$\mathcal{L}_s(\omega) = \int\int\int \frac{2}{\sqrt{\pi}}\sqrt{\mathcal{E}}\mathrm{d}\mathcal{E}\frac{\mathrm{d}\lambda}{4\bar{\omega}_2}\frac{\mathrm{d}k_r}{2\pi}e^{-\mathcal{E}}\left(1+\frac{2U_\parallel}{v_{T_s}}\epsilon_\parallel\sqrt{\mathcal{E}(1-\lambda b)}+\frac{U_\parallel^2}{v_{T_s}^2}\left(2\mathcal{E}(1-\lambda b)-1\right)\right) \frac{n\omega^*_{ns}+n\omega^*_{Ts}(\mathcal{E}-\frac{3}{2})+2(n\omega^*_{U_\parallel}-\frac{U_\parallel}{v_{T_s}}n\omega^*_{Ts})\epsilon_\parallel\sqrt{\mathcal{E}(1-\lambda b)}+\frac{U_\parallel}{v_{T_s}}(\frac{U_\parallel}{v_{T_s}}n\omega^*_{Ts}-2n\omega^*_{U_\parallel})-\varpi}{n\bar{\omega}_{ds}f(\lambda,k_r)\mathcal{E}+\frac{x}{d}\omega_2(\mathcal{E},\lambda)-\varpi+i0^+}J_0^2|\phi_{n\omega}|^2 \tag{2.49}$$

Where $n\omega^*_{Ts} = \frac{nq}{r}\frac{T_s}{e_sB}\frac{\nabla T_s}{T_s} = -k_\theta\frac{T_s}{e_sBR}A_{Ts}$ with:$A_{Ts} = -\frac{R\nabla T_s}{T_s}$, $n\omega^*_{ns} = \frac{nq}{r}\frac{T_s}{e_sB}\frac{\nabla n_s}{n_s} = -k_\theta\frac{T_s}{e_sBR}A_{ns}$ with:$A_{ns} = -\frac{R\nabla n_s}{n_s}$ and $n\omega^*_{U_\parallel} = \frac{nq}{r}\frac{T_s}{e_sB}\frac{\nabla U_\parallel}{v_{T_s}} = -k_\theta\frac{T_s}{e_sBR}A_{us}$ with:$A_{us} = -\frac{R\nabla U_\parallel}{v_{T_s}}$.

Since the equilibrium distributions are Maxwellians, most of the particles have an energy centered around the thermal value. Using this property, the energy integration of the Bessel functions can be approximated by carrying them out separately from the rest as follows:

$$\int_0^{+\infty}\frac{2}{\sqrt{\pi}}\sqrt{\mathcal{E}}e^{-\mathcal{E}}d\mathcal{E}J_0^2(a\mathcal{E}) = e^{-a^2}I_0(a^2) = \mathcal{B}(a) \tag{2.50}$$

The drift frequencies at the denominator depend both on the three variables k_r or x, λ and $\mathcal{E}$. The curvature and ∇B drift frequency and then the transit frequency will be expressed separately for trapped and passing particles and simplified.

Simplification of the curvature and ∇B drift frequency

From equation (2.23), the curvature and ∇B drift frequency, $n\bar{\omega}_{ds}f(\lambda,k_r)\mathcal{E}$, such that: $f(\lambda,k_r) = (2-\lambda b)\left(\cos(k_r d) + (sk_r d - \alpha\sin(k_r d))\sin(k_r d)\right)$ and $n\bar{\omega}_{ds} = k_\theta\frac{T_s}{e_sBR}$. In QuaLiKiz, this frequency is simplified in two different ways for the passing and the trapped particles to reduce the integration numerical cost from 3D down to 2D.

- For trapped particles, $f(\lambda,k_r)$ is replaced by its average over k_r similarly to the derivation presented in [73], except that here, as previously

discussed, the curvature and ∇B drifts are identical which is correct in the low β limit. This leads to:

$$\langle f(\lambda, k_r)\rangle_{k_r} = F_t(\kappa) = 2\frac{E(\kappa)}{K(\kappa)} - 1 + 4s\left(\kappa^2 - 1 + \frac{E(\kappa)}{K(\kappa)}\right) - \frac{4\alpha}{3}\left(1 - \kappa^2(2\kappa^2 - 1) + \frac{E(\kappa)}{K(\kappa)}\right) \tag{2.51}$$

κ is defined by $\lambda = 1 - 2\epsilon\kappa^2$, $K(\kappa)$ and $E(\kappa)$ are respectively the elliptic integrals of the first and second kind, for more details on these functions see the Abramowitz and Stegun: Handbook of Mathematical Functions [74].
The average over k_r is performed over ϖ such as :

$$\varpi = \omega' - \langle k_\theta \gamma_E x\rangle_{k_r} = \omega' - k_\theta \gamma_E x_0 \tag{2.52}$$

As a consequence of this approximation, the Trapped Electron Modes are typically underestimated by QuaLiKiz at intermediate wave numbers ($k_\theta \rho_s \simeq 0.5 - 10$) when compared to codes where these approximations are not done (GENE [22], GKW [29], GS2 [30], GYRO [23]). For the trapped electrons, due to the energy dependence of the collision frequency, the integral with respect to $\mathcal{E}$ is not analytical, therefore the numerical integration is carried on both $\mathcal{E}$ and λ. For trapped ions, the collisions are neglected (they are a factor $\sqrt{\frac{m_e}{m_i}}$ smaller than the electron ones [7]), in this case, the energy integral takes the form of Fried and Conte analytical integrals and only one dimension (λ or κ) remains to be integrated numerically.

- For passing particles, by assuming very passing particles, i.e. with $v_\parallel \gg v_\perp$, the parallel dynamics dominate over the drifts and one can assume that the passing particles "feel" a pitch angle averaged curvature and ∇B drift. By doing this approximation, $f(\lambda, k_r)$ is replaced by its average over λ such that:

$$\langle f(\lambda, k_r)\rangle_\lambda = F_p(k_r) = \frac{4}{3}\left(\cos(k_r d) + (sk_r d - \alpha\sin(k_r d))\sin(k_r d)\right) \tag{2.53}$$

The factor $\frac{4}{3}$ is given by the integral in λ of the curvature and ∇B drift frequency obtained in the fluid limit, i.e. when developing the denominator in the limit $\omega \gg n\bar{\omega}_{ds} f(\lambda, k_r)\mathcal{E} + \frac{x}{d}\omega_2$.

Simplification of the transit frequency

The second frequency at the denominator is the transit frequency $\frac{x}{d}\omega_2$ see equation (2.15). Again, it will be treated differently for trapped and passing

particles.

- For passing particles, $k_\parallel V_\parallel = \frac{x}{d}\omega_2$ is averaged over the pitch angle λ as done for the curvature and ∇B drift. The justification is the same, for deeply passing particles, the drift frequency felt by the particles is the averaged one: $\left\langle k_\parallel v_\parallel \right\rangle_\lambda$. As above, the average is such that the fluid limit value is recovered, i.e. :

$$\left\langle k_\parallel v_\parallel \right\rangle_\lambda = -\frac{1}{\sqrt{3}}\frac{x}{d}\frac{v_{Ts}}{qR} \tag{2.54}$$

- For trapped particles, the bounce frequency is assumed to be much larger than the frequency of the modes ω, therefore a bounce average is performed. Then there is a negligible resonance between bouncing particle and wave, and x can be effectively set as 0 in the denominator. It is similar to the gyroaverage, see [75] for more details. This introduces – for trapped particles – an additional Bessel function multiplying the electrostatic potential such that:

$$\int \frac{dk_r}{2\pi}\mathcal{B}(k_\perp\rho_s)\mathcal{B}(k_r\delta_s)|\phi_{n\omega}(k_r)|^2$$

  Where ρ_s is the Larmor radius of the sepcies s and δ_s the banana width at the thermal velocity such that: $\delta_s = \frac{q}{\sqrt{\epsilon}}\rho_s$ (see [10] for a derivation of the banana width). As $\delta_s \gg \rho_s^{th}$, the main radial width for trapped particles is the banana width. The integral in k_r is done separately from the rest. It is carried out numerically using the fluid eigenfunction for $\phi_{n\omega}(k_r)$ detailed later.

The simplified dispersion relation

The passing particles are assumed very passing $v_\parallel \gg v_\perp$, the integration with respect to λ is highly simplified and they are numerically integrated with respect to $\mathcal{E}$ and k_r as detailed below. For trapped particles, the bounce frequency is assumed larger than the mode frequency, therefore a bounce-average is performed. They are integrated with respect to $\mathcal{E}$ and λ. Therefore, the dispersion relation (2.49) is now written as a sum of trapped and passing particles contributions (respectively $\mathcal{I}_{ts}$ and $\mathcal{I}_{ps}$) such that:

$$\begin{aligned}
&\sum_s \frac{e_s^2 n_s}{T_s}\left(1-\mathcal{L}_s(\omega)\right) = \\
&\sum_s \frac{e_s^2 n_s}{T_s}\left(1-\langle\mathcal{I}_{ps}\mathcal{B}(k_\perp\rho_s)|\phi_{n\omega}(k_r)|^2\rangle_{k_r,\mathcal{E}} - \langle\mathcal{I}_{ts}\rangle_{\lambda,\mathcal{E}}\left\langle\mathcal{B}(k_\perp\rho_s)\mathcal{B}(k_r\delta_s)|\phi_{n\omega}(k_r)|^2\right\rangle_{k_r}\right) = 0
\end{aligned} \tag{2.55}$$

Where the integration over the passing domain is:

$$\langle \cdots \rangle_{k_r,\mathcal{E}} = \int \frac{dk_r}{2\pi} \int_0^\infty \frac{2\sqrt{\mathcal{E}}}{\sqrt{\pi}} \exp(-\mathcal{E}) d\mathcal{E}$$

The integration over the trapped domain reads:

$$\langle \cdots \rangle_{\lambda,\mathcal{E}} = \int_0^\infty \frac{2\sqrt{\mathcal{E}}}{\sqrt{\pi}} \exp(-\mathcal{E}) d\mathcal{E} \int_{\lambda_c}^1 \frac{d\lambda}{4\bar{\omega}_2} \sum_{\epsilon_\parallel=\pm 1} = f_t \int_0^\infty \frac{2\sqrt{\mathcal{E}}}{\sqrt{\pi}} \exp(-\mathcal{E}) d\mathcal{E} \int_0^1 K(\kappa)\kappa d\kappa \sum_{\epsilon_\parallel=\pm 1}$$

With f_t is the fraction of trapped particles, $\lambda = \frac{\mu B(0)}{E}$, $\lambda_c = \frac{\mu B(\pi)}{E} 1 - 2\epsilon$ and $b = \frac{B(\theta)}{B(0)} \simeq 1 - \epsilon cos\theta$ in the circular large aspect ratio limit. κ is related to the pitch-angle via $\lambda = 1 - 2\epsilon\kappa^2$ and K is the complete elliptic integral of the first kind.

The detailed variational expressions, for $\mathcal{I}_{ts}$ and $\mathcal{I}_{ps}$, are given below, for trapped ions, trapped electrons and passing particles [14].

2.2.2 Trapped ions

The trapped ions are treated separately from the trapped electrons. Indeed collisions are taken into account for trapped electrons, which is not the case for trapped ions. When accounting for the simplifications detailed above, one obtains from equation 2.55:

$$\mathcal{I}_{ti} = 2\left(1 + \frac{2U_\parallel}{v_{Ti}}\epsilon_\parallel\sqrt{\mathcal{E}(1-\lambda b)} + \frac{U_\parallel^2}{v_{Ti}^2}\left(2\mathcal{E}(1-\lambda b) - 1\right)\right) \times \frac{A_{ni} + A_{Ti}(\mathcal{E} - \frac{3}{2}) + 2(A_u - \frac{U_\parallel}{v_{Ti}}A_{Ti})\epsilon_\parallel\sqrt{\mathcal{E}(1-\lambda b)} + \frac{U_\parallel}{v_{Ti}}(\frac{U_\parallel}{v_{Ti}}A_{Ti} - 2A_u) - \frac{\varpi}{n\bar{\omega}_{di}}}{F_t(\kappa)\mathcal{E} - \frac{\varpi}{n\bar{\omega}_{di}} + \imath o^+} \tag{2.56}$$

The energy integration over energy $\mathcal{E}$ can be performed analytically under the form of Fried and Conte integrals [74] Z such that:

$$Z(z) = \frac{1}{\sqrt{\pi}} \int_{-\infty}^{+\infty} \frac{e^{-v^2}}{v - z} \mathrm{d}v \tag{2.57}$$

and Z_1, Z_2 and Z_3 are defined are based on the Fried-Conte function Z: $Z_1(z) = z + z^2 Z(z)$, $Z_2(z) = \frac{1}{2}z + z^2 Z_1(z)$ and $Z_3(z) = \frac{3}{4}z + z^2 Z_2(z)$.

Including these functions leads to the following expression of the integrated trapped ions contribution:

$$\langle \mathcal{I}_{ti} \rangle_{\mathcal{E},\lambda} \simeq 2 f_t \int_0^1 \frac{K(\kappa)\kappa}{F_t(\kappa)} \mathrm{d}\kappa \Bigg[\left(1 - \frac{U_\parallel^2}{v_{Ti}^2}\right) \left(A_{Ti} \frac{Z_2(z)}{z} + \left(A_{ni} - \frac{3}{2} A_{Ti} - z^2 F_t(\kappa) \right) \frac{Z_1(z)}{z} \right) - \frac{U_\parallel}{v_{Ti}} \left(2A_u - \frac{U_\parallel}{v_{Ti}} A_{Ti} \right) \Bigg] \tag{2.58}$$

where z is the square root of $\frac{\varpi}{n\bar{\omega}_{di} F_t(\kappa)}$ which has a positive imaginary part. The integration with respect to κ is done numerically. Therefore in QuaLiKiz a one dimensional integral allows to calculate the trapped ions functional.

2.2.3 Trapped electron, accounting for collisions

For the derivation of a collision frequency in a plasma see section 1.6 of Nicholson's book [11]. Here, a Krook type collision operator is included in the linearized Vlasov equation for the perturbed distribution function of trapped electrons δf_e such that:

$$\frac{\partial \delta f_e}{\partial t} + [\delta f_e, H_{0,e}] + [f_{0,e}, \delta H_e] = -\nu_e \left(\delta f_e - \frac{\delta H_e}{T_e} f_0 \right) \tag{2.59}$$

For more details see the appendix of [76].

The collision frequency, as introduced in reference [77], is:

$$\nu_e(\mathcal{E}, \lambda) = \nu_{ei} \left(\mathcal{E}\right)^{-3/2} Z_{eff} \frac{r/R}{\left(1 - r/R - \lambda\right)^2} \frac{0.111\delta + 1.31}{11.79\delta + 1} \tag{2.60}$$

where ν_{ei} is the electron-ion Coulomb collision frequency, λ the pitch angle, v_{th} the electron thermal velocity, and $\delta = \left[\frac{|\omega|}{\nu_{ei} Z_{eff} 37.2R/r} \right]^{1/3}$ with ω the frequency of the unstable mode. The numerical values appearing in (2.60) and in the definition of the parameter δ are calculated in [21] by matching the solutions of equation (2.59) for the perturbed electron distribution function with analytical results and results obtained using a Lorentz collision operator. Electron-electron collisions are neglected since they would give a negligible correction to Z_{eff} in the expression for ν_e for the $\frac{v}{v_{th}} \ll 1$ ordering [21]. Furthermore, the electrons are assumed to be in the banana regime: $\nu_e \ll \frac{r}{R}\omega_{be}$ (where ω_{be} is the electron bounce frequency). Therefore the treatment of collisions on trapped electrons is not valid towards the Last

Closed Flux Surface of tokamak plasmas where the electrons are rather in the Pfirsch-Schlüter regime with $\nu_e > \frac{\omega_{be}}{\epsilon^{1/2}}$. Moreover, Resistive Ballooning Modes cannot be resolved by the code since the collisions on passing electrons are neglected.
Although momentum and energy are not conserved by equation (2.59), the fraction of trapped electrons remains unchanged in the banana regime approximation. Furthermore this equation has the conceptual advantage that, in the limit of high collisionality, it predicts a perturbed density equal to the density of a perturbed Maxwellian distribution. This can be seen by taking the first moment of equation (2.59) in the limit of infinite ν_e. In large aspect ratio tokamaks, trapped electrons exist in a portion of the velocity space proportional to $\epsilon = r/R$. The factor ϵ in the definition of ν_e represents the fraction of trapped particles: the smaller the trapped particle fraction, the smaller the effect of collisions on mode stability. The denominator $(1 - r/R - \lambda)^2$ takes into account the barely-trapped particles, situated in the vicinity of the velocity space boundary between the trapped and passing populations. When λ is finite and close to $(1 - \epsilon)$ the collision operator becomes large thus giving a higher weight to the small population of electrons at the boundary between trapped and passing domains, expected to play an important role in weak collisionality regimes [78]. The last factor in the parenthesis (which depends on δ) is a further correction to the collision operator for $\nu_e/\omega \ll 1$.

The collision modified non-adiabatic response of trapped electrons then becomes:

$$\mathcal{I}_{te} = \left(1 + \frac{2U_\parallel}{v_{th,e}}\epsilon_\parallel\sqrt{\mathcal{E}(1-\lambda b)} + \frac{U_\parallel^2}{v_{th,e}^2}\left(2\mathcal{E}(1-\lambda b) - 1\right)\right)$$
$$\frac{A_{Te}\mathcal{E} + 2(A_u - \frac{U_\parallel}{v_{th,e}}A_{Te})\epsilon_\parallel\sqrt{\mathcal{E}(1-\lambda b)} + A_{ne} - \frac{3}{2}A_{Te} + \frac{U_\parallel}{v_{th,e}}(\frac{U_\parallel}{v_{th,e}}A_{Te} - 2A_u) - \frac{\varpi}{n\bar{\omega}_{de}}}{F_t(\kappa)\mathcal{E} - \frac{\varpi}{n\bar{\omega}_{de}} + \imath\frac{\nu_e(\mathcal{E},\lambda)}{n\bar{\omega}_{de}}} \tag{2.61}$$

For electrons, due to the energy dependence of the collision frequency, the integrals in energy do not have the analytical Fried and Conte form, therefore a 2D numerical integration on $\mathcal{E}$ and λ has to be performed.

2.2.4 Passing particles

For passing particles, the same expression is used for electrons and ions:

$$
\begin{aligned}
&\mathcal{I}_{ps} = \\
&\left(1 + \frac{2U_\parallel}{v_{Ts}}\epsilon_\parallel\sqrt{\mathcal{E}(1-\lambda b)} + \frac{U_\parallel^2}{v_{Ts}^2}\left(2\mathcal{E}(1-\lambda b) - 1\right)\right) \\
&\frac{A_{Ts}\mathcal{E} + 2(A_u - \frac{U_\parallel}{v_{Ts}}A_{Ts})\epsilon_\parallel\sqrt{\mathcal{E}(1-\lambda b)} + A_{ns} - \frac{3}{2}A_{Ts} + \frac{U_\parallel}{v_{Ts}}(\frac{U_\parallel}{v_{Ts}}A_{Ts} - 2A_u) - \frac{\varpi}{n\bar{\omega}_{ds}}}{F_p(k_r)\mathcal{E} + \epsilon_\parallel\frac{x}{d}\frac{v_{Ts}(qR\sqrt{\mathcal{E}})}{n\bar{\omega}_{ds}} - \frac{\varpi}{n\bar{\omega}_{ds}} + \imath o^+}
\end{aligned}
\tag{2.62}
$$

Thanks to the simplified expressions for $k_\parallel v_\parallel$ and $f(\lambda, k_r)$ given in equations (2.54) and (2.53), the integral in λ is easily performed analytically. The integration with respect to $\mathcal{E}$ is carried out analytically using the Fried-Conte functions Z, Z_1, Z_2 and Z_3 defined earlier.
Only the integration with respect to k_r remains to be done numerically such that $\langle\mathcal{I}_{ps}\rangle_{\mathcal{E},\lambda,k_r} = \int \frac{dk_r}{2\pi}\langle\mathcal{I}_{ps}\rangle_{\mathcal{E},\lambda}$ with:

$$
\begin{aligned}
&\langle\mathcal{I}_{ps}\rangle_{\mathcal{E},\lambda} = \frac{f_p}{F_p(k_r)}\Bigg[\\
&2\left[A_{Ts}\frac{Z_2(V_+) - Z_2(V_-)}{V_+ - V_-} + \left(A_{ns} - \frac{3}{2}A_{Ts} - \frac{\varpi}{n\bar{\omega}_{ds}}\right)\frac{Z_1(V_+) - Z_1(V_-)}{V_+ - V_-}\right] + \\
&4\frac{U_\parallel}{v_{Ts}}\left[A_{Ts}\frac{V_+Z_2(V_+) - V_-Z_2(V_-)}{V_+ - V_-} + \left(A_u\frac{v_{Ts}}{U_\parallel} + \left(A_{ns} - \frac{5}{2}A_{Ts} - \frac{\varpi}{n\bar{\omega}_{ds}}\right)\right)\frac{V_+Z_1(V_+) - V_-Z_1(V_-)}{V_+ - V_-}\right] \\
&+ \frac{4}{3}\frac{U_\parallel}{v_{Ts}}\left[A_{Ts}\frac{U_\parallel}{v_{Ts}}\frac{Z_3(V_+) - Z_3(V_-)}{V_+ - V_-} + \left(2A_u + \frac{U_\parallel}{v_{Ts}}\left(A_{ns} - 5A_{Ts} - \frac{\varpi}{n\bar{\omega}_{ds}}\right)\right)\frac{Z_2(V_+) - Z_2(V_-)}{V_+ - V_-}\right] \\
&- 2\frac{U_\parallel}{v_{Ts}}\left[\left(2A_u + \frac{U_\parallel}{v_{Ts}}\left(A_{ns} - \frac{5}{2}A_{Ts} - \frac{\varpi}{n\bar{\omega}_{ds}}\right)\right)\frac{Z_1(V_+) - Z_1(V_-)}{V_+ - V_-}\right]\Bigg]
\end{aligned}
\tag{2.63}
$$

where f_p is the passing particle fraction. The variables V_+ and V_- correspond to the poles of Eq. (2.62). They are defined by:

$$
\begin{aligned}
V_\pm &= \frac{1}{2}\frac{v_{Ts}x}{qRd}\frac{\bar{\omega}_2}{F_p(k_r)n\bar{\omega}_{ds}} \pm \sqrt{\Delta} \\
\Delta &= \left(\frac{1}{2}\frac{v_{T_s}x}{qRd}\frac{\bar{\omega}_2}{F_p(k_r)n\bar{\omega}_{ds}}\right)^2 + \frac{\varpi}{F_p(k_r)n\bar{\omega}_{ds}}
\end{aligned}
\tag{2.64}
$$

The integration over k_r remains to be performed, for passing particles it cannot be simplified as done for trapped particles. Indeed, both the parallel drift frequency $\frac{x}{d}\omega_2$ and $n\omega_{E\times B}$ depend on x. x is an operator in k_r space

such that $x = -i\frac{d}{dk_r}$. Therefore $\langle \mathcal{I}_{ps} \rangle_{\mathcal{E},\lambda}$ is a differential equation. The function solution is an integral over k_r. From [Garbet *et al.* 1990] [68] and [79], the expression of the passing particles functional $\mathcal{L}_s$, $\mathcal{L}_{s,pas.}$ ($\mathcal{L}_{s,pas.} = \int \frac{dk_r}{2\pi} |\phi_{n\omega}|^2(x) \langle \mathcal{I}_{ps} \rangle_{\mathcal{E},\lambda} B_0(k_\perp \rho_s)$) is such that:

$$\mathcal{L}_{s,pas.}(\omega) = -i\langle \tfrac{\omega - n\omega_s^*}{|\omega_2|}|d| \quad \int_0^{+\infty} \quad \int_0^{+\infty} \tfrac{dk_r dk_r^{'}}{2\pi} J_0(k_\perp(k_r)\rho_s)\phi_{n\omega}(k_r) J_0^*(k_\perp(k_r^{'})\rho_s) \\ \phi_{n\omega}^*(k_r^{'}) H(d\tfrac{k_r^{'} - k_r}{\omega_2}) exp(i(\tfrac{\omega - n\omega_{ds}}{\omega_2} d(k_r^{'} - k_r)))\rangle_{\mathcal{E},\lambda} \tag{2.65}$$

where $\bar{\varphi_2} = k_r d$. A Fourier transform is applied on $\phi_{n\omega}$ such that:

$$\phi_{n\omega}(k_r) = \int_{-\infty}^{+\infty} dx e^{-ik_r x} \hat{\phi}_{n\omega}(x)$$

. Finally a change of variables is done as follows:

$$\begin{cases} k_+ = & \frac{k_r + k_r^{'}}{2} \\ k_- = & k_r^{'} - k_r \end{cases}$$

and :

$$\begin{cases} x_+ = & \frac{x + x^{'}}{2} \\ x_- = & x^{'} - x \end{cases}$$

hence :

$$-k_r x + k_r^{'} x^{'} = k_+ x_- + k_- x_+$$

and :

$$dk_r^{'} dk_r = dk_- dk_+$$

$$\mathcal{L}_{s,pas.} = \int_{-\infty}^{\infty} \frac{\mathrm{d}k_+}{2\pi} \iint_{-\infty}^{\infty} \mathrm{d}x_+ \mathrm{d}x_- \\ \phi_{n\omega}(x_+ - \frac{x_-}{2}) \phi_{n\omega}^*(x_+ + \frac{x_-}{2}) e^{\imath k_+ x_-} \langle \mathcal{I}_{ps} \rangle_{\mathcal{E},\lambda} \mathcal{B}_0(k_\perp \rho_s) \tag{2.66}$$

With $\mathcal{B}_0(k_\theta \rho_s) = \int \frac{dk_r}{2\pi} \mathcal{B}(k_\theta \rho_s)$ is integrated in k_r separately, which is sufficient to account for the finite Larmor radius effect leading to a complete stabilization at high enough wave number.
As will be derived in the following section, the eigenfunction is a shifted Gaussian: $\phi_{n\omega}(x) = \phi_0 \exp(-\frac{(x-x_0)^2}{2\mathrm{w}^2})$, with a finite shift when including non-zero values of $U_\parallel$, $\nabla U_\parallel$ and $\mathbf{E} \times \mathbf{B}$ shear. Therefore, the product $\phi_{n\omega}\phi_{n\omega}^*$ can be written as:

$$\phi_{n\omega}\phi_{n\omega}^* = \phi_0^2 \exp\left(-\frac{(x_+ - \Re(x_0) - k_+ \Im(\mathrm{w}^2))^2}{\Re(\mathrm{w}^2)} - \Re(\mathrm{w}^2) \left(k_+ - \frac{\Im(x_0)}{\Re(\mathrm{w}^2)} \right)^2 \right) \tag{2.67}$$

A change of variables from the dimensional x_+ and k_+ to the dimensionless quantities ρ^* and k^* is performed:

$$\begin{aligned}\rho^{*2} &= \frac{(x_+ - \Re(x_0) - k_+\Im(\mathrm{w}^2))^2}{\Re(\mathrm{w}^2)} \\ k^{*2} &= \Re(\mathrm{w}^2)\left(k_+ - \frac{\Im(x_0)}{\Re(\mathrm{w}^2)}\right)^2\end{aligned} \tag{2.68}$$

The x quantity used in ((2.64)) is now replaced by $\rho^*\sqrt{\Re(\mathrm{w}^2)} + \Re(x_0) + k_+\Im(\mathrm{w}^2)$ and $k_r = \dfrac{k^*}{\sqrt{\Re(\mathrm{w}^2)}} + \dfrac{\Im(x_0)}{\Re(\mathrm{w}^2)}$, $\Re(\mathrm{w}^2)$ being positive by definition which ensures $|\phi_{n\omega}|^2$ to be finite. The passing particle functional finally becomes:

$$\mathcal{L}_{s,pass} = \int_{-\infty}^{\infty} \frac{\mathrm{d}k^*}{\sqrt{\pi}} e^{-k^{*2}} \int_{-\infty}^{\infty} \frac{\mathrm{d}\rho^*}{\sqrt{\pi}} e^{-\rho^{*2}} \left\langle \mathcal{I}_{ps} \right\rangle_{\mathcal{E},\lambda} (k^*, \rho^*) \mathcal{B}_0(k_\perp \rho_s) \tag{2.69}$$

The bi-dimensional integration with respect to k^* and ρ^* is performed numerically.

2.3 Eigenfunction: deduced from the fluid limit

In the section above, the gyrokinetic dispersion relation has been expressed in a simplified form solved with, at most, 2D numerical integrals. The eigenfunction $\phi_{n\omega}(x)$ is not solved in this framework. It is derived separately in the fluid limit of the gyrokinetic dispersion relation. This approximation is required to gain additional computational time. A shifted Gaussian eigenfunction will be found. This approximation can be justified since, in the variational approach, an error ϵ in estimating the eigenfunction will lead to a smaller error, ϵ^2, on the eigenvalue. Therefore more approximations are allowed for the eigenfunction determination than for the eigenvalue calculation. In this section, at first the derivation of the eigenfunction in the fluid limit is detailed, and then its validation against a more complete, self-consistent, gyrokinetic approach is illustrated. Most of the elements of this section follow Pierre Cottier's PhD [14] where the impact of $E \times B$ and finite $U_\parallel$ were added to the original derivation [80, 28].

2.3.1 Fluid eigenfunction analytical derivation

As previously mentioned, the eigenfunctions of the problem solved in QuaLiKiz are not consistently calculated but they are taken as the solution of the

fluid limit problem. This means that they are the solutions of the dispersion relation expressed in the limit of very unstable modes such that: $\omega \gg \mathbf{n}\cdot\mathbf{\Omega_J}$, or in the framework of equation (2.55), $\varpi \gg n\omega_{ds}$. Under such condition, equation (2.55) is no longer resonant and it can be developed in powers of $\frac{n\omega_{ds}}{\varpi}$. Due to the assumption of large mode frequency, the so-called fluid limit is valid only far from the gyrokinetic instability threshold. Another approximation is made to enable the analytical calculation. The wave vectors are limited to low values such that: $k_\perp\rho_e \ll k_\perp\delta_e \ll k_\perp\rho_i \ll k_\perp\delta_i \ll 1$. For the electrons, finite Larmor radius and banana width effects are neglected. For ions, the Bessel functions that express the finite Larmor radius and banana width effects are developed in powers of $k_\theta\rho_i$ and $k_r\delta_i$ up to the second order ($k_r\rho_i$ terms are neglected here). Finally, due to the focus on low wave numbers, passing electrons are considered adiabatic. This leads to the following dispersion relation:

$$\begin{aligned}
&\left[\frac{n_e}{T_e}\left(1-\left\langle\left(1-\frac{n\omega_e^*}{\varpi}\right)\left(1+\frac{n\omega_{de}}{\varpi}\right)\right\rangle_{tt}\right)+\right.\\
&\sum_i \frac{n_i Z_i^2}{T_i}\left(1-\left\langle\left(1-\frac{n\omega_i^*}{\varpi}\right)\left(1+\frac{n\omega_{di}}{\varpi}\right)\right)\left(1-\frac{k_r^2\delta_i^2}{4}\right)\right\rangle_{tt}-\\
&\left.\sum_i \frac{n_i Z_i^2}{T_i}\left(\left\langle\left(1-\frac{n\omega_i^*}{\varpi}\right)\left(1+\frac{n\omega_{di}}{\varpi}+\frac{k_\parallel v_\parallel}{\varpi}+\frac{k_\parallel^2 v_\parallel^2}{\varpi^2}+\frac{2n\omega_{di}k_\parallel v_\parallel}{\varpi^2}+\frac{n^2\omega_{di}^2}{\varpi^2}\right)\right)\left(1-\frac{k_\theta^2\rho_i^2}{4}\right)\right\rangle_{pp}\right]\phi_{n\omega}(x\\
&=0
\end{aligned} \tag{2.70}$$

where the integration over passing – $\langle\dots\rangle_{pp}$ – and trapped – $\langle\dots\rangle_{tt}$ – domains are given by the formulas:

$$\begin{aligned}
\langle\dots\rangle_{tt} =& \int_0^\infty \frac{2}{\sqrt{\pi}}\sqrt{\mathcal{E}}e^{-\mathcal{E}}\mathrm{d}\mathcal{E}\int_{\lambda_c}^1 \frac{\mathrm{d}\lambda}{2\bar{\omega}_2}\left(1+2\frac{U_\parallel}{v_{T_s}}\epsilon_\parallel\sqrt{\mathcal{E}(1-\lambda b)}+\frac{U_\parallel^2}{v_{T_s}^2}\left(2\mathcal{E}(1-\lambda b)\right)-1\right)\cdots\\
=&\frac{2\sqrt{2\epsilon}}{\pi}\int_0^\infty \frac{2}{\sqrt{\pi}}\sqrt{\mathcal{E}}e^{-\mathcal{E}}\mathrm{d}\mathcal{E}\int_0^1\left(1+2\frac{U_\parallel}{v_{T_s}}\epsilon_\parallel\bar{\omega}_2\sqrt{\mathcal{E}}+\frac{U_\parallel^2}{v_{T_s}^2}\bar{\omega}_2^2\mathcal{E}\right)K(\kappa)\kappa\mathrm{d}\kappa\cdots\\
=&\left\langle\left(1+2\frac{U_\parallel}{v_{T_s}}\epsilon_\parallel\bar{\omega}_2\sqrt{\mathcal{E}}+\frac{U_\parallel^2}{v_{T_s}^2}\bar{\omega}_2^2\mathcal{E}\right)\dots\right\rangle_t\\
\langle\dots\rangle_{pp} =& \int_0^\infty \frac{2}{\sqrt{\pi}}\sqrt{\mathcal{E}}e^{-\mathcal{E}}\mathrm{d}\mathcal{E}\int_0^{\lambda_c} \frac{\mathrm{d}\lambda}{2\bar{\omega}_2}\left(1+2\frac{U_\parallel}{v_{T_s}}\epsilon_\parallel\sqrt{\mathcal{E}(1-\lambda b)}+\frac{U_\parallel^2}{v_{T_s}^2}\left(2\mathcal{E}(1-\lambda b)\right)-1\right)\cdots\\
=&\left\langle\left(1+2\frac{U_\parallel}{v_{T_s}}\epsilon_\parallel\sqrt{\mathcal{E}(1-\lambda b)}+\frac{U_\parallel^2}{v_{T_s}^2}\left(2\mathcal{E}(1-\lambda b)\right)-1\right)\dots\right\rangle_p
\end{aligned} \tag{2.71}$$

With: $\frac{1}{\bar{\omega}_2} = \oint \frac{d\theta}{2\pi} \frac{1}{\sqrt{1-\lambda b}}$, κ such that $\lambda = 1 - 2\epsilon\kappa^2$ and from equation 2.11:

$$\begin{aligned} n\omega_s^* &= \frac{k_\theta T_s}{e_s B}\left[\frac{R\nabla n_s}{n_s} + \left(\mathcal{E} - \frac{3}{2} - \frac{U_\parallel}{v_{Ts}}\left(\frac{2v_\parallel - U_\parallel}{v_{Ts}}\right)\right)\frac{R\nabla T_s}{T_s} + 2\left(v_\parallel - U_\parallel\right)\frac{R\nabla U_\parallel}{v_{Ts}}\right] \\ &= n\omega_{ns}^* + \left(\mathcal{E} - \frac{3}{2} - \frac{U_\parallel}{v_{Ts}}\left(\frac{2v_\parallel - U_\parallel}{v_{Ts}}\right)\right) n\omega_{Ts}^* + \frac{2\left(v_\parallel - U_\parallel\right)}{v_{Ts}} n\omega_{us}^* \end{aligned} \tag{2.72}$$

For passing particles, assuming strongly ballooned eigenfunctions, hence $\theta \to 0$, the curvature and ∇B drift can be linearized in θ (see the appendix in [76] for more details) such that:

$$\begin{aligned} n\omega_{di} &\simeq -\frac{k_\theta T_i}{Z_i eBR}\mathcal{E}(2 - \lambda b)\left(\cos\theta + (s\theta - \alpha\sin\theta)\sin\theta\right) \\ &\to -\frac{k_\theta T_i}{Z_i eBR}\mathcal{E}(2 - \lambda b)\left(1 + \left(\hat{s} - \alpha - \frac{1}{2}\right)\theta^2\right) \end{aligned} \tag{2.73}$$

Thanks to the lowest order ballooning representation, $k_r^2 d^2$ is used instead of θ^2 in the above expression.
For trapped particles, the integration in λ is done analytically such that: $n\omega_{de} = \frac{k_\theta T_e}{eBR}\mathcal{E}\left\langle f(\lambda, k_r)\right\rangle_{k_r} = \frac{k_\theta T_e}{eBR}\mathcal{E} f(\kappa)$ using equation 2.51. In the following, $n\bar{\omega}_{de}$ is used with $n\bar{\omega}_{de} = \frac{k_\theta T_e}{eBR}$, therefore a positive frequency means a mode drifting in the electron curvature drift direction.

Equation (2.70) is multiplied by ω^3 and $\frac{T_e}{n_e}\frac{1}{f_p}$. Below are detailed the various integrations in θ, $\mathcal{E}$ and λ used as well as the simplifications obtained when multiplying by $\frac{T_e}{n_e}$ the various sums $\sum_i \frac{n_i Z_i^2}{T_i} \ldots$.
Note that:

$$\begin{aligned} \int_0^\infty \frac{2}{\sqrt{\pi}}\sqrt{\mathcal{E}}e^{-\mathcal{E}}\mathrm{d}\mathcal{E} &= 1 \\ \int_0^\infty \frac{2}{\sqrt{\pi}}\mathcal{E}^{3/2}e^{-\mathcal{E}}\mathrm{d}\mathcal{E} &= \frac{3}{2} \\ \int_0^\infty \frac{2}{\sqrt{\pi}}\mathcal{E}^{5/2}e^{-\mathcal{E}}\mathrm{d}\mathcal{E} &= \frac{15}{4} \\ \int_0^\infty \frac{2}{\sqrt{\pi}}\mathcal{E}^{7/2}e^{-\mathcal{E}}\mathrm{d}\mathcal{E} &= \frac{105}{8} \end{aligned} \tag{2.74}$$

The fraction of trapped particles f_t in absence of finite $U_\parallel$ is such that:

$$\langle 1\rangle_t = f_t = 2\int_{-\theta_b}^{+\theta_b}\frac{d\theta}{2\pi}\int_{1-2\epsilon}^{1}\frac{1+\epsilon}{1-\epsilon cos\theta}\frac{\mathrm{d}(\lambda b)}{2\sqrt{1-\lambda b}} = \frac{2}{\pi}\sqrt{2\epsilon} \tag{2.75}$$

Where θ_b is the poloidal angle at which the trapped particles bounce back. With $\lambda = \frac{\mu B(0)}{E}$, $\lambda_c = \frac{\mu B(\pi)}{E}(1-2\epsilon)$ and $b = \frac{B(\theta)}{B(0)} \simeq 1 + \epsilon - \epsilon cos\theta$ in the circular large aspect ratio limit.
The fraction of passing particles is obtained similarly:

$$\langle 1 \rangle_p = f_p = 1 - f_t \tag{2.76}$$

These integrals are applied to all terms of equation 2.70. For the trapped electron terms, since the electron thermal velocity $v_{th,e}$, is much larger than $v_{th,i}$, all terms proportional to $1/v_{th,e}^2$ are neglected. This leads to the following expressions:

$$\begin{aligned}
\langle n\omega_e^* \rangle_{tt} \simeq & f_t n\omega_{ne}^* \\
\langle n\omega_{de} \rangle_{tt} \simeq & \frac{3}{2} n\bar{\omega}_{de} \langle f(\kappa) \rangle_t \\
\langle n\omega_e^* n\omega_{de} \rangle_{tt} \simeq & \frac{3}{2} n\bar{\omega}_{de} \langle f(\kappa) \rangle_t \left(n\omega_{ne}^* + n\omega_{Te}^* \right)
\end{aligned} \tag{2.77}$$

For the ions, in the chosen low Mach number limit, the terms proportional to $\frac{U_\parallel^2}{v_{th,i}^2}$ and higher orders are neglected. In this limit, for the terms expressed above for the electrons, similar expressions are found both for trapped and passing ions:

$$\begin{aligned}
\langle n\omega_i^* \rangle_{tt} \simeq & f_t n\omega_{ni}^* \\
\langle n\omega_i^* \rangle_{pp} \simeq & f_p n\omega_{ni}^* \\
\langle n\omega_{di} \rangle_{tt} \simeq & \frac{3}{2} n\bar{\omega}_{di} \langle f(\kappa) \rangle_t \\
\langle n\omega_{di} \rangle_{pp} \simeq & \frac{3}{2} n\bar{\omega}_{di} \langle 2 - \lambda b \rangle_p \\
\langle n\omega_i^* n\omega_{di} \rangle_{tt} \simeq & \frac{3}{2} n\bar{\omega}_{di} \langle f(\kappa) \rangle_t \left(n\omega_{ni}^* + n\omega_{Ti}^* \right) \\
\langle n\omega_i^* n\omega_{di} \rangle_{pp} \simeq & \frac{3}{2} n\bar{\omega}_{di} \langle 2 - \lambda b \rangle_p \left(n\omega_{ni}^* + n\omega_{Ti}^* \right)
\end{aligned} \tag{2.78}$$

Note that in the low Mach number limit $\langle 1 \rangle_{pp} \simeq \langle 1 \rangle_p = f_p$.

For passing ions, the terms proportional to $v_\parallel$ and $v_\parallel^2$ are expressed as follows:

$$\begin{aligned}
\langle k_\parallel \frac{v_\parallel}{v_{th,i}} \rangle_{pp} \simeq & 3k_\parallel \frac{U_\parallel}{v_{th,i}} \langle 1 - \lambda b \rangle_p \\
\langle n\omega_i^* k_\parallel \frac{v_\parallel}{v_{th,i}} \rangle_{pp} \simeq & 3k_\parallel \frac{U_\parallel}{v_{th,i}} \left(\frac{v_{th,i}}{U_\parallel} n\omega_{ui}^* + n\omega_{ni}^* \right) \langle 1 - \lambda b \rangle_p \\
\langle k_\parallel^2 \frac{v_\parallel^2}{v_{th,i}^2} \rangle_{pp} \simeq & \frac{3}{2} k_\parallel^2 \langle 1 - \lambda b \rangle_p \\
\langle n\omega_i^* k_\parallel^2 \frac{v_\parallel^2}{v_{th,i}^2} \rangle_{pp} \simeq & \frac{3}{2} k_\parallel^2 \langle 1 - \lambda b \rangle_p \left(n\omega_{ni}^* + n\omega_{Ti}^* \right) \\
\langle n\omega_{di} k_\parallel \frac{v_\parallel}{v_{th,i}} \rangle_{pp} \simeq & \frac{15}{2} k_\parallel \frac{U_\parallel}{v_{th,i}} n\bar{\omega}_{di} \left(1 + \left(\hat{s} - \alpha - \frac{1}{2} \right) \theta^2 \right) \langle (2 - \lambda b)(1 - \lambda b) \rangle_p \\
\langle n^2 \omega_{di}^2 \rangle_{pp} \simeq & n^2 \bar{\omega}_{di}^2 \left(1 + 2 \left(\hat{s} - \alpha - \frac{1}{2} \right) \theta^2 \right) \frac{15}{4} \langle (2 - \lambda b)^2 \rangle_p \\
\langle n\omega_i^* n\omega_{di} k_\parallel \frac{v_\parallel}{v_{th,i}} \rangle_{pp} \simeq & \frac{15}{4} k_\parallel \frac{U_\parallel}{v_{th,i}} n\bar{\omega}_{di} \left(1 + \left(\hat{s} - \alpha - \frac{1}{2} \right) \theta^2 \right) \left(2 \frac{v_{th,i}}{U_\parallel} n\omega_{ui}^* + 2n\omega_{ni}^* + 3n\omega_{Ti}^* \right) \\
& \times \langle (2 - \lambda b)(1 - \lambda b) \rangle_p \rangle_p \\
\langle n\omega_i^* n^2 \omega_{di}^2 \rangle_{pp} \simeq & n^2 \bar{\omega}_{di}^2 \left(1 + 2 \left(\hat{s} - \alpha - \frac{1}{2} \right) \theta^2 \right) \frac{15}{4} \left(n\omega_{ni}^* + 2n\omega_{Ti}^* \right) \langle (2 - \lambda b)^2 \rangle_p
\end{aligned} \tag{2.79}$$

Moreover, the sums $\frac{T_e}{n_e} \sum_i \frac{n_i Z_i^2}{T_i} \ldots$ can be simplified. Assuming further that: $\frac{\nabla n_e}{n_e} = \frac{\nabla n_i}{n_i}$, $\frac{\nabla T_e}{T_e} = \frac{\nabla T_i}{T_i}$ and $A_i = 2Z_i$, the following equalities are

obtained:

$$
\begin{aligned}
\frac{T_e}{n_e}\sum_i \frac{n_i Z_i^2}{T_i} n\bar{\omega}_{di} &= -\, n\bar{\omega}_{de} \\
\frac{T_e}{n_e}\sum_i \frac{n_i Z_i^2}{T_i} n\omega^*_{ni} &= -\, n\omega^*_{ne} \\
\frac{T_e}{n_e}\sum_i \frac{n_i Z_i^2}{T_i} n\omega^*_{Ti} &= -\, n\omega^*_{Te} \\
\frac{T_e}{n_e}\sum_i \frac{n_i Z_i^2}{T_i} \frac{v_{th,i}}{U_\parallel} n\omega^*_{ui} &= -\, \frac{v_{th,e}}{U_\parallel} n\omega^*_{ue} = \frac{k_\theta T_e}{eB}\frac{\nabla U_\parallel}{U_\parallel} = n\omega^*_u \\
\frac{T_e}{n_e}\sum_i \frac{n_i Z_i^2}{T_i} n\omega^*_{pi} n\bar{\omega}_{di} &= \frac{\tau}{\bar{\bar{Z}}} n\omega^*_{pe} n\bar{\omega}_{de} \\
\frac{T_e}{n_e}\sum_i \frac{n_i Z_i^2}{T_i} \rho_i^2 &= \frac{\rho_D^2}{\tau} \\
\frac{T_e}{n_e}\sum_i \frac{n_i Z_i^2}{T_i} n\omega^*_{ni} \rho_i^2 &= -\, n\omega^*_{ne} \frac{\rho_D^2}{\bar{z}} \\
\frac{T_e}{n_e}\sum_i \frac{n_i Z_i^2}{T_i} n\omega^*_{pi} n\bar{\omega}_{di} \rho_i^2 &= \tau n\omega^*_{pe} n\bar{\omega}_{de} \rho_{eff}^2 \\
\frac{T_e}{n_e}\sum_i \frac{n_i Z_i^2}{T_i} n\omega^*_{pi} v_{th,i}^2 &= -\, \frac{\tau}{\bar{z}} n\omega^*_{pe} c_{eff}^2 \\
\frac{T_e}{n_e}\sum_i \frac{n_i Z_i^2}{T_i} v_{th,i}^2 &= \frac{c_{eff}^2}{2} \\
\frac{T_e}{n_e}\sum_i \frac{n_i Z_i^2}{T_i} n\bar{\omega}_{di} n\omega^*_{ui} \frac{v_{th,i}}{U_\parallel} &= \frac{\tau}{\bar{z}} n\bar{\omega}_{de} n\omega^*_u \\
\frac{T_e}{n_e}\sum_i \frac{n_i Z_i^2}{T_i} (n\bar{\omega}_{di})^2 &= \frac{\tau}{\bar{z}} (n\bar{\omega}_{de})^2
\end{aligned}
\tag{2.80}
$$

With:

$$
\begin{aligned}
\frac{\tau}{\bar{z}} &= \frac{\sum_i \bigtriangledown_{\mathbf{r}} \mathbf{P_i}}{\bigtriangledown_{\mathbf{r}} \mathbf{P_e}} \\
\frac{1}{\bar{z}} &= \frac{\sum_i n_i}{n_e} \\
\tau &= \frac{T_i}{T_e} \\
\sum_i \frac{n_i}{n_e} \rho_i^2 &= \rho_{eff}^2
\end{aligned}
$$

and $\rho_D^2 = \frac{4m_pT_i}{e^2B^2}$,$\delta_D^2 = \frac{q^2}{2\epsilon}\rho_D^2$, $c_{eff} = \sqrt{\frac{T_e}{m_p}}$.

Note that the ballooning representation used so far is not correct if $\gamma_E \gg \omega$, since, under such conditions, the asymmetrisation of the eigenfunction becomes large, and does not allow to assume eigenfunctions localized around $\theta = 0$. Therefore, in the following γ_E is assumed smaller than ω, which is sufficient to reproduce most tokamak situations, as discussed later. Hence terms proportional to $\gamma_E x^2$ or higher are neglected. Therefore, the x dependence of $n\omega_{\mathbf{E}\times\mathbf{B}}$ is taken into account such that $E_r \rightarrow E_{r0} + \dot{E}_r x$ and therefore $n\omega_{\mathbf{E}\times\mathbf{B}} = k_\theta \frac{E_r}{B} = n\omega_{E0} + k_\theta\gamma_E x + O(x^2)$, with $\gamma_E = \frac{\dot{E}_r}{B}$. It is important here to remember that, although $\nabla_r E_r$ depends on $\nabla_r(\nabla_r P_s)$, such contributions are neglected, see section 2.2.1. ϖ is then replaced by $\varpi_0 - n\omega_{E0} - k_\theta\gamma_E x$ or $\omega - k_\theta\gamma_E x$ since the constant part, $n\omega_{E0}$, acts as a Doppler shift.
$k_\parallel$ is linearized too: $k_\parallel = \dot{k}_\parallel x + O\left(\ddot{k}_\parallel x^2\right)$.

Since x is small, any terms of order $k_\perp^2 x$, x^3, $k_\theta^2\rho_i^2 x$, $k_r^2 d^2 x$, $k_r^2\delta_i^2 x$ or higher are neglected. Since, in the fluid limit $\frac{(n\bar{\omega_{di}})^2}{\omega^2}$ is assumed to be small, the terms proportional to $\frac{(n\bar{\omega_{di}})^2}{\omega^2}k_r^2 d^2$ are neglected. Importantly, the low Mach number approximation is used and all terms in $\frac{U_\parallel}{v_{th,e}}$ or higher order are neglected as well as $\frac{U_\parallel^2}{v_{th,i}^2}$ or higher.
Finally, one obtains the following second order linear differential equation:

$$
\begin{aligned}
&f_p\omega^3 - 3f_p\omega^2 k_\theta\gamma_E x + n\omega^*_{pe} n\bar{\omega}_{de}\frac{3}{2}\left(\langle f(\kappa)\rangle_t\left(1+\frac{\tau}{\bar{z}}\right)+\langle 2-\lambda b\rangle_p\frac{\tau}{\bar{Z}}\right)(\omega - k_\theta\gamma_E x)\\
&- f_p n\omega^*_{ne}\omega\left(\omega - 2k_\theta\gamma_E x\right) + \frac{3}{2}n\bar{\omega}_{de}\omega\left(\omega - 2k_\theta\gamma_E x\right)\langle 2-\lambda b\rangle_p\\
&- k_r^2\omega\Bigg\{\frac{3}{2}n\bar{\omega}_{de}\Bigg[\omega\left(-d^2(s-\alpha-0.5)\left(\langle f(\kappa)\rangle_t + \langle 2-\lambda b\rangle_p\right) + \frac{\delta_D^2}{4\bar{z}}\langle f(\kappa)\rangle_t\right)\\
&+ n\omega^*_{pe}\left(-\frac{\tau}{\bar{z}}d^2(s-\alpha-0.5)\left(\langle f(\kappa)\rangle_t + \langle 2-\lambda b\rangle_p\right) + \tau\frac{\delta^2_{eff}}{4}\langle f(\kappa)\rangle_t\right)\Bigg]\\
&- \omega\left(f_t\frac{\omega}{\tau} + \frac{n\omega^*_{ne}}{\bar{z}}\right)\frac{\delta_D^2}{4}\Bigg\}\\
&+ \frac{k_\theta^2\rho^2_{eff}}{4}\omega\left(\omega\left(f_p\omega + n\omega^*_{ne}\right) - \frac{3}{2}n\bar{\omega}_{de}\langle 2-\lambda b\rangle_p\left(\omega + \frac{\tau}{\bar{z}}n\omega^*_{pe}\right)\right)\\
&- 3\dot{k}_\parallel U_\parallel x\langle 1-\lambda b\rangle_p\omega\left(n\omega^*_u + n\omega^*_{ne} + \frac{Z_{eff}}{\tau}\omega\right) - \frac{3}{2}\dot{k}_\parallel^2 x^2\frac{c^2_{eff}}{2}\langle 1-\lambda b\rangle_p\left(\omega + \frac{\tau}{\bar{Z}}n\omega^*_{pe}\right)\\
&+ \frac{15}{2}\dot{k}_\parallel U_\parallel x\langle(2-\lambda b)(1-\lambda b)\rangle_p n\bar{\omega}_{de}\left(2\omega + \sum_i\frac{n_i Z_i}{n_e}\left(2n\omega^*_{ni} + 3n\omega^*_{Ti} + 2n\omega^*_{ui}\frac{v_{th,i}}{U_\parallel}\right)\right)\\
&+ \frac{15}{4}n^2\bar{\omega}^2_{de}\langle(2-\lambda b)^2\rangle_p\left(-\frac{\tau}{\bar{z}}\left(\omega - k_\theta\gamma_E x\right) + \sum_i\frac{n_i}{n_e}\tau\left(n\omega^*_{ni} + 2n\omega^*_{Ti}\right)\right) = 0
\end{aligned}
\tag{2.81}
$$

This equation is a second order differential equation, indeed $k_r^2 = -\frac{d^2}{dx^2}$. Therefore, the solution of equation (2.81) is a shifted Gaussian such that:

$$
\phi_{n\omega}(x) = \frac{\phi_0}{\left(\pi\Re\left(\mathrm{w}^2\right)\right)^{1/4}}\exp -\frac{(x-x_0)^2}{2\mathrm{w}^2} \tag{2.82}
$$

defined by its mode width w and its shift x_0. The shift, x_0, is a complex number and w^2 should have a positive real part.
By replacing $\phi_{n\omega}(x)$ by its expression, $\mathrm{d}_{xx} = \frac{\mathrm{d}^2}{\mathrm{d}x^2}$ becomes $\frac{x_0^2-\mathrm{w}^2}{\mathrm{w}^4} + \frac{x^2}{\mathrm{w}^4} - \frac{2x_0x}{\mathrm{w}^4}$. One then obtains that equation (2.81) contains terms proportional to x^2, to x or independent of x. This leads to three equations, each equal to zero. From this system of three equations, the three unknowns: w^2 and x_0 and ω can be derived.
The first equation, by balancing the parallel dynamics with the perpendicular

finite width effects gives the expression for the mode width w such that:

$$
\begin{aligned}
&\mathrm{w}^4 = \\
&\frac{1}{\frac{3}{2}\frac{\dot{k_\parallel}^2 c_{eff}^2}{2}\langle 1-\lambda b\rangle_p \left(\frac{\omega}{\tau}+\frac{n\omega_{pe}^*}{\bar{z}}\right)}\times \\
&\left\{\frac{3}{2}\omega n\bar{\omega}_{de}\left[\omega\left(-d^2(s-\alpha-0.5)(\langle f(\kappa)\rangle_t+\langle 2-\lambda b\rangle_p)+\frac{\delta_D^2}{4\bar{z}}\langle f(\kappa)\rangle_t\right)\right.\right. \\
&\left.+n\omega_{pe}^*\left(-\frac{\tau}{\bar{z}}d^2(s-\alpha-0.5)(\langle f(\kappa)\rangle_t+\langle 2-\lambda b\rangle_p)+\tau\frac{\delta_{eff}^2}{4}\langle f(\kappa)\rangle_t\right)\right] \\
&\left.-\omega^2\left(\frac{f_t\omega}{\tau}+\frac{n\omega_{ne}^*}{\bar{z}}\right)\frac{\delta_D^2}{4}\right\}
\end{aligned}
$$

It follows a similar definition as in [28, 76], except that in [28, 76] ω was taken to be the interchange growth rate, whereas now ω is the self consistent solution of equation (2.81). Through ω dependencies, the mode width depends on numerous parameters such as $\nabla T_s/T_s$, $\nabla n_s/n_s$, γ_E, $\nabla U_\parallel$, $U_\parallel$, Z_{eff}, etc.

The second equation allows to estimate the eigenmode shift x_0, which depends only on terms introduced by the existence of a finite $U_\parallel$ and finite γ_E:

$$\frac{x_0}{\mathrm{w}^4} = \frac{Ak_\theta\gamma_E + B\dot{k_\parallel}U_\parallel + C\nabla U_\parallel}{D} \tag{2.83}$$

where:

$$
\begin{aligned}
A =& 3f_p\omega^2 + n\omega^*_{pe} n\bar{\omega}_{de}\frac{3}{2}\left(\langle f(\kappa)\rangle_t\left(1+\frac{\tau}{\bar{\bar{Z}}}\right)+\langle 2-\lambda b\rangle_p\frac{\tau}{\bar{\bar{Z}}}\right) - 2f_p n\omega^*_{ne}\omega \\
&+ 3n\bar{\omega}_{de}\langle 2-\lambda b\rangle_p\omega - \frac{15}{4}n^2\bar{\omega}^2_{de}\langle(2-\lambda b)^2\rangle_p\frac{\tau}{\bar{\bar{z}}} \\
B =& 3\langle 1-\lambda b\rangle_p\omega\left(n\omega^*_{ne}+\frac{Z_{eff}}{\tau}\omega\right) \\
&- \frac{15}{2}\langle(2-\lambda b)(1-\lambda b)\rangle_p n\bar{\omega}_{de}\left(2\omega+\sum_i\frac{n_iZ_i}{n_e}\left(2n\omega^*_{ni}+3n\omega^*_{Ti}\right)\right) \\
C =& -\frac{15}{2}\dot{k}_\parallel\langle(2-\lambda b)(1-\lambda b)\rangle_p n\bar{\omega}_{de}2\sum_i\frac{n_i}{n_e}\frac{k_\theta T_i}{eB} + 3\dot{k}_\parallel\langle 1-\lambda b\rangle_p\omega\frac{k_\theta T_e}{eBR} \\
D =& -2\omega\Bigg\{\frac{3}{2}n\bar{\omega}_{de}\Bigg[\omega\left(-d^2(s-\alpha-0.5)\left(\langle f(\kappa)\rangle_t+\langle 2-\lambda b\rangle_p\right)+\frac{\delta^2_D}{4\bar{z}}\langle f(\kappa)\rangle_t\right) \\
&+ n\omega^*_{pe}\left(-\frac{\tau}{\bar{z}}d^2(s-\alpha-0.5)\left(\langle f(\kappa)\rangle_t+\langle 2-\lambda b\rangle_p\right)+\tau\frac{\delta^2_{eff}}{4}\langle f(\kappa)\rangle_t\right)\Bigg] \\
&- \omega\left(f_t\frac{\omega}{\tau}+\frac{n\omega^*_{ne}}{\bar{z}}\right)\frac{\delta^2_D}{4}\Bigg\}
\end{aligned}
\tag{2.84}
$$

It is interesting to note that the Gaussian eigenfunction is asymmetric with respect to x (or θ) only in cases of either finite γ_E or $U_\parallel$. Indeed the shifted, asymmetric, eigenmode is a signature of a finite rotation and/or $E \times B$ shear [81, 82]. An asymmetric eigenmode will generate a angular momentum flux (or Reynolds stress) as discussed later [83].
The third equation allows to estimate ω. For given w and x_0, one then gets a third order polynomial equation for ω such that:

$$
\begin{aligned}
&f_p\omega^3 + n\omega^*_{pe} n\bar{\omega}_{de}\frac{3}{2}\left(\langle f(\kappa)\rangle_t\left(1+\frac{\tau}{\bar{\bar{Z}}}\right)+\langle 2-\lambda b\rangle_p\frac{\tau}{\bar{\bar{Z}}}\right)\omega \\
&- f_p n\omega^*_{ne}\omega^2 + \frac{3}{2}n\bar{\omega}_{de}\omega^2\langle 2-\lambda b\rangle_p \\
&+ \frac{x_0^2-\mathrm{w}^2}{\mathrm{w}^4}\omega\Bigg\{\frac{3}{2}n\bar{\omega}_{de}\Bigg[\omega\left(-d^2(s-\alpha-0.5)\left(\langle f(\kappa)\rangle_t+\langle 2-\lambda b\rangle_p\right)+\frac{\delta_D^2}{4\bar{z}}\langle f(\kappa)\rangle_t\right) \\
&+ n\omega^*_{pe}\left(-\frac{\tau}{\bar{z}}d^2(s-\alpha-0.5)\left(\langle f(\kappa)\rangle_t+\langle 2-\lambda b\rangle_p\right)+\tau\frac{\delta^2_{eff}}{4}\langle f(\kappa)\rangle_t\right)\Bigg] \\
&- \omega\left(f_t\frac{\omega}{\tau}+\frac{n\omega^*_{ne}}{\bar{z}}\right)\frac{\delta_D^2}{4}\Bigg\} \\
&+ \frac{k_\theta^2\rho^2_{eff}}{4}\omega\left(\omega\left(f_p\omega+n\omega^*_{ne}\right)-\frac{3}{2}n\bar{\omega}_{de}\langle 2-\lambda b\rangle_p\left(\omega+\frac{\tau}{\bar{z}}n\omega^*_{pe}\right)\right) \\
&+ \frac{15}{4}n^2\bar{\omega}^2_{de}\langle(2-\lambda b)^2\rangle_p\left(-\frac{\tau}{\bar{z}}\omega+\sum_i\frac{n_i}{n_e}\tau\left(n\omega^*_{ni}+2n\omega^*_{Ti}\right)\right)=0
\end{aligned}
\tag{2.85}
$$

Numerically, equation **??** is solved thanks to iterations. The mode width is estimated assuming an interchange growth rate thanks to equation **??**. This mode width is used to determined the associated shift using equation 2.83. Then the obtained w and x_0 are inserted in equation**??**. The new value for ω is used to reestimate first w, then x_0 until a convergence on the value of ω is obtained.

2.3.2 Eigenfunction model validation

In this subsection, the eigenfunctions derived in the fluid limit are compared to self-consistent gyrokinetic eigenfunctions. This comparison is carried out using the linear versions of the GKW, GENE and GYRO codes which are all gyrokinetic codes, using field aligned coordinates. In these codes, the energy and pitch angle integrals are treated without any approximations, therefore the trapped and the passing particles are solved in the same framework. The integrals along and perpendicular to the field lines are also done precisely, i.e. the ballooning transform is not used. For consistency with QuaLiKiz, all direct comparisons are realized with the $s-\alpha$ equilibrium using $\alpha=0$ in either GKW, GYRO or GENE. In this equilibrium, the parallel coordinate is equivalent to QuaLiKiz's $\frac{\theta}{2\pi}$ [84].

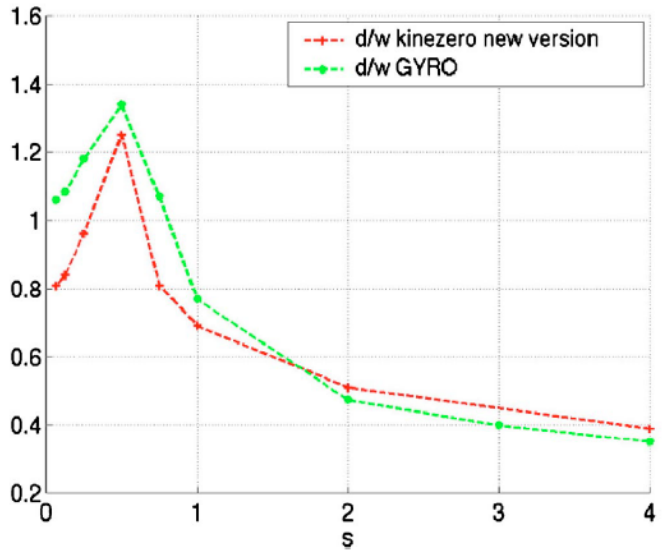

Figure 2.1: Ratio of the distance between two resonant surfaces d to the mode width w plotted versus the magnetic shear s. The red crosses are QuaLiKiz results, based on the fluid limit, the green dots represent GYRO's self-consistent gyrokinetic eigenfunction. The parameters used for this comparison are $q = 2$, $T_e = T_i$, $Z_{eff} = 1$, $R/a = 3$, $r/a = 0.5$, $a/L_T = 8$, $a/L_n = 2$, $\nu_{ei} = 0$, $\alpha = 0$, $k_\theta \rho_s = 0.56$. From M. Romanelli et al, Physics of Plasmas 2007 [76].

Comparison in absence of shift, i.e. $\gamma_E = 0$ and $U_\parallel = 0$

The mode width calculated in QuaLiKiz is compared to the mode width obtained in GYRO (see appendix of [76]) versus the magnetic shear. Figure 2.1 illustrates the fact that the ratio of the mode width to the distance between two resonant surfaces does not diverge as s tends to zero.

Another comparison, based on the so-called GA-standard case parameters, i.e. $q = 2$, $s = 1$ $T_e = T_i$, $Z_{eff} = 1$, $R/a = 3$, $r/a = 0.5$, $R/L_T = 9$, $R/L_n = 3$, $\nu_{ei} = 0$, $\alpha = 0$, was carried out using GENE in [34] at various values of $k_\theta \rho_s$ and magnetic shear s as illustrated by figure 2.2. From Fig.2.2, one can see that the strong ballooning approximation is valid down to $s = 0.1$ and $k_\theta \rho_s = 0.15$.
Since this work, some modifications have been made on the fluid eigenfunction calculation, the effect of α is now included and since Pierre Cottier's PhD the mode width is now estimated using the fluid self-consistent ω rather than using the approximated interchange growth rate. The eigenfunctions

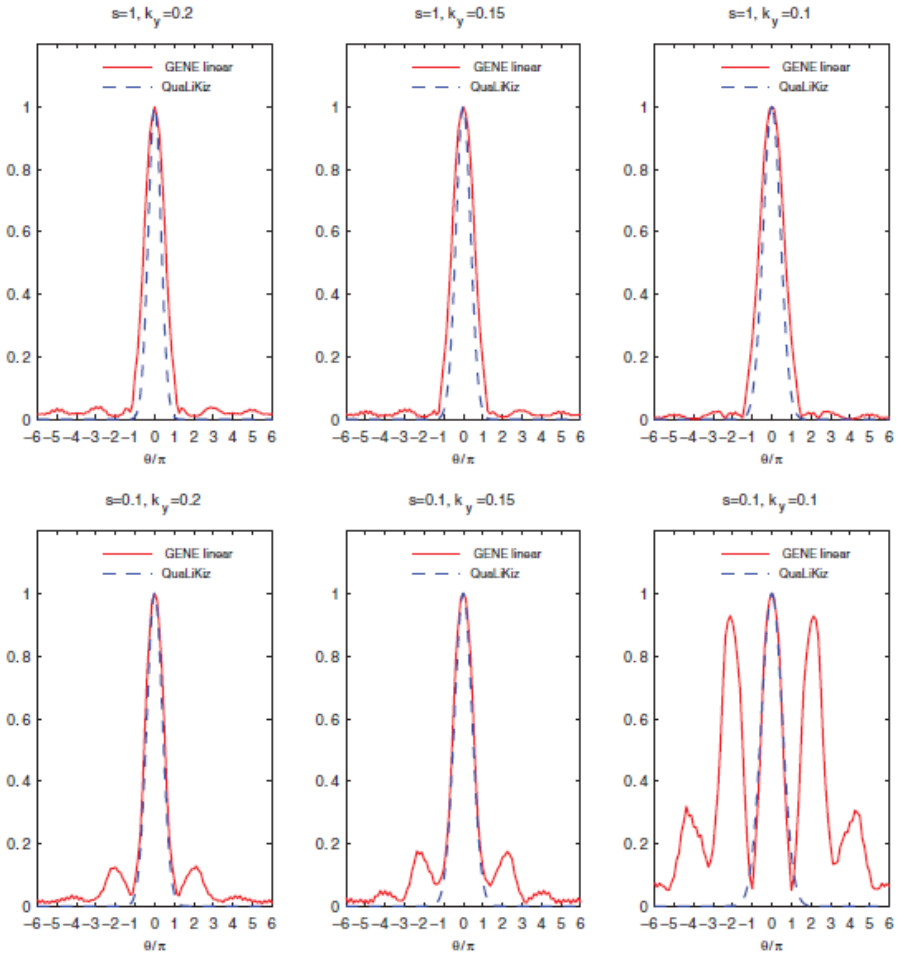

Figure 2.2: Eigenfunctions as a function of the parallel direction θ/π. In the fluid limit for QuaLiKiz in dashed blue and GENE in red. For $s = 1$ upper panel and $s = 0.1$ lower panel using GA standard case parameters. From J. Citrin et al, Physics of Plasmas 2012 [34].

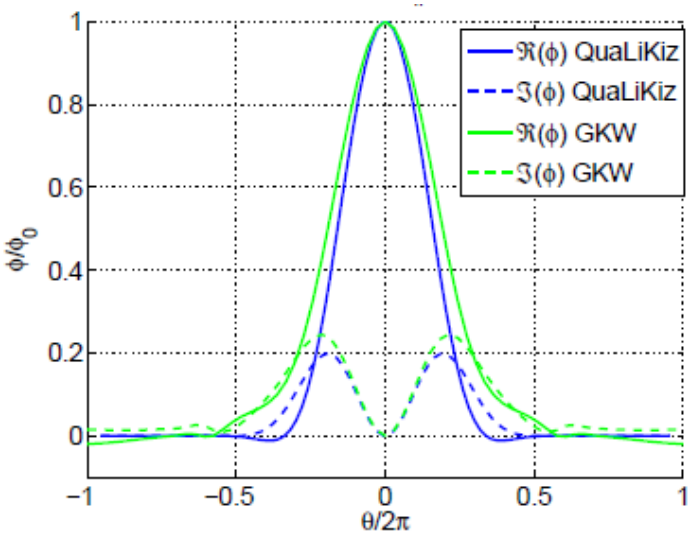

Figure 2.3: Eigenfunctions as a function of the parallel direction $\theta/(2\pi)$. Dashed line: imaginary part, solid line: real part. In the fluid limit for QuaLiKiz in blue and GKW in green for the GA standard case parameters at $k_\theta \rho_s = 0.3$. From P. Cottier et al [42].

now have both real and imaginary parts. This new version of QuaLiKiz has been compared to self-consistent GKW eigenfunctions. The agreement is satisfactory as illustrated for the GA-standard case in figure 2.3.

In QuaLiKiz, the eigenfunction is slightly more peaked around $\theta = 0$ than GYRO (Fig.2.1), GKW (Fig.2.3) and GENE (Fig.2.2), meaning that in QuaLiKiz the mode width is slightly overestimated for $s \leq 1$. From figure 2.1, this tendency seems to reverse for $s \geq 2$. Overall, the mode width is at most 20% away from a self-consistent more complete gyrokinetic calculation. At low s, as expected, see for example a detailed discussion in [71], the eigenfunctions are represented by oscillating Mathieu functions, and under such conditions the strong ballooning approximation used by QuaLiKiz becomes invalid. Figure 2.2 and the discussion in [34] show that this happens at both low magnetic shear and low wave number, i.e for $s \leq 0.1$ and $k_\theta \rho_s \leq 0.15$.
The modes discussed so far are drift in the ion diamagnetic direction, meaning that they are dominated by Ion Temperature Gradient (ITG) driven modes. The eigenfunctions obtained for modes drifting in the electron diamagnetic direction, usually called Trapped Electron eigenmodes (TEM), are now presented in detail. These modes are more extended in θ than ITG [85], therefore the ballooning representation might be inappropriate. To investigate the limit of the ballooning representation used in QuaLiKiz in presence

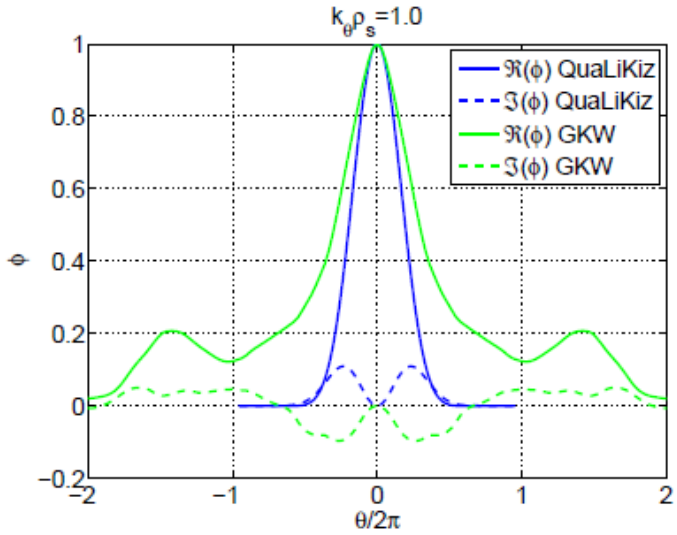

Figure 2.4: Eigenfunctions as a function of the parallel direction $\theta/(2\pi)$. Dashed line: imaginary part, solid line: real part. In the fluid limit for QuaLiKiz in blue and GKW in green for the GA standard case parameters except $-R\nabla T_i T_i = 0$, i.e. TEM dominated regime. At $k_\theta \rho_s = 1$. From P. Cottier et al [42].

of TEM, a clearly TEM dominated regime is chosen: GA-standard case parameters are used except with $R/L_{Ti} = 0$. For such parameters and for large wave numbers such that $k_\theta \rho_s \sim 1$, the eigenfunction found in GKW is extended along the field line as illustrated on figure 2.4. Under such conditions, QuaLiKiz clearly underestimates the eigenfunction extension. This will lead to underestimated growth rates in this spectral range. At lower wave number, the discrepancy between QuaLiKiz and GKW is reduced, as illustrated for $k_\theta \rho_s = 0.2$ on figure 2.5. Since most transport is driven at scales such that $k_\theta \rho_s \leq 0.2$, this explains why QuaLiKiz can model heat and particle fluxes even in the TEM dominant regime as discussed in chapter 4 and in [86].

Comparison in presence of a finite shift, i.e. γ_E and/or $U_\parallel$ are finite

During P. Cottier's PhD [14], the $E \times B$ shear and parallel rotation were implemented in QuaLiKiz. As discussed in the previous subsection, both $E \times B$ and parallel rotation impact the eigenfunction shift as expressed in equation ((2.83)). The QuaLiKiz fluid analytical eigenfunctions are compared to the

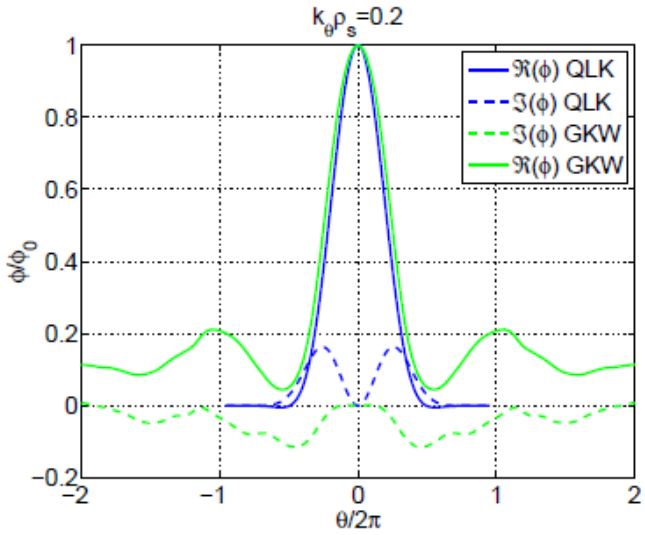

Figure 2.5: Eigenfunctions as a function of the parallel direction $\theta/(2\pi)$. Dashed line: imaginary part, solid line: real part. In the fluid limit for QuaLiKiz in blue and GKW in green for the GA standard case parameters except $-R\nabla T_i T_i = 0$, i.e. TEM dominated regime. At $k_\theta \rho_s = 0.2$. From P. Cottier et al [42].

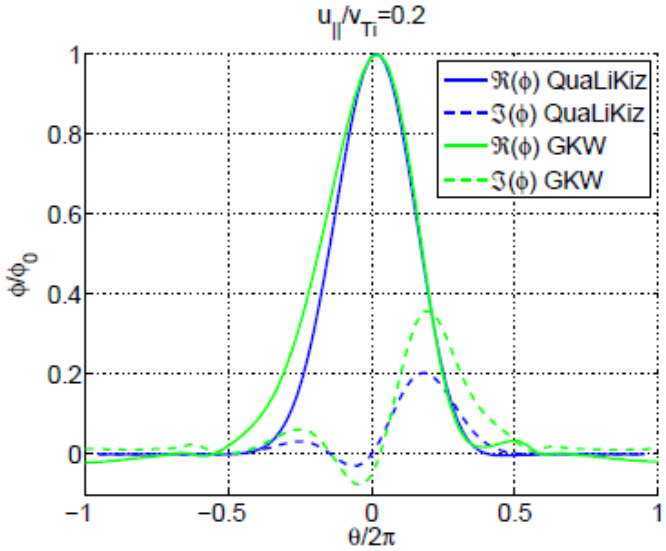

Figure 2.6: Eigenfunctions as a function of the parallel direction $\theta/(2\pi)$. Dashed line: imaginary part, solid line: real part. In the fluid limit for QuaLiKiz in blue and GKW in green for the GA standard case parameters and a rigid body rotation such that $U_{\parallel} = 0.2 \times v_{th,i}$. At $k_\theta \rho_s = 0.3$. From P. Cottier et al [42].

self-consistent gyrokinetic eigenfunctions of GKW focusing on the impact of $E \times B$ shear and parallel rotation on the parallel structure of the eigenmodes. A finite parallel rotation modifies the eigenfunction shift even in the absence of a gradient as illustrated by figure 2.6. The GA-standard parameters are used except the rigid body rotation which is set to $0.2 \times v_{th,i}$ which corresponds to a standard rotation level in core NBI heated tokamak plasmas. A finite gradient of the parallel rotation also modifies the eigenfunction shift as illustrated by figure 2.7. The GA-standard parameters are used except the gradient of the rigid body rotation which is set to $-R\nabla U_{\parallel} = 4v_{th,i}$ which corresponds to large experimentally obtained values in core plasmas, see for example [87, 88]. From figures 2.6 and 2.7 it can be seen that the direction and the shift of the real part of eigenfunction in presence of both a finite rotation or a finite gradient is very well modeled by the fluid analytical approach proposed in QuaLiKiz. In GKW, on top of a shift on the eigenfunction, a tail appears as well on the Gaussian, this loss of symmetry is not reproduced by QuaLiKiz. Since it increases with θ, it mostly modifies lower values of the eigenfunctions and hence will impact less the final dispersion relation.

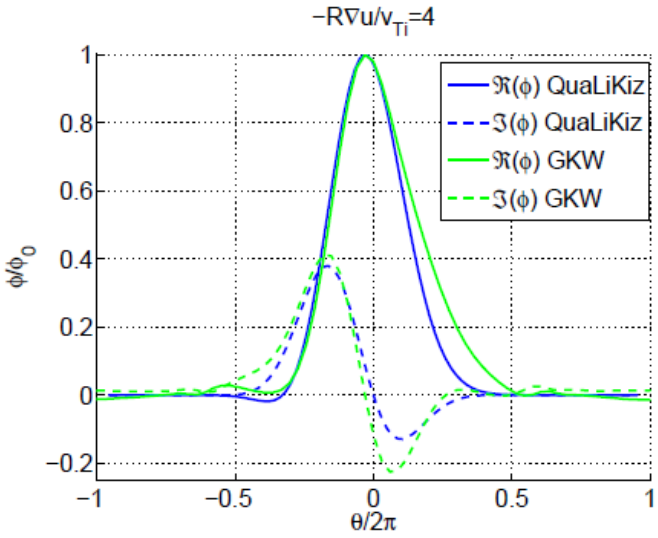

Figure 2.7: Eigenfunctions as a function of the parallel direction $\theta/(2\pi)$. Dashed line: imaginary part, solid line: real part. In the fluid limit for QuaLiKiz in blue and GKW in green for the GA standard case parameters and a gradient of the rigid body rotation such that $-R\nabla U_{\|} = 4v_{th,i}$. At $k_\theta \rho_s = 0.3$. From P. Cottier et al [42].

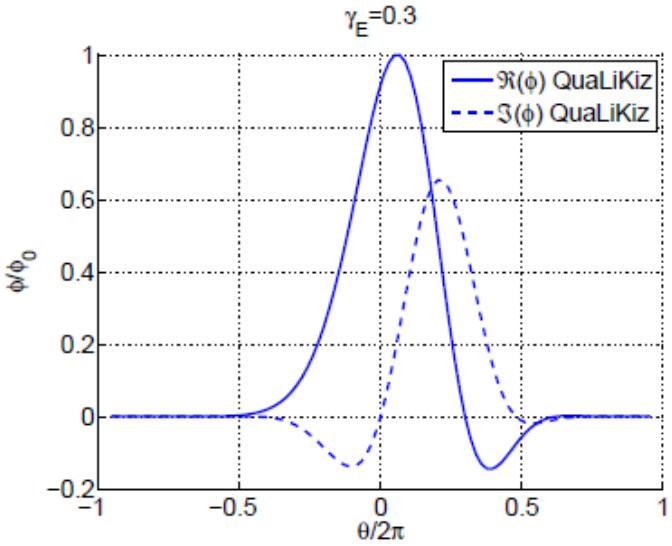

Figure 2.8: QuaLiKiz eigenfunctions as a function of the parallel direction $\theta/(2\pi)$. Dashed line: imaginary part, solid line: real part. For the GA standard case parameters and a finite $\mathbf{E}\times\mathbf{B}$ shear $-\gamma_E = 0.3$. At $k_\theta\rho_s = 0.3$. From P. Cottier et al [42].

In the presence of a finite $\mathbf{E}\times\mathbf{B}$ shear, the imaginary part of the eigenfunction can be of the same order of its real part as illustrated by figure 2.8. In this case, accounting properly for the imaginary part of the eigenfunction is essential. Unfortunately, eigenfunctions with $\mathbf{E}\times\mathbf{B}$ shear in the self-consistent gyrokinetic framework are not available, since the general solutions of the linearized gyrokinetic equation in such conditions are oscillating modes, see [89] for more details. Nonetheless, the growth rates in presence of $\mathbf{E}\times\mathbf{B}$ shear obtained by QuaLiKiz will be compared to GKW later in this chapter.

Summary of the eigenfunction's benchmarks

To summarize, the eigenfunctions in QuaLiKiz are computed thanks to an analytical fluid limit accounting for $U_\parallel$, $\nabla U_\parallel$ and $\mathbf{E}\times\mathbf{B}$. The solution of the second order differential equation is a shifted Gaussian. This fluid analytical eigenfunction used in QuaLiKiz is compared to self-consistent gyrokinetic eigenfunctions provided by GYRO, GENE and GKW. Without rotation and $\mathbf{E}\times\mathbf{B}$ the agreement is very good. Nonetheless wider oscillating eigenfunctions are found in two cases and cannot be properly modeled by QuaLiKiz ballooned eigenfunctions: the first case at low magnetic shear and low wave

number, such that $s \leq 0.1$ and $k_\theta \rho_s \leq 0.15$; the second case at TEM dominated regimes at large wave numbers. The influence of $U_\parallel$ and $\nabla U_\parallel$ on the eigenfunction is successfully benchmarked against GKW. The impact of $\mathbf{E} \times \mathbf{B}$ shear is observed in QuaLiKiz eigenfunctions, but cannot be compared to self-consistent gyrokinetic codes. Although, not perfect, the fluid analytical eigenfunctions computed in QuaLiKiz are similar to self-consistent gyrokinetic eigenvalues in a large number of cases, including cases with a finite rotation. The computed growth rates and quasilinear fluxes accounting for these analytical fluid eigenfunctions will be extensively benchmarked in the rest of this manuscript.

2.4 Searching for the eigenvalues

In QuaLiKiz, the eigenfunctions of the dispersion relation (equation (2.55)) are solved in the fluid limit. The eigenvalues of equation (2.55) are solved in the gyrokinetic framework. In (2.55), the functionals are multidimensional integrals of rapidly varying complex functions. Therefore, an efficient method to look for the eigenvalues of such an equation is needed. A method specific to complex variables functions is used: the Davies Method [90]. It is a generalized Nyquist's method. This method can determine the number of eigenvalues within a given contour, as well as an estimate of their values. Their precise localization is then refined using a standard Newton's method. The method presented by Davies consists in using the argument principle and the residues theorem. The argument principle states that along a closed contour $\mathcal{C}$ the increment of the argument of $\mathcal{D}$ is equal to $2\pi N$, N being the number of zeros within $\mathcal{C}$. On the other hand, from the residues theorem, for ω going along $\mathcal{C}$, a transform of a circle centered on 0, one gets:

$$S_n = \frac{1}{2\pi i} \quad \int_{\mathcal{C}} \omega^n \frac{D^{'}(\omega)}{D(\omega)} d\omega = \sum_{i=1}^{N} \omega_{0i}^n \tag{2.86}$$

$n = 1, ..., N$
Knowing S_n and N, one can construct a polynomial $P_N(\omega)$ which zeros are ω_0 such that:

$$P_N(\omega) = \prod_{j=1}^{N} (\omega - \omega_{0j}) = \sum_{j=0}^{N} A_j \omega^{N-j} \tag{2.87}$$

where A_j are solutions of the following system of N equations:

$$\begin{aligned} S_1 - A_1 &= 0 \\ S_2 - A_1 S_1 - 2A_2 &= 0 \\ S_k - A_1 S_{k-1} + A_2 S_{k-2} + ... + (-1)^k k A_k &= 0 \end{aligned} \tag{2.88}$$

$k = 3, ..., N$.
With this method, from the values of $\mathcal{D}$ over a contour $\mathcal{C}$, the transformation of a zero-centered circle, one can find all the complex eigenvalues of $\mathcal{D}$ enclosed by $\mathcal{C}$.
QuaLiKiz uses this method to find all the unstable eigenvalues. Indeed, only the plane with positive complex ω is explored. The largest complex value limiting the top of the contour is estimated by a fluid limit polynomial estimate of the unstable modes. Indeed, the fluid limit is known to overestimate the gyrokinetic eigenvalues. The lowest complex value of the contour is $0.01 \times k_\theta \rho_s \frac{T}{eBR}$. The real axis is scanned by shifting the contours along the positive and the negative direction until the largest value of the frequency of the mode obtained in the fluid limit is reached. The points used along the contour to estimate the number of eigenvalues are at first 25. The jump in angle between two consecutive points has to be smaller than $\pi/3$, if it is not the case the number of points along the contour is multiplied by two, until reaching 200. At 200, if the angle jump is still larger than $\pi/3$ the search for the number of enclosed eigenvalues is stopped. This problem can occur for barely unstable modes having eigenvalues standing very close to the contour itself. Once the number of eigenvalues is found, their values are estimated thanks to the method presented above. Note that the vast majority of the time only one eigenmode per contour is found.
Finally, the dispersion relation of these eigenvalue is calculated : $\mathcal{D}(\omega_0)$. Ideally one should find $\mathcal{D}(\omega_0) = 0$. In practice, if $\mathcal{D}(\omega_0) > 100$, the eigenvalues are not stored at all, whereas, if $\mathcal{D}(\omega_0) \leq 100$, the eigenvalues are refined thanks to a Newton's method. This numerical scheme has been recently further optimized, since the rapidity of the code is a key issue for the use of QuaLiKiz in an integrated modeling platform [35].

2.5 Linear benchmark of the growth rates

QuaLiKiz uses the forms of the functionals given above, with the eigenfunction derived in the fluid limit and the eigenvalues then found using the Davies method. Presently, two ions and electrons can be treated. Additional ions could be easily added, this work is presently in progress.
The code is written in Fortran 90. It has been based on the Numerical Algorithm Group library for the Fried and Conte integrals, the Bessel functions, the elliptical integrals and the adaptive 1D and 2D integration methods. The NAG routines are being replaced by similar open source functions at the moment.
QuaLiKiz, or Kinezero as it was called previously, has been often bench-

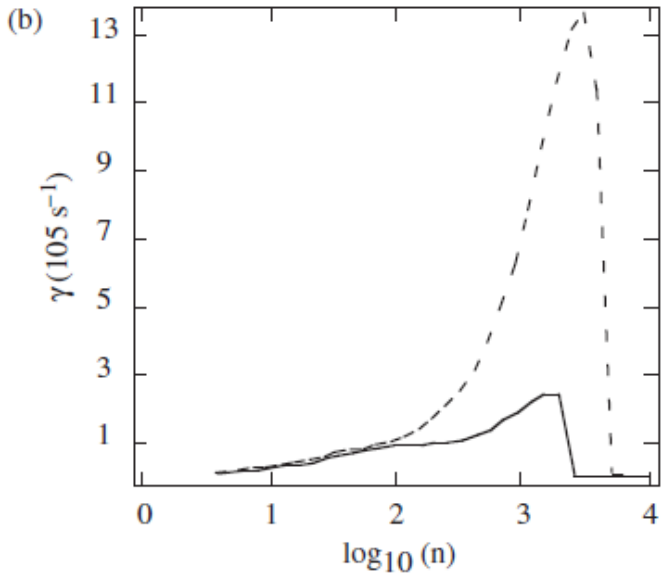

Figure 2.9: Textor pulse 68812 at 2.3 s and $\rho = 0.75$. Kinezero growth rate spectrum from [28]. solid line: $Z_{eff} = 2.7$, dashed line: $Z_{eff} = 1.2$.

marked against more complete gyrokinetic codes.
The first benchmark was presented in [28] and showed that the stabilizing impact of Z_{eff} was found in both Kinezero Fig.2.9 and GS2 Fig.2.10 for a TEXTOR set of parameters. The stabilizing impact of an increased Z_{eff} is seen in both codes on the ETG branch of the spectrum. The order of magnitude of the growth rates are similar in both codes although Kinezero underestimates them.

Following the implementation of collisions on trapped electrons in Kinezero [76], their stabilizing impact on TEM was tested through a comparison with GS2 published in [91]. In both cases, at low collisionality, where TEM dominate, a higher normalized density gradient $A_n = \frac{R}{L_n} = \frac{-R\nabla n_e}{n_e}$ is destabilizing; whereas at lower collisionality, where ITG dominate, a higher A_n is stabilizing. The case calculated by GS2 is illustrated on figure 2.11, the case using Kinezero is displayed in figure 2.12.

More recently, the impact of the magnetic shear on quasilinear fluxes was investigated [34]. The QuaLiKiz growth rates were compared to GENE. The set of parameters used is the GA-standard case mentioned earlier for $k_\theta \rho_s = 0.3$. In this s scan, α is forced to zero. As expected from the dependance of the curvature drift, the interchange is maximized where the curvature drift intensity is maximized, i.e. at $s = 0.5$ for ballooned modes in the case of $\alpha = 0$.

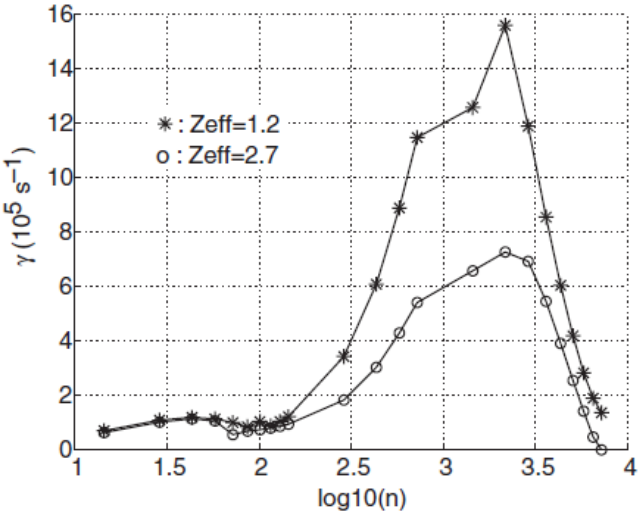

Figure 2.10: Textor pulse 68812 at 2.3 s and $\rho = 0.75$. GS2 growth rate spectrum from [28]. Circles: $Z_{eff} = 2.7$, asterisks: $Z_{eff} = 1.2$.

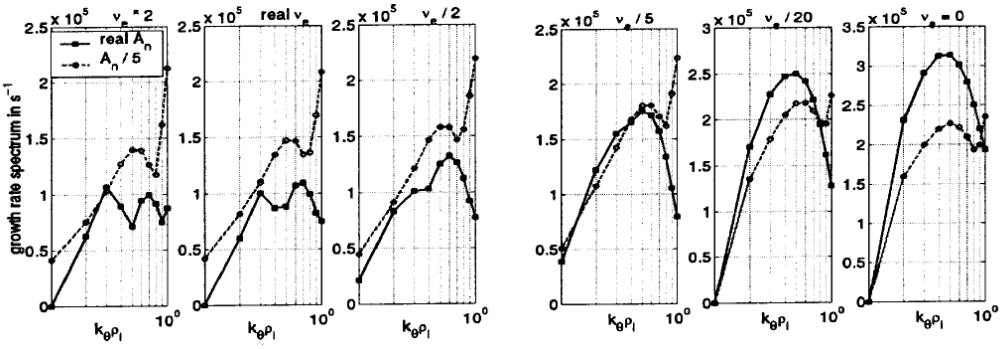

Figure 2.11: FTU pulse 12747 at 0.7 s and $\rho = 0.7$. GS2 growth rate spectrum from [91].

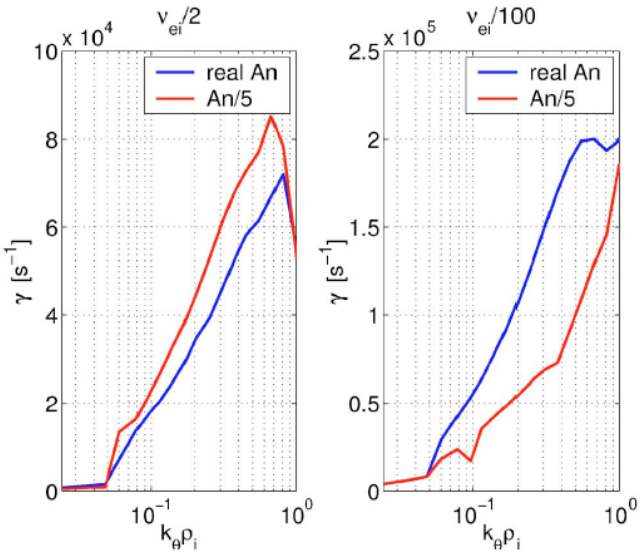

Figure 2.12: FTU pulse 12747 at 0.7 s and $\rho = 0.7$. Kinezero growth rate spectrum from [76]. Blue line: experimental value of A_n, red line artificially reduced A_n, $A_n/5$.

For both GENE and QuaLiKiz, the growth rates do indeed peak for $s \simeq 0.5$. For larger values of s the growth rates are ultimately stabilized. In figure 2.13, one can see that in QuaLiKiz the stabilization for negative values of s is overestimated. It could be due to the fact that the integration of the passing particles is done such that the transit frequency $k_{\|}V_{\|}$ is averaged over the pitch angle λ rather than correctly integrated. This approximation might lead to an underestimation of the slab branch which becomes dominant in this region where the interchange branch is weakened.
Finally, during Pierre Cottier's PhD the linear growth rates of QuaLiKiz in the presence of finite rotation and/or $E \times B$ shear was extensively benchmarked against GKW. Two examples are given based on GA standard case parameters for $k_\theta \rho_s = 0.3$. First, on figure 2.14, the destabilizing impact of larger parallel velocity gradient is compared for three values of the normalized temperature gradient $\frac{-R\nabla T}{T} = \frac{-R\nabla T_e}{T_e} = \frac{-R\nabla T_i}{T_i} = 3, 6$ and 9. The overall agreement is satisfactory, the growth rates calculated by QuaLiKiz have the correct response to both $\frac{-R\nabla T}{T}$ and $\frac{-R\nabla U_{\|}}{v_{th,i}}$. The order of magnitude is also acceptable, although QuaLiKiz growth rates are slightly underestimated. The impact of $\mathbf{E} \times \mathbf{B}$ shear is investigated independently, see figure 2.15. In initial value codes such as, GKW or GENE, the presence of oscillating Floquet modes required the modification of the temporal averaging

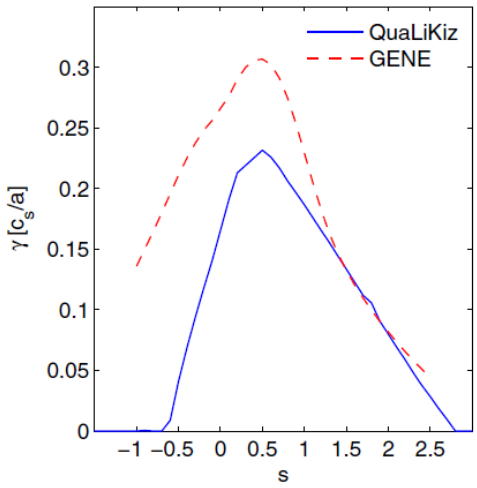

Figure 2.13: GENE in dashed line red and QuaLiKiz in solid line blue. The normalized growth rates are plotted versus s for $k_\theta \rho_s = 0.3$. The parameters used are the GA-standard case parameters. From [34].

method. More details on this point are given in [14], [42] as well as in [92] where a slightly different method is proposed than the one used for the plot below. The stabilizing impact of increased $\mathbf{E} \times \mathbf{B}$ in QuaLiKiz is observed to agree well with the GKW stabilization when using the modified temporal averaging.

In the various cases presented here, the agreement between QuaLiKiz (or Kinezero for the earlier benchmarks) is not perfect, the discrepancy can be large, for example for negative values of s. Nonetheless, the qualitative parametric dependencies are well captured by QuaLiKiz as illustrated for Z_{eff}, density gradient, collisionality, s, parallel velocity gradient, and $\mathbf{E} \times \mathbf{B}$ shear. Moreover, in most cases the order of magnitude of the growth rate is correct within a few tens of %. QuaLiKiz tends to underestimate the growth rates. The reason is that the eigenfunctions are more narrow in θ and wider in ρ in QuaLiKiz, leading to a weaker stabilizing impact of $k_\parallel V_\parallel$ (see discussion in chapter 3 on the impact of magnetic shear). In chapter 4, the benchmark exercise will be extended to quasilinear fluxes.

2.6 Conclusion

Thanks to the numerous approximations carried out ($s-\alpha$ equilibrium, electrostatic, ballooning transform, simplified integrations, fluid eigenfunctions,

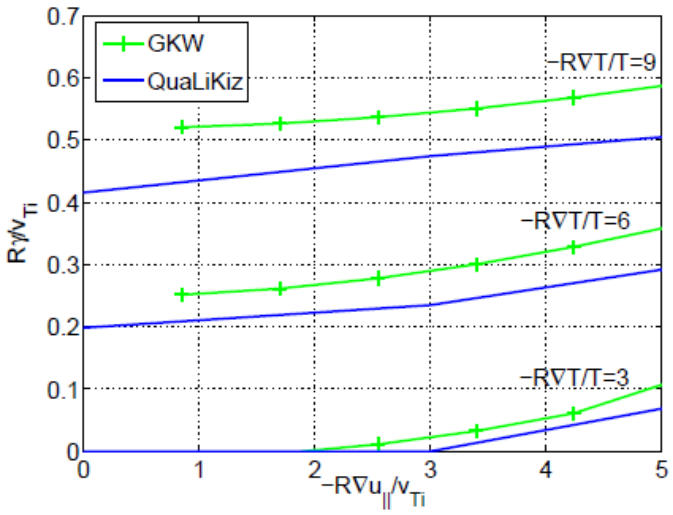

Figure 2.14: GKW in green solid line with crosses and QuaLiKiz in blue plain solid line. The normalized growth rates are plotted versus $\frac{-R\nabla U_{\parallel}}{v_{th,i}}$ for $k_\theta \rho_s = 0.3$. The parameters used are the GA-standard case parameters. From [14], [42].

optimized eigenvalues search), QuaLikiz gyrokinetic linear calculation is a factor 10 000 faster than more precise gyrokinetic codes such as GYRO, GKW, GS2 or GENE. The obtained growth rates, for electrostatic cases and in the $s - \alpha$ equilibrium, are validated against these codes. QuaLiKiz is therefore available to analyze extensively experimental discharges and discuss their stability, and further examples thereof are given in chapter 3. The code can also to be used to compute quasilinear fluxes, which gains an additional speedup factor of 100 versus nonlinear fluxes, as detailed in chapter 4. With the total approximate 1 million speedup factor this approach is thus suitable for predictive integrated modeling.

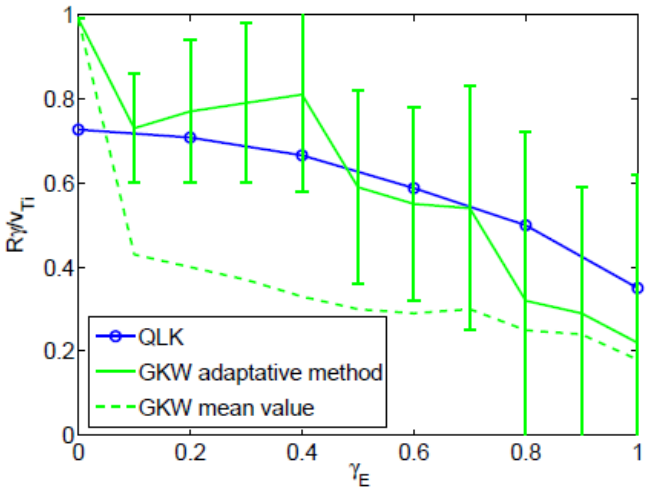

Figure 2.15: GKW in green dashed line for the case without modifying the temporal averaging. GKW in solid green line for the case using the modified temporal average, the error bars stand for the standard deviation around the third quartile value. QuaLiKiz in blue plain solid line. The normalized growth rates are plotted versus $\frac{\gamma_E}{v_{th,i}/R}$ for $k_\theta \rho_s = 0.3$. The parameters used are the GA-standard case parameters. From [14], [42].

Chapter 3

Use of linear gyrokinetic stability analysis

Before addressing the estimate of the transport fluxes through the quasilinear approximation, the use of linear gyrokinetic analysis is presented. Two classes of analysis are outlined. First, the impact of a given parameter on the growth rates and the instability threshold can be tested. Second, the dominant modes in a given experimental pulse can be investigated. Both usages are presented here.

3.1 Linear stability and its parametric dependencies

Before presenting linear stability limits, the two main branches of instabilities are presented. They are introduced in the approximated framework of the fluid theory. As the reader will see, knowing their trends will be helpful when studying the stability limit parametric trends illustrated in this section.

3.1.1 The two main types of instabilities derived from the fluid dispersion relation

The two main classes of instabilities are the curvature-type and the slab-type. The curvature-type instability couples the diamagnetic frequency due to the density and temperature gradients to the curvature and ∇B-drift frequencies. It is also called the interchange instability branch, for more detailed explanations on the mechanisms at play see [14, 13, 10]. The slab-type instability couples the diamagnetic frequency to the transit frequency along the magnetic field lines, and survives at infinite aspect ratio, i.e. it does not depend

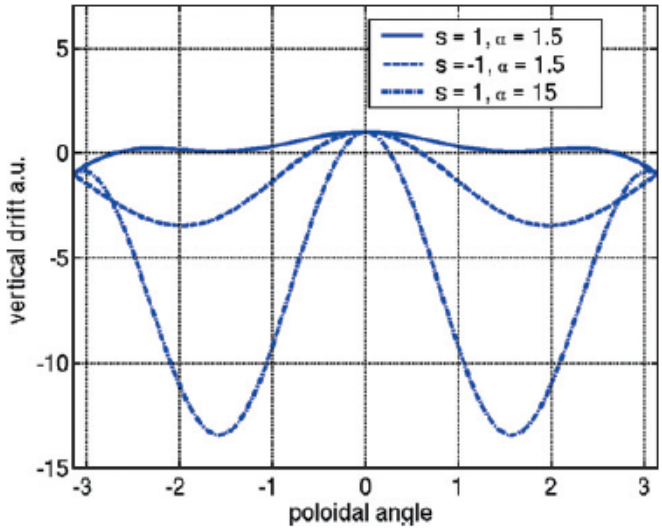

Figure 3.1: Curvature drift in arbitrary units versus θ for three pairs of (s, α) values. From [95].

on the curvature. These two unstable branches have been well described by Biglari et al in [93] and by Kadomstev in [94] by means of fluid calculations. In the gyrokinetic approach, it is very difficult to isolate one branch or the other since the growth rates of the unstable modes are the eigenvalues of the dispersion relation introduced previously (equation (2.55)) where all types of particles and drifts contribute to the final eigenvalues. Nevertheless, one still observes some trends reproducing the behavior expected in the simplified fluid limit. These trends are summarized below.
Two unstable branches are derived in a simplified fluid limit. In this limit, as detailed earlier, the frequency of the unstable modes is greater than the transit and curvature frequencies. Moreover, it is assumed here that the density gradient is negligible in comparison to the temperature gradient. One then finds the following expression for the curvature-type growth rate, γ_{int}:

$$\gamma_{int,s}^2 = n\omega_{ds} \cdot n\omega_{ps}^* \tag{3.1}$$

The impacts of s and α on the curvature drift are illustrated in figure 3.1. If s and α are such that the flux surface average of the curvature and ∇B drifts is reduced or reverses sign, then the drive for the dominant interchange instability is reduced or even suppressed. Indeed, from the cases illustrated by figure 3.1, reversing s from 1 to -1 leads to reduced positive curvature and ∇B drive at the low field side. Also, by increasing α one obtains a similar effect on the interchange drive due to reduced curvature and ∇B drifts.

The stabilizing impact of large α has a potential beneficial side effect. Indeed, when increasing $\frac{-R\nabla P}{P}$, $n\omega_d$ decreases and can possibly compensate the destabilizing increase of $n\omega_p^*$. Actually, there is a threshold above which the stabilization through α beats the destabilization due to higher $\frac{-R\nabla P}{P}$ (see [60] for discussion of this effect on Internal Transport Barrier plasmas obtained in JET and JT-60U). Above this threshold or for negative s, the slab branch dominates the reduced interchange branch.
One can evaluate the slab growth rate, γ_{slab}, employing a simplified approach, similar to that used in the derivation of eq. (3.1), but in the limit where the major radius, R, tends to infinity, i.e. the torus tends towards a cylinder. With very large R, the fluid equation has the following solution:

$$\gamma_{slab}^3 = (k_\parallel V_T)^2 \cdot n\omega_p^* \tag{3.2}$$

Therefore, an increasing pressure gradient always leads to a higher slab growth rate. In the sheared slab case, $k_\parallel = \frac{k_\theta |s| x}{r}$, thus, the slab growth rate increases with $|s|$ independently of its sign.
This demonstrates that in a simplified electrostatic calculation there are two unstable branches, the slab and the interchange branches, with very different parametric dependencies with respect to s and α. Some of these qualitative behaviors will be discussed later in this chapter.

3.1.2 Linear stability limit

A linear gyrokinetic stability limit can be deduced from the above approach. Plotted in the plane $-R\nabla T/T$ versus $-R\nabla n/n$, this limit provides a useful visualization of the key mechanisms at play. It is important to note that such curves are far from being universal. They are valid only for given values of collisionality, ratios of T_e/T_i and $\frac{-R\nabla T_e/T_e}{-R\nabla T_i/T_i}$, Z_{eff}, s, α and q. It is to note that the discussion below is done in absence of $\mathbf{E}\times\mathbf{B}$ shear and parallel rotation. First of all, the fluid limit in the plane $(-R\nabla T/T, -R\nabla n/n)$ is derived and plotted, then it is compared to gyrokinetic limits with and without including trapped electrons.

Linear stability in the fluid limit

It is rather simple to derive the fluid stability limit. It is based on the existence of a solution of a second order polynomial with a positive imaginary part, i.e. a positive growth rate. The second order polynomial dispersion relation is based on a simplification of the fluid dispersion relation derived in equation (**??**) assuming very low wave numbers such that $k_\theta \rho_{eff} \simeq 0$ and very localized modes such that $x \simeq 0$:

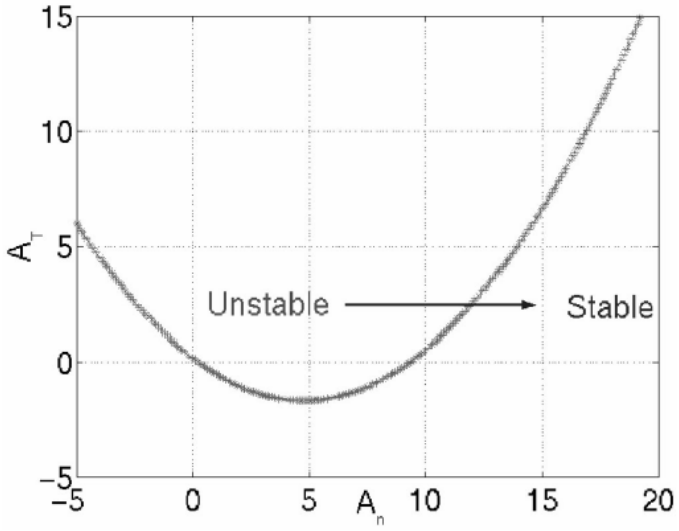

Figure 3.2: Fluid limit between the stable and the unstable regions of the plane (A_n, A_T). For the assumptions made for the derivation see the main text. From [91].

$$\Omega^2 + \Omega\left(A_n(1+f_t) + 3/2\right) + \frac{3}{2}\frac{f_t}{1-f_t}(A_n + A_T) = 0 \tag{3.3}$$

with $Z_{eff} = 1$, $T_i = T_e$, $\omega = \frac{\omega}{\bar{\omega_d}}$ and $\bar{\omega_d} = \frac{k_\theta T_e}{eBR}$, as usual $A_n = -R\nabla n/n$ and $A_T = -R\nabla T/T$. Here s and α are such that:

$$\langle \cos\theta - (s\theta - \alpha\sin\theta)\sin\theta \rangle = 1$$

The solutions having a positive imaginary part of equation (3.3) are such that:

$$A_T > \frac{1-f_t}{6f_t}\left((1+f_t)A_n + 3/2\right)^2 - A_n \tag{3.4}$$

This limit is plotted in the (A_n, A_T) plane in figure 3.2.

From the fluid limit given by figure 3.2, one can see that the modes are unstable as soon as A_T has a positive value for low values of A_n, meaning that in such cases there is no critical temperature gradient. For larger values of the density gradients, the critical temperature gradient threshold increases. These modes are called the $\eta = A_T/A_n$ modes [10, 51]. They are destabilized by larger A_T and stabilized by larger A_n.

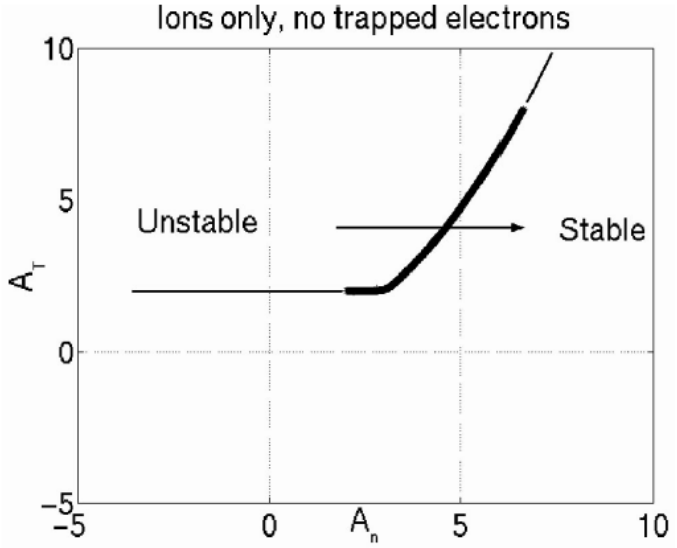

Figure 3.3: Gyrokinetic stability limit of the plane (A_n, A_T) with $\gamma = 9.10^{-4} c_{se}/a$ and $k_\theta \rho_i = 0.5$. For pure ITG modes. From [91].

Linear stability in the gyrokinetic case

For the same parameters as above, the gyrokinetic stability limit is derived. It is based on the dispersion relation calculated for $\omega = \omega_r + i9.10^{-4} c_{se}/a$ with $c_{se} = \sqrt{T/m_e}$ and $T = 1$ keV. At a given wave number and for a chosen ω_r, the system of two equations $Im(\mathcal{D}(\omega_1)) = 0$ and $Re(\mathcal{D}(\omega_1)) = 0$ is solved. The two unknowns, A_T and A_n, correspond to the critical gradient lengths at which the growth rate is almost null. By scanning the frequency ω_r, new pairs (A_n, A_T) are found. By plotting all the (A_n, A_T) pairs, one then obtains the gyrokinetic stability limit above which the growth rates are greater than the initially chosen small value, here $9.10^{-4} c_{se}/a$.

- Linear stability in the gyrokinetic case: ITG only

  A first case is plotted using the dispersion relation assuming adiabatic electrons, i.e. for ions only, see figure 3.3. From figure 3.3, unlike in the fluid case, one can see that for any value of A_n a finite critical temperature gradient exists. By comparing figure 3.3 to figure 3.2, it is clear that the fluid approximation leads to a wider unstable domain and that it does not compute the correct stability threshold. For pure ITG, as A_n gets larger, the modes are stabilized by larger density gradient as found in the fluid limit. Indeed, for large values of A_n and A_T the fluid limit is an exact representation of the gyrokinetic dispersion

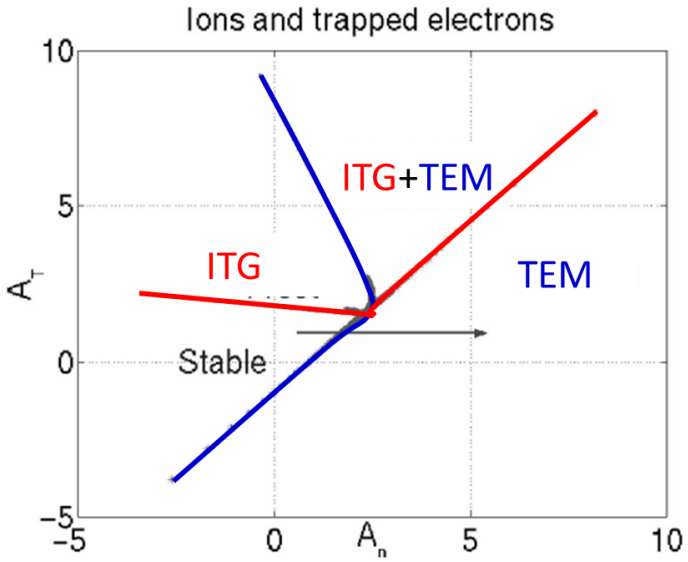

Figure 3.4: Gyrokinetic stability limit of the plan (A_n, A_T) with $\gamma = 9.10^{-4} c_{se}/a$ and $k_\theta \rho_i = 0.5$. For ions and trapped electrons contributing to the dispersion relation. From [91].

relation.

- Linear stability in the gyrokinetic case: ITG and TEM

  Now the trapped electron response is kept in the dispersion relation with $A_T = A_{T_i} = A_{T_e}$. The stability limit is plotted in figure 3.4. IN this case, two stability curves co-exist. In addition to the ITG stability limit, the TEM stability limit appears. The TEM are destabilized by larger A_n. At low A_n the ITG critical normalized temperature gradient is much lower than the TEM gradient. On the other hand, for larger values of A_n, as A_T increases, TEM are destabilized first.

- Linear stability in the gyrokinetic case: ETG only

  Finally in the high $k_\theta \rho_s$ limit, where the only species responding to the fluctuations are the passing electrons, the ETG stability limit can be derived. It is illustrated by figure 3.5. It is very similar to the ITG stability limit, indeed the dispersion relations of pure ITG (adiabatic electrons) and pure ETG (adiabatic ions) are isomorphic.

In the following, the impact of some parameters on the stability limits are reviewed. The focus is on the ITG-TEM case which is the relevant framework

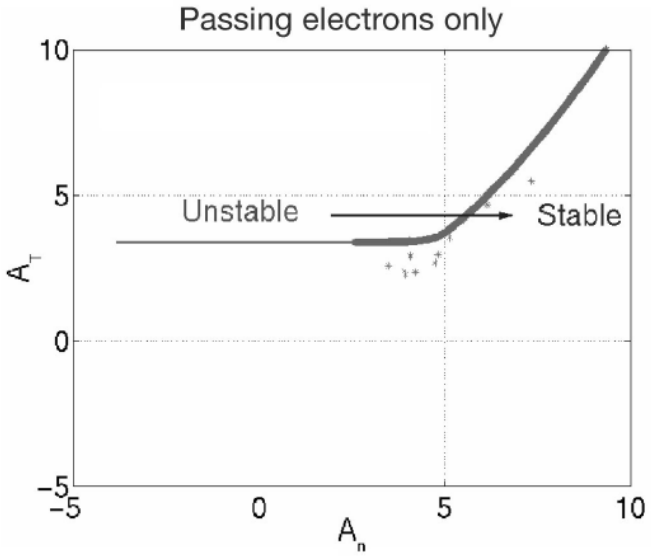

Figure 3.5: Gyrokinetic stability limit of the plane (A_n, A_T) with $\gamma = 9.10^{-4} c_{se}/a$ and $k_\theta \rho_e \simeq 1$. For ETG. From [91].

for tokamak plasma low-k turbulence.

Linear stability in the gyrokinetic case: parametric dependencies

- Impact of collisionality

  When increasing the collisionality acting on trapped electrons, the electrons are continuously detrapped. Above a certain level of collisionality, the trapped electrons no longer contribute to the dispersion relation and the pure ITG stability limit is recovered. This process is illustrated by figure 3.6, where the collisionality normalized to $k_\theta T/eBR$, $A_{\nu e}$, is increased from very low values, 10^{-3}, on the top left plot, up to very large values, 10^9, on the bottom right plot. Tokamak relevant values are also plotted: 10^5 for JET-like plasmas in the top right plot, and 10^7 for FTU-like plasmas in the bottom left plot.
  Experimentally, in high density plasmas of FTU, the presence of additional pellet fueling led to an improvement of the energy confinement. This experimental trend was partially explained by the expected TEM stabilization at higher collisionalities [91], see also [96] for Asdex-Upgrade's results for example.

- Impact of T_i/T_e

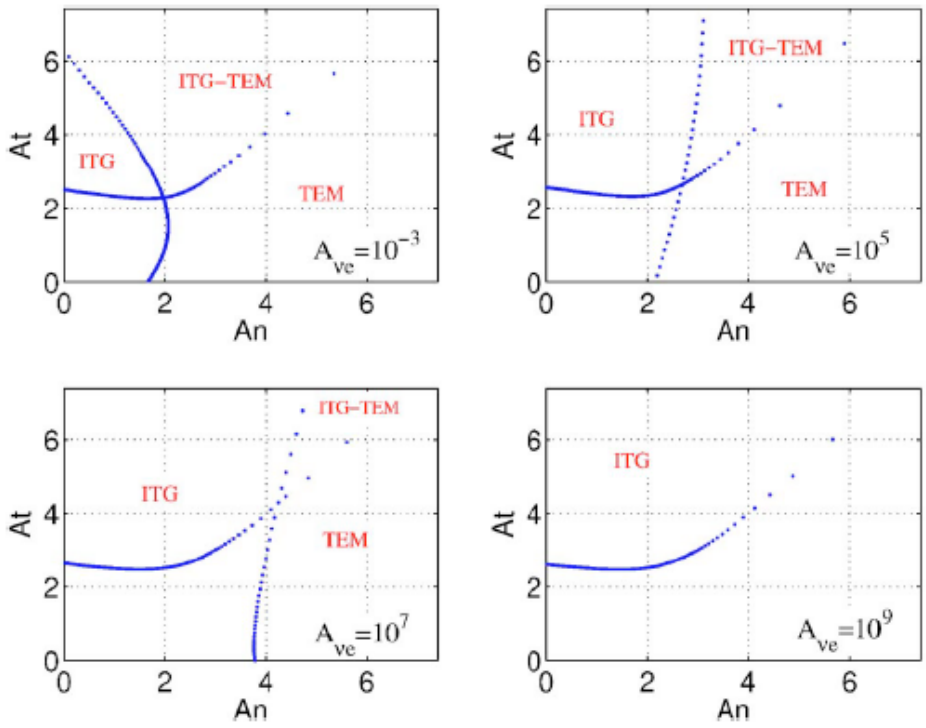

Figure 3.6: Gyrokinetic stability limit on the plane (A_n, A_T). For the ITG-TEM case and for four values of the ratio of the collisionality to $k_\theta T/eBR$, $A_{\nu e} = 10^{-3}, 10^5, 10^7, 10^9$ from the top left to bottom right plot. From [76].

The impact of the ratio T_i/T_e has been discussed in details in [97]. In that paper, it is shown that the T_i/T_e impact derived from the simple fluid limit expressed in (3.3) leads to destabilized ITG when increasing T_i/T_e. This tendency is recovered at the high A_n branch of the ITG stability limit plotted on figure 3.7, where the ITG unstable domain increases when going from $T_i/T_e = 0.5$, 1 and 2. On the contrary, for low values of A_n, the critical temperature gradient becomes higher as T_i/T_e is increased. This reversed tendency is explained by the fact that at low A_n, and therefore low A_T, the kinetic resonant effects are dominant and lead to a stabilizing impact at larger T_i/T_e. For more details see [97]. For the TEM stability branch, the impact of T_i/T_e for large values of A_n is as expected in the fluid limit, i.e. a higher T_i/T_e is stabilizing. For lower values of A_n the behavior is reversed and is dominated by kinetic resonance effects. A similar complex behavior is seen with respect to Z_{eff} as explained in chapter 4 of [80]. Therefore a kinetic approach is essential to obtain not only a precise stability limit as discussed previously but also to capture the correct parametric dependencies of the threshold.
Experimentally, the stabilization of the turbulent transport for large T_i/T_e values, commonly named "hot ion mode" has been widely reported on DIII-D, JET [98, 99] and TFTR [100]. The improved confinement is a signature of the ITG stabilization occurring for larger T_i/T_e.

- Impact of magnetic shear Until now, the focus was on the threshold and its parametric dependencies. While the threshold parametric dependencies are important, it is important to also study the behavior above the threshold. The sensitivity of the degree of stability to a given parameter above the threshold can be in contradiction to the sensitivity of the threshold value itself. For example, higher magnetic shear leads to an upshift in temperature gradient threshold. This is due to the fact that $k_\parallel V_\parallel \propto \frac{s}{q}$, hence a higher s leads to a higher $k_\parallel V_\parallel$ frequency which is stabilizing. Indeed feeling more frequent oscillations in the magnetic field line direction is analogous to a car driving faster on a bumpy road: it feels less the bumps. But if the bumps are felt, i.e. if the mode frequency ω increases beyond $k_\parallel V_\parallel$, then higher $k_\parallel V_\parallel$ (and therefore higher s) is destabilizing. This is illustrated by figure 3.8, where the normalized growth rates at a given $k_y = k_\theta \rho_s = 0.2$, at a given $A_n = 3$, are plotted versus both s and $A_T = R/L_T$. This figure shows that the widest unstable region is obtained for $s \simeq 0.5$ as discussed previously. It also shows that for s values above 0.5, the

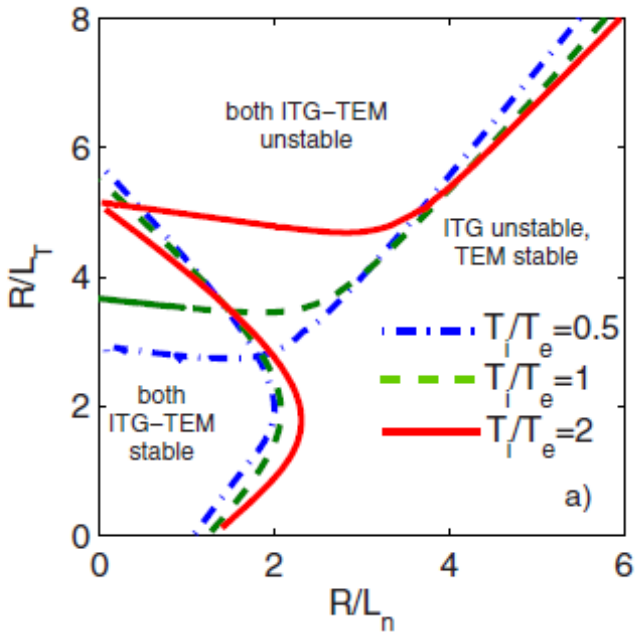

Figure 3.7: Gyrokinetic stability limit on the plane (A_n, A_T). For the ITG-TEM case and for three values of T_i/T_e. In this case $A_{Ti} = 0.65 A_{Te}$. From [97].

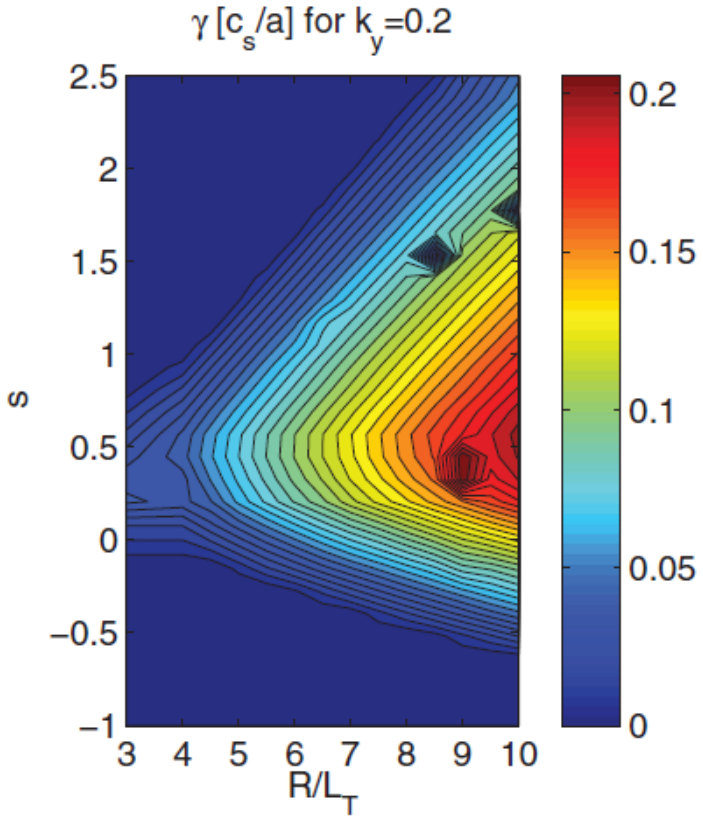

Figure 3.8: Gyrokinetic stability limit on the plane (s, A_T). For the GA standard case parameters at $k_\theta \rho_s = 0.2$. From [34].

temperature gradient threshold linearly increases. However, above the threshold, the growth rates increase less rapidly at $s = 0.5$ compared with $s = 1$ for example. It is said that the stiffness is weaker at lower s values. Depending on the wave number and the pair of s which is compared, the growth rates can even cross as illustrated by figure 3.9, reversing the s impact at the threshold and far above it. This phenomenon recalls the T_i/T_e contrasted impact reported in the previous subsection.

Experimentally, large internal inductance pulses are known to have improved confinement trends as observed with Low Hybrid Current Drive on Tore Supra [101] and reported due to large bootstrap current on TFTR [102] and DIII-D [103]. Large s are also observed to shift up the critical temperature gradient thresholds [104, 96]. For a wider discussion of the current profile impact on confinement see [105].

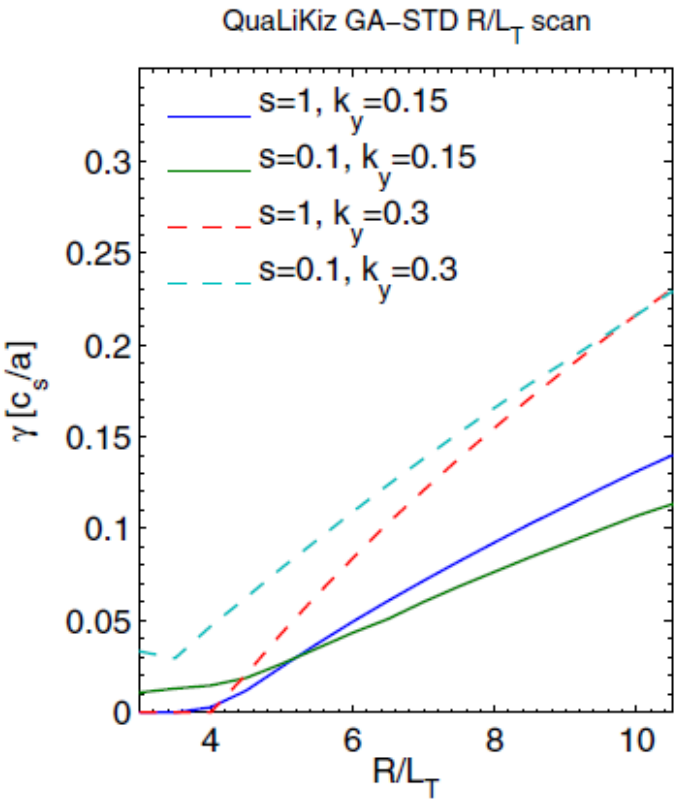

Figure 3.9: Normalized growth rate versus $A_T = R/L_T$. For the GA standard case parameters for four pairs of $(s, k_y = k_\theta \rho_s)$. From [34].

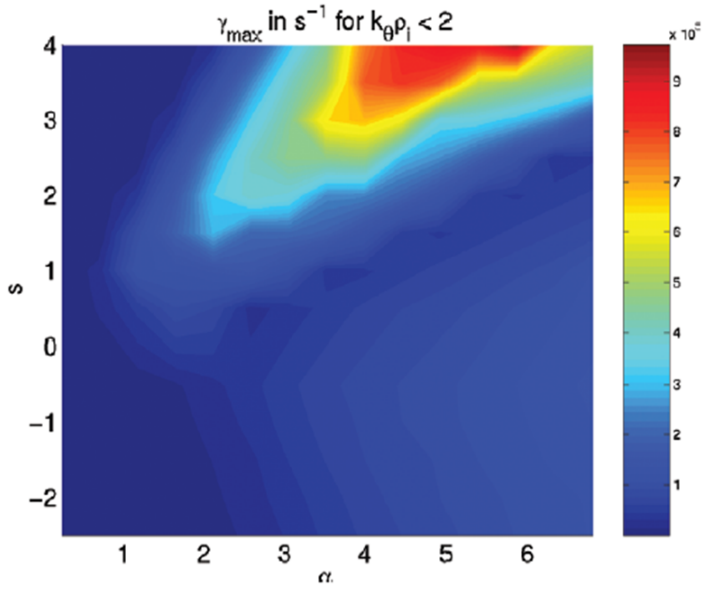

Figure 3.10: Maximum of growth rates for $k_\theta \rho_s < 2$ (ITG-TEM) in s^{-1} versus s and α. For $q = 2$, $T_e = T_i$, $A_T/A_n = 4$ and $\frac{-R\nabla P}{P} \simeq 11\alpha$, no collisions. From [95].

Also negative magnetic shear has been widely reported to be associated with Internal Transport Barriers, in particular on the electron heat and particle channels, see for example the very clear TCV experimental demonstration [106], for a review on ITB physics [107].

- Impact of α

  In a previous section, two limits of the dispersion relation have been discussed, the interchange branch and the slab branch. In figure 3.10, the growth rates in s^{-1} are plotted versus s and α, with $\alpha = q^2\beta\frac{-R\nabla P}{P}$. In this figure γ is the maximum of the growth rates over the part of the spectrum below $k_\theta \rho_s = 2$. The interchange branch is dominant. It is highly asymmetric with respect to s, indeed negative s values strongly stabilize it, see equation (3.1). Such $s - \alpha$ diagrams are found for all curvature driven modes, usually called ballooning modes. At these low k, the slab branch has weaker growth rates, as expected since the curvature drift dominates the transit frequency.
  For the passing electrons, the slab dynamics is much more important due to the large parallel velocities of the electrons which are therefore less sensitive to the curvature. This can be seen on figure 3.11, where the symmetric branch versus s is clearly dominant as expected by equa-

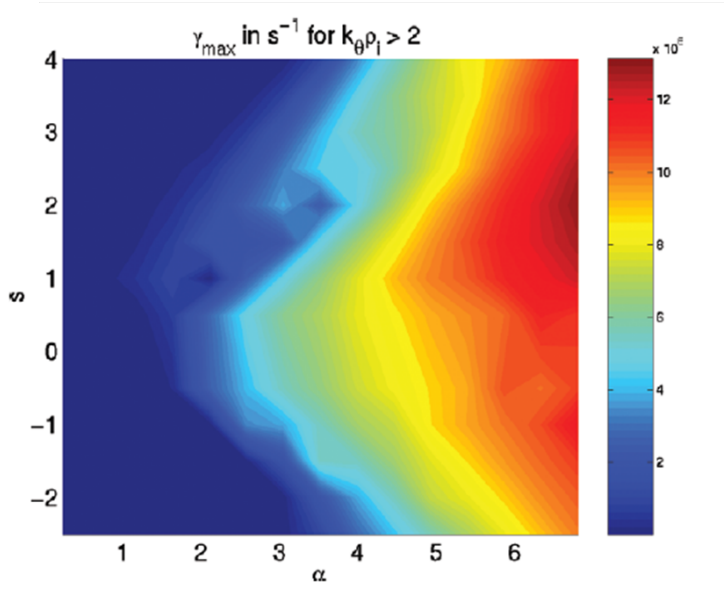

Figure 3.11: Maximum of growth rates for $k_\theta \rho_s > 2$ (ETG) in s^{-1} versus s and α. For $q = 2$, $T_e = T_i$, $A_T/A_n = 4$ and $\frac{-R\nabla P}{P} \simeq 11\alpha$, no collisions. From [95].

tion (3.2).

Experimentally, the particularly strong ITB observed in JT-60U have been reported as being potentially partially stabilized by large α values [95]. The role of fast particles are also contributing to larger α and are stabilizing through this mechanism as reported on JET in [108]. Recently, additional non-linear electromagnetic effects associated to large β have been shown to be a key factor in reproducing a set of ion heat transport experiments on the JET tokamak [92]. Such non-linear electromagnetic effects are presently not implemented in QuaLiKiz.

3.2 Linear analysis of an experimental pulse

The linear analysis of an experimental pulse is presented through its two main steps: the input preparation and the interpretation of the output. In particular, the reader will be made aware of the importance of diagnostics and the impact of their resolutions on the stability analysis performed.

3.2.1 Experimental input data to a linear gyrokinetic analysis

The input is the information necessary to solve the dispersion relation (2.55). Therefore, the ratios between the species in the sum $\sum_s \frac{n_s Z_s^2}{T_s}$, namely $\frac{n_s}{n_e}$ and $\frac{T_s}{T_e}$ far the various ions are required, including the charge Z_s of each ion. Then the input to calculate the various frequencies such as $n\omega^*$, $n_2\omega_2$ and $n_3\omega_3$ is needed. The is comprised of, for each species, $\frac{-R\nabla T_s}{T_s}$, $\frac{-R\nabla n_s}{n_s}$, as well as equilibrium quantities: s, α, q, r/R and information on the parallel rotation: $\frac{-R\nabla u_\parallel}{V_T}$, $\frac{u_\parallel}{V_T}$, γ_E. Based on such data, for each value of wave number n (or of $k_\theta \rho_s$ depending on the normalization chosen), the code calculates the eigenvalues. Up to 5 are searched for, but practically with three species (electrons and two ions) at most three simultaneous unstable modes can be found.

When analyzing experimental data, the inputs are deduced from fits of the experimentally measured quantities such as T_e, T_i, n_e, Z_{eff}, q. The profiles are not simple quantities to obtain. The diagnostic measurements are typically carried out in different poloidal and toroidal locations. Some measurements are line integrated, such as the density measured by interferometer or Z_{eff} by Bremsstrahlung emission. The plasma composition is extrapolated from a line integral Z_{eff} unless some charge exchange measurements allows to obtain the C density profile. For a C machine, in absence of charge exchange measurements, the C density profile is assumed to be homothetic to the D density although CX measurements showed that this was not the case in JET C wall [109]. For a metallic machine, using W and Be, such as JET with the ITER-Like-Wall, more than one impurity has to be accounted for, especially since the W is not completely ionized, therefore various W ionization stages have to be modeled. The implementation an infinite number of ions in QuaLiKiz is now possible [35].

Moreover, an equilibrium reconstruction coherent with the fitted pressure and current profiles is a key element. It can be produced by simple magnetic equilibrium reconstruction such as the Tprof tool used in Tore Supra, or by more sophisticated codes where the current diffusion is modeled such as CRONOS [46] run in its interpretative mode. The current profile is not directly measured, unless there is Motional Stark Effect diagnostics operational, which is not the case in Tore Supra. In Tore Supra, it is deduced from the current diffusion equation using CRONOS. The current evolution is constrained by the internal inductance (li), the Faraday angle measurements and by the magnetic flux consumption.

When analyzing an experimental plasma, preparing the input for a gyroki-

netic analysis is extremely demanding. It requires to know well the diagnostics used and their uncertainties. It is often the case that for example two density measurements, one by interferometry and one by reflectometry, will give slightly different results. The physicist in charge of the gyrokinetic analysis needs to discuss with the diagnosticians to understand which measurement to favor most. The fits need to be carefully done since the gradients are then used. The physicist has to be aware of the uncertainties of the measurements he/she uses since it will strongly impact the confidence one can have in the gyrokinetic analysis results. A measurement typically has uncertainties both on its absolute value and on its radial location.
Efforts have been made in order to use the Bayesian probability theory [110, 111]. Such methods produce profiles starting from the raw data, for example the temperature profile is reconstructed starting from Electron Cyclotron Emission and/or Thomson Scattering diagnostics. The uncertainties produced allow to estimate precisely the uncertainty on the gradient of the profile. Recently, a method based on the measurements produced by the data analysis of the diagnostics has been proposed: the Gaussian process regression. This technique provides uncertainties on the fits and on their gradients [112].
Below, a more basic illustration of the impact of the uncertainties on the gradient length is presented for the ion temperature measured by charge exchange spectroscopy. When using charge exchange spectroscopy measurements, one has to account for the beam extension for the uncertainty on the radial location and for the signal to noise ratio for the value of the temperature measured. To account for the uncertainties in both directions, one needs to use probabilistic theories as discussed earlier. An alternative option, is to assume a shape for the fit of the measurements, for example for T_i :

$$T_i(r) = T_i(0)(1-\rho^2)^{\alpha_T} \tag{3.5}$$

Then a linear regression allows to estimate properly the uncertainty on α_T such that:

$$(\Delta\alpha_T)^2 = \left(\frac{\partial\alpha_T}{\partial T_i}\right)^2 (\Delta T_i)^2 + \left(\frac{\partial\alpha_T}{\partial\rho}\right)^2 (\Delta\rho)^2 \tag{3.6}$$

This uncertainty is calculated for a Tore Supra pulse 43319, where T_i was measured by charge exchange spectroscopy. The radial extension of the diagnostic beam is 3 cm at the LCFS and 6 cm on the magnetic axis [113], and it is assumed to linearly vary along the minor radius. With the fit proposed in (3.5), one finds that $\alpha_T = 0.73 \pm 0.05$ as illustrated by figure 3.12. Unfortunately, as can be seen in figure 3.12, the fit does not pass through all the measured points. This is the weakness of this approach, although

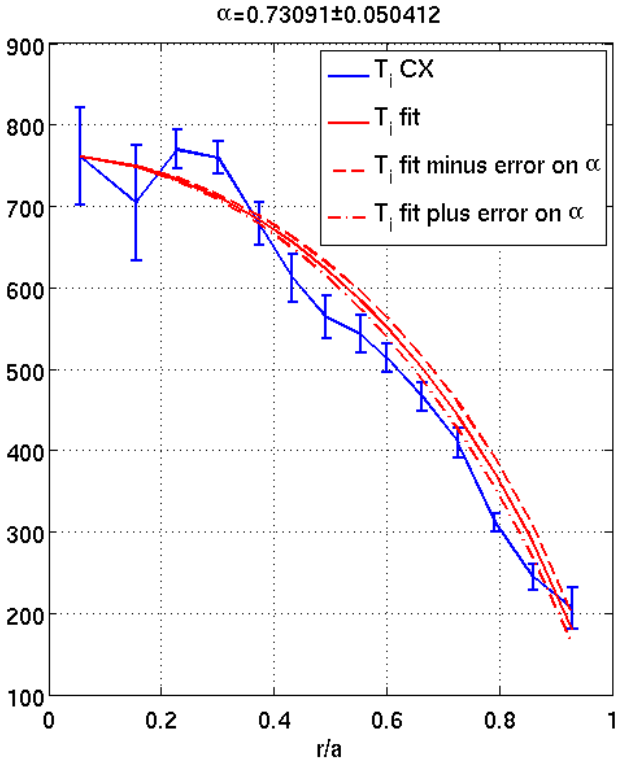

Figure 3.12: T_i measured by charge exchange for the Tore Supra pulse 43319 in blue. In red the fit is represented assuming $T_i(r) = T_i(0)(1-\rho^2)^{\alpha_T}$, with $\alpha_T = 0.73$, the dashed lines represent the fits accounting for the uncertainty range on α_T.

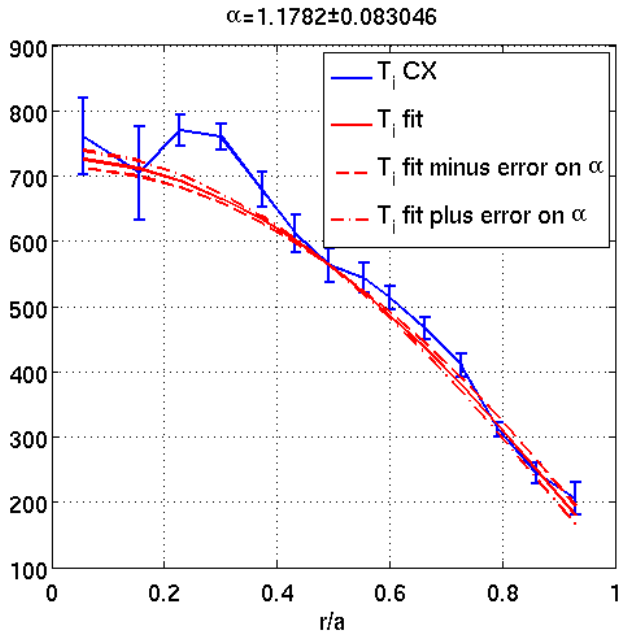

Figure 3.13: T_i measured by charge exchange for the Tore Supra pulse 43319 in blue. In red is represented the fit assuming $T_i(r) = T_i(0.5)(1.25 - \rho^2)^{\alpha_T}$, with $\alpha_T = 1.18$, the dashed lines represent the fits accounting for the uncertainty range on α_T.

it allows to estimate precisely the uncertainties, it is limited by an a priori choice for the fitting function. To slightly improve the fit quality, another function is chosen:

$$T_i(r) = T_i(0.5)(1.25 - \rho^2)^{\alpha_T} \tag{3.7}$$

In this case one obtains $\alpha_T = 1.18 \pm 0.08$ as illustrated by figure 3.13. Although the fit better reproduces the measurements, the choice of the fitting function remains highly arbitrary. Nonetheless the fit allows to estimate correctly the uncertainties on the normalized T_i gradient which is an input data of prime importance for linear stability analysis. The uncertainty on the gradient of T_i, ∇T_i, is given by:

$$(\Delta(\nabla T_i))^2 = \left(\frac{\nabla T_i}{\partial \alpha_T}\right)^2 (\Delta\alpha_T)^2 + \left(\frac{\partial \nabla T_i}{\partial \rho}\right)^2 (\Delta\rho)^2 + \left(\frac{\partial \nabla T_i}{\partial T_i(\rho_0)}\right)^2 (\Delta T_i(\rho_0))^2 \tag{3.8}$$

The uncertainty on T_i is given by:

$$(\Delta(T_i))^2 = \left(\frac{T_i}{\partial \alpha_T}\right)^2 (\Delta\alpha_T)^2 + \left(\frac{\partial T_i}{\partial \rho}\right)^2 (\Delta\rho)^2 + \left(\frac{\partial T_i}{\partial T_i(\rho_0)}\right)^2 (\Delta T_i(\rho_0))^2 \tag{3.9}$$

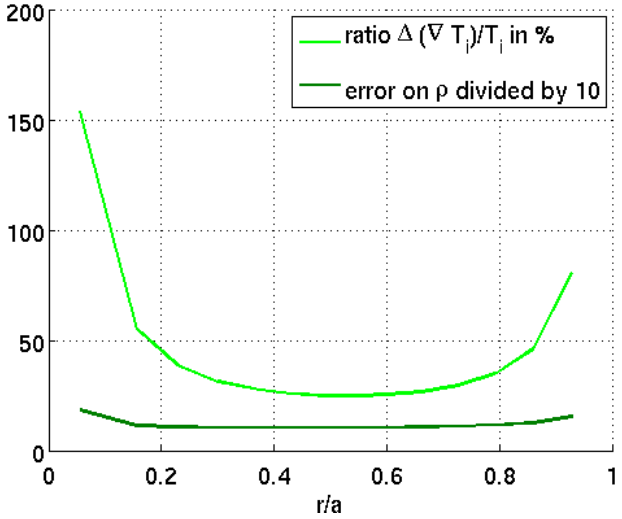

Figure 3.14: Uncertainties on $\nabla T_i/T_i$ based on a fit assuming $T_i(r) = T_i(0)(1-\rho^2)^{\alpha_T}$, with $\alpha_T = 0.73$, for Tore Supra pulse 43319. In light green with the actual uncertainties on the radial location, in darker green assuming reduced uncertainties on the radial location, i.e. 0.3 cm instead of 3 cm at the LCFS and 0.6 cm instead of 6 cm on the magnetic axis.

The uncertainty on $\nabla T_i/T_i$ is then:

$$\left(\Delta(\nabla T_i/T_i)\right)^2 = \left(\frac{1}{T_i}\right)^2 \left(\Delta(\nabla T_i)\right)^2 + \left(\frac{\nabla T_i}{T_i^2}\right)^2 \left(\Delta(T_i)\right)^2 \tag{3.10}$$

One then obtains the uncertainties, shown for the $\rho_0 = 0$ case in figure 3.14, and for $\rho_0 = 0.5$ in figure 3.15. Therefore, one can see, that at least an uncertainty of the order of 20% at mid-radius on $\nabla T_i/T_i$ has to be taken into account when performing the linear stability analysis. Inside $\rho = 0.2$ the uncertainty becomes larger than 100%, therefore it is usually extremely difficult to perform a stability analysis in the deep core due to larger uncertainties on the input data. It is also interesting to note that the uncertainty on the radial location of the measurements has a very strong impact on the uncertainty obtained on the normalized gradient. Indeed reducing it by a factor 10 leads to strongly reduced uncertainties at all radii, as illustrated on figure 3.14.
Usually the situation is better for T_e profiles as long as the Electron Cyclotron Emission diagnostic is available. This is the case on Tore Supra with a very high spatial resolution. However, in presence of fast electrons produced by the Lower Hybrid heating scheme, the ECE measurement is pol-

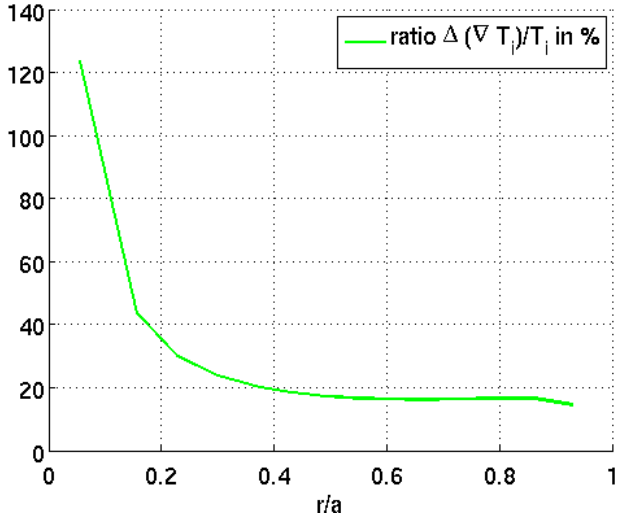

Figure 3.15: Uncertainties on $\nabla T_i/T_i$ based on a fit assuming $T_i(r) = T_i(0.5)(1.25 - \rho^2)^{\alpha_T}$, with $\alpha_T = 1.18$, for Tore Supra pulse 43319.

luted and cannot be used above mid-radius. Unfortunately, in Tore Supra, the Thomson Scattering measurement is not well resolved. As a consequence, the fits for T_e in presence of LH are poorly resolved in the outer part of the plasma. Recently various tokamaks have been equipped with very well spatially and timely resolved Thomson Scattering diagnostics, so called High Resolution Thomson Scattering (MAST [114], JET [115] for examples). For the electron density, reflectometers provide excellent spatially resolved density profile. However, the problem with this measurement technique is that it depends on the B field and is therefore sensitive to the uncertainties on this field where the first measurement is made, leading to a poor estimate of the absolute radial location. Alternatively, another diagnostic such as the interferometer can be used in lieu of better options. HRTS also provides well resolved density profiles. For T_i, profiles can be provided by either a charge exchange system [116] or 2D spectrometer [117]. The same diagnostics deliver the toroidal rotation. It is noteworthy to mention that in both cases the T_i and toroidal rotation are actually of an impurity species. For charge exchange it is usually the Carbon. The Z_{eff} profile is typically never provided. Rather, it is measured by line integrated Bremsstrahlung emission. In principle a tomographic inversion is possible but not routinely performed. For transport code input the plasma composition is an important piece of information, but is however often poorly known. An exception is C wall machines with good charge exchange diagnostics which resolve the C density.

Last but not least, the resolution required on the current profile measurement is challenging. Indeed the magnetic shear $s = \frac{r\nabla q}{q}$ plays an important role in the stability of the modes. Unfortunately, no direct measurement of the current profile is possible. It can be deduced from Faraday angles measured by polarimetry, which are then used to constrain a magnetic equilibrium reconstruction see for example [118]. The measured angles need to be cleared from noise and around 10 angles seem to be necessary to constrain the profile. Nonetheless in the center the uncertainty on the current profile remains very large since this method typically does not allow to differentiate a flat from a hollow q profile. Another way to indirectly measure the inclination of the field lines is to measure the Motional Stark Effect. It is based the measurement of the orientation of the polarization state of light emitted from an atomic hydrogen-like beam. This diagnostic can resolve hollow core current profiles, as illustrated on TFTR in [119]. This discussion on the various diagnostics, their strengths and their limitations can be endless. One has to remember that some knowledge on the uncertainties is essential since the fits performed highly depend on the diagnostics capabilities and as a consequence the confidence one can have in the input used for the stability analysis performed either by QuaLiKiz or any other gyrokinetic code such as GYRO, GS2, GENE, GKW. For more details on tokamak diagnostics the reader is referred to the book by Hutchinson [120].
A careful experimental analysis of the impact of collisionality on plasma confinement has been carried out in Tore Supra in Bourdelle et al, Nuclear Fusion 2011 [121]. This work contains a detailed discussion of diagnostic issues and propagation of uncertainties on the scaling law. The reader if referred to this work as an example of the degree of care and precision required from experimental data prior to the inference of any theoretical interpretation and extrapolation to future devices.

3.2.2 Output data of the linear gyrokinetic analysis of experimental profiles

In this section, solely the linear output are presented, the quasilinear fluxes will be presented in the next chapter.
The eigenvalues of the dispersion relation $\sum_s \frac{n_s Z_s^2}{T_s}(1 - \mathcal{L}_{ts}(\omega) - \mathcal{L}_{ps}(\omega)) = 0$ extensively discussed above are the frequencies and the growth rates of the unstable modes, respectively the real ω_r and the imaginary γ parts of ω. Indeed, as introduced earlier $\tilde{\phi}(\vec{J}, \vec{\vartheta}, t) = \sum_{\vec{n}\omega} \tilde{\phi}_{\vec{n}\omega}(\vec{J}) e^{i(\vec{n}.\vec{\vartheta} - \omega t)}$, therefore one can see that a positive imaginary part in ω leads to $\tilde{\phi}(\vec{J}, \vec{\vartheta}, t) \propto e^{-i(\omega_r + i\gamma)t}$ i.e. $\tilde{\phi}(\vec{J}, \vec{\vartheta}, t) \propto e^{-i\omega_r t} e^{\gamma t}$. Hence the real part of ω gives the oscillation fre-

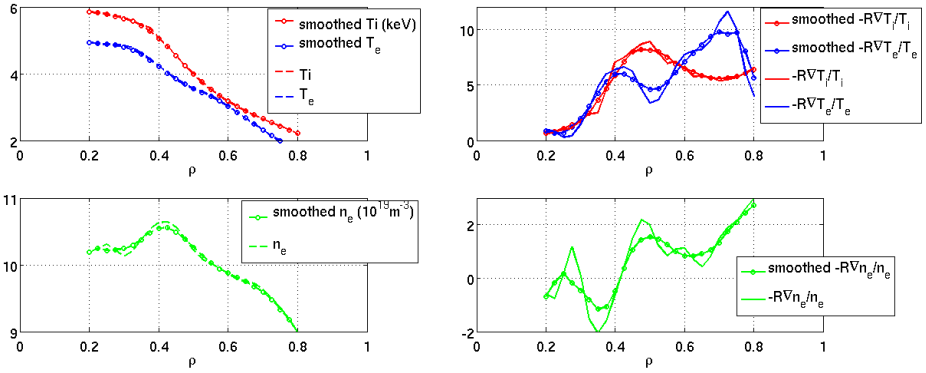

Figure 3.16: JET pulse 79698 at 13 s. Illustration of the T_e, T_i profiles on the top and n_e profile at the bottom with their associated normalized gradients on the right. The lines with circles correspond to the smoothed profiles, see legend on figures.

quency of the fluctuating eigenfunction, while γ is the linear growth rate of the mode. A positive γ means a linearly unstable mode that will grow until counterbalanced by a nonlinear saturation mechanism. The saturation mechanisms will be discussed in the next chapter.
The dispersion relation is a function of the wave number n, since n modifies all the frequencies: $n\omega^*$, $n_2\omega_2$ as well as $n_3\omega_3$. Therefore a linear dispersion relation is solved for a range of n values providing a spectrum of modes. Instead of n the dimensionless wave vector $k_\theta\rho_s = \frac{nq}{r}\frac{\sqrt{T_e m_D}}{eB}$ with m_D the mass of deuterium is typically used. The pulse used to illustrate QuaLiKiz output is a baseline H mode from JET C wall, with pulse number 79698, at high current 4.5 MA, 3.6 T using 23 MW of Neutral Beam Injection heating and 2.5 MW of Ion Cyclotron Resonance Heating. The linear analysis of the pulse is typically carried out for a given time slice. In this case, it is done at 13 s. The fits of the temperature and density for the JET discharge have been performed in the transport code TRANSP [122] using the HRTS and charge exchange measurements. The q profile is based on the equilibrium code EFIT estimate constrained by MSE measurements in this case, and the Z_{eff} profile is based on the C density provided by charge exchange. The T and n profiles led to jagged normalized gradients, and therefore they have been smoothed. The smoothing leads to very similar fits but nonetheless significantly different gradients as illustrated by figure 3.16. The profiles of the key input ingredients are illustrated on figure 3.17. For each radial location similar results are produced. Since QuaLiKiz is an eigenvalue code more than one unstable mode can be simultaneously found, where typically

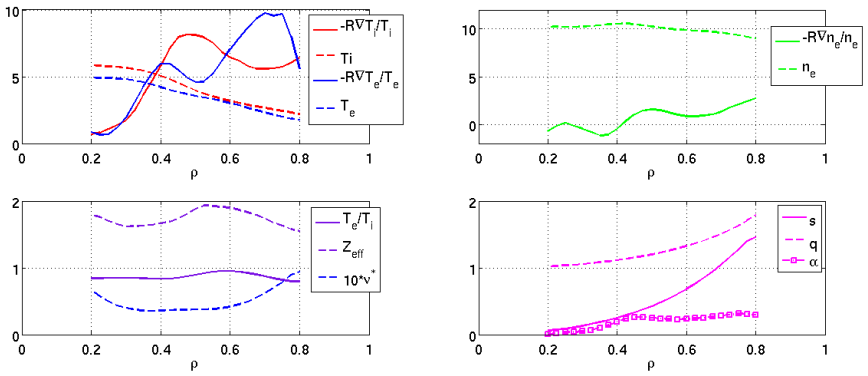

Figure 3.17: JET pulse 79698 at 13 s. Smoothed fits from TRANSP (run by I. Voitsekhovitch numbered I10). Top right plot: dashed line, T_e and T_i fits in keV of the profiles based on HRTS for T_e and charge exchange for T_i. The normalized gradient are also plotted $-\frac{R\nabla T_e}{T_e}$ in blue and $-\frac{R\nabla T_i}{T_i}$ in red. Top left plot: n_e profile in $10^{19}m^{-3}$ based on HRTS in dashed green line, and in solid line $-\frac{R\nabla n_e}{n_e}$. Bottom right plot: Z_{eff} from charge exchange C density, the ratio T_e/T_i and the normalized collisionality ν^*. Bottom left plot: the q profile in dashed line is given by an EFIT reconstruction constrained by MSE and then integrated in TRANSP, s is the magnetic shear in solid line, and α is plotted with the squares.

no more than three are seen when only accounting for two ion types and electrons. The convention is such that a negative frequency means a mode drifting in the ion diamagnetic drift direction and a positive frequency a mode drifting in the electron diamagnetic drift direction. For $k_\theta \rho_s < 1$, if the most unstable mode drifts in the ion diamagnetic direction it is now being called an Ion Temperature Gradient driven mode. In experimental cases, the electrons are never adiabatic, therefore a pure ITG mode does not rigorously exist. This means that, although the mode drifts in the ion direction, nonetheless the electrons do play a role on the eigenvalue of the dispersion relation. If one wants to check the strength of the electron impact, one can artificially strongly increase the electron-ion collisionality in order to detrap more electrons. Typically one will see that at least $20 - 30\%$ of the growth rate is actually due to the electron contribution in the dispersion relation. If the most unstable modes, on the contrary, drift in the electron diamagnetic direction, they are called Trapped Electron Modes. The same discussion is also valid here, indeed, in a tokamak, pure TEM does not exist, therefore the ions will always contribute to the dispersion relation although its eigenvalue is drifting in the electron direction. Theoretical cases can be pure TEM, for example if one sets to zero the ion temperature gradient such that $\frac{-R\nabla T_i}{T_i} = 0$. Now, for higher wave numbers such that $k_\theta \rho_s \gg 1$ ions modes are stabilized by finite Larmor radius effect, indeed the Bessel function for ions tends to zero at these wave numbers. As the wave number increases, the characteristic length of the modes becomes smaller that the Larmor radius and hence the fluctuations at these scales are ultimately averaged out by the cyclotronic motion. Therefore only modes drifting in the electron direction remain. From around $k_\theta \rho_s \simeq 1$ up to $k_\theta \rho_e \simeq 0.05$ trapped electron modes typically dominate. Then the passing electrons are the only unstable species in the dispersion relation, indeed the trapped electron modes are also slowly averaged out due to finite banana width effect. The modes around $0.05 < k_\theta \rho_e < 1$ are called Electron Temperature Gradient modes, they are only carried by passing electrons, meaning that, unlike ITG modes, the ETG modes are always pure ETG modes.

In the JET case presented here, the collisionality was high enough to detrap the electrons and no modes are unstable in the intermediate k_θ region when accounting for collisions. Therefore, to illustrate spectra with modes unstable at all wave numbers the JET case without collisions was run. A typical output of QuaLiKiz is plotted in figure 3.18, where only the imaginary part of the most unstable eigenvalue is plotted (γ) versus the radii and the wave numbers scanned. Typically to obtain such results takes on the order of a few minutes. In such a plot, the ETG branch dominates and it is difficult to resolve by eye the results at lower $k_\theta \rho_s$. Indeed ETG have the largest

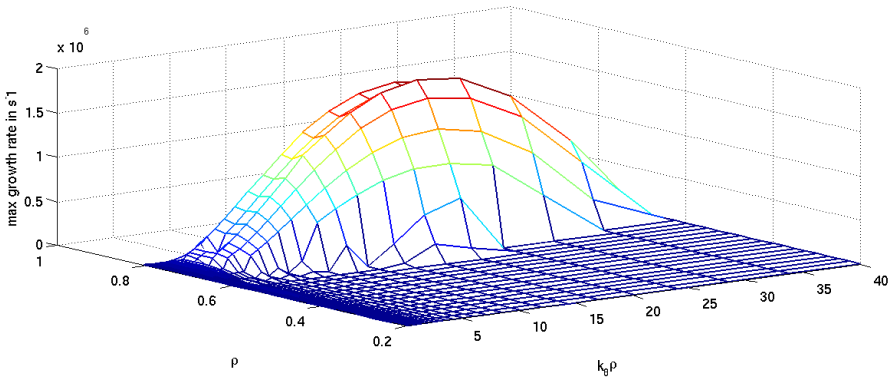

Figure 3.18: JET pulse 79698 at 13 s without collisions. Growth rates in s^{-1} versus the radial position ρ and the wave number $k_\theta \rho_s$.

growth rates due to the fact that they are mostly of the slab type, hence they scale with the electron thermal velocity which is 60 times larger than the ion thermal velocity. Nonetheless, from a quasilinear perspective they are not expected to contribute much to the turbulent fluxes. Indeed, their characteristic spatial scales are 60 times smaller. Hence, a diffusivity, expressed in $m^2 s^{-1}$ scaling roughly as $\lambda_c^2 \gamma$, will be such that the ETG diffusivity is overall 60 times smaller than the ITG-TEM contribution. For the curious reader, it is to note that non-linear structures named streamers have been reported in ETG gyrokinetic simulations [123, 124]. Such streamers can either enhance the ETG driven transport [123] or the transport level can remain at the level estimated by the quasilinear theory [124]. In this later case, the wave-particle decorrelation is the dominant mechanism for electron transport and the turbulent fluxes do not have time to interact with the streamers developed in the saturated electrostatic potential. More details on these notions will be given in the following chapter on quasi-linear fluxes.
In the work presented here, the focus is on the small wave vectors such that $k_\theta \rho_s < 1$, assuming that ETG streamers are not key players, hence that the larger scale modes contribute dominantly to the turbulent transport. Figure 3.19 shows the growth rates and the frequencies at $\rho = 0.5$ for $k_\theta \rho_s$ up to 1. A single unstable mode is present drifting in the ion direction. At this radius no ETG are present at higher $k_\theta \rho_s$. Figure 3.20 is located at $\rho = 0.7$, at this radius two modes are simultaneously unstable. The lowest growth rates are those of the mode drifting in the ion direction, i.e. an ITG dominated mode. The mode drifting in the electron direction is growing with larger $k_\theta \rho_s$ and ultimately merges with ETG. It drifts in the electron direction. It is a TEM. The collisions have been artificially zeroed out in this case. With the

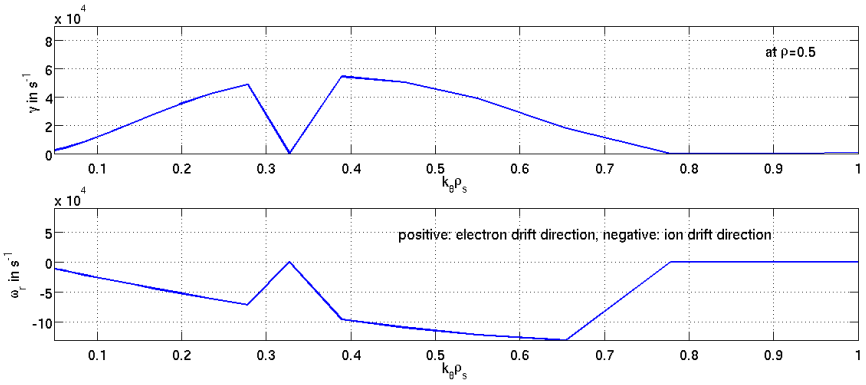

Figure 3.19: JET pulse 79698 at 13 s without collisions. At a given radius, here $\rho = 0.5$, the spectrum of the growth rate γ is plotted as a function of $k_\theta \rho_s$, top panel. Bottom panel: the spectrum of the frequency is illustrated.

collisions on, even though the collisionality of this JET pulse is rather low, the intermediate $k_\theta \rho_s$ TEM branch is completely stabilized and only ITG remains at low $k_\theta \rho_s$, and ETG at higher $k_\theta \rho_s$.

Some further illustrations of detailed linear gyrokinetic analysis of experimental pulses using QuaLiKiz/Kinezero can be found in [28, 125, 126].

3.3 Summary

In this chapter, the impact of various key parameters on the linear stability are reviewed. The gyrokinetic approach allows to derive properly the linear stability limit. The derived critical temperature and density gradient lengths are sensitive to various parameters such as the magnetic shear, the MHD α parameter, the ion to electron temperature ratio, the safety factor value, collisionality, etc. The physics behind these trends is now well understood and is a very precious guide when working on experimental data interpretation. Nonetheless, the so called "fixed gradient" approach used here produces results very sensitive to the quality of the input data, namely the profile gradient lengths. Therefore the reader has been extensively warned about the extra care one has to take when preparing input data for such stability analysis. Overall, numerous qualitative experimental trends are well reproduced by such linear stability analysis among which the stability impact of reversed magnetic shear, of dominant ion heating, of larger collisionalities, etc. This linear stability analysis work has allowed to gain confidence in the relevance of the physical mechanisms described by a linear gyrokinetic approach. It is

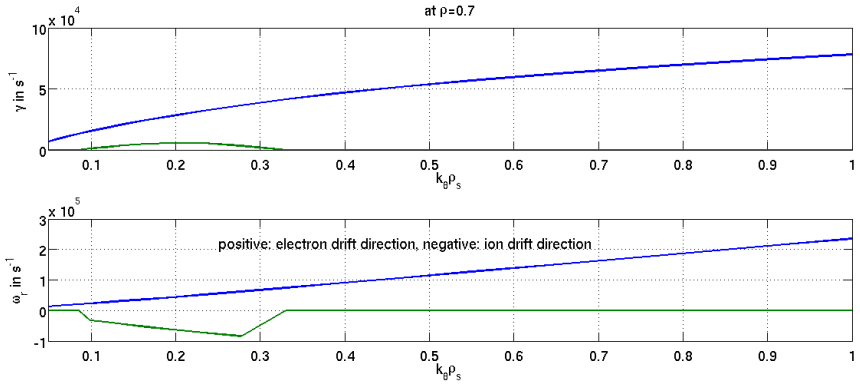

Figure 3.20: JET pulse 79698 at 13 s without collisions. At a given radius, here $\rho = 0.7$, the spectrum of the growth rate γ is plotted as a function of $k_\theta \rho_s$, top panel. Bottom panel: the spectrum of the frequency is illustrated. Here the figure is zoomed on the ITG-TEM part of the spectrum i.e. $k_\theta \rho_s < 1$.

now time to address the quasi-linear gyrokinetic fluxes derivation and validation against both non-linear models and experiments.

Chapter 4

Quasi-linear fluxes derivation and validation

In this chapter, the calculation of quasilinear fluxes by QuaLiKiz is presented. First, other quasilinear works will be introduced. The use of nonlinear simulations and turbulence measurements as key elements for validating the quasilinear approach will be explained. Then the main approximations of the quasilinear modeling are tested in detail. The quasilinear fluxes are finally built and compared to non-linear gyrokinetic fluxes.

4.1 Introduction

QuaLiKiz is placed in context by first summarizing previous work on the computation of quasilinear transport fluxes. First, are introduced main widely used quasilinear models. Comparisons of their results versus nonlinear gyrokinetic simulations are detailed. Finally, some highlights of intensive tests of quasilinear fluxes against experiments are summarized.

4.1.1 Quasi-linear modeling

After more than 50 years from the first pioneering papers [127, 128], quasilinear theory remains an active field of research. Indeed the two main assumptions, namely (1) a low level of fluctuations (such that $\delta f \ll f_0$) and (2) no captured particles in the saturated potential field are both generally fulfilled in the core of tokamak plasmas.
Although most part of the theoretical efforts in quasi-linear theory has been applied to 1D plasma turbulence [129, 130], several quasi-linear transport models have been proposed as interpretative and predictive tools for the evo-

lution of the thermodynamic quantities in tokamak plasmas. These quasi-linear models were initially based on a fluid approach as in the Weiland model [131] (embedded in the MMM model [132, 133]), and the IFS-PPPL model [21]. A quasilinear fluid model was developed, tuned to linear gyrokinetic and nonlinear fluid calculations, and named GLF23 in [134]. This model is still actively being developed, and has been extended to the TGLF model [135, 136]. QuaLiKiz is the first quasi-linear gyrokinetic transport model [32].
More recently, highly developed gyrokinetic codes, which can be run either in a linear or nonlinear mode, were used to calculate quasilinear fluxes for obtaining results on a fast time scale. The features of such quasilinear fluxes are then compared rather successfully to experimental trends. This approach has been widely used for particle [137], impurity, momentum [41] flux investigations. The gyrokinetic codes used are either GS2 [30], GKW [84] or GENE [22].

4.1.2 Comparison between quasilinear and nonlinear fluxes

The quasilinear fluxes computed with the gyrokinetic codes have been compared to nonlinear calculations. For example in [38], the phase of collisionless trapped electron mode turbulence is found to agree remarkably well with the linear cross-phases for particle and energy transport. In [39], nonlinear ETG simulations are investigated. Characteristic times are deduced from the nonlinear simulation. It is shown that, despite the fact that streamers are visible in the saturated electrostatic potential, the shortest time in the system is the wave-particle decorrelation time, resulting in a good agreement between the quasilinear heat conductivity and the value measured from the nonlinear simulations. In [40], 83 nonlinear GYRO simulated ion and electron heat fluxes as well as particle fluxes are shown to agree reasonably well with TGLF quasilinear fluxes (respectively with an RMS error of 17, 20 and 44%) over a large range of parameters, including ITG and TEM contributions. Therefore, work from different authors, using different codes and points of view all show that nonlinear features can be captured by quasilinear models for ITG, TEM and ETG types of modes.

4.1.3 Comparison of quasilinear fluxes with experimental profiles

In the integrated framework, quasilinear codes such as the Weiland model, MMM, GLF23 and TGLF have been widely used to predict temperature, density and more recently rotation profiles. They have demonstrated to lead to reasonable agreement. For example in [40] 96 standard H modes from three tokamaks: JET, DIII-D and TFTR are modeled by TGLF and the electron and ion temperature and the density are modeled with an averaged RMS error of respectively 16, 15 and 12% for normalized radii larger than the sawtooth inversion radius and smaller than 0.8. Hybrid scenarios [138] and ITB have also been modeled [139]. Despite these successes, numerous issues remain to be addressed, such as: the pedestal height prediction [140], the underestimated transport level in the deep core, the transport level in the L mode edge region [141], the combined role of MHD and turbulence on the confinement, the impact of finite β in particular in hybrid scenarios [92], etc.

Nevertheless, the successes of the quasilinear approach for modeling turbulent transport in tokamak plasmas are de facto demonstrating that the quasilinear approach is an option. Indeed, thanks to turbulence measurements and non-linear simulations, the two main assumptions, namely (1) a low level of fluctuations and (2) no captured particles in the saturated potential field are both shown to fulfilled, as detailed in the further in this chapter. It is an important result which points towards the attainability of predictive capabilities for tokamak profiles within reasonable CPU time. It is in this framework that the quasilinear code QuaLiKiz has been developed. This code is based on a linear gyrokinetic eigenvalue solver detailed in chapter 2. In the following, the quasilinear fluxes derived in QuaLiKiz are expressed in detail. The main approximations are reported. Finally, by comparing QuaLiKiz's results with both nonlinear simulations in this chapter and experimental results in chapter 5, further evidences of the success of the quasilinear approach are given. Throughout this chapter, further insights are provided on key features of tokamak plasmas justifying the approximation of quasilinear turbulent transport.

4.2 How to construct quasilinear fluxes?

The quasilinear approach can be used if a time scale, τ, exists which is much smaller than the equilibrium time scale, T_0, i.e. the time scale of temperature,

density, and rotation profile evolution; and much larger than the turbulence time scale which is of the order of an inverse growth rate $1/\gamma$. Indeed, if $1/\gamma < \tau < T_0$, then the equilibrium distribution function f_0 is equivalent to the time average distribution function $\langle f \rangle_\tau$ and the Vlasov equation time averaged over τ can be written as:

$$\frac{\partial f_0}{\partial t} - \langle [\delta H, \delta f] \rangle_\tau = 0 \tag{4.1}$$

By writing the above equation, is assumed also that $\frac{\delta f}{f_0} \simeq \frac{\delta H}{H_0} << 1$. Therefore, clearly the quasilinear approach can be used to model phenomena occurring on time scales shorter than the profile evolution time scale. This means that observed large scale phenomena such as MHD events or so called non-local transport or turbulence spreading [142] (and references therein) cannot be modeled within the quasilinear framework. Indeed, observations of ÂŞturbulence spreadingÂŤ suggest that nonlinear interactions can transport fluctuation energy into locally stable regions which in turn modify the profiles on turbulence time scales. While such phenomenology is not captured by the quasilinear approach, nonetheless, as reported in the previous section, the quasilinear models succeed in capturing a large proportion of transport phenomena, since they can predict density and temperature profiles with less than 20% averaged RMS errors.
Now, going back to equation (4.1), after an integration in parts, one obtains, when using the angle variables $\vec{\vartheta}$ and the action variables $\vec{J}$:

$$\frac{\partial f_0}{\partial t} - \int_0^\tau \frac{dt}{\tau} \int_0^{2\pi} \frac{d^3\vec{\vartheta}}{(2\pi)^3} \left(\frac{\partial \delta H}{\partial \vec{\vartheta}} \frac{\partial \delta f}{\partial \vec{J}} - \delta f \frac{\partial \delta H}{\partial \vec{\vartheta} \vec{J}} \right) = 0 \tag{4.2}$$

Therefore, the flux, $\vec{\Gamma}$, carried by f is given by:

$$\frac{\partial f_0}{\partial t} + \nabla_{\vec{J}} \vec{\Gamma} = 0 \tag{4.3}$$

With:

$$\vec{\Gamma} = -\mathrm{Re} \left[\int_0^\tau \frac{dt}{\tau} \int_0^{2\pi} \frac{d^3\vec{\vartheta}}{(2\pi)^3} \delta f \frac{\partial \delta H}{\partial \vec{\vartheta}} \right] \tag{4.4}$$

Since $\frac{\delta f}{f_0} \simeq \frac{\delta H}{H_0} \ll 1$, the linearized Vlasov equation derived in equation (2.8) is used. The fluctuating quantities δf and δH are expressed with the Fourier sums as introduced in equation (2.7). Finally, since τ is larger than the time characterizing the fluctuations of δf and δH, $1/\gamma$, integration in time over the fluctuating part, $\delta f \delta H$, is set to zero. Implementing all these in equation (4.4) leads to:

$$\vec{\Gamma} = \sum_{\vec{n},\omega} \vec{n} \mathrm{Im} \left(\vec{n} \cdot \frac{df_0(\vec{J})}{d\vec{J}} \frac{1}{\omega - \vec{n} \cdot \vec{\Omega_J} + i0^+} |H_{\vec{n}\omega}(\vec{J})|^2 \right) \tag{4.5}$$

In the above formulation of the quasilinear flux, it is important to understand that the frequency ω is real, whereas it was complex in the linearized Vlasov equation (2.8). Indeed, here the time averaging has been carried out. The flux corresponds to the saturated phase of a well developed turbulence. The small positive imaginary part 0^+ is needed to insure the causality property such that the fluctuations cancel out for a time t tending towards $-\infty$. Also, it is interesting to note that with $0^+ \to 0$, the term $\mathrm{Im}\left(\frac{1}{\omega - \vec{n}.\vec{\Omega_J} + i0^+}\right)$ tends towards a Dirac function, singular in ω and $\vec{n}$, leading to a flux being a sum of discrete values. This is not physical. Therefore a finite imaginary part is needed at the denominator. This aspect will be discussed further in the subsection dedicated to the frequency spectrum.

Note that the density, energy, and momentum transport fluxes come from moments of the formulation of a quasilinear flux of the distribution function f derived in equation (4.5).

For a given set of density, temperature and rotation profiles, the dispersion relation given by equation (2.55) is solved, its eigenvalues being ω, which real part is then used for the quasi-linear fluxes estimate based on equation (4.5). The unknown which remains to be determined is the saturated potential $|H_{\vec{n}\omega}(\vec{J})|^2$ or $|\phi_{\vec{n}\omega}(\vec{J})|^2$ in the electrostatic case considered here. Actually, the validity of assuming a linear response governed by the frequency ω derived from the linear dispersion relation remains also to be proven, as well as the existence of an intermediate time scale larger than $1/\gamma$.

To determine the saturated potential, and to test the validity of the quasilinear approximations, nonlinear gyrokinetic codes are required. In the following, first the success of nonlinear gyrokinetic codes in reproducing various well measured quantities such as the density fluctuation level, the k spectra and the effective heat diffusivity is reported. A further important element is to trust the nonlinear simulations which are then used to validate the quasilinear approximation and to construct the saturated potential. Both aspects are treated in the following sections.

4.3 Comparing nonlinear simulations to turbulence measurements

The validation of the quasilinear approach detailed later in this chapter relies strongly on insight from nonlinear simulations. Since the aim of the quasi-

linear approach is to have a fast and reliable tool for improving predicting capabilities, it is essential to be convinced that nonlinear gyrokinetic modeling robustly reproduces features of experimentally measured turbulence. The aim of this section is to review some of the works carried out on comparing turbulence measurements against nonlinear simulations.
In the early 2000's, some of the nonlinear gyrokinetic codes became open source and available to the entire fusion community. Simultaneously, the availability of high performance computing systems – such as the NERSC in the US (www.nersc.gov) – increased substantially. This enabled more routine execution of the massively parallel codes to a wider user base. The first code leading the way was GS2 [30, 143], followed by GYRO [23], GENE [22] and GKW [29].
Before this period, detailed turbulence diagnosis of the core tokamak plasma was already ongoing (we will not detail here turbulence measurements carried out in the open field line region, the Scrape-Off-Layer). In the core, most measurements are of density fluctuations, using CO_2 laser scattering [144], later Doppler backscattering [145, 146], and standard reflectometry [20]. Beam Emission Spectroscopy also provides detailed information of such fluctuations [147]. Phase Contrast Imaging can also deliver valuable information, but is limited (as is CO_2 laser scattering) by the difficulty of establishing a precise radial localization of the measurements [148]. Electron temperature fluctuations are measured with Correlation Electron Cyclotron Emission (CECE) radiometry [149]. Another very interesting diagnostic is the Heavy Ion Beam Probe which provides the fluctuating electrostatic potential [150].
Since the mid-2000s, the combination of a larger community of nonlinear gyrokinetic code users and more systematic turbulence investigation has led to the emergence of code to diagnostic comparison. This exercise requires simultaneous good knowledge of the diagnostics principles and of the code outputs. Indeed, signal mimicking the experimental measurements must be produced by the codes. This is commonly referred to as "synthetic diagnostics". On DIII-D, simultaneous measurements of the density and temperature fluctuations have provided a challenging set of data. Nonlinear GYRO simulations have been ran extensively and compared to this data [25, 26, 27, 141]. Overall, one can say that within a normalized radius of $\rho \simeq 0.7$ the agreement between GYRO and the measurements, including the phase between the temperature and the density fluctuations [26], is satisfactory. A similar trend of good agreement for ITG dominated regimes is reported for core data between GYRO and Phase Contrast Imaging in C-Mod [148]. However, it should be stressed that the gyrokinetic results are highly sensitive to the inputs as pointed out in chapter 3. The fact that most of the simulations are run in a fixed gradient manner leads to results highly sensitive to the

input. A solution would be to use flux-driven nonlinear codes such as ORB5 [151], GT5D [66], GYSELA [65], but unfortunately, they are not open source and the CPU resources needed are very large for extensive comparisons with experiments. Indeed, comparison with experiments is CPU demanding in the sense that the electrons as well the ions have to be kinetic, the collisionality included, typically at least one impurity taken into account, and the impact of the electromagnetic effects have to be assessed. While this is now achievable with fixed gradient codes, it is not yet a routine feature for fixed source codes. This limitation is addressed by using GYRO in an iterative manner, similarly to the inclusion in an integrated modeling platform, with a source implemented close to the values of the experimentally inferred one. This way of using GYRO is called TGYRO [152]. A similar approach has been attempted with GS2, named TRINITY [153]. To date, these versions of GYRO and GS2 are not yet widely used. Towards the edge, in L mode, the disagreement between fixed gradient codes and fluctuation measurements is clear and out of the uncertainties due to the input. The fixed gradient gyrokinetic modeling systematically under-predicts the turbulent levels of both the density fluctuations and the temperature fluctuations. Nonetheless, a recent attempt on addressing this issue with the code GENE shows a much weaker disagreement [154]. This work is presently ongoing. Non-local phenomena, as turbulence spreading from the core, refereed as the "beach effect" or inward spreading from an unstable edge could also explain the observed disagreement as proposed by [155]. Indeed, the very edge ($\rho > 0.95$) of L mode in DIII-D and Tore Supra has been found to be linearly unstable to Resistive Ballooning Modes [70]. Also the role of impurities at the edge should be investigated in greater details, indeed hollow impurity profiles can be expected in this region and hence impact strongly the stability of the modes. This has not yet been investigated, mostly due to lack of precise impurity profile information needed as input to the codes.

In this context, turbulence measurements in Tore Supra plasmas have been quantitatively compared to predictions by nonlinear gyrokinetic simulations. The plasma investigated is an L-mode Ohmic case. Three experimental pieces of information have been tested simultaneously: (a) the magnitude of effective heat diffusivity, (b) rms values of density fluctuations, and (c) wave-number spectra in both the directions perpendicular to the magnetic field. The effective heat diffusivity is provided by a power balance analysis carried out with the CRONOS platform [46]. The density fluctuation level and the spectra information are the result of complementary microwave diagnostics, and fast-sweeping [156] and Doppler [145] reflectometers. The radial region probed ranges from $\rho = 0.4$ to 0.7. A good agreement between GYRO and the experimental data was found simultaneously for the effective heat

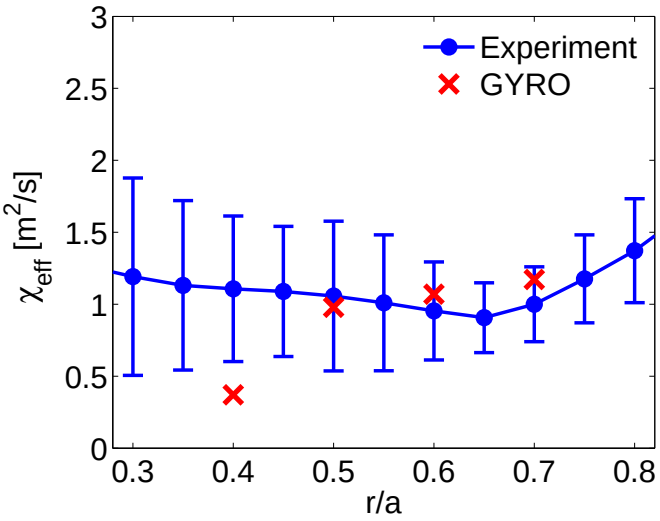

Figure 4.1: Radial profile of the experimental heat diffusivity inferred by CRONOS and comparison with GYRO non-linear predictions. From [157].

diffusivity, the density fluctuation level and both wave-number spectra as reported in Alessandro Casati's letter [157] and as illustrated below by figures 4.1 for the effective heat diffusivity, 4.2 for the density fluctuations, 4.3 and 4.4 for the wave-number spectra. In Alessandro Casati's PhD [13], the frequency spectrum was also been compared between nonlinear GYRO and the Doppler reflectometry for various $k_\theta \rho_s$ values at $\rho = 0.7$. The frequency width FWHM$= 2\Delta\omega_k$ is plotted versus $k_\theta \rho_s$ on figure 4.5. The agreement between GYRO and the the measured width is very good and is shown to agree with a T function, i.e. neither Lorentzian nor Gaussian (more details in [13]).

Up to now, the comparison between experimental measurements and nonlinear codes is limited by the sensitivity of the fixed gradient codes to the input data uncertainties. Nevertheless, for $\rho < 0.7$ there is an overall fair agreement between the code predictions and the measured density and temperature fluctuations (phase, amplitude, spectra) as well as with the power balance heat diffusivity. These results are encouraging. Therefore, in the following, nonlinear flux results are used to test the validity of the quasilinear approximation and to construct the saturated potential.

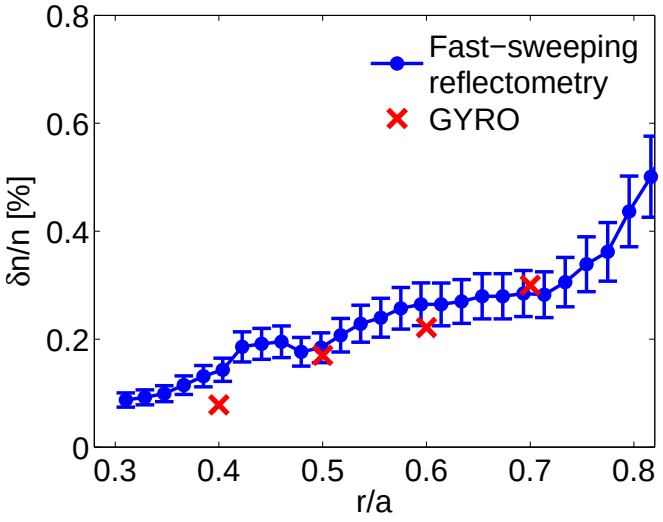

Figure 4.2: Radial profile of the experimental rms $\delta n/n$ from fast sweeping reflectometry and comparison with GYRO non-linear predictions. From [157].

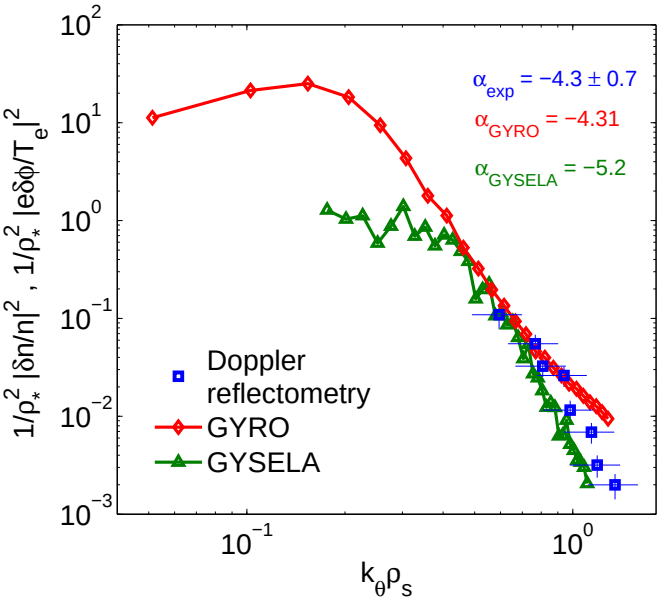

Figure 4.3: At $\rho = 0.7$. Experimental density fluctuations k_θ spectrum from Doppler reflectometry and comparison with GYSELA and GYRO non-linear predictions. From [157].

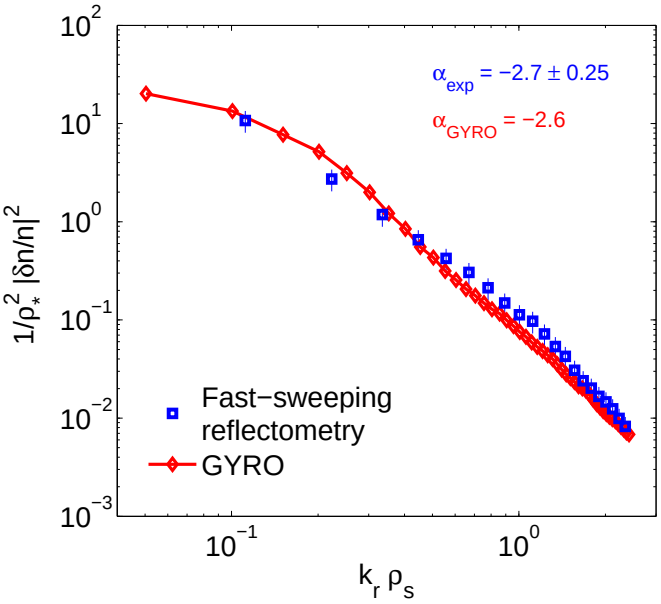

Figure 4.4: At $\rho = 0.7$. Experimental density fluctuations k_r spectrum from fast sweeping reflectometry and comparison with GYRO non-linear predictions. From [157].

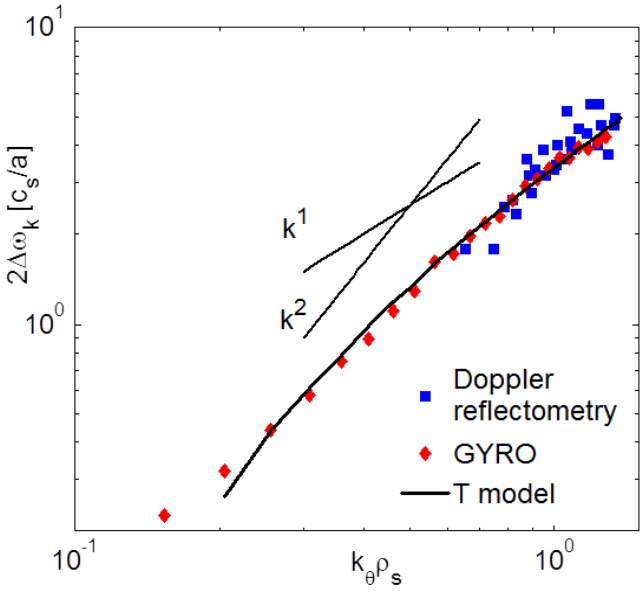

Figure 4.5: At $\rho = 0.7$. Experimental density fluctuations frequency width FWHM from Doppler reflectometry and comparison with GYRO non-linear predictions. From [13].

4.4 Validity of the quasi-linear approximation

Earlier in this chapter, the main approximations used to derive the gyrokinetic quasilinear fluxes were presented. A time scale, smaller than the equilibrium time scale and more importantly larger than the fluctuation time scale has to exist to allow for the temporal averaging of the Vlasov equation. Secondly, the linearized Vlasov equation is used with a frequency ω assumed to be the real part of the linearized dispersion relation presented in (2.55). In the following, both approximations are tested. First the time scale comparison is considered, since it is the central approximation of the quasilinear theory.

4.4.1 The Kubo number

Historically, the standard quasilinear theory was elaborated for test particles [158]. A condition of validity for this quasilinear framework is that the particles should not be trapped in the field. This means that the lifetime of the eddies in the saturated electrostatic potential, referred here as an Eulerian autocorrelation time τ_{ac}, should be longer than the time that a particle spends in it, referred here as particle flight time τ_f. The ratio of these two times is known as the Kubo number $K = \frac{\tau_f}{\tau_{ac}}$ [159, 130]. It should, hence, be lower than unity. To compute the Kubo number, one should compute these two times from nonlinear simulations. In the present cases, the simulations are based on Vlasov equation, and calculate the distribution functions directly. Hence the Kubo number definition must be adapted. The particle flight time is defined as $\tau_f = \frac{\lambda_x}{\langle v_x \rangle}$, where λ_x is the radial correlation decay length and $\langle v_x \rangle$ the root mean square radial velocity.
To estimate τ_{ac}, first the method proposed in [39] was used in [33]. It was such that: $\tau_{ac} = \frac{2D}{\langle |v_x|^2 \rangle}$, with D the particle diffusivity. This definition has the drawback of assuming a priori that the particle transport is due to a random-walk process. Therefore later, another derivation was been proposed in [34], where τ_{ac} is directly calculated from the fluctuating potential field from well saturated non-linear GENE simulations. The time correlation function is $C(\Delta t) = \frac{\phi(x,y,t)\phi(x,y,t+\Delta t)}{\langle |\phi|^2 \rangle}$, averaging over the x and y directions. The parallel coordinate is kept fixed at the low-field side. The correlation time is taken as the $1/e$ time of this function. All $n = 0$ modes are not included in the calculation, which thus considers only the flux inducing $n > 0$ background drift-wave population. λ_x is calculated as the $1/e$ length of the function $C(\Delta x) = \frac{\phi(x,0,t)\phi(x+\Delta x,0,t)}{<|\phi|^2>}$. And $\langle v_x \rangle$ is calculated with the same averaging

procedure as τ_{ac} for consistency, such that: $\langle v_x \rangle = \frac{\sqrt{\langle E_y^2 \rangle}}{B_{ref}}$. With B_{ref} the reference magnetic field used in GENE normalizations.
In [34], the Kubo number was calculated for 16 cases, at 4 different magnetic shear values and 4 sets of normalized gradients. The four sets of input parameters are summarized in table 4.1.

Set name	R/L_{Ti}	R/L_{Te}	R/L_n	T_i/T_e	q
A (GASTD case)	9	9	3	1	2
B	7.6	6.7	4	1.4	1.4
C	6.3	5.5	3.3	1.4	1.4
D	7.6	6.7	4	1.4	1

Table 4.1: Input parameters for the GENE magnetic shear scans. From [34]

For all cases reported in table 4.2, including low magnetic shear cases, $K < 1$ is found. Note that even for K of the order unity, the quasi-linear approximation still holds [160]. Therefore, from nonlinear gyrokinetic simulations, it is demonstrated that well developed turbulence for typical tokamak plasma parameters is such that random walk processes do take place and can be modeled by the quasilinear theory. This is an important feature of tokamak plasma turbulence, which justifies the use of reduced models for attaining fast predictive capabilities. It is coherent with results reported earlier in this chapter regarding the overall success of quasilinear models in reproducing temperature and density profiles within less than 20% averaged RMS error [40].

4.4.2 The linear response

In a nonlinear simulation, over a significant time window of the saturated phase, the nonlinear flux normalized to the saturated potential can be defined as a nonlinear transport weight w_k^{NL} such that:

$$w_k^{NL} = \left\langle \frac{< \Gamma_k(x,y,t) >_{x,y}}{< |\phi_k(x,y,t)|^2 >_{x,y}} \right\rangle_t \tag{4.6}$$

This weight has an amplitude and a phase. Its phase can be compared to the linear phase ω_r for a series of k values. This has been done in [33] using the initial value code GYRO. The probability density function (PDF) of the cross-phase between the transported quantities (density, ion and electron energies) and the fluctuating potential $\tilde{\phi}$ for each k was calculated in the nonlinear saturation regime and compared with the linear cross-phase from

Table 4.2: Correlation times, lengths and Kubo numbers for the GENE nonlinear runs for the for sets of parameters summarized in table 4.1. Units are Larmor radii for the lengths, R/c_s for the times. From [34].

Run	$\sqrt{\langle E_y^2 \rangle}$	λ_x	τ_{ac}	K
A: s=1	8.6	12.60	1.85	0.42
A: s=0.6	11.78	11.2	2.05	0.72
A: s=0.1	12.23	7.12	0.58	0.33
A: s=-0.4	9.66	6.94	1.85	0.86
B: s=1	8.7	12.70	2.14	0.49
B: s=0.6	10.8	10.50	1.74	0.60
B: s=0.1	8.59	6.90	1.09	0.45
B: s=-0.4	7.93	6.87	2.14	0.82
C: s=1	5.37	13.67	1.90	0.27
C: s=0.6	8.48	10.92	3.44	0.89
C: s=0.1	6.69	7.30	1.44	0.44
C: s=-0.4	5.5	6.08	2.01	0.61
D: s=1	7.38	9.76	0.96	0.24
D: s=0.6	9.23	8.41	1.38	0.50
D: s=0.1	7.67	5.88	1.20	0.52
D: s=-0.4	6.9	5.93	1.96	0.76

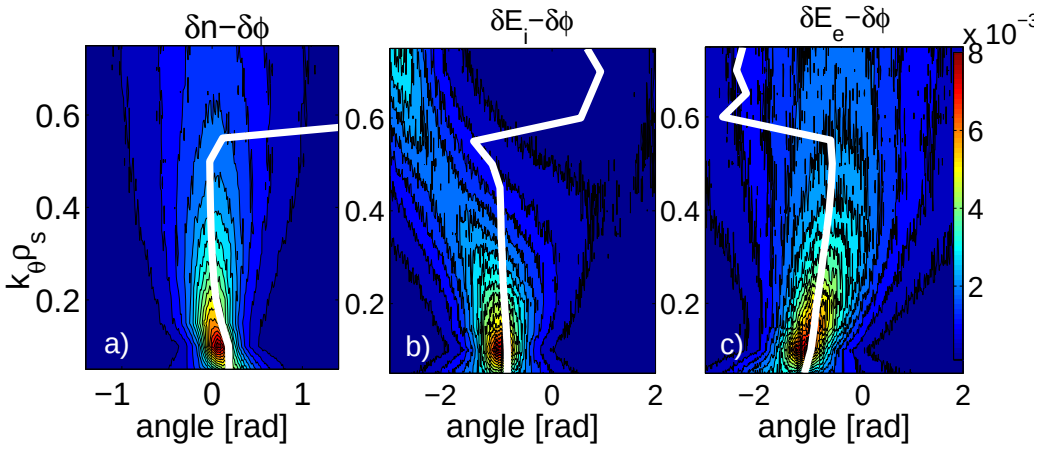

Figure 4.6: PDF of the nonlinear cross-phases (color contour plot) and the linear cross-phase on the most unstable mode (white line) between (a) $\tilde{n}$ and $\tilde{\phi}$, (b) $\tilde{E}_i$ and $\tilde{\phi}$, (c) $\tilde{E}_e$ and $\tilde{\phi}$ from the local GYRO simulation on the GA-standard case (set A of table 4.1 with $s = 1$). From [33].

the most unstable mode. Figure 4.6 shows a very good agreement between the nonlinear and the linear phases in the plane $\theta = 0$, where the interchange instability is supposed to be dominant. This test of validity of the quasilinear approach, introduced by [38] for pure TEM turbulence, has been in this case successfully extended to coupled ITGâĂŞ-TEM turbulence. Nevertheless, when the plasma parameters are close to the ITG/TEM transition, figure 4.7 where the ion temperature gradient is lowered from $R/L_{Ti} = 9$ down to 6, the linear phase of the most unstable mode fails to predict the correct particle transport (see panel (a)), whereas very interestingly the linear cross-phase for the energy fluxes remain reasonably close to the nonlinear values (panels (b) and (c)).

In all cases, figures 4.6 and 4.7, it is interesting to note that the agreement between the nonlinear cross-phases and the most unstable modes holds only for $k_\theta \rho_s \leq 0.4$. At lower spatial scales, or higher $k_\theta \rho_s$, the potential saturates at small scales and the particles happen to be finally trapped in the field, leading to a phase departing from its linear value. This mechanism is expected. It is interesting to see that it happens at wave-numbers which do not dominate the transport. Indeed, most of the nonlinear transport occurs around $k_\theta \rho_s \simeq 0.2$ where the trapping does not occur as will be detailed below.

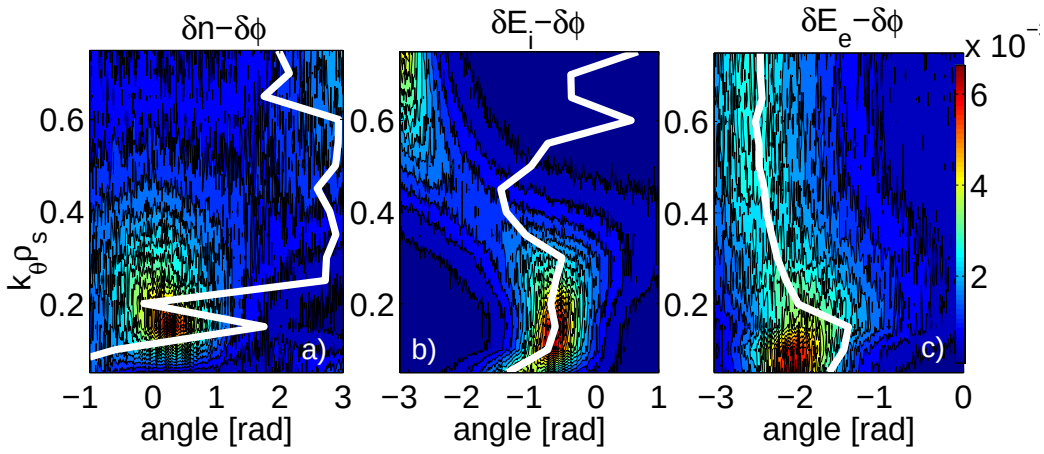

Figure 4.7: PDF of the nonlinear cross-phases (color contour plot) and the linear cross-phase on the most unstable mode (white line) between (a) $\tilde{n}$ and $\tilde{\phi}$, (b) $\tilde{E}_i$ and $\tilde{\phi}$, (c) $\tilde{E}_e$ and $\tilde{\phi}$ from the local GYRO simulation on the GA-standard case with a modified $R/L_{Ti} = 6$. From [33].

4.5 How to build the saturated potential?

Now that the quasilinear approximation has been shown to be valid due to low Kubo numbers, and that the linear response using the linear dispersion relation frequency has been shown to apply at the relevant wave-numbers, the formula:

$$\Gamma = \sum_{\vec{n},\omega} \vec{n} \mathrm{Im} \left(\vec{n}.\frac{df_0(\vec{J})}{d\vec{J}} \frac{1}{\omega - \vec{n}.\vec{\Omega}_J + i0^+} e_s^2 |\phi_{\vec{n}\omega}(\vec{J})|^2 \right) \tag{4.7}$$

can be used. It is therefore time to address the issue of the saturated potential $|\phi_{\vec{n}\omega}(\vec{J})|^2$. To determine it, nonlinear gyrokinetic simulations are used, as well as turbulence fluctuation measurements. Three pieces of information are needed: the frequency spectrum shape, the wave-number spectral shape and the overall saturation level.

4.5.1 The frequency spectrum

As mentioned earlier, a finite positive imaginary part is required in the denominator of equation (4.5) to guarantee causality. It was also mentioned, that in the case of $0^+ \to 0$, the term $\mathrm{Im}\left(\frac{1}{\omega - \vec{n}\cdot\vec{\Omega}_J + i0^+}\right)$ tends towards a Dirac function $-\pi\delta(\omega - \vec{n}\cdot\vec{\Omega}_J)$. To avoid these singularities and obtain continuous wave-number and frequency spectra, a finite positive imaginary part is

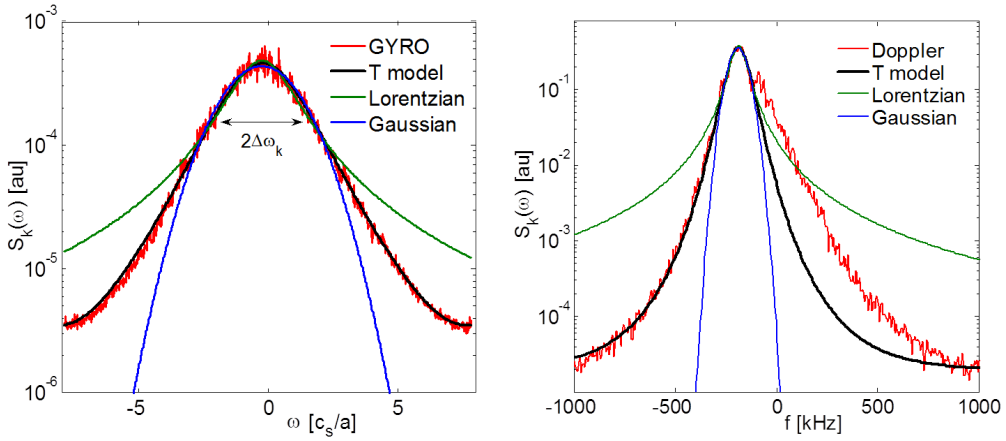

Figure 4.8: At $\rho = 0.7$, TS39596. Experimental density fluctuation frequency spectrum from Doppler reflectometry at $k_\theta \rho_s = 0.82$ on the right hand side and comparison with GYRO nonlinear predictions at the same k_θ value on the left hand side. From [13].

required. This is often referred as the renormalized quasilinear theory, also called the Resonance Broadening Theory as initiated by Dupree [161]. The resonance broadening comes from the fact that, if a finite imaginary part ν_{QL} is assumed instead of 0^+, one obtains:

$$\mathrm{Im}\frac{1}{\omega - \vec{n}\cdot\vec{\Omega}_J + i\nu_{QL}} = \frac{\nu_{QL}}{(\omega - \vec{n}\cdot\vec{\Omega}_J)^2 + \nu_{QL}^2} \tag{4.8}$$

which is a Lorentzian of width ν_{QL}. Two questions have now to be answered: is the Lorentzian an appropriate shape, and what is the value of ν_{QL}.
In tokamak plasmas, the frequency spectrum is measured by Doppler reflectometry and its shape has been compared to Lorentzian as well as Gaussian fits. The same procedure has been carried out for a GYRO nonlinear frequency spectrum as reported in [13]. Neither of the two shapes are correct, as illustrated by figure 4.8. This means that the turbulence cannot be approximated by either a purely diffusive or convective model (for more details see section 4.1.3 of [13] and references therein). It lies between these two extremes. Nevertheless, both fits capture the majority of the spectrum (note that the figure is in a semi-log scale), and although not exact, a Lorentzian fit is seen to be acceptable.
The width of the Lorentzian fit ν_{QL} can be estimated from a crude approximation assuming that for each mode, the linear growth rate competes with the nonlinear damping. Within this picture, saturation is then linked to the

resonance broadening mechanism, when the nonlinear dissipation balances the linear instability drive, leading to:

$$\nu_{QL} = \gamma \tag{4.9}$$

This hypothesis is now tested in nonlinear simulations corresponding to the four sets of data given in table 4.1 as reported in [34] and illustrated by figure 4.9.

From figure 4.9, for $k_y \simeq k_\theta \rho_s < 0.3$ and for $s = 1$ and $s = 0.6$, the Lorentzian fit with a width equal to the linear growth rate of the most unstable mode represents rather well the nonlinear width, except for the case D at the lowest q value, hence closer to the instability threshold. Since most of the transport occurs for $k_\theta \rho_s < 0.3$, the Lorentzian of width γ is a reasonable assumption for most cases.
Nonetheless, even in these cases where $\nu_{QL} = \gamma$, where the frequency spectrum modeled in QuaLiKiz reproduces well the nonlinear saturated potential frequency spectrum, a disagreement remains. This disagreement does not concern the saturated potential but rather the nonlinear weight defined above when compared to the quasilinear response. For such a comparison, the saturated potential in the quasilinear calculation is set identical to the nonlinear case for the same input parameters. Therefore the ratio of the nonlinear flux to the nonlinear saturated potential, w_k^{NL}, can be compared to $\mathrm{Im}\left(\vec{n} \cdot \frac{df_0(\vec{J})}{d\vec{J}} \frac{1}{\omega - \vec{n} \cdot \vec{\Omega}_J + i0^+}\right)$, from equation (4.5), with ω the real part of the linear eigenvalue, shown to agree with its nonlinear counterpart, see figures 4.6 and 4.7. In such a case the quasilinear weight depends on the choices of the resonance and the frequency broadening. For example, in QuaLiKiz, a Lorentzian frequency spectrum of width γ is assumed, while 0^+ is kept for the linear response. Actually, this choice is equivalent to assuming no frequency spectrum and replacing 0^+ by γ as demonstrated in [33]. To avoid being sensitive to such choices, the quasilinear weight is estimated within the GYRO (or GENE) framework as proposed in [162]. The ratios of the quasilinear to the nonlinear fluxes for particle, electron and ion heat are computed. The quasilinear weight computed this way accounts for the most unstable mode only. An alternative method is proposed in [162] to account for the entire spectrum, but this does not respect the ambipolarity condition. It is found that the ratio of the quasilinear to the nonlinear transport weights is around 1.4. This value is independent of $k_\theta \rho_s$ in the low k range dominating the transport as illustrated in [33] and [34], see figure 4.10. In [162], this ratio is shown not to depend on the normalized temperature gradient. Therefore, the cross-phase agrees between the quasilinear and the nonlinear approaches, but the amplitude is 1.4 times larger in the quasilinear case than in the non-

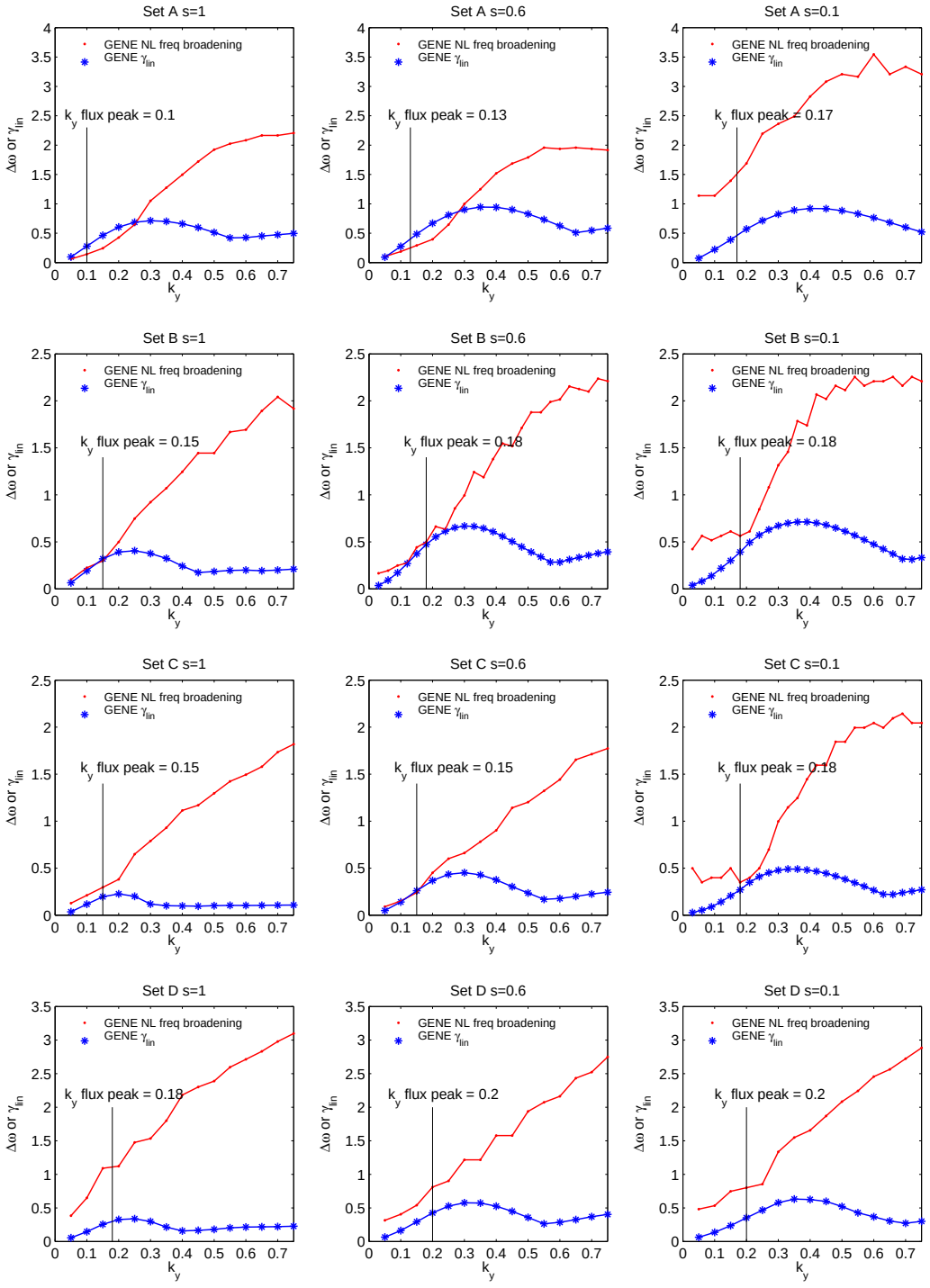

Figure 4.9: Nonlinear frequency spectra fitted Lorentzian widths and linear growth rates are compared for a range of k_y (or $k_\theta \rho_s$), for the four sets of parameters of table 4.1 and for three values of magnetic shear $s = 1$ (left column), $s = 0.6$ (central column) and $s = 0.1$ (right column). From [34].

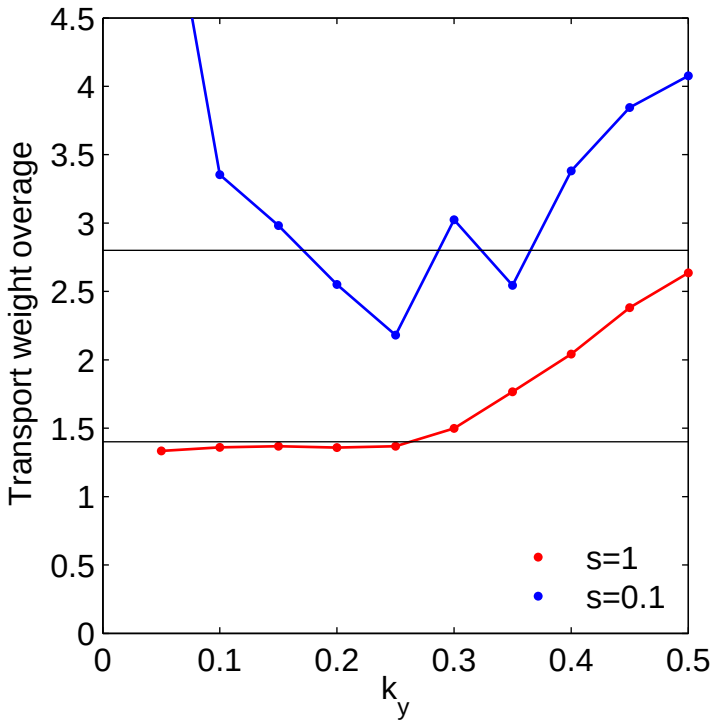

Figure 4.10: Ratio of quasilinear to nonlinear transport weights for the GA-standard case (set A in table 4.1) for $s = 1$ in red and $s = 0.1$ in blue. From [34].

linear case. The origin of this number could be linked to nonlinear transfer of energy through zonal flows or through transfer towards stable eigenmodes as proposed in [163]. These hypotheses point towards the need for a more theoretically robust renormalized quasilinear theory as the behavior at low s further illustrates. Indeed, on figure 4.10, as s is reduced from 1 down to 0.1, the transport weight overage is increased from 1.4 up to larger values, even at low k_θ where the transport takes place.
The potential role of the zonal flows will be mentioned in various parts of this chapter. The zonal flows are poloidal rotation fluctuations generated by the turbulence itself and leading to turbulence stabilization. This behavior can lead to intermittent regimes, where zonal flows and turbulence alternate. For a review on zonal flows generation and impact see [164].
For $s = 0.1$, it is interesting to note that the linear growth rate underestimates the frequency width significantly even for the lowest $k_\theta \rho_s$, see figure 4.9. This is consistent with the generally lower auto-correlation times observed at low magnetic shear, as seen in Table 4.2. This increased frequency

broadening at low magnetic shear may be a result of nonlinear decorrelation mechanisms, such as zonal flows, which play a stronger role at low magnetic shear as discussed in [34]. Also in the set with lowest flux, set D, where the impact of zonal flows is also expected to be stronger due to the vicinity to the instability threshold, the frequency broadening is greater than the linear growth rate estimation even at $s = 0.6$ and $s = 1$. The role of the zonal flow shearing rate affects the value of ν_{QL} which becomes such that it departs from the linear growth rate γ as follows:

$$\nu_{QL}^2 = \gamma^2 + \alpha_0 \left(\frac{\partial}{\partial r} V_E(r) \right)^2 \tag{4.10}$$

where V_E is the zonal flow velocity. Such a reduction of the fluxes due to perpendicular flow shear is similar to that employed in the gyro-Landau fluid and trapped gyro-Landau-fluid models GLF23 [134] and TGLF [40, 165] for external toroidal velocity. Due to the challenge in parameterizing the zonal flow shear rate and given the minor effect the zonal flow shearing of low k_y modes has on determining k_{max} as discussed below, it was decided not to include a zonal flow growth rate quench model in QuaLiKiz.
An ad-hoc rule is proposed to reproduce the frequency spectrum widening at low s. From averaging over all four sets of parameters, the ratio between the non-linear width $\Delta\omega_k$ to the linear growth rate γ_k is such that:

$$\frac{\langle \Delta\omega_k/\gamma_k \rangle_{s=0.1}}{\frac{1}{2}\langle \Delta\omega_k/\gamma_k \rangle_{s=1} + \frac{1}{2}\langle \Delta\omega_k/\gamma_k \rangle_{s=0.6}} = 2.5 \tag{4.11}$$

In the absence of more rigorous theory, an additional shear dependent normalization factor as been included on top of the 1.4 factor in the fluxes calculated by QuaLiKiz, for $|s| < 0.6$, in the form of:

$$2.5(1 - |s|) \tag{4.12}$$

This normalization factor roughly captures the effect of the decreased autocorrelation time due to increased frequency broadening (possibly due to zonal flows) at low magnetic shear. A more theoretically based model using a renormalized quasi-linear theory valid at low magnetic shear is needed to accurately model the frequency broadening at low $|s|$.

4.5.2 The wave number spectrum and the maximum saturated potential

On most experiments [166, 167, 168], the density fluctuation wave-number spectrum : $S(k_\perp) = \left|\frac{\delta n(k_\perp)}{n}\right|^2$ shows a decay for $k_\perp \rho_s \geq 0.3$ such that:

$S(k_\perp) \simeq k_\perp^{\alpha_\perp}$ with $\alpha_\perp = -3.5 \pm 0.5$. From [157], as illustrated by figures 4.3 and 4.4, the two reflectometers provide different fluctuation spectral exponents in the perpendicular plane: $\alpha_\theta = -4.3 \pm 0.7$ and $\alpha_r = -2.7 \pm 0.25$. These two dissimilar exponents are attributed to the range of low radial wave numbers accounted for in the Doppler case. In GYRO, when accounting for all radial wave numbers, one obtains $\alpha_\theta \simeq -2.9$, as illustrated by figure 4.11. Therefore both in measurements and in nonlinear simulations isotropic k spectra are found with a decay of around -3. Moreover this decay is successfully recovered by the shell model proposed in [169]. This choice is hence retained in QuaLiKiz.

For the inverse cascade, below the peak of the saturated potential, although measurements found a symmetric slope around the maximum [170], nonlinear simulations rather find a linear increase as illustrated by figure 4.11. This asymmetry around the maximum is kept in QuaLiKiz.

Now that the slope above and below the maximum potential are determined, it is necessary to set the k value of the maximum potential: k_{max}. The maximum value of $|\tilde{\phi}^2_{n\omega}|$ at k_{max} is chosen such that the effective diffusivity, D_{eff}, follows the mixing length rule:

$$max\left(D_{eff} \simeq \frac{R\Gamma_s}{n_s}\right)_{k_{max}} = \frac{R}{n_s}\frac{k_\theta}{B}\frac{n_s e_s}{T_s}|\tilde{\phi}^2_{n\omega}|_{k_{max}} = \frac{\gamma}{\langle k_\perp^2\rangle_{k_{max}}} \tag{4.13}$$

By making use of the mixing length rule, a random Gaussian statistics for the saturated electrostatic potential is assumed [130]. This result is based on the picture that the nonlinear damping rate, $D_{eff}\langle k_\perp^2\rangle_{k_{max}}$ balances the linear growth rate γ [4]. Hence $D_{eff}\langle k_\perp^2\rangle_{k_{max}}$ is equal to the previously introduced ν_{QL} and is broadened in presence of zonal flows for example, see [171].

The choice for $\langle k_\perp^2\rangle$ is based on both experimental observations and nonlinear simulation results. It should lead to a maximum $|\phi^2_{n\omega}|$ around $k_\theta\rho_s \simeq 0.2$ as reported by numerous nonlinear simulations, including the previously reported GYRO runs illustrated by figure 4.11 from [157], and as observed with Beam Emission Spectroscopy [170]. It should also depend on q as observed in nonlinear simulations [38, 172]. A pertinent choice for $\langle k_\perp^2\rangle$ combining these two aspects has been proposed by [38, 173, 137]. In [32], it was proposed to account for the MHD α parameter on the curvature drift as well as on the magnetic shear s. In this case, for strongly ballooned modes, one obtains:

$$\langle k_\perp^2\rangle = k_\theta^2\left[1 + (s-\alpha)^2 < \theta^2 >\right] \tag{4.14}$$

with:

$$< \theta^2 >= \frac{\int \theta^2 |\phi_{n\omega}(\theta)|^2 d\theta}{\int |\phi_{n\omega}(\theta)|^2 d\theta} \tag{4.15}$$

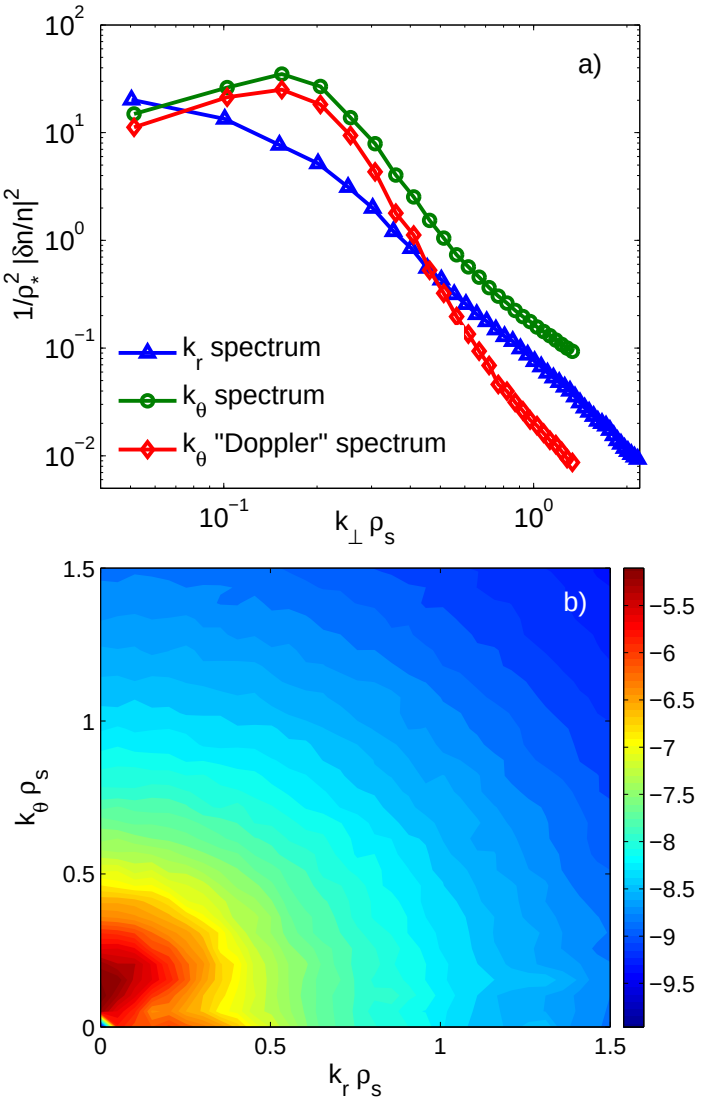

Figure 4.11: At $\rho = 0.7$. (a) $\left|\frac{\delta n(k_\perp)}{n}\right|^2$ from GYRO illustrating the impact of reconstructing the Doppler spectrum on the k_θ spectrum. (b) contour plot of GYRO $log_{10}\left|\frac{\delta n(k_\perp)}{n}\right|^2$. From [157].

As detailed in the chapter 2, the eigenfunction $|\phi_{n\omega}(\theta)|^2$ is a shifted Gaussian, therefore:

$$\langle\theta^2\rangle = \frac{\int \theta^2\phi_{n\omega}(\theta)\mathrm{d}\theta}{\int \phi_{n\omega}(\theta)\mathrm{d}\theta} = \frac{2d^2}{\mathrm{Re(w^2)}}\frac{\Gamma(0.75)}{\Gamma(0.25)} + \frac{\mathrm{Im}(\mathbf{x}_0)^2 d^2}{\mathrm{Re(w^2)}^2} \tag{4.16}$$

Hence, symmetry breaking in $\langle k_\perp^2\rangle$ is enacted through the imaginary part of the eigenfunction shift $\mathrm{Im}(\mathbf{x}_0)$ and the real part of the mode width, the latter being proportional to the growth rate found in the fluid model.
The expression for $\langle k_\perp^2\rangle$, proposed in [32], has been revisited in [34] to improve QuaLiKiz fluxes estimation at low magnetic shear. It reads:

$$\begin{aligned}&\langle k_\perp^2\rangle = k_\theta^2 + k_r^2 = \\ &k_\theta^2 + \left(\sqrt{k_\theta^2\hat{s}^2\langle\theta^2\rangle} + \frac{0.4\exp(-2\hat{s})}{\sqrt{q}} + 1.5(k_\theta - 0.2/\rho_s)H(k_\theta - 0.2/\rho_s)\right)^2\end{aligned} \tag{4.17}$$

The expression of k_r in QuaLiKiz mixing length rule was modified because it was found that at low magnetic shear, the $k_r^2 = k_\theta^2\hat{s}^2\langle\theta^2\rangle$ resulting from magnetic field line shearing, is underestimated with respect to nonlinear k_r [34]. The factor $\frac{0.4\exp(-2\hat{s})}{\sqrt{q}}$ was found to represent well the non linear isotropization at low magnetic shear. Finally, the term $1.5(k_\theta - 0.2/\rho_s)H(k_\theta - 0.2/\rho_s)^2$ (H is the Heaviside function) is present for completeness, to correctly capture the approximate isotropy at high wave-numbers, but typically plays a negligible role is setting the maximum value of $\gamma/\langle k_\perp^2\rangle$.
From the above equation (4.17), it is clear that the mixing length needed to estimate the saturated level is the Achilles heel of the quasi-linear flux construction. Nonetheless, some models, such as GLF23 [134], have attempted to include Zonal Flows and Geodesic Acoustic Modes impact in an ad-hoc manner. The interplay between the waves with themselves, with Zonal Flows and with Geodesic Acoustic Modes has been studied using extensive non-linear GYRO simulations in [165] showing that all saturation mechanisms co-exist.
To conclude, the saturated potential computed in QuaLiKiz is compared to the saturated potential obtained by GKW [86] accounting for the impact of the $\mathbf{E}\times\mathbf{B}$ shear, see figure 4.12. It should be stressed that the amplitude of the saturated potential peak is normalized in QuaLiKiz by a unique constant, such that the quasilinear ion heat flux for the GA-standard case reproduces the nonlinear result. In the simulations presented here, the GA-std case parameter set was employed with $U_\parallel = \nabla U_\parallel = 0$. Three values of $\mathbf{E}\times\mathbf{B}$ shear are chosen corresponding to an experimentally relevant range of γ_E from 0 to $0.5R/v_{Ti}$.

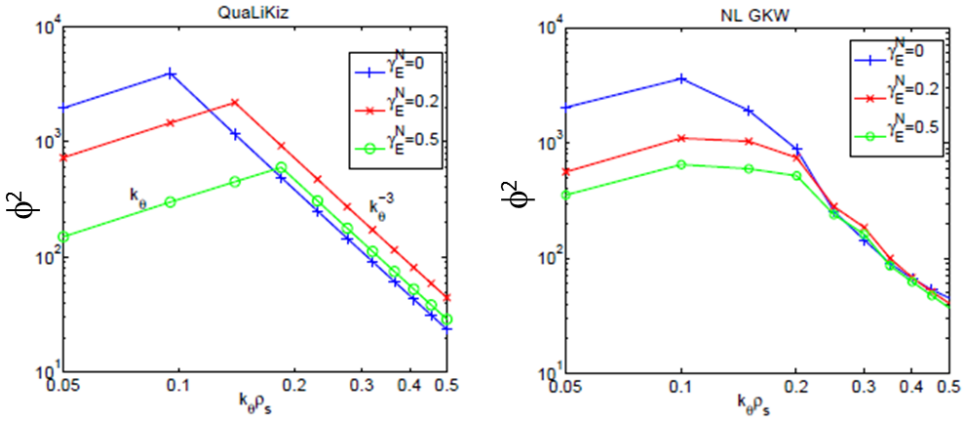

Figure 4.12: Left panel: QuaLiKiz saturated electrostatic potential. Right panel: GKW nonlinear saturated electrostatic potential. For three values of the $\mathbf{E} \times \mathbf{B}$ shear, γ_E normalized to the ratio of the ion thermal velocity to the major radius, v_{Ti}/R, 0 in blue, 0.2 in red and 0.5 in green. From [42].

For both QuaLiKiz and GKW, as $\mathbf{E} \times \mathbf{B}$ shear is increased, the amplitude of the saturated potential is reduced at the largest scales (lowest wave numbers). Both codes exhibit a weak dependence of their saturated potential with γ_E at $k_\theta \rho_s > 0.2$. Despite some quantitative differences, the nonlinear flux quenching with $\mathbf{E} \times \mathbf{B}$ shear is captured qualitatively with a shifted eigenfunction calculated in the fluid limit. Moreover the linear k_θ dependence up to the maximum, the value of k_{max} and the slope in k_θ^{-3} above k_{max} all reproduce fairly well the nonlinear simulation saturated potential. This validates the choices made for the k spectrum and the maximum saturated potential.

4.6 The quasilinear versus nonlinear fluxes for heat, particle and momentum

In the section above, it was demonstrated that for typical tokamak plasma parameters, the turbulence which develops in nonlinear gyrokinetic simulations is such that the equivalent flight time of the distribution function is shorter than the auto-correlation time of the saturated potential structures. Under such conditions, i.e. a Kubo number below 1, the quasilinear approximation holds. Therefore, the fluxes can be constructed following the expression given in equation 4.4, i.e. as the product of a linear response by

a saturated potential which can be schematically written as:

$$Flux^{NL,QL} = \mathrm{Re}\left[\sum_k \langle \delta f_k^{NL,QL} \delta v_{r,k}^{NL,QL} \rangle \propto \sum_k Weight_k^{NL,QL} \times (Saturated\ potential)_k\right] \tag{4.18}$$

The sum over k is typically done over 20 values from $k_\theta \rho_s = 0.05$ up to 2. Moreover, in nonlinear gyrokinetic simulations, it has been shown that the cross-phase of $\langle \delta f_k \delta v_{r,k} \rangle$ agrees between the nonlinear and the quasilinear cases. This reinforces the validity of the quasilinear approach. The ratios of the weights was be found to lead to quasilinear weights a constant factor 1.4 larger than the nonlinear weights, independent of k and gradient values. This ratio had to be adapted to model plasmas with low magnetic shear ($|s| < 0.6$). Finally a saturated potential has been successfully constructed, using a mixing length rule and Lorentzian frequency spectrum, which hence assumes the validity of random Gaussian statistics. The potentials have been shown to reproduce well nonlinear and measured k and frequency spectra, validating the approximations made. One unique free parameter remains and is adjusted such that the quasilinear ion heat flux for the GA-standard case in absence of rotation and $\mathbf{E} \times \mathbf{B}$ shear reproduces the nonlinear one. It is therefore now pertinent to test whether this model can adequately reproduce the ion heat flux for other sets of parameters, as well as in the deep TEM regime or very close to the temperature threshold, while including $\mathbf{E} \times \mathbf{B}$ shear and a finite parallel rotation. It is also pertinent to investigate whether the electron heat, the particle, and the momentum fluxes are also properly modeled.

4.6.1 Derivation of the quasilinear fluxes

The particle, heat, and momentum fluxes are calculated in QuaLiKiz. QuaLiKiz particle and energy fluxes are the advection of particle or energy by the fluctuating $\mathbf{E} \times \mathbf{B}$ drift in the radial direction. The gyrokinetic quasilinear formulation of the particle Γ_s and energy Q_s fluxes for each plasma species s, follows from the velocity moments integration of the diffusion coefficient embedded in Eq. (4.7), such that:

$$\Gamma_s = \sum_{k_\theta,\omega,\omega_k} \mathrm{Re}\left\langle \delta n_s \frac{i k_\theta \delta \phi^*}{B} \right\rangle \tag{4.19a}$$

$$Q_s = \sum_{k_\theta,\omega,\omega_k} \mathrm{Re}\left\langle \frac{3}{2} \delta P_s \frac{i k_\theta \delta \phi^*}{B} \right\rangle \tag{4.19b}$$

Note that in QuaLiKiz, the fluxes result of the sum over all unstable modes. This means that, in case of two or more unstable branches, the total flux is

the sum of the fluxes calculated with each unstable eigenvalues. The factor k_θ/B comes from the fact that the fluxes in QuaLiKiz are expressed in the $s-\alpha$ equilibrium and not with respect to the poloidal flux. Hence $\frac{\imath k_\theta \phi}{B}$ is the fluctuating $\mathbf{E}\times\mathbf{B}$ drift frequency.
Below, only the momentum flux is detailed, from [14, 42]. Similar derivations are carried out for the energy and particle fluxes of each species.
Rigorously, the toroidal momentum flux Π_φ is the quantity to calculate since the total toroidal momentum is a conserved quantity[174]. In conventional tokamaks (at aspect ratio of 3 or more), the flow is almost parallel [175]. Therefore, the parallel component of the toroidal momentum flux is much larger than the perpendicular one; making the parallel momentum flux a good proxy of Π_φ:

$$\Pi_\parallel = \sum_s \mathrm{Re}\left\langle m_s R v_\parallel \delta n_s \frac{\imath k_\theta \delta\phi^*}{B} \right\rangle \tag{4.20}$$

δf_s is the perturbed distribution function determined by the linearized gyrokinetic electroneutrality equation. R is the tokamak major radius averaged over a flux surface. In the high aspect ratio approximation, R_0 is used instead of R.
Using the formalism presented in chapter 2, the complete expression of $\Pi_\parallel$ is:

$$\begin{aligned}
\Pi_\parallel = &- \sum_{\epsilon_\parallel=\pm1,s,n} n_s m_s \left(\frac{nq}{rB}\right)^2 \\
&\left\langle \epsilon_\parallel \sqrt{\mathcal{E}(1-\lambda b)} e^{-\mathcal{E}} \left(1 + 2\frac{U_\parallel}{v_{Ts}}\epsilon_\parallel\sqrt{\mathcal{E}(1-\lambda b)} + \frac{U_\parallel}{v_{Ts}}^2 (2\mathcal{E}(1-\lambda b)-1)\right)\right. \\
&\left[\frac{R\nabla n_s}{n_s} + \left(\mathcal{E} - \frac{U_\parallel}{v_{Ts}}\left(2\epsilon_\parallel\sqrt{\mathcal{E}(1-\lambda b)} - \frac{U_\parallel}{v_{Ts}}\right) - \frac{3}{2}\right)\frac{R\nabla T_s}{T_s} + \right. \\
&\left.\left. 2\left(\epsilon_\parallel\sqrt{\mathcal{E}(1-\lambda b)} - \frac{U_\parallel}{v_{Ts}}\right)\frac{R\nabla u_\parallel}{v_{Ts}} + \frac{\varpi}{n\omega_{ds}}\right] \mathrm{Im}\left(\frac{1}{\omega - n\Omega_J(\mathcal{E},\lambda) + \imath 0^+}\right) |\phi_{n\omega}|^2 \right\rangle_{\mathcal{E},\lambda,k_r}
\end{aligned} \tag{4.21}$$

Compared to equations (2.56), (2.61) and (2.62), the momentum flux expression is similar, hence the same techniques are employed. The contributions from trapped and passing particles to the momentum flux are treated separately:

$$\Pi_\parallel = -\sum_{\epsilon_\parallel=\pm1,s,n} n_s\sqrt{2m_sT_s}\left(\frac{nq}{rB}\right)^2\Big\{$$
$$\int_{-\infty}^{\infty}\frac{\mathrm{d}k^*}{\sqrt{\pi}}e^{-k^{*2}}\int_{-\infty}^{\infty}\frac{\mathrm{d}\rho^*}{\sqrt{\pi}}e^{-\rho^{*2}}\mathrm{Re}(\langle\mathcal{J}_{ps}\rangle_{\mathcal{E},\lambda}(k^*,\rho^*))\mathcal{B}_0(k_\perp\rho_s)\left|\phi_{n\omega}\right|^2 \tag{4.22}$$
$$+\langle\mathcal{J}_{ts}\rangle_{\mathcal{E},\lambda}\int\frac{\mathrm{d}k_r}{2\pi}\mathcal{B}_0(k_\perp\rho_s)\mathcal{B}_0(k_r\delta_s)|\phi_{n\omega}(k_r)|^2\Big\}$$

The expression for $\mathcal{J}_{ps}$ is detailed in equation (4.23). Its expression is very close to that of equation (2.62). A notable difference is that even functions — $Z_1(v)$, $Z_2(v)$, $Z_3(v)$ — are replaced by odd functions — $vZ_1(v)$, $vZ_2(v)$, $vZ_3(v)$ —, such that without symmetry breaking due to rotational effects the momentum flux is zero.

$$\langle\mathcal{J}_{ps}\rangle_{\mathcal{E},\lambda} = \frac{f_p}{F_p(k_r)}\Big[$$
$$2\Big[A_{Ts}\frac{V_+Z_2(V_+)-V_-Z_2(V_-)}{V_+-V_-}+\left(A_{ns}-\frac{3}{2}A_{Ts}-\frac{\varpi}{n\bar{\omega}_{ds}}\right)\frac{V_+Z_1(V_+)-V_-Z_1(V_-)}{V_+-V_-}\Big]+$$
$$4\frac{U_\parallel}{v_{Ts}}\Big[A_{Ts}\frac{Z_3(V_+)-Z_3(V_-)}{V_+-V_-}+\left(A_u\frac{v_{Ts}}{U_\parallel}+\left(A_{ns}-\frac{5}{2}A_{Ts}-\frac{\varpi}{n\bar{\omega}_{ds}}\right)\right)\frac{Z_2(V_+)-Z_2(V_-)}{V_+-V_-}\Big]+$$
$$\frac{4}{3}\frac{U_\parallel}{v_{Ts}}\Big[\frac{U_\parallel}{v_{Ts}}A_{Ts}\frac{V_+Z_3(V_+)-V_-Z_3(V_-)}{V_+-V_-}+\left(2A_u+\frac{U_\parallel}{v_{Ts}}\left(A_{ns}-5A_{Ts}-\frac{\varpi}{n\bar{\omega}_{ds}}\right)\right)\frac{V_+Z_2(V_+)-V_-Z_2(V_-)}{V_+-V_-}\Big]-$$
$$\frac{2U_\parallel}{v_{Ts}}\Big[2A_u+\frac{U_\parallel}{v_{Ts}}\left(A_{ns}-\frac{5}{2}A_{Ts}-\frac{\varpi}{n\bar{\omega}_{ds}}\right)\frac{V_+Z_1(V_+)-V_-Z_1(V_-)}{V_+-V_-}\Big]\Big] \tag{4.23}$$

For trapped particles, the multiplication by $v_\parallel=\sqrt{\mathcal{E}(1-\lambda b)}v_{Ts}$ implies that there is no contribution to the momentum flux at lowest order in $\epsilon=r/R$ because the corresponding terms are odd in $\mathcal{E}$. However, the term in $\sqrt{\epsilon}$ is even in $\mathcal{E}$. Therefore the trapped particles bear a net contribution:

$$\mathcal{J}_{ts} =$$
$$2\bar{\omega}_b\left[\left(A_u+\frac{U_\parallel}{v_{Ts}}\left(A_n-\frac{5}{2}A_T-\frac{\varpi}{n\bar{\omega}_{ds}}\right)\right)\frac{Z_2(z)}{z}+\frac{U_\parallel}{v_{Ts}}A_T\frac{Z_3(z)}{z}\right]\int\frac{\mathrm{d}k_r}{2\pi}\mathcal{B}_0(k_\perp\rho_s)\mathcal{B}_0(k_r\delta_s)\tilde{\phi}_n(k_r) \tag{4.24}$$

Given the expressions of the passing and trapped particle contributions, the momentum flux, (equation (4.22)) can formally be written in the form:

$$\Pi_\parallel = \sum_s m_sn_sR(-\chi_\parallel\nabla U_\parallel+V_\parallel U_\parallel)+\Pi_{RS} \tag{4.25}$$

$\chi_\parallel$ represents the momentum diffusivity, $V_\parallel$ the momentum convection and Π_{RS} is the residual stress. However, the identification of $\chi_\parallel$, $V_\parallel$ and Π_{RS} with equation (4.21) is not as straightforward as it may appear. From equations (4.23) and (4.24), it is clear that $\Pi_\parallel$ contains terms directly depending on $U_\parallel$ and $\nabla U_\parallel$. They are called Π_u and $\Pi_{\nabla u}$. However, they do not contain all contributions from $U_\parallel$ and $\nabla U_\parallel$. Indeed, the remaining terms depend on the linear eigenfunction shift $\mathbf{x}_0$ which, itself, is a function of $\nabla U_\parallel$, $U_\parallel$ and γ_E as expressed by ((2.83)) [176]. The terms proportional to the eigenfunction shift are called Π_{x0}. If $\mathbf{E}\times\mathbf{B}$ shear is the only symmetry breaker, then $\Pi_{\text{x0}} \equiv \Pi_{RS}$. Otherwise, $\Pi_{\text{x0}} \propto U_\parallel, \nabla U_\parallel, \gamma_E$ cannot be identified with Π_{RS} since $\Pi_{\nabla u}$ (or Π_u) does not contain all conductive (or convective) contributions to the momentum flux. This direct separation gives an estimate of the importance of the eigenfunction contribution to the conductive and convective part of the momentum flux as discussed in greater detail below.
For the particle flux, in the absence of rotation, the convective and diffusive parts can be properly identified as detailed in [32]. Indeed, in this case, the particle flux is:

$$\Gamma_s = -\frac{n_s}{R}\sum_k \left(\frac{q}{rB}\right)^2 n^2 \left\langle \sqrt{\mathcal{E}} e^{-\mathcal{E}} \left(\frac{R\nabla_r n_s}{n_s} + \left(\mathcal{E} - \frac{3}{2}\right)\frac{R\nabla_r T_s}{T_s} + \frac{n\omega_s\left(\mathcal{E},\lambda\right)}{n\omega_{ds}} \right) J_0^2 \right\rangle_{\mathcal{E},\lambda} |\phi_{n\omega}|^2 = \frac{n_s}{R}\left(-D_s \frac{R\nabla_r n_s}{n_s} - C_s^{th}\frac{R\nabla_r T_s}{T_s} + RC_s^C \right) \tag{4.26}$$

In this case, the contributions to the flux from diffusion, D_s, thermo-diffusion, C_s^{th}, and due to parallel and perpendicular compressibility, C_s^C, can be extracted. For an analytical derivation of these terms and a discussion of their directions in various turbulent regimes, the reader is referred to [32]. QuaLiKiz provides these terms together with the total fluxes. In the presence of finite rotation, an additional convective term proportional to the parallel velocity shear appears and is referred to as the rotodiffusion coefficient [177]. As for the angular momentum flux, in presence of a finite rotation, due to the finite shift x_0, the residual pure convection term depends also on the velocity gradient, therefore the identification of the individual contributions is not straightforward anymore.

4.6.2 The energy and particle fluxes

During Alessandro Casati's PhD thesis, [33, 13], the energy and particle fluxes without rotation nor $\mathbf{E}\times\mathbf{B}$ shear were extensively compared to non-

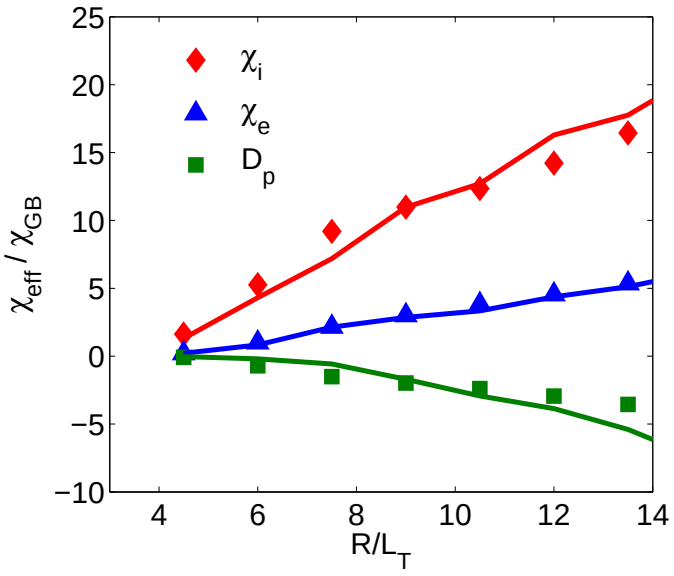

Figure 4.13: Ion energy, electron energy and particle effective diffusivities from GYRO (points) and QuaLiKiz (lines) for the R/L_T scan based on the GA-standard case. From [33].

linear GYRO simulations. The case around which parameters have been scanned is the collisionless GA-standard case. The quantities that are compared are the effective energy and particle diffusivities such that: $\Gamma_s = -D_s \nabla_r n_s$ and $q_s = -n_s \chi_s \nabla_r T_s$ for each species s.
In the first scan, both the ion and electron temperature gradients are simultaneously varied on a wide range: $4.5 < R/L_{Ti} = R/L_{Te} < 13.5$. The effective energy and particle diffusivities are expressed in GyroBohm units $\chi_{GB} = \rho_s^2 c_s / a$. Across the whole scan, the ion and electron energy and particle fluxes computed by QuaLiKiz and GYRO agree within 15%. Both the ratio between the transport channels and the parametric dependence are well captured by the quasilinear approach.
A second example is a direct application to an experimental collisionality ν_* scan realized on Tore Supra plasmas [121]. This has been realized as a dimensionless scaling experiment, since the two other relevant dimensionless parameters, ρ_s and β, are both kept constant across the different discharges, thanks to a coherent variation of the magnetic field and the temperatures, so that only the dimensionless collisionality is changed. The main plasma parameters are here summarized in Table 4.3.

The ν_* scaling of transport is a crucial test for quasilinear models. Two

R_0/a	r/a	R/L_{Ti}	R/L_{Te}	R/L_n	q	s	T_i/T_e	Z_{eff}	ρ_*	β
3.25	0.5	8.0	6.5	2.5	1.48	0.72	1.0	1.0	0.002	0

Table 4.3: Plasma parameters of the Tore Supra dimensionless collisionality scan at $r/a = 0.5$. With respect to the experimental values, only β is artificially set to 0 in the GYRO simulations.

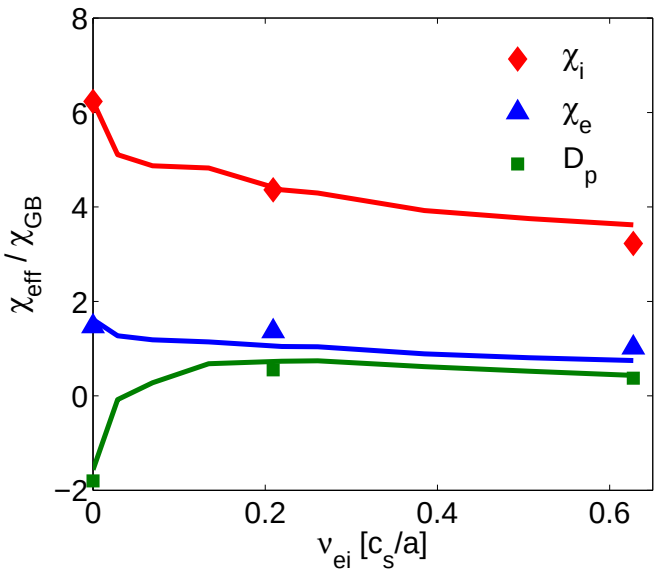

Figure 4.14: Ion energy, electron energy and particle effective diffusivities from GYRO (points) and QuaLiKiz (lines) for the collisionality scan based on the Tore Supra discharges. From [33].

effects are potentially at play with opposite consequences on the total flux levels. A collisional damping of zonal flows would in fact result into an increase of the turbulence level at higher collisionality; hence the fluxes would be enhanced, as pointed out in [178]. This effect is not taken into account in QuaLiKiz, which does not include zonal flows. Conversely, the linear collisional TEM damping would act in the opposite direction, reducing the linear instability drive hence the total turbulent flux at higher collisionality.
For the plasma parameters here explored, the GYRO simulations find a visible reduction of the transport level when increasing the collisionality, as shown in Fig. 4.14. Therefore the linear TEM damping is found to be dominant in these nonlinear simulations with respect to the collisional drag of sheared flows. Finally, Fig. 4.14 demonstrates that, for experimental values

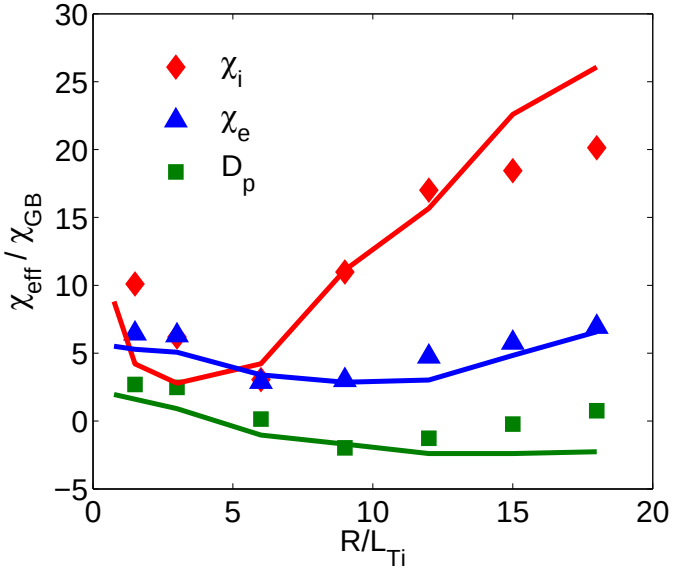

Figure 4.15: Ion energy, electron energy and particle effective diffusivities from GYRO (points) and QuaLiKiz (lines) for the TEM to ITG transition based on the GA-standard case, fixing $R/L_{Te} = 9.0$ and varying R/L_{Ti}. From [33].

of collisionality, the quasilinear modeling by QuaLiKiz is able to well reproduce the nonlinear diffusivities predicted by GYRO simulations, performed with pitch-angle scattering operators on both electrons and ions. The coupled dynamics between ion and electron non-adiabatic responses is crucial for both GYRO and QuaLiKiz. In particular, the particle flux reverses direction as ν_* increases, as already pointed out in Ref. [137].
Fig. 4.15 illustrates the TEM to ITG transition on the GA-standard case, realized keeping fixed $R/L_{Te} = 9.0$ and varying only the ion gradient R/L_{Ti} from 1 to 18.
The electron energy fluxes are well matched; discrepancies are instead observed on the particle fluxes for strong ITG turbulence and for the ion energy flux for $R/L_{Ti} < 4$ and $R/L_{Ti} > 13$. At $R/L_{Ti} < 4$, TEM become the dominant unstable modes, while the marginal conditions for ITG turbulence could be responsible for this quasilinear failure on the ion energy flux. The quasilinear model TGLF for example, adopts a modified mixing length rule that is proportional to $\gamma + \gamma^{1.5}$ instead of the simple linear relation with γ. On the other hand, above $R/L_{Ti} = 13$, the QuaLiKiz overestimation can be ascribed to a more pronounced effect of zonal flows in the nonlinear saturation of the ion energy transport for ITG dominated turbulence. Hence, the impact of

zonal flows and marginal turbulence on the quasilinear transport modeling deserve dedicated additional analysis.
When approaching the critical temperature threshold, the impact of zonal flows in pure ITG turbulence has been shown to lead to an upshift of the threshold referred to as the "Dimits upshift" [179]. It was, for the Cyclone base case and with adiabatic electrons, a shift in normalized temperature gradient units such that: $\Delta(R/L_T) \simeq 2$. In presence of kinetic electrons, this up-shift has been shown to be reduced from $\Delta(R/L_T) \simeq 2$ down to $\Delta(R/L_T) \simeq 0.8$ [180]. Here the $R/L_T = R/L_{Te} = R/L_{Ti}$ scan is pushed down to the linear threshold using realistic plasma parameters, i.e. kinetic electrons and a reasonable collisionality, detailed in table 4.4. From figure 4.16, for $R/L_T = 3.8$ the nonlinear fluxes are null, for $R/L_T = 4.5$ they are finite and in agreement with the quasilinear fluxes. Therefore one can conclude that, for this set of parameters, a Dimits shift, if existing, is smaller than $\Delta(R/L_T) = 0.7$. It is very challenging to run the nonlinear codes close to the stability threshold in the sense that the runs are more demanding in term of resolution and their convergence should be carefully checked. Therefore for the time being the conclusion is on an upper limit to the Dimits shift. Nevertheless, if the quasilinear simulations were largely underestimating the temperature gradient threshold, this would lead to largely underestimated temperature profiles, which is not what is reported in [40] where the RMS error on the predicted profiles is of 15-16%. Therefore, realistic cases, including kinetic electrons and collisions, lead to reduced Dimits shift, demonstrating that the quasilinear models are correct also close to the thresholds.

R_0/a	r/a	R/L_n	q	s	T_i/T_e	Z_{eff}	ρ_*	β	ν_{ei} in units of c_s/a
2.8	0.5	2.24	1.4	0.78	1.0	1.0	0.006	0	0.03

Table 4.4: Plasma parameters of $R/L_T = R/L_{Te} = R/L_{Ti}$ scan of figure 4.16.

4.6.3 Impact of the magnetic shear

In Jonathan Citrin PhD's work published in [34], the impact of q and more specifically of magnetic shear s was extensively investigated. As reported earlier, this led to an improved mixing length rule (see equation (4.17)) and to a new renormalization of the weight (see equation (4.12)). The particle and heat flux predictions from QuaLiKiz are compared to the nonlinear simulations, for all GENE runs carried out, as well as GYRO for the GA-standard

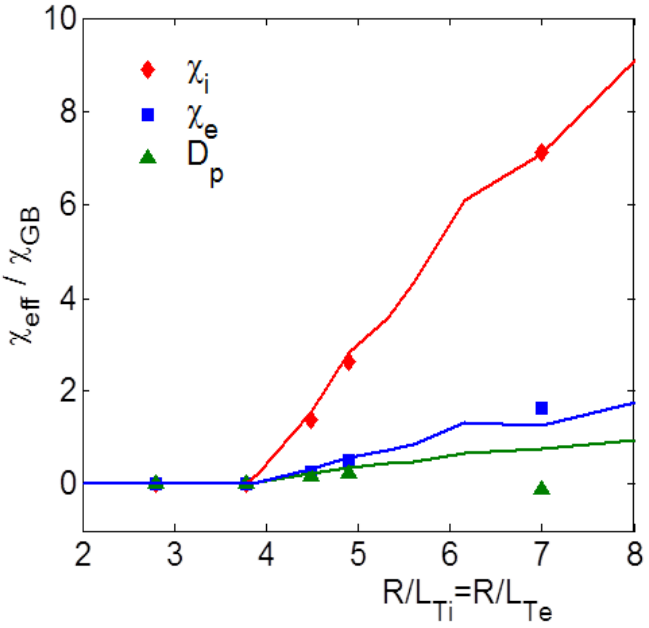

Figure 4.16: Ion energy, electron energy and particle effective diffusivities from GYRO (points) and QuaLiKiz (lines) for the parameters of table 4.4 plotted versus $R/L_T = R/L_{Te} = R/L_{Ti}$.

magnetic shear, q-profile, and R/L_T scans. The results are displayed in figure 4.17. The four sets of parameters detailed in table 4.1 are analyzed with respect to s. The RMS error between the particle and heat fluxes between QuaLiKiz and the non-linear GENE and GYRO simulations are listed. The RMS error is defined as $\sigma = \sqrt{\sum_i \epsilon_i^2 / \sum_j \chi_{j(NL)}^2}$, where ϵ_i is the flux difference between QuaLiKiz and the nonlinear prediction for a given simulation, and $\chi_{j(NL)}$ the flux from the nonlinear simulation; for the ion heat flux $\sigma = 0.26$, for electron heat flux $\sigma = 0.33$ and particle flux $\sigma = 1$.

4.6.4 Impact of rotation and E × B shear on angular momentum flux

During Pierre Cottier's PhD [14, 42] the impact of $\mathbf{E} \times \mathbf{B}$ shear and finite rotation was studied. At first, the GA-standard case set of parameters was used without rotation, i.e. $U_\parallel$ and $\nabla U_\parallel$ set to 0, but with a finite $\mathbf{E} \times \mathbf{B}$ shear. QuaLiKiz predictions of ion and electron energy and particle fluxes are compared to published results from nonlinear GYRO [136] and GKW[181]. QuaLiKiz energy and particle fluxes are smoothly reduced and quenched

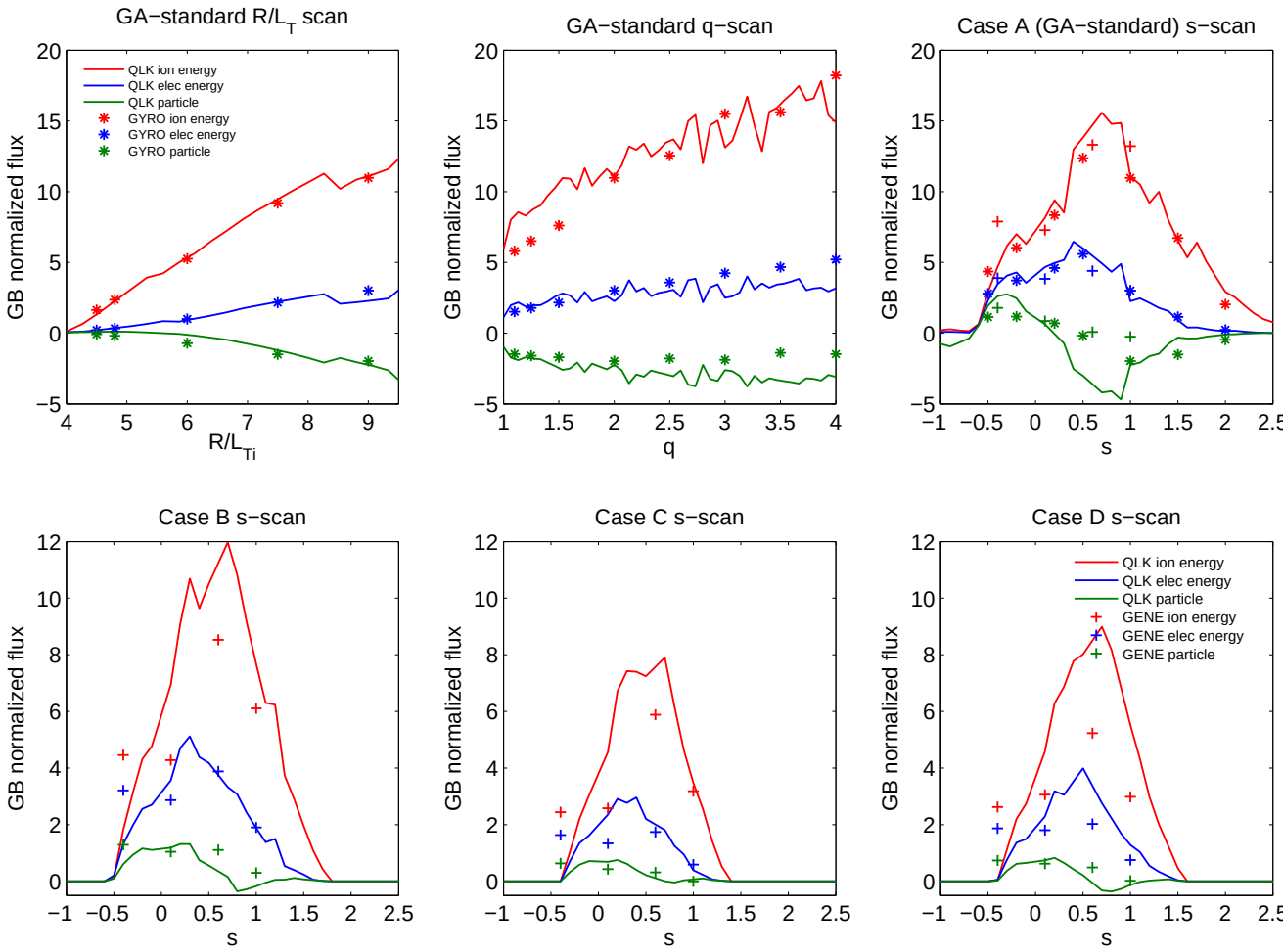

Figure 4.17: Comparison of QuaLiKiz with the 4 sets of GENE runs, and with the GYRO GA-standard case s-scan, q-scan, and R/L_T scan. From [34].

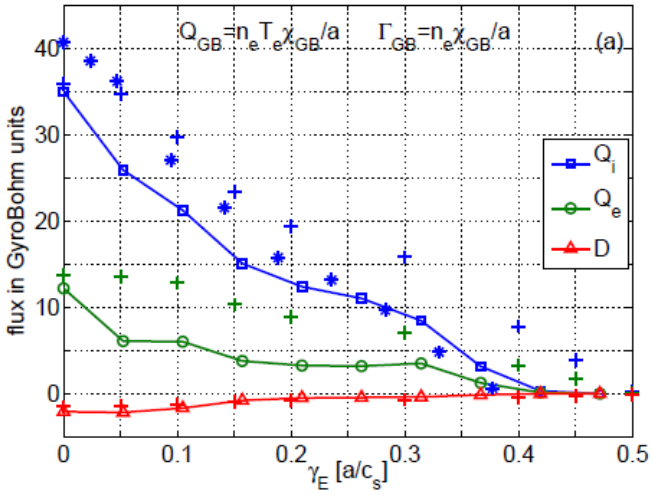

Figure 4.18: Ion energy, electron energy and particle effective diffusivities from GYRO (crosses), GKW (asterisks) and QuaLiKiz (lines) for the GA standard case plotted versus γ_E normalized to c_s/a .

for $\gamma_E > 0.4 c_s/a$ as illustrated by Figure 4.18. GKW was run using the $s-\alpha$ equilibrium, as was QuaLiKiz, whereas GYRO used Miller equilibrium. QuaLiKiz predictions for the flux amplitudes lies between nonlinear GKW and nonlinear GYRO for the ion energy flux.
For this scan, the angular momentum flux $\Pi_{\|}$ corresponds to the residual stress Π_{RS}. In absolute value, the momentum flux increases at first with γ_E due the $\mathbf{E}\times\mathbf{B}$ shear asymmetrization of the eigenfunction. Then, the momentum flux is slowly reduced due to the turbulence quenching by the $\mathbf{E}\times\mathbf{B}$ shear. This qualitative trend is found for GYRO, GKW and QuaLiKiz as illustrated on figure 4.19.
Quantitatively, QuaLiKiz overestimates the momentum flux found with GKW by $\sim 50\%$. The discrepancy between QuaLiKiz and GKW is related to the overestimation of the saturated potential amplitude at lower $k_\theta \rho_s$ and intermediate values of γ_E in QuaLiKiz as detailed in the previous section, see figure 4.12. Nevertheless, QuaLiKiz gives reasonable values for the residual stress and the turbulence quench by $\mathbf{E}\times\mathbf{B}$ shear. This means that the QuaLiKiz fluid derived shifted Gaussian eigenfunction used to determine the saturated potential, as illustrated in Figure 4.12, captures the essential physical mechanisms of the $\mathbf{E}\times\mathbf{B}$ shear action on the turbulence. Nonetheless, as discussed in section 2.2.1, in QuaLiKiz the $\mathbf{E}\times\mathbf{B}$ shear is estimated assuming that the $\nabla_r(\nabla_r(P_s))$ terms are negligible, hence assuming that $\nabla_r U_{\|}$ is

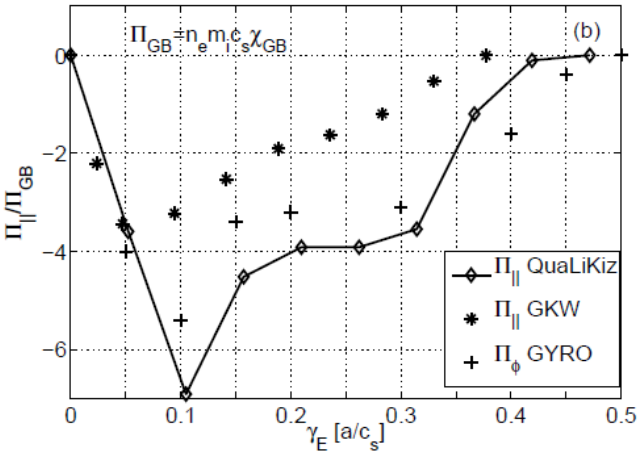

Figure 4.19: Parallel angular momentum flux from GYRO (crosses) using the Miller equilibrium [182], GKW (asterisks) using a $s-\alpha$ equilibrium as in QuaLiKiz (lines) for the GA-standard case plotted versus γ_E normalized to c_s/a. From [42].

the dominant contribution. This approximation is not always justified, as in [183], non-linear GYRO simulations show that the neglected terms can provide a residual stress comparable to the profile velocity shear contribution. Depending on the respective signs, the two contributions can be additive or minor each other.

The effect of $\nabla U_\parallel$ and $U_\parallel$ on the momentum flux are analyzed with the aid of dimensionless quantities: the Prandtl number $\frac{\chi_\parallel}{\chi_i}$ and the pinch number $\frac{RV_\parallel}{\chi_\parallel}$. They facilitate the comparison with nonlinear simulations as the saturated potential does not appear in these ratios. As discussed above, in QuaLiKiz, isolating conductive (diagonal) and convective (off diagonal) contributions to the momentum flux is not straightforward and requires two simulations. To evaluate the total conductive part of the momentum flux, a simulation with only $\nabla U_\parallel$ as a symmetry breaker ($U_\parallel = \gamma_E = 0$) is performed. The ratio of the momentum flux to the ion heat flux then gives the Prandtl number. To evaluate the convective part, a simulation with only $U_\parallel$, i.e. $\nabla U_\parallel = \gamma_E = 0$, is carried out. The ratio between the resulting momentum flux to the previous $\nabla U_\parallel$-only momentum flux gives the pinch number. Using this method, the contribution of the eigenfunction shift to the conductive and convective parts of the momentum flux can be quantified. Therefore, two QuaLiKiz simulations based on GA-std case parameters are performed such that:

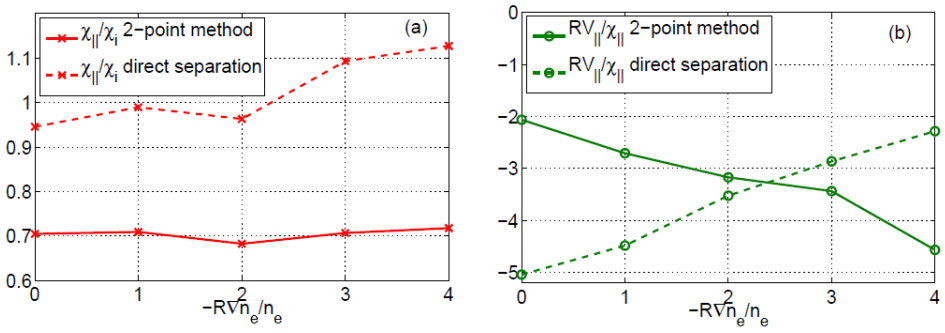

Figure 4.20: (a) Prandtl (red crosses) and (b) pinch number (green circles) calculated with the direct separation method (dashed curves) and with the 2-point method (plain curves) plotted versus R/L_n. From [42].

- one with $\frac{-R\nabla U_\parallel}{v_{Ti}} = 1$, $\frac{U_\parallel}{v_{Ti}} = 0$;
- one with $\frac{-R\nabla U_\parallel}{v_{Ti}} = 0$, $\frac{U_\parallel}{v_{Ti}} = 0.2$.

This method provides the correct values and is referred to as the 2-point method and it is compared to the direct incorrect estimation of the diffusive and convective parts as presented in equation (4.25). This comparison illustrate the impact of the eigenfunction shift on $\chi_\parallel$ and $V_\parallel$.
A normalized density gradient R/L_n scan is chosen to illustrate this comparison. Indeed, results from nonlinear gyrokinetic simulations indicate a strong correlation between R/L_n and the pinch number [184, 83], whereas the Prandtl number is weakly correlated. In Figure 4.20, the QuaLiKiz Prandtl pinch numbers for the two methods are plotted versus R/L_n. The Prandtl number deduced from the 2-point method is found to be close to 0.7 agreeing with quasilinear [88] and nonlinear simulations [83]. Due to the omission of the eigenfunction shift effect, the direct separation in QuaLiKiz gives a higher Prandtl number, close to one, as predicted in early theoretical calculations [185]. Using the 2-point method, the pinch number $\frac{RV_\parallel}{\chi_\parallel}$ is found to vary from -2 to -5, with a strong correlation with R/L_n, as in [83]. When neglecting the eigenfunction shift effects, i.e. with the direct separation technique, the correlation with R/L_n is inverted. Taking the ratio of the momentum fluxes amplifies the error. This illustrates that the eigenfunction shift is a key element and that QuaLiKiz models correctly its impact on the momentum flux convective and diffusive parts.

4.7 Summary

To summarize this chapter, the ion and electron energy, particle and momentum quasilinear fluxes computed by QuaLiKiz are successfully benchmarked against nonlinear gyrokinetic simulations from either GYRO, GKW or GENE. In terms of CPU time, the QuaLiKiz quasilinear approximation combined with a test eigenfunction in the simplest ballooning limit leads to a gain of the order six (i.e. roughly 1 million times faster). This gain in CPU time is shown to be compatible with well modeled energy, particle and momentum fluxes. The impact of the temperature gradient length, the collisionality, T_i/T_e, Z_{eff}, q, s, $\mathbf{E} \times \mathbf{B}$, etc are properly modeled. Some discrepancies remain for the pure ITG case ($R/L_{Ti} > 1.3 \times R/L_{Te}$) see figure 4.15, for the peak value of the residual stress on figure 4.19. As has been seen for the low magnetic shear cases, there may exist some other regions in parameter space where the renormalization of the weight must be adjusted. However, for the time being no such issue for the wide range of parameters studied is foreseen. Nevertheless, gaining more theoretical insight on the renormalization factor of 1.4, adjusted for low s, would be a very valuable contribution in making the quasilinear approach even more robust.
Given the success of the QuaLiKiz benchmark against nonlinear gyrokinetic codes, it is now pertinent to compare QuaLiKiz predictions with experimental observations, either in a standalone version or within an integrated framework.

Chapter 5

Quasi-linear fluxes vs experiments

In the previous chapter, the main approximations leading to quasilinear fluxes were reviewed and validated against nonlinear simulations. Energy, particle and momentum quasilinear fluxes are calculated by QuaLiKiz. These fluxes agree well when compared to nonlinear gyrokinetic predictions. The gain in terms of CPU time is approximately four orders of magnitude in comparison to full nonlinear modeling. This allows for systematical modeling of experiments. Below such results are presented. They concern electron particle transport, impurity particle transport, heat transport and finally momentum transport. Results obtained in a standalone manner are presented. For particle and heat transport, results obtained by running QuaLiKiz within the integrated platform CRONOS [46] are reported.

5.1 Electron particle transport

The electron particle mechanisms have been extensively analyzed. The quasi-linear expression of the particle flux is similar to the one derived in the previous chapter for the angular momentum, see equation (4.26). It has been derived in [32, 31]. In the quasi-linear particle flux expression, four types of contributions can be easily identified. The diffusion part which is proportional to ∇n, the other three terms being various contributions to the convective flux. One part of the convective flux is proportional to ∇T and is known as the thermodiffusion, another scales with ∇U and is called the roto-diffusion, finally the last convective term is named here the compressibility term. The thermodiffusion, C_e^{th}, has long been identified as a velocity convection for sufficiently high $\frac{\nabla T/T}{\nabla n/n}$ [186, 187, 188] due to cold

particles diffusing faster than hot particles. This mechanism is also observed in electron drift wave turbulence simulation in a slab geometry [22]. The roto-diffusion term, C_e^{rot}, has been more recently expressed in [189, 177]. It is negligible for electrons since their thermal velocity is very large. However, it is significant for impurities, in particular heavy ones. The compressibility convection, C_e^C, is made of two terms: the parallel compressibility [32, 43] and the curvature and ∇B drifts. The later is due to the fact that an inhomogeneous magnetic field induces an inhomogeneous density profile [190, 191]. It is also called the turbulence equi-partition term. This mechanism is well described in [192], where it is found that the density of trapped electrons is proportional to $1/q$ leading to a peaked density profile. When the effects of collisions and passing ions are included, the magnetic field gradient term is proportional to magnetic shear, as shown in [193, 194]. The collisions can detrap some of the trapped electrons and, therefore, weaken the role of the curvature and ∇B pinch [195, 196].
As a consequence of these four expected terms, electron particle fluxes Γ_e are often formulated as follows:

$$\Gamma_e = \frac{n_e}{R}\left(-D_e\frac{R\nabla n_e}{n_e} - C_e^{th}\frac{R\nabla T_e}{T_e} - C_e^{rot}\frac{R\nabla U_e}{V_{th}} + RC_e^C\right) \qquad (5.1)$$

The convection terms for electrons can change sign depending on the limit and on the dominant instability. An analytical derivation in the fluid limit is detailed in [32]. The resulting trends are summarized by table 5.1 for the two main mechanisms contributing to the convection: compressibility (or turbulence equipartition) and thermodiffusion. The interested reader is also referred to [31] for an additional outlook on these issues. In light of

	Thermodiffusion ITG	Thermodiffusion TEM	Compressibility ITG	Compressibility TEM
Curvature and ∇B only	Inward	Outward	Inward	Inward
Slab limit	Inward	Inward	Outward	Inward

Table 5.1: Direction of the electron convection terms obtained in two quasi-linear analytic limits: curvature only and slab. From [32].

these various well characterized theoretical mechanisms, the experimental trends are observed. First of all, the existence of an inward turbulent particle convection has been unequivocally identified in Tore Supra experiments [197], where a peaked density profile was reported as illustrated by figure 5.1. The particle source was demonstrated to be localized at the edge of the plasma, see figure 5.1. Moreover, the equivocalness of the results was based

on the fact that the neoclassical convection term was zeroed out. This was guaranteed by a parallel electric field $E_{//}$ zeroed across the whole plasma. Indeed, the neoclassical convection known as the Ware pinch [198] is linearly proportional to the local value of $E_{//}$. For zero $E_{//}$, a fully non-inductive plasma must be run over a time larger than the current diffusion time. This was achieved in Tore Supra long pulses where the current was driven by lower hybrid waves. The measured peaked electron density profile therefore demonstrated the existence of an inward turbulent convection. This turbulent transport is expected to depend on numerous parameters such as the nature of the turbulence, either ITG or TEM.

The impact of the nature of the turbulence on the particle pinch has been extensively studied. In [199], for $r/a \leq 0.3$ for a given $\nabla q/q$ range, the particle peaking $-\nabla n_e/n_e$ was found to increase for increasing normalized temperature gradient $-\nabla T_e/T_e$, whereas for $0.35 \leq r/a \leq 0.6$ it was decreasing with increasing $-\nabla T_e/T_e$ as illustrated by figure 5.2. This experimental observation was found to be coherent with pure ITG being unstable in the core and a stronger contribution of TEM in the gradient region. Indeed, as summarized by table 5.1, in the presence of ITG an inward convection due to thermodiffusion is expected, hence a positive correlation between $-\nabla n_e/n_e$ and $-\nabla T_e/T_e$. The opposite trend is expected in the case where TEM plays a more important role. This is what is observed. Also, in the gradient region, $0.3 \leq r/a \leq 0.6$, $-\nabla n_e/n_e$ was found to correlate more strongly with $\nabla q/q$ than with $-\nabla T_e/T_e$, as expected in this region where the fraction of trapped particle is large, leading to a significant inward compressibility term carried by the curvature and ∇B term. Similar results were reported on FTU [200]. So far only the behavior of the density peaking has been reported as an experimental indication on the convection velocity. In principle, density modulation techniques could provide more direct information on the convection velocity. This is what has been recently investigated on Tore Supra using modulated ion cyclotron resonance heating to generate perturbations of density and temperature. We note that the convection in this case is the convection of the particle perturbation. The analysis of these pulses show that, when a critical gradient mixing R/L_n and R/L_T is exceeded, the particle flux increases sharply and the convective velocity reverses from inward to outward. These observations are in agreement with QuaLiKiz calculations showing that the critical gradient corresponds to a transition from pure ITG to mixed ITG and TEM as illustrated by figure 5.3 from [45]. This illustrates a significant contribution from the thermodiffusion term even at radii such as $r/a = 0.5 - 0.6$.

This dominant impact of the current profile on the density profiles was reported for TCV L-modes [201] and JET [202]. In H-mode, although the den-

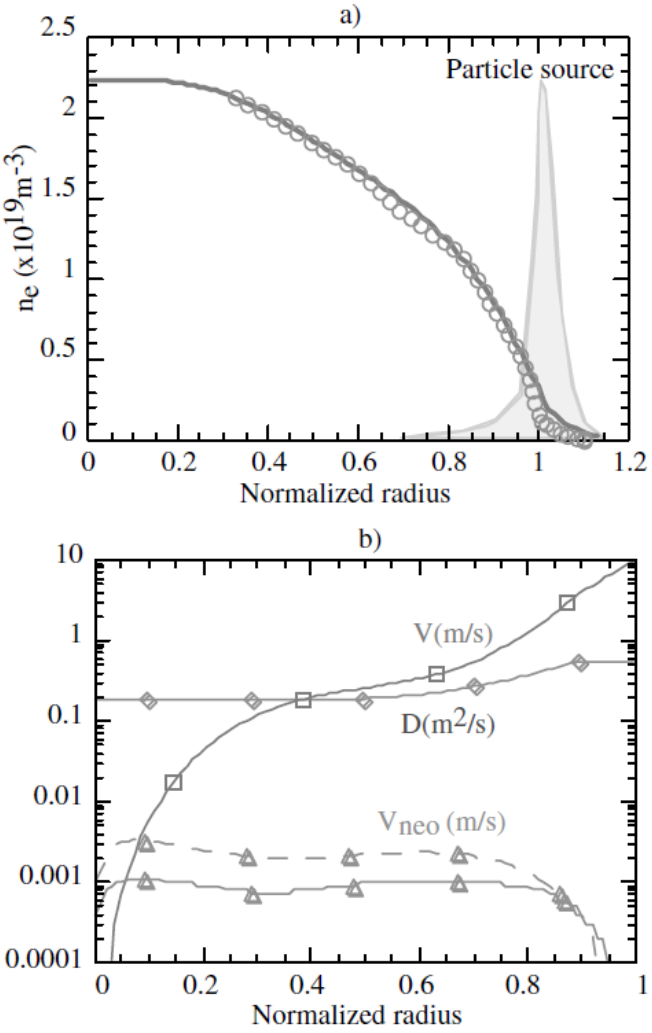

Figure 5.1: 1D simulation of discharge 30428, at 30 s: (a) density profile (line: simulation; circles: reflectometry measurements); (b) pinch velocity (squares) and diffusion coefficient (diamonds) used to reproduce measured density profile, V_{neo} given by NCLASS (triangles), V_{neo} when assuming $Z_{eff} = 6$ instead of 2 and iron impurity only (dashed line/triangles). From [197].

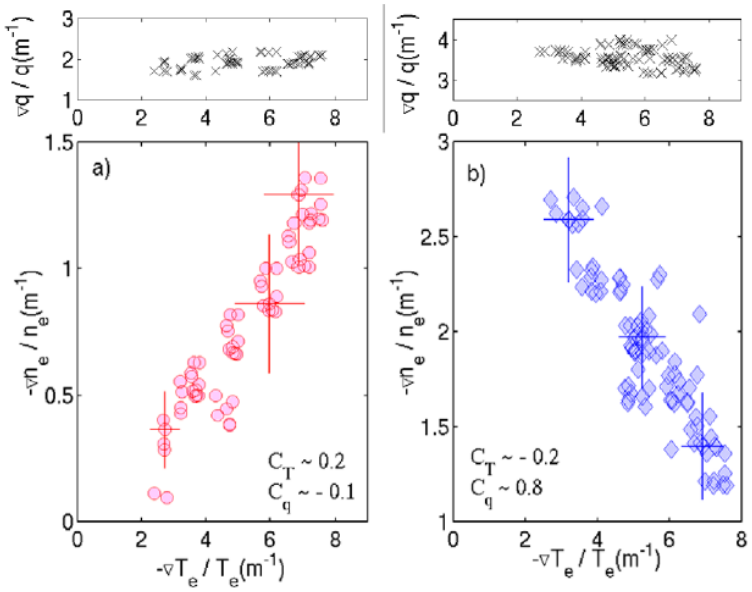

Figure 5.2: $-\nabla n_e/n_e$ versus $-\nabla T_e/T_e$ from a set of seven discharges: (a) for $r/a \leq 0.3$, $T_e/T_i = 2 \pm 0.4$, $\nabla T_e/\nabla T_i = 3.8 - 4.8$; (b) for $0.35 \leq r/a \leq 0.6$, $T_e/T_i = 1.2 \pm 0.4$, $\nabla T_e/\nabla T_i = 0.7 - 3.5$. Corresponding variations of $\nabla q/q$ are displayed on the top panels (crosses). From [199].

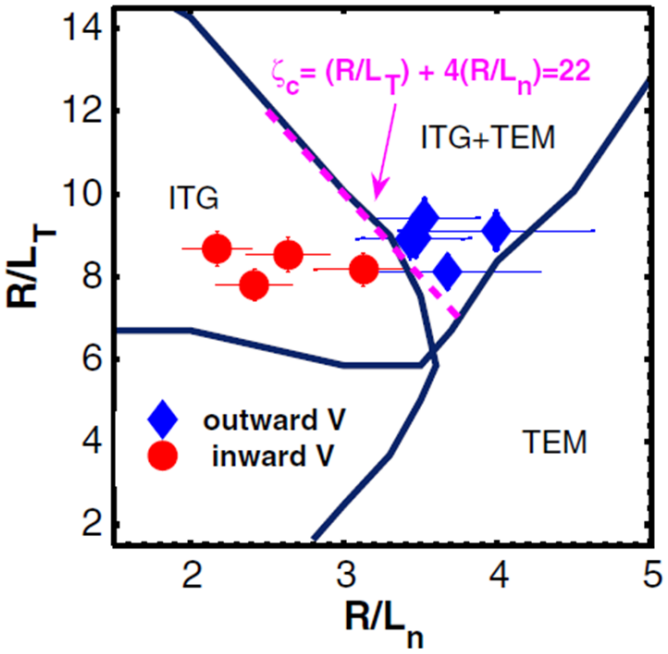

Figure 5.3: Turbulence stability diagram computed by QuaLiKiz for the experimental parameters, black lines. In colored symbols, the direction of the convection is given. From [45].

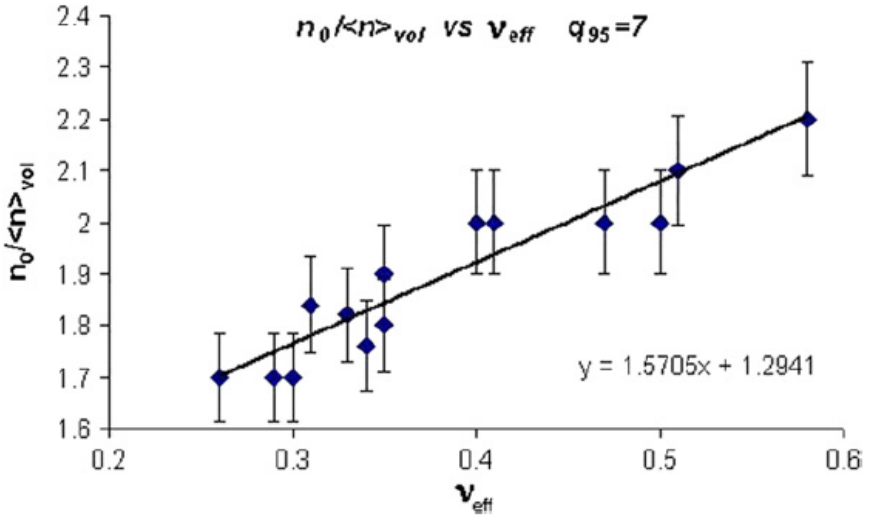

Figure 5.4: Density peaking factor versus collisionality for FTU L mode LHCD electron heated discharges. From [200].

sity peaking is correlated with the current profile peaking in JET [203], the correlation is stronger with collisionality as reported from ASDEX Upgrade, JET [204, 205, 203] and others [206]. In [203], GS2 quasilinear estimations of the particle fluxes were found to reproduce well the parametric dependencies of the electron particle flux. In the case of dominant ITG at all collisionalities, increasing the collisionality leads to a weaker contribution from the trapped particles. The trapped particles lead to peaked density profiles due to the role of the compressibility. Hence, less trapped means less inward compressibility pinch. This is how the anti-correlation between density peaking and collisionality is understood [207].
In the case of dominant TEM however, larger collisionality is expected to lead to weaker TEM and more dominant ITG, leading to a reversal of the thermodiffusion convection from outward to inward. Hence, in such cases the density peaking is expected to correlate with a larger collisionality, as is reported for FTU fully non-inductive cases where $R/L_{Te} > R/L_{Ti}$ [200], see figure 5.4. In a Tore Supra dedicated dimensionless collisionality scan, no impact of collisionality on the density profiles was observed [121].
To summarize, turbulence certainly plays a key role on particle transport. Various experimentally observed features can be explained through quasilinear gyrokinetic modeling. However, when doing such comparisons, the particle source inside the radius of analysis has to be demonstrated to be

negligible which is not always an easy task. Moreover additional neoclassical fluxes related to the Ware pinch or heating waves contributions have to be ruled out. A large tokamak such as Tore Supra using gas puff only and running at zero loop voltage was an ideal machine for such studies. Assuming that such conditions were reached. It was observed, in the deep core of the discharge, that thermodiffusion dominates. On the other hand, the gradient region is thought to be dominated by compressibility terms. A larger trapped particle fraction in this region, together with larger current profile peaking, lead to density peaking which correlates linearly with the current peaking. Under such conditions, an increased collisionality is expected to weaken the trapped particle contribution, and hence the peaking. Indeed in H-mode the collisionality impact dominates, whereas the role of the current peaking is weaker. In L-mode, a weaker or even opposite sensitivity to collisionality is reported, whereas a stronger impact of $\nabla q/q$ is observed. The reason might be that at the zero-flux point, an increase in R/L_n with increasing shear is predicted to occur in the presence of a dominant TEM instability, while it is not predicted to occur in the presence of a dominant ITG instability. And since the L-mode cases are mostly with dominant electron heating, TEM are likely dominant, whereas in the H-mode cases, the dominant heating is on the ions and ITG are likely dominant [206]. For more exhaustive reviews on electron particle transport, the interested reader is referred to three review articles [208, 207, 177] and to Angioni's Habilitation [31].

5.1.1 Time evolving modeling of particle transport

Following the overall success of quasilinear models in reproducing numerous features of the electron particle transport at a given time slice, it is natural to now use such models in an integrated modeling framework to model density profile evolution. The experimental case on which the focus is made concerns high plasma current JET H-mode discharges ($I_p > 2.0 - 2.5$ MA, depending on plasma shape), with naturally higher plasma densities for which NBI penetration is poorer. Under these conditions, the core density evolves in much longer timescales than the edge density leading to the formation of rather hollow density profiles. These hollow density profiles persist for timescales of several energy confinement times until they are usually terminated by a sawtooth. When extrapolated towards ITER in D-T operation, such hollow density profiles can be deleterious since they reduce the core density peaking and hence the α central heating necessary to maintain the H mode. To address this issue, modeling of such a JET pulse thanks to QuaLiKiz embedded in CRONOS has been carried out by B. Baiocchi [49]. Since the edge is not modeled, the results are sensitive to the edge source and extra care has to

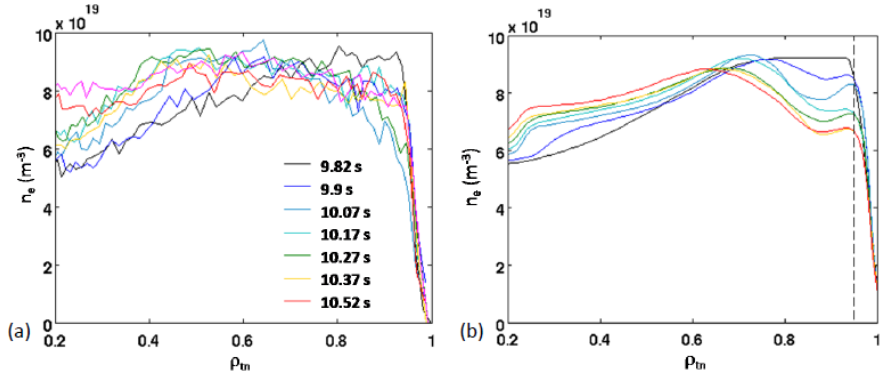

Figure 5.5: Evolution of the density profile (a) from HRTS in the experimental JET pulse 79676 and (b) as obtained by the QuaLiKiz simulation in CRONOS. Different colors correspond to the times of the legend of fig. (a). The experimental density profile at 10.6 s, after the first sawtooth, is included in the graph (a) in purple. The dashed line of (b) corresponds to the radial location of the imposed boundary conditions. From [49].

be taken when setting up the initial conditions. Provided this is done and that the density pedestal is recovered, QuaLiKiz predicted hollow density profiles is consistent with the experiment as illustrated by figure 5.5. The hollow profile is maintained since the diffusion – initially directed outward – is not counterbalanced by sufficient inward convection. Therefore, it seems that indeed the sawtooth has a key role in filling up the density in the core region. This allows to tackle ITER scenario modeling, including the density profile, with more confidence.

5.2 Impurity particle transport

Impurity particle transport can be explored experimentally thanks to perturbation techniques. In a tokamak environment, an impurity is defined as an ion which contributes to the dilution of the fusion fuel (D or D/T) and which can potential radiate and cool down the plasma core. At the edge, where plasma wal interactions are at play, injecting impurities allow to reduce the peak heat flux on the divertor. Experimentally, to study their transport, traces of impurities are injected by laser blow-off. A trace here means that the background plasma (density, turbulence level, rotation etc.) is not impacted by the puffed ions. The injected impurities are diagnosed by soft X-ray cameras, bolometric lines and V/UV spectrometers, see for example [209, 210, 44, 211]. Codes have been developed to reconstruct the measured

signals and provide the transport coefficients of the trace impurity. The radial transport analysis is performed using 1D transport codes such as ITC [212], SANCO [213] or STRAHL [214]. It solves the system of continuity equations coupling all the ionization stages of the injected impurity over the time interval during which the injected impurity is present in the plasma. The impurity flux, Γ_Z, can be schematically written as :

$$\Gamma_Z = -D_Z \nabla n_Z + V_Z n_Z \tag{5.2}$$

where D_Z is the diffusion coefficient of the trace impurity Z and V_Z is its convection velocity. D_Z and V_Z are assumed to be time independent. As ITC is a 1D code, homogeneous quantities on the flux surfaces are assumed. From an initial guess of D_Z and V_Z profiles, ITC solves the system of equations to obtain the radial density profile of each ionization stage of the impurity. Then, from the resulting impurity density profile it reconstructs the UV line and soft X-ray brightnesses according to the geometry of these diagnostics. Finally, a minimization procedure is applied, more details are given in [215]. Such experimental data, which provides diffusion coefficients and convection velocities, can be easily compared to QuaLiKiz predictions. This is what has been done for various cases summarized below.

5.2.1 Z impact, prediction versus experimental results

Among various qualitative studies which can be made by the linear models of turbulent transport, the role of the impurity charge Z on its transport can be predicted. The convection velocity (in absolute value) is predicted to decrease with increasing Z, down to an asymptotically null value. Also, the sign of the convection velocity could vary depending on the nature of the turbulence: this is intended to be used as a control tool of impurity behavior in fusion devices. This prediction has been the object of recent experimental publications [214, 109, 216, 210]. The role of the impurity charge Z is of particular interest as various species will be found in ITER, ranging from helium ($Z = 2$) to Tungsten (up to $Z = 74$). In JET, the experimental work has been carried out [109] and analyzed by a gyrokinetic code [217], where, the reported weak impact of Z on the transport coefficients has been well reproduced by the simulations.
An analytical derivation of the trace impurity flux in the fluid limit is presented in details in [32] as well as in [31]. Two limit cases are considered: (1) the curvature and ∇B drifts dominate the transit dynamics called here "curvature only" and (2) the parallel dynamic dominates the curvature and ∇B one called here "slab limit". These simplified cases are used in the table below to report on the impact of the charge number Z and of the mass

number A. Note that the fluid limit is not rigorously correct, but allows to anticipate some parametric trends ahead of the experiments and serves as a guidance for the first level interpretation.

In this context, in Tore Supra, L-mode experiments were performed where

	Compressibility	Thermodiffusion
Curvature only	No dependencies	Scales as 1/Z
Slab limit	Scales as Z/A	Scales as 1/A

Table 5.2: Dependencies of trace heavy impurities convection terms vs their charge and mass numbers (Z and A) obtained in the quasilinear analytic limit.

lower-hybrid current drive was used in order to suppress sawteeth. To investigate the impact of the charge Z, metallic impurities (Aluminum $Z = 13$, Chromium $Z = 24$, Nickel $Z = 28$ and Germanium $Z = 32$) were injected. The analysis of these pulses was carried out during Thomas Parisot's PhD [218]. Taking into account error bars, in the center ($r/a < 0.2$) the diffusion was found to be reduced in the case of lighter impurities, leading to longer confinement time for Aluminum compared to Germanium. Unfortunately in this central region, QuaLiKiz found no unstable modes. For $r/a > 0.2$, no dependence in Z was found on D_Z and the inward inferred convective velocity was found directed inward with a larger amplitude for Aluminium than Germanium for $r/a > 0.4$ [210]. For $r/a > 0.15$, the diffusivity computed by QuaLiKiz is not affected by Z and the convection is directed inward in agreement with the experimental observation in this radial region, see figure 5.6. The modeled convection velocity, V_Z, is not impacted much by Z variation except for $0.2 < r/a < 0.3$, where a higher Z leads to a more inward velocity, see figure 5.6. The observed Z impact on the modeled gyrokinetic V_Z differs from the expectations derived in fluid limit summarized in table 5.2. Such differences are regularly found, a fluid limit analytical derivation being only a tool to predict and discuss trends far above the threshold. The parametric trend found with a more accurate gyrokinetic derivation can hence be different. Moreover the Z impact on the modeled V_Z is opposite to the experimental trends at $0.4 < r/a < 0.8$.

It is important to note that towards the center, experimentally a diffusivity larger than the neoclassical predictions is found whereas QuaLiKiz does not predict any turbulent transport. This underestimation of the turbulent fluxes by quasilinear or nonlinear gyrokinetic codes in the center of tokamak plasmas is often reported and is due to central normalized gradients that are below the linear stability threshold. To reconcile the modeling with the

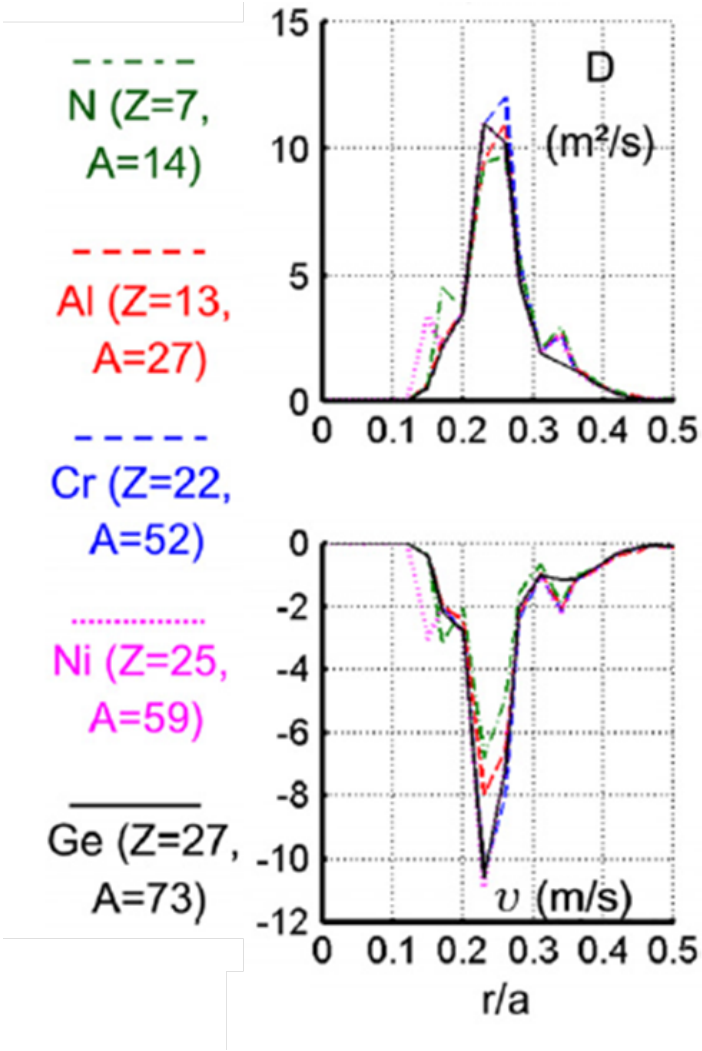

Figure 5.6: QuaLiKiz D_Z and V_Z for Tore Supra L mode plasma profiles for various trace impurities. From [210]

experimental observations, nonlinear turbulence spreading effects should be taken into account. Unfortunately, to date, although mechanisms responsible for turbulence spreading have been studied, see for example [155], no flux driven nonlinear code has addressed this issue while accounting for conditions close to experimental core parameters.

5.2.2 Critical temperature gradient

As introduced in chapter 2, turbulent transport can be triggered by normalized temperature gradient larger than a given threshold, see figure 3.4 for example. For impurity transport dominated by TEM turbulent transport, an influence of $R/L_{Te} = -\nabla T_e/T_e$ is expected. This was studied during Daniel Villegas's PhD [215] and published in [44]. Three sawtooth and MHD-free circular Tore Supra L-mode plasmas heated by 250 kW of electron cyclotron resonance continuous wave power were studied. In two discharges, the same ECH power was injected at different locations: $r/a = 0.35$ and $r/a = 0.6$. In a third discharge, the same power was equally distributed between these two radial locations. The impurity studied, Nickel, was injected as a trace by a laser blow-off system. The inferred D_Z and V_Z are compared to QuaLiKiz modeling. As pointed out in chapter 3, the stand alone fixed gradient analysis shown here is highly sensitive to the input data. Therefore the results are strongly impacted by modified gradient lengths for example. In figure 5.7, the uncertainties on the temperature gradients have been tested and lead to the large shaded areas corresponding to the resulting uncertainties on the QuaLiKiz predictions.
Within the uncertainties, QuaLiKiz reproduces the diffusion and convection of Nickel reasonably well. As observed in the previous impurity transport work, the convection is directed inward, leading, a priori, to an accumulation of impurities in the core.
By comparing the three depositions of ECRH power, R/L_{Te} is significantly modified in the core [44]. The Nickel diffusion is found to respond strongly to this modification at $r/a = 0.1$ as illustrated on figure 5.8. At $r/a = 0.3$, the diffusion is unaffected by the modified R/L_{Te}. These observations are in agreement with dominant TEM found at $r/a = 0.1$ and dominant ITG at $r/a = 0.3$. Nonetheless, the uncertainties on the T_i profile are very large since it was not measured in the analyzed pulse. By varying R/L_{Ti} within its uncertainty range, the modes can be found to be stable. This is illustrated by the shaded area on figure 5.8. This aspect is further discussed in [215]. It is interesting to note that in this case, very central unstable modes are found linearly unstable thanks to a very large density gradient length $R/L_n = 6.4$ leading to unstable TEM. This central density peaking is linked to the pres-

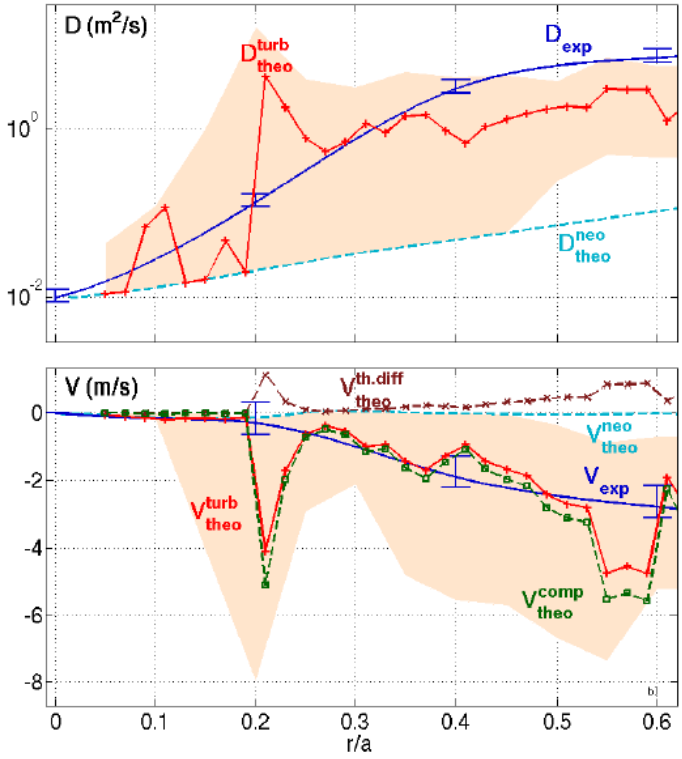

Figure 5.7: Inner ECRH deposition case. Radial transport coefficient profiles. The upper plot corresponds to the diffusion coefficient, with the experimental profile (dark blue), neoclassical computation (light blue dashed line), and the sum of NCLASS and QuaLiKiz results (red with + markers). The bottom plot corresponds to the convection velocity, with the experimental profile (blue), neoclassical profile (light blue dashed line), QuaLiKiz thermodiffusion pinch (brown with x markers), curvature pinch (green squares), and the sum of all theoretical terms (red with + markers). The yellow shaded areas show error bars on QuaLiKiz results deduced from the propagation of the experimental uncertainties on the ion and electron temperature gradients. From [215, 219].

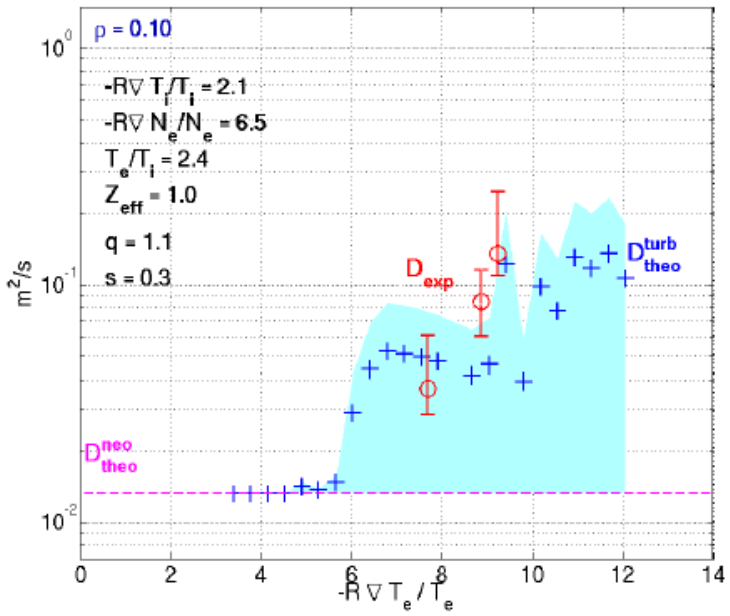

Figure 5.8: QuaLiKiz turbulent diffusion D^{turb}_{theo} (crosses) versus the normalized electron temperature gradient at $r/a = 0.1$ with experimental points corresponding to the three ECRH deposition situations (circles). The shaded color band corresponds to the error bar on D^{turb}_{theo} due to the R/L_{Ti} uncertainty. From [44].

ence of ECH.
In ASDEX Upgrade, in the presence of central electron heating, average Z impurities have been shown to have either a weak or even a positive convection. This leads to weaker core impurity accumulation. The theoretical understanding of this mechanism is thought to be due to the passing electron compressibility term, leading to an outward convection in case of dominant TEM as reported in [43, 220]. It is shown that an outward convection is obtained only if both R/L_{Ti} is low and R/L_{Te} is high. To reproduce ASDEX Upgrade's result R/L_{Te} has to be increased above its experimental value. This mechanism cannot explain results obtained in JET on Nickel transport [216]. It is important to note that this contribution is not modeled properly in the QuaLiKiz framework where extended eigenfunctions along the field line are not compatible with the lowest order ballooning representation. Therefore complementary gyrokinetic simulations have to be carried out when investigating central electron heating cases leading to outward convection of impurities. It is also to note that, in Tore Supra dominantly electron heated

pulses, the impurity convection has never been found directed outward.

5.2.3 Further work on W

Since 2011, JET operates with metallic walls, namely Tungsten in the divertor and Beryllium on the walls as will be the case in ITER. Another important tokamak (ASDEX Upgrade) operates with both Tungsten wall and divertor. At IRFM, CEA, the implementation of a Tungsten divertor in Tore Supra (WEST project) has started. Operation will start in 2016. In this context, it is of prime importance to understand the transport of Tungsten from the divertor to the core of the plasma. Indeed Tungsten in the plasma core has to be avoided since it radiates very efficiently and therefore cools down the discharge. In JET and ASDEX Upgrade, means of controlling Tungsten accumulation are extensively tested. In particular, central electron heating has allowed avoiding Tungsten accumulation [211, 221]. Understanding these mechanisms is very important to prepare WEST operation as well as ITER's. The Z impact on impurity confinement observed experimentally in the very core (low Z impurities having better confinement than heavier ones [210]), reported in subsection 5.2.1, has not been reproduced by QuaLiKiz modeling where no unstable modes are found in this central region. The impact of an increased R/L_{Te} on Nickel has been evidenced in the very core in subsection 5.2.2 and modeled successfully [44], but this was done in the particular case of large central density peaking leading to linearly unstable TEM. Even in this restricted case, it is interesting to note that with larger R/L_{Te}, the diffusion of the impurity is increased while its convection is unchanged. Therefore, the mechanisms explaining less core impurity accumulation seem to rely on larger diffusion rather than on modified convection. This means that a degraded core energy confinement is favorable for less core impurity accumulation. In JET, with W, this trend has been recently reported in [221], where the energy confinement time seemed to correlate with the W confinement time. Ideally, one would like to be able to decorrelate degraded energy confinement and degraded impurity confinement. To achieve such a goal the convection should be the key player. While in principle the convection can be inward and outward [32], in practice, the compressibility term dominates and the overall convection for experimental cases, such as the ones reported above, tends to be directed inward. To be relevant, any future work has to account for the rotation impact on impurity transport, in particular for the case of Tungsten where the centrifugal force is significantly at play. For heavy impurities such as Tungsten, the neoclassical contributions are larger and have to be properly modeled, also including the centrifugal effects. This is done in the code NEO [222]. Such detailed modeling has started and has been

shown to successfully model JET results at fixed pulse timeslices [223]. In the core, MHD kink instabilities named sawteeth are often at play and their effect on the impurity transport has to be accounted for as shown in [11]. The dynamics of Tungsten transport is nontrivial since, by radiating, it modifies the electron temperature. Therefore self-consistent modeling of both Tungsten and electron thermal confinement must be carried out. This topic will be during S. Breton's PhD starting in January 2015 using both QuaLiKiz and a neoclassical transport code within the CRONOS framework, where the radiative losses due to Tungsten are also implemented.

5.3 Heat transport

In the following, experimental reported trends of the heat fluxes are compared to linear and quasilinear gyrokinetic modeling.

5.3.1 Critical temperature gradient

The turbulence onsets above some critical gradients. Such gradients have been derived theoretically. In particular the ion temperature gradient was formulated in the fluid limit accounting for resonant mechanisms in [224, 225] for the ITG case. For the ETG case, a fit based on gyrokinetic simulations was proposed in [226] leading to similar parametric dependencies:

$$\frac{R}{L_{Te}}|_c = \left(1 + Z_{eff}\frac{T_e}{T_i}\right)\left(1.33 + 1.91\frac{s}{q}\right) \tag{5.3}$$

The impact of T_e/T_i on the critical temperature threshold was presented in chapter 3 and is further discussed in [97]. The impacts of s and q were also introduced in chapter 3 and is further detailed in [125].
Experimentally, evidence supporting the existence of critical gradients has been reported for both electron and ion thermal transport [104, 227, 96, 228, 229]. Experimental evidence of a threshold accompanied by increased turbulence level is reported in [230]. In Tore Supra, the radial profile of this critical gradient is determined from a set of discharges characterized by similar plasma parameters with fast wave powers ranging from 0.75 to 7.4 MW. The dependence of the electron heat flux on the gradient length is found to be offset linearly. The offset term increases linearly with the ratio of the local magnetic shear to the safety factor as illustrated by figure 5.9. The linear fit gives:

$$\frac{R}{L_{Te}}|_c = 5(\pm 1) + 10(\pm 2)\frac{|s|}{q} \tag{5.4}$$

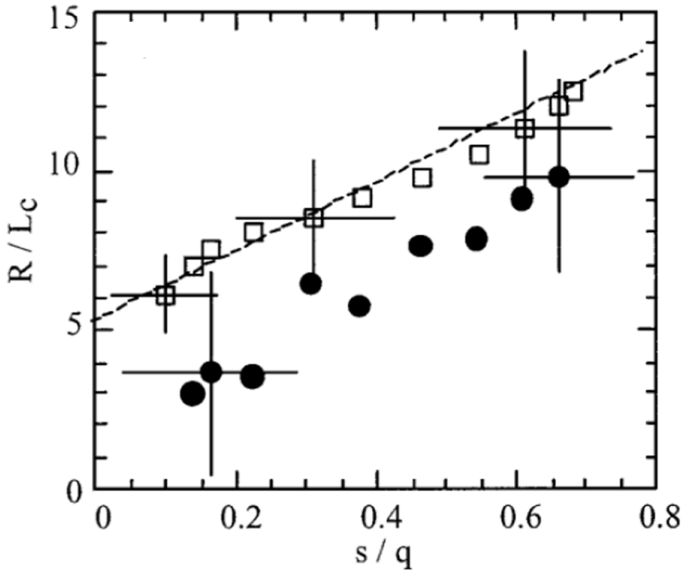

Figure 5.9: Critical electron temperature gradient versus s/q provided by power balance analysis (squares) and gyrokinetic stability analysis (circles). From [104].

which is in agreement with linear gyrokinetic modeling, where dominant unstable TEM were found.
Regarding the ion temperature gradient, the critical value and the stiffness of the ion heat flux above this threshold measured in JET low density L-mode pulses [231] have been shown to be properly modeled by nonlinear gyrokinetic simulations, provided that nonlinear electromagnetic stabilization by suprathermal pressure gradients is included [92]. In this particular case, nonlinear physics plays a key role by enhancing the stabilization due to larger β. QuaLiKiz in its present form (electrostatic and quasilinear) cannot model such electromagnetic nonlinear mechanisms. The linear stabilization due to larger β could be easily implemented. Concerning the non-linear effects, work is ongoing on how to account for such physics within the saturation rule present in the quasilinear framework.

5.3.2 Dimensionless collisionality impact

Dimensionless analysis is of common use in physics [232]. In tokamak plasmas, a set of dimensionless parameters have been identified [233]. The main dependencies of the normalized global confinement time τ_E/τ_B with respect

to dimensionless parameters are expressed by a scaling law of the form :

$$\tau_E/\tau_B \propto \rho^{*\alpha_\rho}\beta^{\alpha_\beta}\nu^{*\alpha_\nu}M^{\alpha_M}q^{\alpha_q}\epsilon^{\alpha_\epsilon}\kappa^{\alpha_\kappa}T_i/{T_e}^{\alpha_T}{Z_{eff}}^{\alpha_Z} \tag{5.5}$$

The energy confinement time τ_E is normalized to the Bohm confinement time, defined by $\tau_B = a^2B/T \propto B^{-1}\rho^{*-2}$, where a is the minor radius. β is the plasma pressure normalized to the magnetic pressure and stands for the electromagnetic effects on confinement. ρ^* is the normalized toroidal Larmor radius. Its impact allow to discriminate among Bohm or gyroBohm scaling of the effective conductivity. Note that a gyroBohm electrostatic collisionless turbulence is such that $\tau_B \propto \rho^{*-3}$. ν^* is the ratio of the collision frequency over the trapped electron bounce frequency. It gives information on the collisionality impact on transport. M is the ratio of average ion mass over the proton mass, q, the cylindrical safety factor, ϵ, the inverse aspect ratio r/R, κ, the plasma elongation, T_i/T_e the ion to electron temperature ratio, Z_{eff} the effective charge of the plasma. In a first step, only three parameters are explored, assuming that the other parameters are kept fixed: ν^*, β and ρ^*. So one can rewrite :

$$B\tau_E \propto \rho^{*\alpha_\rho}\beta^{\alpha_\beta}\nu^{*\alpha_\nu} \tag{5.6}$$

Searching for the global dependencies of the confinement time with respect to these parameters is crucial when projecting present measured confinement times to ITER or reactor scale devices. Experimentally, the effect of collisions is explored following two approaches: multi-machine fits and specific studies on dedicated plasma discharges [234, 235].
The multi-machine fits are made from large databases of plasma discharges on different tokamaks. The first global scaling law (ITER89-P), made from L-mode plasma discharges comprised from six tokamaks, [236], predicts the global scaling :

$$B\tau_E \propto \rho^{*-2.05}\beta^{-0.52}\nu^{*-0.28} \tag{5.7}$$

A more recent ITER scaling law (IPB98-L) on L-mode plasma discharges from 14 tokamaks [237] predicts the global scaling :

$$B\tau_E \propto \rho^{*-1.85}\beta^{-1.41}\nu^{*0.19} \tag{5.8}$$

The ν^* scaling remains weak but is reversed between these two L-mode scaling laws. This could be due to the fact that in the ITER89-P scaling law τ_E was deduced from the total stored energy, i.e. including fast particle energy, whereas in IPB98-L only the thermal energy was considered. Different behaviors are also predicted with respect to ν^* between L and H-mode. Also, depending on the way multi-parameter fits are done, very different collisionality scalings are predicted. For example for H-mode, $B\tau_E$ scales from ν^{*0} to

$\nu^{*-0.3}$ when the errors on power loss are included [238]. This variability of ν^* scaling in global scaling laws is a strong motivation for dedicated experiments. Moreover, the experimental results can be easily compared to local gyrokinetic simulations (i.e. $\rho \ll L$). Indeed for ρ^* scaling investigation, global gyrokinetic codes, where $\rho \simeq L$ is allowed, need to be used.
In this context, well-controlled discharges are performed by varying only one dimensionless parameter, holding the others as constant as possible [234, 235]. The resulting scaling is based on a short list of plasma discharges: the statistical approach is replaced by a more detailed analysis. Such a study on ν^* scaling was made on dedicated TFTR L-mode [239], DIII-D L and H-mode plasma discharges [240]; see [235, 234] for a complete review. In DIII-D experiments, ν^* was varied over a factor 7-8 in 3 points. A global analysis showed that ν^* has almost no effect on L-mode normalized confinement time: $B\tau_E \propto \nu^{*0.08}$. These scalings were obtained by linear fits between $log(B\tau_E)$ and $log(\nu^*)$. On the other hand, more recently, Cordey in [241] pointed out the strong effect of the underlying scaling versus ρ^* and β on the exponent α_ν. Cordey's formula has been extended to multiple point scaling in [242] and will be used for Tore Supra data analysis.
The effect of collisionality has also been identified on particle transport as reported in the previous section.
On the theory side, collisions are believed to have a strong effect on turbulence. In the plasma core, TEM are linearly stabilized by higher collisionality [243, 200]. A competing destabilizing mechanism is observed when nonlinear self-generated zonal flows are linearly damped by collisions in ITG simulations [178]. More recently, this effect has been demonstrated to be very weak in simulations done in presence of kinetic electrons [180, 244]. On the L mode confined edge, Resistive Ballooning Modes are found to be unstable and are destabilized by larger collisionality [70].
In order to elucidate these issues, Tore Supra L-mode plasmas, with no external momentum input, are useful to isolate the core transport characteristics from the pedestal physics with respect to collisions and to compare them to core theoretical predictions performed by gyrokinetic codes. In [121], the dimensionless collisionality ν^* has been varied by a factor 7 ± 2, while keeping β, ρ^*, q, Z_{eff} and T_e/T_i as constant as possible [245, 121]. The confinement time has been carefully defined and the global ν^* scaling accounts for the underlying β and ρ^* scalings. The global analysis is completed by a local transport analysis and by density fluctuation measurements using two types of reflectometers. The experimental results were then compared to linear and nonlinear gyrokinetic simulations.
The magnetic field was varied from 2.4 to 3.9 T across two Ohmic and two ICRF heated discharges at low additional power (< 1 MW), leading to a ν^*

scan of a factor 7 ± 2 in a rather high ν^* range > 0.1. As already proposed by Perkins [239], to minimize the uncertainties due to radiative losses, the confinement time is defined inside a radius where less than 20% of the power is radiated, $r/a = 0.9$ for the type of plasmas studied here. The normalized confinement time scales such that:

$$B\tau_E \propto \nu^{*0.0\pm0.7} \tag{5.9}$$

This scaling is obtained following [241, 242] assuming a GyroBohm scaling accounting for the variability of ρ^* within its 7% error bars, no β dependency, uncertainties on the absorbed power within 10% and on the thermal energy within 20%. The present analysis pointed out the need for accounting for the underlying ρ^* and β scalings [241]. Indeed, if no ρ^* dependence would have been assumed, one would have found $\alpha_\nu = -0.3 \pm 0.2$ as suggested by a traditional fit of $B\tau_E$ versus ν^*. In the subset of the 2 Ohmic discharges, where both Z_{eff} and T_e/T_i agree well, and where ν^* is scanned over a factor 2.0 ± 0.6, the following scaling law is obtained:

$$B\tau_E \propto \nu^{*-0.9\pm0.6} \tag{5.10}$$

This subset allows to conclude that the global confinement tendency is rather a decrease of $B\tau_E$ with higher ν^*.

The local transport analysis is restricted to radii inside which at least 80% of the power is absorbed, to limit the effect of unknown uncertainties due to the modeling of the power absorption. In the discharges studied here, this limits the local transport analysis to $r/a > 0.6$. As for the global analysis, to avoid uncertainties due to radiative losses, the radial zone is restricted to radii below which less than 20% of the power is radiated, in this scan $r/a < 0.9$. Unfortunately, for the four discharges analyzed here, the T_i profile measurement was not available at radii above $r/a = 0.6$. Hence the local transport analysis is restricted to a single radial location, around $r/a = 0.6$. At this location no variation of χ_{eff}/χ_B with higher ν^* is observed.

The limitations of both the global and local transport analyses call for additional means to shed more light on the turbulence properties in such a scan. In this scan, the turbulence was measured by 2 types of reflectometers: the fast-sweeping and the Doppler reflectometers, measuring respectively k_r and k_θ spectra. For $r/a < 0.7$, no effect on the density fluctuations outside error bars is observed. At $r/a > 0.7$, for the Ohmic pair of discharges where Z_{eff} and T_e/T_i are well matched, no variation outside the error bars is observed, apart for the lowest k_θ measured, where the fluctuation level increases with higher ν^*.

The linear gyrokinetic analysis done by QuaLiKiz shows that the Z_{eff} mismatches (from 1.6 to 2.3) affect the growth rates in a consistent manner.

This is not the case for the T_e/T_i or q mismatches which have a small impact on the gyrokinetic linear results. Qualitatively the stabilizing effect of Z_{eff} is coherent with the decrease of the density fluctuation level observed for $r/a > 0.7$ between the Ohmic and ICRH discharges. The linear gyrokinetic code was also used to study the effect of collisions on the modes. The dominant mode is found to rotate in the ion drift direction (ITG type). To obtain a mode rotating in the electron drift direction (TEM type) ν^* needs to be divided by 40 compared to the lowest experimental value. Nevertheless, part of the turbulence is carried by the trapped electrons since a ν^* increase in the experimental range leads to a decrease of the growth rate as expected by the detrapping effect. This is confirmed by nonlinear gyrokinetic simulations done with the code GYRO. The destabilizing impact of collisions through zonal flows damping is negligible despite rather high values of ν^*. Hence, a quasilinear modeling of the collisionality impact would capture the observed trend.
To conclude, the global confinement dependence versus ν^*, $B\tau_E \propto \nu^{*0.0\pm0.7}$, is consistent with both ITER L-mode scaling laws [236, 237] and with previous L-mode dedicated scaling experiments [235]. The weak impact of collisionality on global confinement is confirmed by both local transport analysis and density fluctuation measurements. Indeed, for $r/a < 0.7$, density fluctuation levels and k_r spectra are not affected by ν^*. GYRO nonlinear simulations reproduce these observations. Nevertheless, at outer radii, $r/a > 0.7$, k_θ spectra measured by the Doppler reflectometer show an increase of the fluctuation level with higher ν^* at the lowest measured k_θ only. This observation is in qualitative agreement with the global scaling extracted from the subset of 2 Ohmic discharges $B\tau_E \propto \nu^{*-0.9\pm0.6}$. Similar Doppler reflectometer observations have been confirmed in another set of ν^* scans reported in [19]. The dispersion relation and the k spectrum modifications by ν^* case are presently challenging ITG-TEM turbulence models [19].

5.3.3 Heat flux in a time evolving framework

The ITG-TEM gyrokinetic models have been successfully compared to measured temperature threshold dependence with respect to s and q. The weak impact of collisionality on the energy confinement is also consistent with gyrokinetic modeling for $r/a \leq 0.7$. Based on these successes, QuaLiKiz can be used inside CRONOS to predict temperature profiles. However, QuaLiKiz is expected to be inadequate for regimes where fast particle and electromagnetic contributions are significant. To test this, during Benedetta Baiocchi's post-doc, QuaLiKiz in CRONOS was run on four JET pulses: two baseline H modes and two hybrid H-modes [48]. For the two baseline H-modes, Qua-

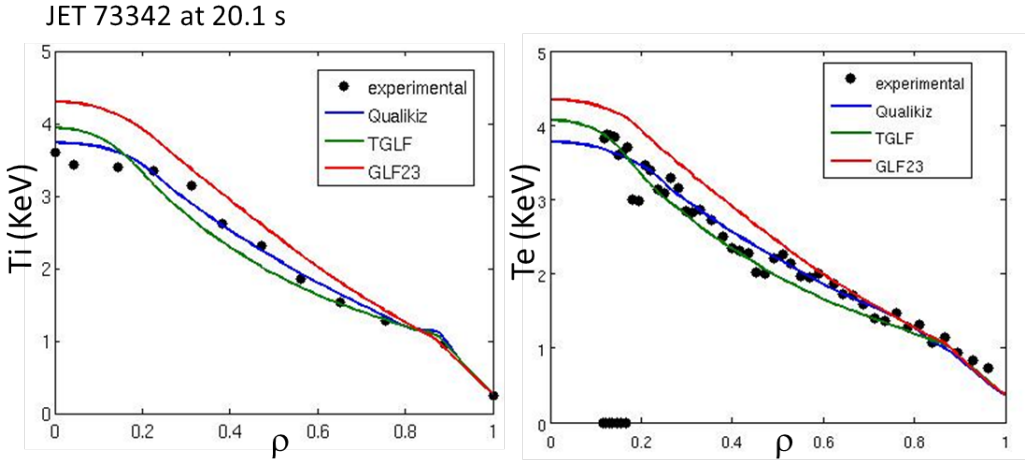

Figure 5.10: Left panel: ion temperature. Charge exchange measurements (black points). Right panel: electron temperature. High resolution Thomson scattering measurements (black points). The measured profiles are compared to various quasilinear models predicted profiles for $0.1 \leq r/a \leq 0.8$: QuaLiKiz in blue, TGLF in green and GLF23 in red. From [48].

LiKiz inside CRONOS predicts very well the ion and electron temperature profiles as illustrated by figure 5.10. It is to note that this is expected since the heat transport is so called "stiff", therefore is the threshold is correctly predicted the resulting predicted temperature profile is expected to be correct as well. The hybrid H-modes modeling performed more poorly, likely due to the role of fast particles on the β impact being larger, and not taken into account in QuaLiKiz. Furthermore, the version of QuaLiKiz presently implemented does not include the rotation and $E \times B$ effects whereas they are implemented in the standalone version. The validation of QuaLiKiz momentum flux results versus experimental observation is reported in the next section.

5.4 Angular momentum transport

To determine experimentally the momentum convective term, modulations of the momentum sources are necessary. Such experiments have been carried out in JET H-mode pulses, where the momentum source was modulated by modulating the Neutral Beam Injection [246]. To examine evidence for presence of a momentum pinch, the amplitude and phase of the modulated toroidal velocity was simulated. It was demonstrated that both the ampli-

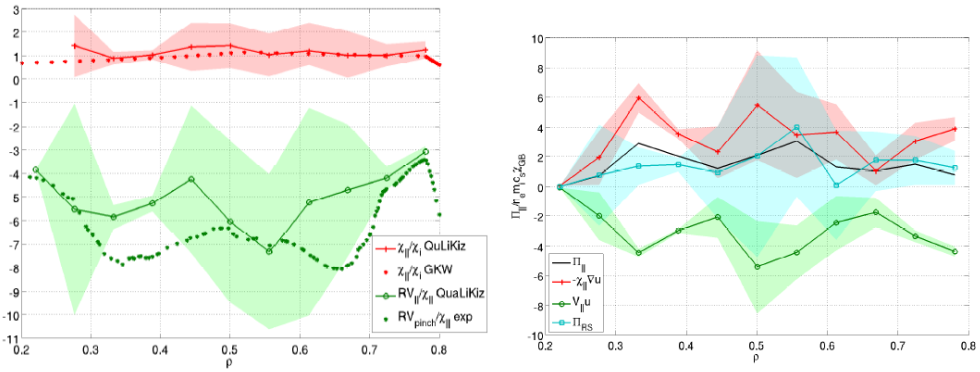

Figure 5.11: Left panel: Prandtl number (red crosses) and pinch number (green circles) calculated by a 3-point method. Right panel: Details of the different contributions to the parallel momentum flux. From [42].

tude and phase of the modulated toroidal velocity from the experiment are best reproduced when a momentum pinch is taken into account. In this analysis, the residual stress contribution was neglected. During Pierre Cottier's PhD, this JET pulse was analyzed by QuaLiKiz with the aim of comparing its predictions to the experimentally reported Prandtl and pinch numbers [42]. QuaLiKiz separation of the various momentum contributors is performed as explained in chapter 2. The various contributions are illustrated by figure 5.11. The resulting Prandtl and pinch numbers are given on the left panel of figure 5.11. The colored areas on the left panel correspond to the uncertainties linked to the linearization performed to extract these numbers. They are calculated by performing 5 simulations with different modifications of the velocity. The estimated Prandtl number lies within 0.8 and 1.4, close to GKW predictions used in [246]. The pinch number calculated with QuaLiKiz ranges from 3 to 7, in good agreement with the experimental values ranging from 3 to 8. As detailed on the right panel of figure 5.11, the residual stress is not a negligible contribution. However a definitive conclusion would require smaller error bars. Moreover some significant contributions to the residual stress reviewed in [83] are not taken into account in local models such as QuaLiKiz.

5.5 Summary

The quasi-linear gyrokinetic fluxes computed by QuaLiKiz have been compared extensively to experimental measurements in both stand alone and time evolving fashions. The medium Z impurities transport is correctly mod-

eled, the existence of a critical temperature gradient observed for Nickel on Tore Supra was successfully reproduced. The pinch contribution to the angular momentum flux observed on JET was reproduced by QuaLiKiz as well, the residual stress contribution was shown to be non-negligible. When integrated in the transport code CRONOS, QuaLiKiz allowed to predict temperature and density profiles. The particle transport, unlike the heat transport, is not stiff due to large inward and outward convection terms. The fact that QuaLiKiz in CRONOS could reproduce fairly well a slow hollow density profile evolution from JET is therefore a success. Further work has to be carried out now using more extensively QuaLiKiz in various transport codes (CRONOS, TRANSP, JETTO, etc), as it is done for TGLF. At first to test further the predictions against experimental measured profiles, then to work more intensively on future ITER scenarios.

Chapter 6

Concluding summary

The gyrokinetic quasilinear approach has been shown to be adequate for the core of tokamak plasmas because (1) the turbulence level is relatively low (typically from 1 to 10%) and (2) the particles are not trapped in the saturated fluctuating potential. Therefore the linear gyrokinetic response can be used to predict turbulent fluxes. The saturated level has to be built using the mixing length rule and non-linear simulation results on the k and frequency spectra. This operation is very delicate, and in some cases, such as at low magnetic shear, ad hoc modifications have to be performed. It is thought to be due to non-linear saturation mechanisms such as zonal flows or interplay with damped modes. The quasilinear fluxes resulting of the product of the linear gyrokinetic response with the constructed saturated potential are then compared to more complete non-linear gyrokinetic predictions given by GS2, GENE, GYRO or GKW. Over a wide range of relevant core parameters, the gyrokinetic quasilinear heat, particle and momentum fluxes computed by QuaLiKiz agree reasonably well with non-linear results. The computed fluxes by QuaLiKiz require roughly 1 million time less CPU time. This rapidity allows for intensive comparison with experimental observations. In particular, the convection mechanisms of particle (electron and impurities) and angular momentum have been successfully compared to dedicated experiments. QuaLiKiz predicted fluxes have been implemented in the transport code CRONOS, and the slow evolution of a JET hollow density profile has been reproduced. Nonetheless numerous open issues remain to be tackled:

- A finite β due to a large contribution of fast particles has been shown to modify significantly the ion heat flux stiffness. This can be modeled successfully only when accounting for presently not well understood nonlinear physics.

- For the momentum flux, the residual stress due to $E \times B$ is properly

modeled, but it is shown to be of the same order as nonlocal effects [183], which are not included in QuaLiKiz.

- A more self-consistent renormalized quasilinear theory is needed to avoid using ad hoc coefficients in constructing the saturated potential, as it is presently unfortunately the case for low magnetic shear.

- The deep core is typically found linearly stable, whereas finite fluxes above the neoclassical ones are measured. The physical mechanisms at play behind the deep core turbulent transport need to be investigated with non-linear flux driven global approaches. The insight gained could then be implemented in a simplified approach such as QuaLiKiz.

- Above $r/a = 0.8$ or in some cases even as low as $r/a = 0.6$, nonlinear and quasilinear modeling is found to underestimate the fluxes and the fluctuation levels. This issue is actively investigated at the moment. For prediction, in particular for ITER, it is essential to be able to model the plasma up to the last closed flux surface, which is not the case presently.

- The use of QuaLiKiz implemented in CRONOS and in other transport platforms has to be promoted. Indeed more extensive comparison of simultaneousy predicted time evolution of temperature, density, rotation with measured profiles will allow to explore further the strengths and limits of such codes.

- Most plasmas are shaped with elongation κ well above 1 whereas QuaLiKiz uses the $s - \alpha$ circular concentric magnetic surfaces equilibrium. A way of relaxing this constrain without slowing down the code has to be found.

To tackle these issues, two main axes are presently actively followed:

- From the list above, it is evident that QuaLiKiz must be further sped up while simultaneously incorporating more physics (electromagntic effects, more general equilibrium, etc). Recent optimization of the present QuaLiKiz version has allowed to gain an additional factor 20 in terms of CPU time reaching simulations now roughly a factor 1 million faster than non-linear gyrokinetic codes. The optimization was motivated by the use of novel proposed analytical functions and open source modules [36], as well as further optimization of the eigenvalue solver algorithm [35]. This addresses the rapidity aspect but does not take into account additional physics. Therefore in parallel, a new project

has been launched. The idea to to use optimized regression techniques, such as neural networks, on a large database of linear and nonlinear gyrokinetic runs performed by GENE, GKW, GS2 and GYRO. Indeed, the amount of CPU available nowadays allows for the construction of an extensive international database. The biggest challenge is in the robustness of an efficient regression technique in producing the correct trends in a parameter space of at least 9 dimensions: R/L_{Te}, R/L_{Ti}, R/L_n, q, s, β, T_e/T_i, Z_{eff}, κ. Very recently, a proof of principle based of 5 dimensions QuaLiKiz dataset has been shown to produce correct results in a much shorter time than QuaLiKiz (S. Breton's M.Sc. project [35]). Such perspective of an extremely fast turbulent transport code is also very interesting in the real time control framework.

- The other important axis is the understanding of the mechanisms responsible for the exponential increase of turbulence levels in L-mode pulses when going towards the last closed flux surface. For $r/a \geq 0.95$ linearly Resistive Ballooning Modes are found unstable [70]. The presence of resistive modes is shown to be coherent with the impact of Z_{eff} on the L-H power threshold [247]. This is an encouraging experimental hint on the validity of this hypothesis. Furthermore, when combined with $E \times B$ stabilization, RBM are shown to reproduce a number of parametric dependencies of the L to H mode temperature threshold [248]. Nevertheless, modeling work of an eventual inward spreading of these modes has not yet been carried out. This would require a vast amount of CPU hours for computation in the gyrokinetic framework. Some theoretical work on this topic has been done by [36]. The flux driven gyrokinetic code GYSELA is exploring the beach effect coming from core turbulence based on realistic Tore Supra L-mode parameters [249]. In parallel, fluid flux-driven approaches including RBM and a neoclassical radial electric field has successfully led to the modeling of an L to H like transition [250].

Bibliography

[1] D Clery. A piece of the sun. *Gerald Duckworth & Co Ltd*, 2013.

[2] *http://fire.pppl.gov/*.

[3] J. Jacquinot. Fifty years in fusion and the way forward. *Nuclear Fusion*, 50(1):014001, January 2010.

[4] B. B. Kadomtsev, M. N. Rosenbluth, and W. B. Thompson. Plasma physics: Lectures presented at the seminar on plasma physics organized by and held at the international centre for theoretical physics, trieste, october 1964. *International Atomic Energy Agency: Vienna*, 1965.

[5] R Sagdeev. The making of a soviet scientist: My adventures in nuclear fusion and space from stalin to star wars. *John Wiley & Sons*, 1994.

[6] Interview with dr. marshall rosenbluth. *American Institute of Physics*, 2003.

[7] John Wesson. Tokamaks (second edition). *Oxford Engineering Science Series, Clarendon Press*, (ISBN 0-19-856293-4), 1997.

[8] E.J. Doyle (Chair Transport Physics), W.A. Houlberg (Chair Confinement Database, Modelling), Y. Kamada (Chair Pedestal, Edge), V. Mukhovatov (co Chair Transport Physics), T.H. Osborne (co Chair Pedestal, Edge), A. Polevoi (co Chair Confinement Database, Modelling), G. Bateman, J.W. Connor, J.G. Cordey (retired), T. Fujita, X. Garbet, T.S. Hahm, L.D. Horton, A.E. Hubbard, F. Imbeaux, F. Jenko, J.E. Kinsey, Y. Kishimoto, J. Li, T.C. Luce, Y. Martin, M. Ossipenko, V. Parail, A. Peeters, T.L. Rhodes, J.E. Rice, C.M. Roach, V. Rozhansky, F. Ryter, G. Saibene, R. Sartori, A.C.C. Sips, J.A. Snipes, M. Sugihara, E.J. Synakowski, H. Takenaga, T. Takizuka, K. Thomsen, M.R. Wade, H.R. Wilson, ITPA Transport Physics Topical Group, ITPA Confinement Database, Modelling Topical Group,

ITPA Pedestal, and Edge Topical Group. Chapter 2: Plasma confinement and transport. *Nuclear Fusion*, 47(6):S18, 2007.

[9] B.B. Kadomtsev. Plasma turbulence. *Academic Press, London, New-York*, 1965.

[10] Y. Sarazin. Turbulence and transport. *Formation aux Sciences de la Fusion, Master 2 : Physique et Sciences de la Matière, Spécialité : Sciences de la Fusion, Parcours : Fusion par Confinement Magnétique*, 2013.

[11] Dwight R. Nicholson. Introduction to plasma theory. *John Wiley & Sons Inc.*, (ISBN 0-471-09045-X), 1983.

[12] M. Beer. Gyrofluid models of turbulent transport in tokamaks. *Ph. D. Thesis, Princeton University*, 1994.

[13] A. Casati. A quasi-linear gyrokinetic transport model for tokamak plasmas. *PhD thesis, Université de Provence, Aix-Marseille I*, 2009.

[14] P. Cottier. Modélisation du transport turbulent de moment angulaire dans les plasmas de tokamak. *PhD thesis,Graduate School, Ecole Polytechnique*, 2013.

[15] A. Hirose. Lecture notes on plasma waves, http://physics.usask.ca/ hirose/p862/notes.htm.

[16] A. Schekochihin. *http://www-thphys.physics.ox.ac.uk/people/AlexanderSchekochihin/notes/*

[17] E Mazzucato, S H Batha, M Beer, M Bell, R E Bell, R V Budny, C Bush, T S Hahm, G W Hammet, F M Levinton, R Nazikian, H Park, G Rewoldt, G L Schmidt, E J Synakowski, W M Tang, G Taylor, and M C Zarnstorff. Turbulent fluctuations in TFTR configurations with reversed magnetic shear. *Phys. Rev. Lett.*, 77:3145–3148, 1996.

[18] L. Schmitz, A. E. White, G. Wang, J. C. DeBoo, J. S. deGrassie, G. R. McKee, J. C. Hillesheim, W. A. Peebles, T. L. Rhodes, T. A. Carter, E. D. Doyle, L. Zeng, K. H. Burrell, C. C. Petty, J. Kinsey, W. A. Solomon, G. M. Staebler, and Diii-D. Team. Observation of reduced core electron temperature fluctuations and intermediate wavenumber density fluctuations in h-mode plasmas. *Nuclear Fusion*, 49(9), 2009.

[19] L. Vermare, P. Hennequin, Oe D. Guercan, C. Bourdelle, F. Clairet, X. Garbet, R. Sabot, and Team Tore Supra. Impact of collisionality

on fluctuation characteristics of micro-turbulence. *Physics of Plasmas*, 18(1), 2011.

[20] R. Sabot. La réflectométrie : un diagnostic pour l'étude du transport et des fluctuations de densité dans les plasmas de fusion magnétique. *Thése d'habilitation à diriger des recherches, Université de Provence Aix-Marseille I*, 2011.

[21] M. Kotschenreuther, W. Dorland, M. A. Beer, and G. W. Hammett. Quantitative predictions of tokamak energy confinement from first principles simulations with kinetic effects. *Physics of Plasmas (1994-present)*, 2(6):2381–2389, 1995.

[22] F. Jenko. *Computer Physics Communications*, 125(1-3):196–209, 2000.

[23] J. Candy and R.E. Waltz. An eulerian gyrokinetic-maxwell solver. *Journal of Computational Physics*, 186(2):545 – 581, 2003.

[24] V. Grandgirard, M. Brunetti, P. Bertrand, N. Besse, X. Garbet, P. Ghendrih, G. Manfredi, Y. Sarazin, O. Sauter, E. SonnendrÃijcker, J. Vaclavik, and L. Villard. A drift-kinetic semi-lagrangian 4d code for ion turbulence simulation. *Journal of Computational Physics*, 217(2):395 – 423, 2006.

[25] A. E. White, L. Schmitz, G. R. McKee, C. Holland, W. A. Peebles, T. A. Carter, M. W. Shafer, M. E. Austin, K. H. Burrell, J. Candy, J. C. DeBoo, E. J. Doyle, M. A. Makowski, R. Prater, T. L. Rhodes, G. M. Staebler, G. R. Tynan, R. E. Waltz, and G. Wang. Measurements of core electron temperature and density fluctuations in diii-d and comparison to nonlinear gyrokinetic simulations. *Physics of Plasmas*, 15(5), 2008.

[26] A. E. White, W. A. Peebles, T. L. Rhodes, C. H. Holland, G. Wang, L. Schmitz, T. A. Carter, J. C. Hillesheim, E. J. Doyle, L. Zeng, G. R. McKee, G. M. Staebler, R. E. Waltz, J. C. DeBoo, C. C. Petty, and K. H. Burrell. Measurements of the cross-phase angle between density and electron temperature fluctuations and comparison with gyrokinetic simulations. *Physics of Plasmas*, 17(5), 2010.

[27] C. Holland, L. Schmitz, T. L. Rhodes, W. A. Peebles, J. C. Hillesheim, G. Wang, L. Zeng, E. J. Doyle, S. P. Smith, R. Prater, K. H. Burrell, J. Candy, R. E. Waltz, J. E. Kinsey, G. M. Staebler, J. C. DeBoo, C. C. Petty, G. R. McKee, Z. Yan, and A. E. White. Advances in validating

gyrokinetic turbulence models against l- and h-mode plasmas. *Physics of Plasmas*, 18(5), 2011.

[28] C. Bourdelle, X. Garbet, G.T. Hoang, J. Ongena, and R.V. Budny. *Nuclear Fusion*, 42(7):892, 2002.

[29] A. G. Peeters and D. Strintzi. The effect of a uniform radial electric field on the toroidal ion temperature gradient mode. *Physics of Plasmas*, 11(8):3748–3751, 2004.

[30] Mike Kotschenreuther, G. Rewoldt, and W.M. Tang. Comparison of initial value and eigenvalue codes for kinetic toroidal plasma instabilities. *Computer Physics Communications*, 88(2-3):128–140, 1995.

[31] C. Angioni. Theoretical and experimental research on particle and impurity transport in the core of tokamak plasmas. *Thèse d'habilitation à diriger des recherches, Université de Provence, Aix-Marseille I*, 2010.

[32] C. Bourdelle, X. Garbet, F. Imbeaux, A. Casati, N. Dubuit, R. Guirlet, and T. Parisot. A new gyrokinetic quasilinear transport model applied to particle transport in tokamak plasmas. *Physics of Plasmas*, 14(11), 2007.

[33] A. Casati, C. Bourdelle, X. Garbet, F. Imbeaux, J. Candy, F. Clairet, G. Dif-Pradalier, G. Falchetto, T. Gerbaud, V. Grandgirard, Oe D. Guercan, P. Hennequin, J. Kinsey, M. Ottaviani, R. Sabot, Y. Sarazin, L. Vermare, and R. E. Waltz. Validating a quasi-linear transport model versus nonlinear simulations. *Nuclear Fusion*, 49(8), 2009.

[34] J. Citrin, C. Bourdelle, P. Cottier, D. F. Escande, Oe D. Guercan, D. R. Hatch, G. M. D. Hogeweij, F. Jenko, and M. J. Pueschel. Quasilinear transport modelling at low magnetic shear. *Physics of Plasmas*, 19(6), JUN 2012.

[35] C. Bourdelle et al J. Citrin. *ITPA Transport and Confinement, October 2014, Cadarache*, 2014.

[36] Ö. D. Gürcan. Numerical computation of the modified plasma dispersion function with curvature. *Journal of Computational Physics*, 269(0):156 – 167, 2014.

[37] J. Citrin. Turbulent transport in tokamaks advanced scenarios. *Ph. D. Thesis, Eindhoven University of Technology, the Netherlands*, 2012.

[38] T. Dannert and F. Jenko. Gyrokinetic simulation of collisionless trapped-electron mode turbulence. *Physics of Plasmas*, 12(7):072309, 2005.

[39] Y. Lin, J. Rice, S. Wukitch, M. Greenwald, a. Hubbard, a. Ince-Cushman, L. Lin, M. Porkolab, M. Reinke, and N. Tsujii. Observation of Ion-Cyclotron-Frequency Mode-Conversion Flow Drive in Tokamak Plasmas. *Physical Review Letters*, 101(23):235002, December 2008.

[40] J. E. Kinsey, G. M. Staebler, and R. E. Waltz. The first transport code simulations using the trapped gyro-landau-fluid model. *Physics of Plasmas (1994-present)*, 15(5), 2008.

[41] H. Weisen, Y. Camenen, A. Salmi, T. W. Versloot, P. C. de Vries, M. Maslov, T. Tala, M. Beurskens, C. Giroud, and JET-EFDA Contributors. Identification of the ubiquitous Coriolis momentum pinch in JET tokamak plasmas. *NUCLEAR FUSION*, 52(4), APR 2012.

[42] P Cottier, C Bourdelle, Y Camenen, Ö D Gürcan, F J Casson, X Garbet, P Hennequin, and T Tala. Angular momentum transport modeling: achievements of a gyrokinetic quasi-linear approach. *Plasma Physics and Controlled Fusion*, 56(1):015011, 2014.

[43] C. Angioni and A. G. Peeters. Direction of impurity pinch and auxiliary heating in tokamak plasmas. *Phys. Rev. Lett.*, 96:095003, Mar 2006.

[44] D. Villegas, R. Guirlet, C. Bourdelle, G. T. Hoang, X. Garbet, and R. Sabot. Experimental electron temperature gradient dependence of heavy impurity transport in fusion devices. *Physical Review Letters*, 105(3), 2010.

[45] W. L. Zhong, X. L. Zou, C. Bourdelle, S. D. Song, J. F. Artaud, T. Aniel, and X. R. Duan. Convective Velocity Reversal Caused by Turbulence Transition in Tokamak Plasma. *Physical Review Letters*, 111(26):265001, December 2013.

[46] J. F. Artaud, V. Basiuk, F. Imbeaux, M. Schneider, J. Garcia, G. Giruzzi, P. Huynh, T. Aniel, F. Albajar, J. M. Ane, A. Becoulet, C. Bourdelle, A. Casati, L. Colas, J. Decker, R. Dumont, L. G. Eriksson, X. Garbet, R. Guirlet, P. Hertout, G. T. Hoang, W. Houlberg, G. Huysmans, E. Joffrin, S. H. Kim, F. Koechl, J. Lister, X. Litaudon, P. Maget, R. Masset, B. Pegourie, Y. Peysson, P. Thomas, E. Tsitroneand, and F. Turco. The cronos suite of codes for integrated tokamak modelling. *Nuclear Fusion*, 50(4), 2010.

[47] A. Loarte, M.J. Leyland, J.A. Mier, M.N.A. Beurskens, I. Nunes, V. Parail, P.J. Lomas, G.R. Saibene, R.I.A. Sartori, L. Frassinetti, and JET EFDA Contributors. Plasma density and temperature evolution following the h-mode transition at jet and implications for iter. *Nuclear Fusion*, 53(8):083031, 2013.

[48] Baiocchi B., Garcia J., Beurkens M., Bourdelle C., F. Crisanti, C. Giroud, J. Hobirk, F. Imbeaux, I. Nunes, EU-ITM ITER Scenario Modelling group, and JET EFDA contributors. Turbulent transport analysis of jet h-mode and hybrid plasmas using qualikiz and tglf. *Submitted to plasma physics and controlled fusion*, 2015.

[49] Baiocchi B., Bourdelle C., Angioni C., Imbeaux F., Loarte A., Maslov M., and JET EFDA contributors. Transport analysis and modelling of the evolution of hollow density profiles plasmas in jet and implication for iter. *Submitted to plasma physics and controlled fusion*, 2015.

[50] A. Samain. Dynamic stabilization of a confined plasma. *Nuclear Fusion*, 10(3):325, 1970.

[51] X. Garbet. Instabilités, turbulence et transport dans un plasma magnétisé. *Thèse d'habilitation à diriger des recherches, Université de Provence, Aix-Marseille I*, 2001.

[52] J. W. Connor, R. J. Hastie, and J. B. Taylor. High mode number stability of an axisymmetric toroidal plasma. *Proceedings of the Royal Society of London. A. Mathematical and Physical Sciences*, 365(1720):1–17, 1979.

[53] V.I. Arnold. Mathematical methods of classical mechanics. *Springer Verlag, New York*, 1978.

[54] X. Garbet, J. Abiteboul, E. Trier, O. Gurcan, Y. Sarazin, A. Smolyakov, S. Allfrey, C. Bourdelle, C. Fenzi, V. Grandgirard, P. Ghendrih, and P. Hennequin. Entropy production rate in tokamaks with nonaxisymmetric magnetic fields. *Physics of Plasmas*, 17(7), 2010.

[55] P. Helander and D. J. Sigmar. Collisional transport in magnetized plasmas. *Cambridge University Press, Cambridge, UK*, 2002.

[56] MD Kruskal. Rendiconti del terzo congresso internazionale sui fenomeni d'ionizzazione nei gas. *Societa Italiani di Fisica, Milan*, 1957.

[57] R. D. Hazeltine and J. D. Meiss. Plasma confinement. *Addison-Wesley, Redwood City*, 1992.

[58] J. W. Connor, R. J. Hastie, and J. B. Taylor. Shear, periodicity, and plasma ballooning modes. *Phys. Rev. Lett.*, 40:396–399, Feb 1978.

[59] X. Lapillonne, S. Brunner, T. Dannert, S. Jolliet, A. Marinoni, L. Villard, T. Goerler, F. Jenko, and F. Merz. Clarifications to the limitations of the s-alpha equilibrium model for gyrokinetic computations of turbulence. *Physics of Plasmas*, 16(3), 2009.

[60] C Bourdelle, W Dorland, X Garbet, GW Hammett, M Kotschenreuther, G Rewoldt, and EJ Synakowski. Stabilizing impact of high gradient of beta on microturbulence. *Physics of Plasmas*, 10(7):2881–2887, JUL 2003.

[61] Thomas M. Antonsen and Barton Lane. Kinetic equations for low frequency instabilities in inhomogeneous plasmas. *Physics of Fluids (1958-1988)*, 23(6):1205–1214, 1980.

[62] T. S. Hahm. Nonlinear gyrokinetic equations for tokamak microturbulence. *Physics of Fluids*, 31(9), 1988.

[63] A. J. Brizard and T. S. Hahm. Foundations of nonlinear gyrokinetic theory. *Review of Modern Physics*, 79(2), 2007.

[64] J. Abiteboul. Transport turbulent et néoclassique de quantité de mouvement toroïdale dans les plasmas de tokamak. *PhD thesis*, 2012.

[65] Y Sarazin, a Strugarek, G Dif-Pradalier, J Abiteboul, S Allfrey, X Garbet, Ph Ghendrih, V Grandgirard, and G Latu. Flux-driven gyrokinetic simulations of ion turbulent transport at low magnetic shear. *Journal of Physics: Conference Series*, 260:012017, November 2010.

[66] Y. Idomura, S. Tokuda, and Y. Kishimoto. Global profile effects and structure formations in toroidal electron temperature gradient driven turbulence. *Nuclear Fusion*, 45(12):1571–1581, 2005.

[67] M.N. Rosenbluth and N. Rostoker. Int. conf. peaceful uses atomic energy. *Proc. 2nd Int. Conf.*, 12:152, 1959.

[68] X. Garbet et al. *Journal of computational physics*, 87:249, 1990.

[69] C. Nguyen, X. Garbet, and A. I. Smolyakov. Variational derivation of the dispersion relation of kinetic coherent modes in the acoustic frequency range in tokamaks. *Physics of Plasmas*, 15(11):112502, 2008.

[70] C Bourdelle, X Garbet, R Singh, and L Schmitz. *Plasma Physics and Controlled Fusion*, 54(11):115003, 2012.

[71] M.N. Rosenbluth J. Candy, R. Waltz. *Physics of Plasmas*, 11(5):1879, 2004.

[72] P. Beyer. Turbulence et transport dans les plasmas chauds magnétisés. *Thèse d'habilitation à diriger des recherches, Université de Provence Aix-Marseille I*, 2004.

[73] F. Zonca, P. Buratti, A. Cardinali, L. Chen, J.-Q. Dong, Y.-X. Long, A.V. Milovanov, F. Romanelli, P. Smeulders, L. Wang, Z.-T. Wang, C. Castaldo, R. Cesario, E. Giovannozzi, M. Marinucci, and V. Pericoli Ridolfini. Electron fishbones: theory and experimental evidence. *Nuclear Fusion*, 47(11):1588, 2007.

[74] Abramowitz and Stegun. Handbook of mathematical functions. *Dover*.

[75] G Depret, X Garbet, P Bertrand, and A Ghizzo. Trapped-ion driven turbulence in tokamak plasmas. *Plasma Physics and Controlled Fusion*, 42(9):949, 2000.

[76] M. Romanelli, G. T. Hoang, C. Bourdelle, C. Gormezano, E. Giovannozzi, M. Leigheb, M. Marinucci, D. Marocco, C. Mazzotta, L. Panaccione, V. Pericoli, G. Regnoli, O. Tudisco, and F. T. U. Team. Parametric dependence of turbulent particle transport in high density electron heated ftu plasmas. *Plasma Physics and Controlled Fusion*, 49(6):935–946, 2007.

[77] G. Rewoldt, W. M. Tang, and M. S. Chance. Electromagnetic kinetic toroidal eigenmodes for general magnetohydrodynamic equilibria. *Physics of Fluids (1958-1988)*, 25(3):480–490, 1982.

[78] M. N. Rosenbluth, R. D. Hazeltine, and F. L. Hinton. Plasma transport in toroidal confinement systems. *Physics of Fluids*, 15(1):116–140, 1972.

[79] F. Romanelli. Ion temperature gradient driven modes and anomalous ion transport in tokamaks. *Physics of Fluids B: Plasma Physics (1989-1993)*, 1(5):1018–1025, 1989.

[80] C. Bourdelle. Analyse de stabilité de plasmas de tokamak. *PhD thesis, Université Joseph Fourier, Grenoble I*, 2000.

[81] J. Q. Dong and W. Horton. Kinetic quasitoroidal ion temperature gradient instability in the presence of sheared flows. *Physics of Fluids B: Plasma Physics (1989-1993)*, 5(5):1581–1592, 1993.

[82] X. Garbet, Y. Sarazin, P. Ghendrih, S. Benkadda, P. Beyer, C. Figarella, and I. Voitsekhovitch. Turbulence simulations of transport barriers with toroidal velocity. *Physics of Plasmas (1994-present)*, 9(9):3893–3905, 2002.

[83] A.G. Peeters, C. Angioni, A. Bortolon, Y. Camenen, F.J. Casson, B. Duval, L. Fiederspiel, W.A. Hornsby, Y. Idomura, T. Hein, N. Kluy, P. Mantica, F.I. Parra, A.P. Snodin, G. Szepesi, D. Strintzi, T. Tala, G. Tardini, P. de Vries, and J. Weiland. Overview of toroidal momentum transport. *Nuclear Fusion*, 51(9):094027, September 2011.

[84] A. G. Peeters, Y. Camenen, F. J. Casson, W. A. Hornsby, A. P. Snodin, D. Strintzi, and G. Szepesi. The nonlinear gyro-kinetic flux tube code GKW. *Computer Physics Communications*, 180(12):2650–2672, 2009.

[85] S. Brunner, M. Fivaz, T. M. Tran, and J. Vaclavik. Global approach to the spectral problem of microinstabilities in tokamak plasmas using a gyrokinetic model. *Physics of Plasmas (1994-present)*, 5(11):3929–3949, 1998.

[86] F. J. Casson, a. G. Peeters, Y. Camenen, W. a. Hornsby, a. P. Snodin, D. Strintzi, and G. Szepesi. Anomalous parallel momentum transport due to $E \times B$ flow shear in a tokamak plasma. *Physics of Plasmas*, 16(9):092303, 2009.

[87] P.C. de Vries, M.-D. Hua, D.C. McDonald, C. Giroud, M. Janvier, M.F. Johnson, T. Tala, K.-D. Zastrow, and JET EFDA Contributors. Scaling of rotation and momentum confinement in jet plasmas. *Nuclear Fusion*, 48(6):065006, 2008.

[88] A. G. Peeters and C. Angioni. Linear gyrokinetic calculations of toroidal momentum transport in a tokamak due to the ion temperature gradient mode. *Physics of Plasmas*, 12(7):072515, 2005.

[89] R. E. Waltz, R. L. Dewar, and X. Garbet. Theory and simulation of rotational shear stabilization of turbulence. *Physics of Plasmas (1994-present)*, 5(5):1784–1792, 1998.

[90] B Davies. Locating the zeros of an analytic function. *Journal of Computational Physics*, 66(1):36 – 49, 1986.

[91] M. Romanelli, C. Bourdelle, and W. Dorland. Effects of high density peaking and high collisionality on the stabilization of the electrostatic turbulence in the frascati tokamak upgrade. *Physics of Plasmas*, 11(8):3845–3853, 2004.

[92] J. Citrin, F. Jenko, P. Mantica, D. Told, C. Bourdelle, J. Garcia, J. W. Haverkort, G. M. D. Hogeweij, T. Johnson, and M. J. Pueschel. Nonlinear Stabilization of Tokamak Microturbulence by Fast Ions. *Physical Review Letters*, 111(15):155001, October 2013.

[93] H Biglari, PH Diamond, and MN Rosenbluth. Toroidal ion-pressure-gradient-driven drift instabilities and transport revisited. *Physics of Fluids B*, 1(1):109–118, 1989.

[94] O.P. Poguste B.B. Kadomstev. *reviews of Plasma Physics, edited by M.A. Leontovitch Consultant Bureau, New York*, 5:249, 1970.

[95] C Bourdelle, GT Hoang, X Litaudon, CM Roach, T Tala, ITPA Topical Grp Transport ITB Phy, and Int ITB Database Working Grp. Impact of the alpha parameter on the microstability of internal transport barriers. *Nuclear Fusion*, 45(2):110–130, FEB 2005.

[96] F. Ryter, C. Angioni, A. G. Peeters, F. Leuterer, H.-U. Fahrbach, W. Suttrop, and ASDEX Upgrade Team. Experimental study of trapped-electron-mode properties in tokamaks: Threshold and stabilization by collisions. *Phys. Rev. Lett.*, 95, 2005.

[97] Alessandro Casati, C. Bourdelle, X. Garbet, and F. Imbeaux. Temperature ratio dependence of ion temperature gradient and trapped electron mode instability thresholds. *Physics of Plasmas*, 15(4), 2008.

[98] E. Thompson, D. Stork, H. P. L. de Esch, and the JET Team. The use of neutral beam heating to produce high performance fusion plasmas, including the injection of tritium beams into the joint european torus. *Physics of Fluids B*, 5(7):2468–2480, 1993.

[99] JET Team (prepared by P.R. Thomas). Alpha particle studies during jet dt experiments. *Nuclear Fusion*, 39(11Y):1619, 1999.

[100] J. D. Strachan, M. Bitter, A. T. Ramsey, M. C. Zarnstorff, V. Arunasalam, M. G. Bell, N. L. Bretz, R. Budny, C. E. Bush, S. L.

Davis, H. F. Dylla, P. C. Efthimion, R. J. Fonck, E. Fredrickson, H. P. Furth, R. J. Goldston, L. R. Grisham, B. Grek, R. J. Hawryluk, W. W. Heidbrink, H. W. Hendel, K. W. Hill, H. Hsuan, K. P. Jaehnig, D. L. Jassby, F. Jobes, D. W. Johnson, L. C. Johnson, R. Kaita, J. Kampershroer, R. J. Knize, T. Kozub, B. LeBlanc, F. Levinton, P. H. La Marche, D. M. Manos, D. K. Mansfield, K. McGuire, D. H. McNeill, D. M. Meade, S. S. Medley, W. Morris, D. Mueller, E. B. Nieschmidt, D. K. Owens, H. Park, J. Schivell, G. Schilling, G. L. Schmidt, S. D. Scott, S. Sesnic, J. C. Sinnis, F. J. Stauffer, B. C. Stratton, G. D. Tait, G. Taylor, H. H. Towner, M. Ulrickson, S. von Goeler, R. Wieland, M. D. Williams, K-L. Wong, S. Yoshikawa, K. M. Young, and S. J. Zweben. High-temperature plasmas in a tokamak fusion test reactor. *Phys. Rev. Lett.*, 58:1004–1007, Mar 1987.

[101] G.T. Hoang, C. Gil, E. Joffrin, D. Moreau, A. Becoulet, P. Bibet, J.P. Bizarro, R.V. Budny, J. Carrasco, J.P. Coulon, C. De Michelis, T. Dudok de Wit, P. Monier-Garbet, M. Goniche, R. Guirlet, T. Hutter, S.M. Kaye, J. Lasalle, L. Laurent, P. Lecoustey, X. Litaudon, M. Mattioli, Y. Peysson, A.-L. Pecquet, G. Rey, S.A. Sabbagh, B. Saoutic, G. Tonon, and J.C. Vallet. Improved confinement in high l i lower hybrid driven steady state plasmas in tore supra. *Nuclear Fusion*, 34(1):75, 1994.

[102] S. A. Sabbagh, R. A. Gross, M. E. Mauel, G. A. Navratil, M. G. Bell, R. Bell, M. Bitter, N. L. Bretz, R. V. Budny, C. E. Bush, M. S. Chance, P. C. Efthimion, E. D. Fredrickson, R. Hatcher, R. J. Hawryluk, S. P. Hirshman, A. C. Janos, S. C. Jardin, D. L. Jassby, J. Manickam, D. C. McCune, K. M. McGuire, S. S. Medley, D. Mueller, Y. Nagayama, D. K. Owens, M. Okabayashi, H. K. Park, A. T. Ramsey, B. C. Stratton, E. J. Synakowski, G. Taylor, R. M. Wieland, M. C. Zarnstorff, J. Kesner, E. S. Marmar, and J. L. Terry. High poloidal beta equilibria in the tokamak fusion test reactor limited by a natural inboard poloidal field null. *Physics of Fluids B: Plasma Physics (1989-1993)*, 3(8):2277–2284, 1991.

[103] E. A. Lazarus, G. A. Navratil, C. M. Greenfield, E. J. Strait, M. E. Austin, K. H. Burrell, T. A. Casper, D. R. Baker, J. C. DeBoo, E. J. Doyle, R. Durst, J. R. Ferron, C. B. Forest, P. Gohil, R. J. Groebner, W. W. Heidbrink, R.-M. Hong, W. A. Houlberg, A. W. Howald, C.-L. Hsieh, A. W. Hyatt, G. L. Jackson, J. Kim, L. L. Lao, C. J. Lasnier, A. W. Leonard, J. Lohr, R. J. La Haye, R. Maingi, R. L. Miller, M. Murakami, T. H. Osborne, L. J. Perkins, C. C. Petty, C. L. Rettig,

T. L. Rhodes, B. W. Rice, S. A. Sabbagh, D. P. Schissel, J. T. Scoville, R. T. Snider, G. M. Staebler, B. W. Stallard, R. D. Stambaugh, H. E. St. John, R. E. Stockdale, P. L. Taylor, D. M. Thomas, A. D. Turnbull, M. R. Wade, R. Wood, and D. Whyte. Higher fusion power gain with current and pressure profile control in strongly shaped diii-d tokamak plasmas. *Phys. Rev. Lett.*, 77:2714–2717, Sep 1996.

[104] GT Hoang, C Bourdelle, X Garbet, G Giruzzi, T Aniel, M Ottaviani, W Horton, P Zhu, and RV Budny. Experimental determination of critical threshold in electron transport on Tore Supra. *Physical review Letters*, 87(12), SEP 17 2001.

[105] G.T. Hoang. Key role of the current density profile on core confinement and transport in tokamak fusion plasmas: Electron heat and particle transport. *Thèse d'habilitation à diriger des recherches, Université de Provence, Aix-Marseille I*, 2007.

[106] O. Sauter, S. Coda, T. P. Goodman, M. A. Henderson, R. Behn, A. Bottino, E. Fable, An. Martynov, P. Nikkola, and C. Zucca. Inductive current density perturbations to probe electron internal transport barriers in tokamaks. *Phys. Rev. Lett.*, 94:105002, Mar 2005.

[107] J.W. Connor, T. Fukuda, X. Garbet, C. Gormezano, V. Mukhovatov, M. Wakatani, the ITB Database Group, the ITPA Topical Group on Transport, and Internal Barrier Physics. A review of internal transport barrier physics for steady-state operation of tokamaks. *Nuclear Fusion*, 44(4):R1, 2004.

[108] M Romanelli, A Zocco, F Crisanti, and JET-EFDA Contributors. Fast ion stabilization of the ion temperature gradient driven modes in the joint european torus hybrid-scenario plasmas: a trigger mechanism for internal transport barrier formation. *Plasma Physics and Controlled Fusion*, 52(4):045007, 2010.

[109] C. Giroud, R. Barnsley, P. Buratti, I.H. Coffey, M. von Hellermann, C. Jupén, K.D. Lawson, A. Meigs, M. O'Mullane, A.D. Whiteford, K.-D. Zastrow, and the JET EFDA contributors. Method for experimental determination of z dependence of impurity transport on jet. *Nuclear Fusion*, 47(4):313, 2007.

[110] R Fischer, C Wendland, A Dinklage, S Gori, V Dose, and the W7-AS team. Thomson scattering analysis with the bayesian probability theory. *Plasma Physics and Controlled Fusion*, 44(8):1501, 2002.

[111] R Fischer, A Dinklage, and E Pasch. Bayesian modelling of fusion diagnostics. *Plasma Physics and Controlled Fusion*, 45(7):1095, 2003.

[112] M.A. Chilenski et al. *submitted to Nucl. Fusion. Preprint: PSFC report PSFC/JA-14-22*, 2015.

[113] Gil C et al. *Fusion Science and Technology*, 56(3):1219–1252, 2009.

[114] R. Scannell, M. J. Walsh, M. R. Dunstan, J. Figueiredo, G. Naylor, T. O Gorman, S. Shibaev, K. J. Gibson, and H. Wilson. A 130 point nd:yag thomson scattering diagnostic on mast. *Review of Scientific Instruments*, 81(10), 2010.

[115] L. Frassinetti, M. N. A. Beurskens, R. Scannell, T. H. Osborne, J. Flanagan, M. Kempenaars, M. Maslov, R. Pasqualotto, M. Walsh, and JET-EFDA Contributors. Spatial resolution of the jet thomson scattering system. *Review of Scientific Instruments*, 83(1), 2012.

[116] B. P. Duval. Charge exchange recombination spectroscopy on fusion devices. *AIP Conference Proceedings*, 1438(1):189–196, 2012.

[117] K. W. Hill, M. Bitter, L. Delgado-Aparicio, D. Johnson, R. Feder, P. Beiersdorfer, J. Dunn, K. Morris, E. Wang, M. Reinke, Y. Podpaly, J. E. Rice, R. Barnsley, M. O Mullane, and S. G. Lee. Development of a spatially resolving x-ray crystal spectrometer for measurement of ion-temperature (ti) and rotation-velocity (v) profiles in itera). *Review of Scientific Instruments*, 81(10), 2010.

[118] Y. G. Li, Ph. Lotte, W. Zwingmann, C. Gil, and F. Imbeaux. *Fusion Science and Technology*, 59(2):397–405, 2011.

[119] F. M. Levinton, M. C. Zarnstorff, S. H. Batha, M. Bell, R. E. Bell, R. V. Budny, C. Bush, Z. Chang, E. Fredrickson, A. Janos, J. Manickam, A. Ramsey, S. A. Sabbagh, G. L. Schmidt, E. J. Synakowski, and G. Taylor. Improved confinement with reversed magnetic shear in tftr. *Phys. Rev. Lett.*, 75:4417–4420, Dec 1995.

[120] I. H. Hutchinson. Principles of plasma diagnostics. *Cambridge University Press*, 2005.

[121] C. Bourdelle, T. Gerbaud, L. Vermare, A. Casati, T. Aniel, J. F. Artaud, V. Basiuk, J. Bucalossi, F. Clairet, Y. Corre, P. Devynck, G. Falchetto, C. Fenzi, X. Garbet, R. Guirlet, Oe Guercan, S. Heuraux, P. Hennequin, G. T. Hoang, F. Imbeaux, L. Manenc, P. Monier-Garbet,

P. Moreau, R. Sabot, J. L. Ségui, A. Sirinelli, D. Villegas, and Team Tore Supra. Collisionality scaling in tore supra: detailed energy confinement analysis, turbulence measurements and gyrokinetic modelling. *Nuclear Fusion*, 51(6), 2011.

[122] R.V. Budny, M.G. Bell, H. Biglari, M. Bitter, C.E. Bush, C.Z. Cheng, E.D. Fredrickson, B. Grek, K.W. Hill, H. Hsuan, A.C. Janos, D.L. Jassby, D.W. Johnson, L.C. Johnson, B. LeBlanc, D.C. McCune, D.R. Mikkelsen, H.K. Park, A.T. Ramsey, S.A. Sabbagh, S.D. Scott, J.F. Schivell, J.D. Strachan, B.C. Stratton, E.J. Synakowski, G. Taylor, M.C. Zarnstorff, and S.J. Zweben. Simulations of deuterium-tritium experiments in tftr. *Nuclear Fusion*, 32(3):429, 1992.

[123] F. Jenko, W. Dorland, M. Kotschenreuther, and B. N. Rogers. Electron temperature gradient driven turbulence. *Physics of Plasmas*, 7(5):1904–1910, 2000.

[124] Z. Lin, I. Holod, L. Chen, P. H. Diamond, T. S. Hahm, and S. Ethier. Wave-particle decorrelation and transport of anisotropic turbulence in collisionless plasmas. *Phys. Rev. Lett.*, 99:265003, Dec 2007.

[125] C Fourment, G T Hoang, L-G Eriksson, X Garbet, X Litaudon, and G Tresset. Role of the current density profile on drift wave stability in internal transport barrier reversed magnetic shear experiments at JET and Tore Supra. *Plasma Physics and Controlled Fusion*, 45(3):233–250, March 2003.

[126] Yu F Baranov, C Bourdelle, T Bolzonella, M De Baar, C D Challis, C Giroud, N C Hawkes, E Joffrin, and V Pericoli Ridolfini. Effect of hysteresis in JET ITB plasma with LHCD. *Plasma Physics and Controlled Fusion*, 47(7):975–993, 2005.

[127] A.A. Vedenov, E.P. Velikhov, and R.Z. Sagdeev. Quasi-linear theory of plasma oscillations. *Nuclear Fusion, Supplement*, 1962.

[128] WB Drummond and D Pines. *Nuclear Fusion, Supplement*, 3:1049, 1962.

[129] Guy Laval and Denis Pesme. Controversies about quasi-linear theory. *Plasma Physics and Controlled Fusion*, 41(3A):A239, 1999.

[130] John A. Krommes. Fundamental statistical descriptions of plasma turbulence in magnetic fields. *Physics Reports*, 360(1 - 4):1 – 352, 2002.

[131] J. Weiland, A.B. Jarmèn, and H. Nordman. Diffusive particle and heat pinch effects in toroidal plasmas. *Nuclear Fusion*, 29(10):1810, 1989.

[132] Glenn Bateman, Arnold H. Kritz, Jon E. Kinsey, Aaron J. Redd, and Jan Weiland. Predicting temperature and density profiles in tokamaks. *Physics of Plasmas (1994-present)*, 5(5):1793–1799, 1998.

[133] T. Rafiq, A. H. Kritz, J. Weiland, A. Y. Pankin, and L. Luo. Physics basis of multi-mode anomalous transport module. *Physics of Plasmas (1994-present)*, 20(3), 2013.

[134] RE Waltz, GM Staebler, W Dorland, GW Hammett, M Kotschenreuther, and JA Konings. A gyro-Landau-fluid transport model. *Physics of Plasmas*, 4(7):2482–2496, JUL 1997.

[135] G. M. Staebler, J. E. Kinsey, and R. E. Waltz. Gyro-landau fluid equations for trapped and passing particles. *Physics of Plasmas (1994-present)*, 12(10), 2005.

[136] G. M. Staebler, R. E. Waltz, J. Candy, and J. E. Kinsey. New paradigm for suppression of gyrokinetic turbulence by velocity shear. *Phys. Rev. Lett.*, 110:055003, Jan 2013.

[137] C. Angioni, A.G. Peeters, X. Garbet, A. Manini, F. Ryter, and ASDEX Upgrade Team. Density response to central electron heating: theoretical investigations and experimental observations in asdex upgrade. *Nuclear Fusion*, 44(8):827, 2004.

[138] F. Imbeaux and Y. Peysson. Ray-tracing and fokker-planck modelling of the effect of plasma current on the propagation and absorption of lower hybrid waves. *Plasma Physics and Controlled Fusion*, 47(11):2041–2065, 2005.

[139] T Tala, F Imbeaux, V.V Parail, C Bourdelle, G Corrigan, X Garbet, D.J Heading, X Litaudon, P.I Strand, J Weiland, and Jet-Efda Contributors. Fully predictive time-dependent transport simulations of ITB plasmas in JET, JT-60U and DIII-D. *Nuclear Fusion*, 46(5):548–561, May 2006.

[140] J.E. Kinsey, G.M. Staebler, J. Candy, R.E. Waltz, and R.V. Budny. Iter predictions using the gyro verified and experimentally validated trapped gyro-landau fluid transport model. *Nuclear Fusion*, 51(8):083001, 2011.

[141] C. Holland, J.E. Kinsey, J.C. DeBoo, K.H. Burrell, T.C. Luce, S.P. Smith, C.C. Petty, A.E. White, T.L. Rhodes, L. Schmitz, E.J. Doyle, J.C. Hillesheim, G.R. McKee, Z. Yan, G. Wang, L. Zeng, B.A. Grierson, A. Marinoni, P. Mantica, P.B. Snyder, R.E. Waltz, G.M. Staebler, and J. Candy. Validation studies of gyrofluid and gyrokinetic predictions of transport and turbulence stiffness using the DIII-D tokamak. *Nuclear Fusion*, 53(8):083027, August 2013.

[142] Ö. D. Gürcan, P. H. Diamond, and T. S. Hahm. Radial transport of fluctuation energy in a two-field model of drift-wave turbulence. *Physics of Plasmas*, 13(5):052306, 2006.

[143] W. Dorland, F. Jenko, M. Kotschenreuther, and B. N. Rogers. Electron temperature gradient turbulence. *Physical Review Letters*, 85(26):5579–5582, 2000.

[144] Hennequin P et al. *26th EPS Conf. on Controlled Fusion and Plasma Physics, Maastricht*, 23J:1041, 1999.

[145] P. Hennequin, C. Honoré, A. Truc, A. Quéméneur, C. Fenzi-Bonizec, C. Bourdelle, X. Garbet, G.T. Hoang, and the Tore Supra team. Fluctuation spectra and velocity profile from doppler backscattering on tore supra. *Nuclear Fusion*, 46(9):S771–S779, 2006.

[146] G. D. Conway, C. Angioni, F. Ryter, P. Sauter, J. Vicente, and Asdex Upgrade Team. Mean and oscillating plasma flows and turbulence interactions across the l-h confinement transition. *Physical Review Letters*, 106(6), 2011.

[147] G. McKee, R. Ashley, R. Durst, R. Fonck, M. Jakubowski, K. Tritz, K. Burrell, C. Greenfield, and J. Robinson. The beam emission spectroscopy diagnostic on the diii-d tokamak. *Review of Scientific Instruments*, 70(1):913–916, 1999.

[148] L. Lin, M. Porkolab, E. M. Edlund, J. C. Rost, C. L. Fiore, M. Greenwald, Y. Lin, D. R. Mikkelsen, N. Tsujii, and S. J. Wukitch. Studies of turbulence and transport in Alcator C-Mod H-mode plasmas with phase contrast imaging and comparisons with GYRO. *Physics of Plasmas*, 16(1):012502, 2009.

[149] A. E. White, L. Schmitz, W. A. Peebles, T. A. Carter, T. L. Rhodes, E. J. Doyle, P. A. Gourdain, J. C. Hillesheim, G. Wang, C. Holland, G. R. Tynan, M. E. Austin, G. R. McKee, M. W. Shafer, K. H. Burrell,

J. Candy, J. C. DeBoo, R. Prater, G. M. Staebler, R. E. Waltz, and M. A. Makowski. A correlation electron cyclotron emission diagnostic and the importance of multifield fluctuation measurements for testing nonlinear gyrokinetic turbulence simulationsa). *Review of Scientific Instruments*, 79(10), 2008.

[150] A. V. Melnikov, I. S. Bondarenko, S. L. Efremov, N. K. Kharchev, S. M. Khrebotv, L. I. Krupnik, I. S. Nedzelskij, L. G. Zimeleva, and Yu. V. Trofimenko. Hibp diagnostics on t10. *Review of Scientific Instruments*, 66(1):317–319, 1995.

[151] S. Jolliet, A. Bottino, P. Angelino, R. Hatzky, T.M. Tran, B.F. Mcmillan, O. Sauter, K. Appert, Y. Idomura, and L. Villard. A global collisionless {PIC} code in magnetic coordinates. *Computer Physics Communications*, 177(5):409 – 425, 2007.

[152] J. Candy, C. Holland, R. E. Waltz, M. R. Fahey, and E. Belli. Tokamak profile prediction using direct gyrokinetic and neoclassical simulation. *Physics of Plasmas (1994-present)*, 16(6), 2009.

[153] M. Barnes, I. G. Abel, W. Dorland, T. GÃűrler, G. W. Hammett, and F. Jenko. Direct multiscale coupling of a transport code to gyrokinetic turbulence codesa). *Physics of Plasmas (1994-present)*, 17(5), 2010.

[154] D. Told, F. Jenko, T. GÃűrler, F. J. Casson, E. Fable, and ASDEX Upgrade Team. Characterizing turbulent transport in asdex upgrade l-mode plasmas via nonlinear gyrokinetic simulations. *Physics of Plasmas (1994-present)*, 20(12), 2013.

[155] Ö. D. Gürcan, L. Vermare, P. Hennequin, V. Berionni, P.H. Diamond, G. Dif-Pradalier, X. Garbet, P. Ghendrih, V. Grandgirard, C.J. McDevitt, P. Morel, Y. Sarazin, a. Storelli, and C. Bourdelle. Structure of nonlocality of plasma turbulence. *Nuclear Fusion*, 53(7):073029, July 2013.

[156] F Clairet, C Bottereau, J M Chareau, M Paume, and R Sabot. Edge density profile measurements by X-mode reflectometry on Tore Supra. *Plasma Physics and Controlled Fusion*, 43(4):429–441, 2001.

[157] A. Casati, T. Gerbaud, P. Hennequin, C. Bourdelle, J. Candy, F. Clairet, X. Garbet, V. Grandgirard, Oe D. Guercan, S. Heuraux,

G. T. Hoang, C. Honore, F. Imbeaux, R. Sabot, Y. Sarazin, L. Vermare, and R. E. Waltz. Turbulence in the tore supra tokamak: Measurements and validation of nonlinear simulations. *Physical Review Letters*, 102(16), 2009.

[158] John A. Krommes. Fundamental statistical descriptions of plasma turbulence in magnetic fields. *Physics Reports*, 360(1 - 4):1 – 352, 2002.

[159] Ryogo Kubo. Stochastic liouville equations. *Journal of Mathematical Physics*, 4(2):174–183, 1963.

[160] M. Ottaviani. Scaling laws of test particle transport in two-dimensional turbulence. *EPL (Europhysics Letters)*, 20(2):111, 1992.

[161] T. H. Dupree. A perturbation theory for strong plasma turbulence. *Physics of Fluids (1958-1988)*, 9(9):1773–1782, 1966.

[162] R. E. Waltz, a. Casati, and G. M. Staebler. Gyrokinetic simulation tests of quasilinear and tracer transport. *Physics of Plasmas*, 16(7):072303, 2009.

[163] D. R. Hatch, P. W. Terry, W. M. Nevins, and W. Dorland. Role of stable eigenmodes in gyrokinetic models of ion temperature gradient turbulence. *Physics of Plasmas*, 16(2):022311, 2009.

[164] P. H. Diamond, S. I. Itoh, K. Itoh, and T. S. Hahm. Zonal flows in plasma - a review. *Plasma Physics and Controlled Fusion*, 47(5):R35–R161, 2005.

[165] R. E. Waltz and C. Holland. Numerical experiments on the drift wave - zonal flow paradigm for nonlinear saturation. *Physics of Plasmas (1994-present)*, 15(12), 2008.

[166] C.P. Ritz, D.L. Brower, T.L. Rhodes, R.D. Bengtson, S.J. Levinson, N.C. Luhmann Jr., W.A. Peebles, and E.J. Powers. Characterization of tokamak edge turbulence by far-infrared laser scattering and langmuir probes. *Nuclear Fusion*, 27(7):1125, 1987.

[167] P Devynck, X Garbet, C Laviron, J Payan, S K Saha, F Gervais, P Hennequin, A Quemeneur, and A Truc. Localized measurements of turbulence in the tore supra tokamak. *Plasma Physics and Controlled Fusion*, 35(1):63, 1993.

[168] P Hennequin, R Sabot, C Honoré, G T Hoang, X Garbet, A Truc, C Fenzi, and A Quéméneur. Scaling laws of density fluctuations at high-k on tore supra. *Plasma Physics and Controlled Fusion*, 46(12B):B121–B133, 2004.

[169] Ö. D. Gürcan and R. Grappin. Anisotropic shell model of turbulence. *Phys. Rev. E*, 84:066308, Dec 2011.

[170] G.R. McKee, C.C. Petty, R.E. Waltz, C. Fenzi, R.J. Fonck, J.E. Kinsey, T.C. Luce, K.H. Burrell, D.R. Baker, E.J. Doyle, X. Garbet, R.A. Moyer, C.L. Rettig, T.L. Rhodes, D.W. Ross, G.M. Staebler, R. Sydora, and M.R. Wade. Non-dimensional scaling of turbulence characteristics and turbulent diffusivity. *Nuclear Fusion*, 41(9), 2001.

[171] Kimitaka Itoh and Sanae-I Itoh. The role of the electric field in confinement. *Plasma Physics and Controlled Fusion*, 38(1):1, 1996.

[172] A Hirose, S Livingstone, and A.K Singh. On q dependence of thermal transport in tokamaks. *Nuclear Fusion*, 45(12):1628–1633, December 2005.

[173] F Jenko, T Dannert, and C Angioni. Heat and particle transport in a tokamak: advances in nonlinear gyrokinetics. *Plasma Physics and Controlled Fusion*, 47(12B):B195–B206, December 2005.

[174] J. Abiteboul, X. Garbet, V. Grandgirard, S. J. Allfrey, Ph. Ghendrih, G. Latu, Y. Sarazin, and a. Strugarek. Conservation equations and calculation of mean flows in gyrokinetics. *Physics of Plasmas*, 18(8):082503, 2011.

[175] S L Newton, S C Cowley, and N F Loureiro. Understanding the effect of sheared flow on microinstabilities. *Plasma Physics and Controlled Fusion*, 52(12):125001, December 2010.

[176] Ö. D. Gürcan, P. H. Diamond, T. S. Hahm, and R. Singh. Intrinsic rotation and electric field shear. *Physics of Plasmas*, 14(4):042306, 2007.

[177] C. Angioni, Y. Camenen, F.J. Casson, E. Fable, R.M. McDermott, a.G. Peeters, and J.E. Rice. Off-diagonal particle and toroidal momentum transport: a survey of experimental, theoretical and modelling aspects. *Nuclear Fusion*, 52(11):114003, November 2012.

[178] G. L. Falchetto and M. Ottaviani. Effect of collisional zonal-flow damping on flux-driven turbulent transport. *Physical Review Letters*, 92(2):025002, 2004.

[179] A. M. Dimits, G. Bateman, M. A. Beer, B. I. Cohen, W. Dorland, G. W. Hammett, C. Kim, J. E. Kinsey, M. Kotschenreuther, A. H. Kritz, L. L. Lao, J. Mandrekas, W. M. Nevins, S. E. Parker, A. J. Redd, D. E. Shumaker, R. Sydora, and J. Weiland. Comparisons and physics basis of tokamak transport models and turbulence simulations. *Physics of Plasmas*, 7(3):969–983, 2000.

[180] D.R. Mikkelsen and W. Dorland. *Phys. Rev. Lett.*, 101:135003, 2008.

[181] F. J. Casson, a. G. Peeters, C. Angioni, Y. Camenen, W. a. Hornsby, a. P. Snodin, and G. Szepesi. Gyrokinetic simulations including the centrifugal force in a rotating tokamak plasma. *Physics of Plasmas*, 17(10):102305, 2010.

[182] R. L. Miller, M. S. Chu, J. M. Greene, Y. R. Lin-Liu, and R. E. Waltz. Noncircular, finite aspect ratio, local equilibrium model. *Physics of Plasmas (1994-present)*, 5(4):973–978, 1998.

[183] R. E. Waltz, G. M. Staebler, and W. M. Solomon. Gyrokinetic simulation of momentum transport with residual stress from diamagnetic level velocity shears. *Physics of Plasmas*, 18(4):042504, 2011.

[184] T. S. Hahm, P. H. Diamond, O. D. Gurcan, and G. Rewoldt. Nonlinear gyrokinetic theory of toroidal momentum pinch. *Physics of Plasmas*, 14(7):072302, 2007.

[185] N Mattor and PH Diamond. Momentum and thermal transport in neutral-beam-heated tokamaks. *Physics of Fluids (1958-1988)*, 31(5):1180–1189, 1988.

[186] B. Coppi and C. Spight. Ion-mixing mode and model for density rise in confined plasmas. *Phys. Rev. Lett.*, 41:551–554, Aug 1978.

[187] G. S. Lee and P. H. Diamond. Theory of ion temperaturegradient driven turbulence in tokamaks. *Physics of Fluids (1958-1988)*, 29(10):3291–3313, 1986.

[188] K. C. Shaing. Neoclassical quasilinear transport theory of fluctuations in toroidal plasmas. *Physics of Fluids (1958-1988)*, 31(8):2249–2265, 1988.

[189] Y. Camenen, A. G. Peeters, C. Angioni, F. J. Casson, W. A. Hornsby, A. P. Snodin, and D. Strintzi. Impact of the background toroidal rotation on particle and heat turbulent transport in tokamak plasmas. *Physics of Plasmas*, 16(1), 2009.

[190] V. Naulin, J. Nycander, and J. Juul Rasmussen. Equipartition and transport in two-dimensional electrostatic turbulence. *Phys. Rev. Lett.*, 81:4148–4151, Nov 1998.

[191] X Garbet, J Abiteboul, a Strugarek, Y Sarazin, G Dif-Pradalier, P Ghendrih, V Grandgirard, C Bourdelle, G Latu, and a Smolyakov. Thermodynamics of neoclassical and turbulent transport. *Plasma Physics and Controlled Fusion*, 54(5):055007, May 2012.

[192] J. Nycander and V. V. Yankov. Anomalous pinch flux in tokamaks driven by the longitudinal adiabatic invariant. *Physics of Plasmas (1994-present)*, 2(8):2874–2876, 1995.

[193] K W Gentle, B Richards, and F Waelbroeck. A measurement of hydrogen ion transport parameters in Tokamak discharges. *Plasma Physics and Controlled Fusion*, 29(9):1077–1092, September 1987.

[194] M. B. Isichenko, A. V. Gruzinov, and P. H. Diamond. Invariant measure and turbulent pinch in tokamaks. *Phys. Rev. Lett.*, 74:4436–4439, May 1995.

[195] P. W. Terry. Anomalous particle pinch for collisionless plasma. *Physics of Fluids B: Plasma Physics (1989-1993)*, 1(9):1932–1934, 1989.

[196] R. E. Waltz and R. R. Dominguez. Note on detailed models for trapped electron transport in tokamaks. *Physics of Fluids B: Plasma Physics (1989-1993)*, 1(9):1935–1937, 1989.

[197] GT Hoang, C Bourdelle, B Pegourie, B Schunke, JF Artaud, J Bucalossi, F Clairet, C Fenzi-Bonizec, X Garbet, C Gil, R Guirlet, F Imbeaux, J Lasalle, T Loarer, C Lowry, JM Travere, E Tsitrone, and Tore Supra Team. Particle pinch with fully noninductive lower hybrid current drive in Tore Supra. *Physical review Letters*, 90(15), APR 18 2003.

[198] A. A. Ware. Pinch effect for trapped particles in a tokamak. *Phys. Rev. Lett.*, 25:15–17, Jul 1970.

[199] GT Hoang, C Bourdelle, X Garbet, JF Artaud, V Basiuk, J Bucalossi, F Clairet, C Fenzi-Bonizec, C Gil, JL Segui, JM Travere, E Tsitrone, and L Vermare. Parametric dependence of turbulent particle transport in tore supra plasmas. *PHYSICAL REVIEW LETTERS*, 93(13), SEP 24 2004.

[200] M. Romanelli, G. Regnoli, and C. Bourdelle. Numerical study of linear dissipative drift electrostatic modes in tokamaks. *Physics of Plasmas*, 14(8), 2007.

[201] H. Weisen, I. Furno, S. Alberti, C. Angioni, K. Appert, R. Behn, P. Blanchard, P. Bosshard, S. Coda, I. Condrea, A. Degeling, B.P. Duval, P. Gomez, T.P. Goodman, M.A. Henderson, F. Hofmann, J.-P. Hogge, B. Joye, J.B. Lister, X. Llobet, A. Manini, Y. Martin, A. Martynov, J.-M. Mayor, E. Minardi, J. Mlynar, J.-M. Moret, P. Nikkola, Z.A. Pietrzyk, R.A. Pitts, A. Pochelon, H. Reimerdes, J.H. Rommers, O. Sauter, E. Scavino, G. Tonetti, M.Q. Tran, and A. Zabolotsky. Shape dependence of sawtooth inversion radii and profile peaking factors in tcv l mode plasmas. *Nuclear Fusion*, 42(2):136, 2002.

[202] H Weisen, A Zabolotsky, X Garbet, D Mazon, L Zabeo, C Giroud, H Leggate, M Valovic, K-D Zastrow, and contributors to the JET-EFDA Workprogramme. Shear and collisionality dependences of particle pinch in jet l-mode plasmas. *Plasma Physics and Controlled Fusion*, 46(5):751, 2004.

[203] M. Maslov, C. Angioni, H. Weisen, and JET-EFDA contributors. Density profile peaking in jet h-mode plasmas: experiments versus linear gyrokinetic predictions. *Nuclear Fusion*, 49(7):075037, 2009.

[204] H. Weisen, A. Zabolotsky, C. Angioni, I. Furno, X. Garbet, C. Giroud, H. Leggate, P. Mantica, D. Mazon, J. Weiland, L. Zabeo, K.-D. Zastrow, and JET-EFDA contributors. Collisionality and shear dependences of density peaking in jet and extrapolation to iter. *Nuclear Fusion*, 45(2):L1–L4, 2005.

[205] C. Angioni, H. Weisen, O.J.W.F. Kardaun, M. Maslov, A. Zabolotsky, C. Fuchs, L. Garzotti, C. Giroud, B. Kurzan, P. Mantica, A.G. Peeters, J. Stober, the ASDEX Upgrade Team, and contributors to the EFDA-JET Workprogramme. Scaling of density peaking in h-mode plasmas based on a combined database of aug and jet observations. *Nuclear Fusion*, 47(9):1326, 2007.

[206] C Angioni E Fable M Greenwald M Maslov A G Peeters H Takenaga and H Weisen. Particle transport in tokamak plasmas, theory and experiment. *Plasma Physics and Controlled Fusion*, 51(0):124017, 2009.

[207] C. Angioni, J. Candy, E. Fable, M. Maslov, a. G. Peeters, R. E. Waltz, and H. Weisen. Particle pinch and collisionality in gyrokinetic simulations of tokamak plasma turbulence. *Physics of Plasmas*, 16(6):060702, 2009.

[208] C Bourdelle. Turbulent particle transport in magnetized fusion plasma. *Plasma Physics and Controlled Fusion*, 47(5A, SI):A317–A326, 2005.

[209] R. Guirlet, A. Sirinelli, T. Parisot, R. Sabot, J. F. Artaud, C. Bourdelle, X. Garbet, P. Hennequin, G. T. Hoang, F. Imbeaux, J. L. Ségui, D. Mazon, and D. Villegas. Particle transport in low core turbulence tore-supra plasmas. *Nuclear Fusion*, 50(9), 2010.

[210] T. Parisot, R. Guirlet, C. Bourdelle, X. Garbet, N. Dubuit, F. Imbeaux, and P. R. Thomas. Experimental impurity transport and theoretical interpretation in a tore supra lower-hybrid heated plasma. *Plasma Physics and Controlled Fusion*, 50(5), 2008.

[211] R Dux, R Neu, a G Peeters, G Pereverzev, a M ck, F Ryter, J Stober, and Asdex Upgrade Team. Influence of the heating profile on impurity transport in ASDEX Upgrade. *Plasma Physics and Controlled Fusion*, 45(9):1815–1825, September 2003.

[212] M. Mattioli, R. Giannella, R. Myrnas, C. Demichelis, B. Denne-Hinnov, T. Dudok De Wit, and G. Magyar. Laser blow-off injected impurity particle confinement times in jet and tore supra. *Nuclear Fusion*, 35(9):1115, 1995.

[213] L. Lauro-Taroni and et al. *Proc. 21st EPS Conf. on Controlled Fusion and Plasma Physics, Montpellier, I*, 1994.

[214] R. Dux, A.G. Peeters, A. Gude, A. Kallenbach, R. Neu, and ASDEX Upgrade Team. Z dependence of the core impurity transport in asdex upgrade h mode discharges. *Nuclear Fusion*, 39(11):1509, 1999.

[215] D. Villegas. Etude expérimentale de l'influence du gradient de température électronique sur le transport turbulent des impuretés dans un plasma de fusion. *PhD thesis, Université de Provence, Aix-Marseille I*, 2010.

[216] M. E. Puiatti, M. Valisa, C. Angioni, L. Garzotti, P. Mantica, M. Mattioli, L. Carraro, I. Coffey, C. Sozzi, and JET-EFDA contributors. Analysis of metallic impurity density profiles in low collisionality joint european torus h-mode and l-mode plasmas. *Physics of Plasmas (1994-present)*, 13(4), 2006.

[217] H Nordman, A Skyman, P Strand, C Giroud, F Jenko, F Merz, V Naulin, T Tala, and the JET-EFDA Contributors. Fluid and gyrokinetic simulaftions of impurity transport at jet. *Plasma Physics and Controlled Fusion*, 53(10):105005, 2011.

[218] T. Parisot. Dépendances paramétriques expérimentales du transport des impuretés métalliques dans le tokamak tore supra. *PhD thesis, Université de Provence, Aix-Marseille I*, 2007.

[219] D. Villegas, R. Guirlet, C. Bourdelle, X. Garbet, G.T. Hoang, R. Sabot, F. Imbeaux, and J.L. Ségui. Experimental and theoretical study of nickel transport dependence on gradients in tore supra. *Nuclear Fusion*, 54(7):073011, 2014.

[220] C Angioni, R Dux, E Fable, and a G Peeters. Non-adiabatic passing electron response and outward impurity convection in gyrokinetic calculations of impurity transport in ASDEX Upgrade plasmas. *Plasma Physics and Controlled Fusion*, 49(12):2027–2043, December 2007.

[221] T Pütterich, R Dux, R Neu, M Bernert, M N a Beurskens, V Bobkov, S Brezinsek, C Challis, J W Coenen, I Coffey, a Czarnecka, C Giroud, P Jacquet, E Joffrin, a Kallenbach, M Lehnen, E Lerche, E de la Luna, S Marsen, G Matthews, M-L Mayoral, R M McDermott, a Meigs, J Mlynar, M Sertoli, and G van Rooij. Observations on the W-transport in the core plasma of JET and ASDEX Upgrade. *Plasma Physics and Controlled Fusion*, 55(12):124036, December 2013.

[222] E A Belli and J Candy. Kinetic calculation of neoclassical transport including self-consistent electron and impurity dynamics. *Plasma Physics and Controlled Fusion*, 50(9):095010, 2008.

[223] C. Angioni, P. Mantica, T. Pütterich, M. Valisa, M. Baruzzo, E.A. Belli, P. Belo, F.J. Casson, C. Challis, P. Drewelow, C. Giroud, N. Hawkes, T.C. Hender, J. Hobirk, T. Koskela, L. Lauro Taroni, C.F. Maggi, J. Mlynar, T. Odstrcil, M.L. Reinke, M. Romanelli, and JET EFDA Contributors. Tungsten transport in jet h-mode plasmas

in hybrid scenario, experimental observations and modelling. *Nuclear Fusion*, 54(8):083028, 2014.

[224] T. S. Hahm and W. M. Tang. Properties of ion temperature gradient drift instabilities in h mode plasmas. *Physics of Fluids B: Plasma Physics (1989-1993)*, 1(6):1185–1192, 1989.

[225] S. C. Guo and F. Romanelli. The linear threshold of the ion-temperature-gradient-driven mode. *Physics of Fluids B: Plasma Physics*, 5(2):520, 1993.

[226] F. Jenko, W. Dorland, and G. W. Hammett. Critical gradient formula for toroidal electron temperature gradient modes. *Physics of Plasmas*, 8(9):4096, 2001.

[227] D. R. Baker, C. M. Greenfield, K. H. Burrell, J. C. DeBoo, E. J. Doyle, R. J. Groebner, T. C. Luce, C. C. Petty, B. W. Stallard, D. M. Thomas, M. R. Wade, and DIII-D Team. Thermal diffusivities in diii-d show evidence of critical gradients. *Physics of Plasmas (1994-present)*, 8(9):4128–4137, 2001.

[228] Y Camenen, A Pochelon, A Bottino, S Coda, F Ryter, O Sauter, R Behn, T P Goodman, M A Henderson, A Karpushov, L Porte, and G Zhuang. Electron heat transport in shaped tcv l-mode plasmas. *Plasma Physics and Controlled Fusion*, 47(11):1971, 2005.

[229] P. Mantica, D. Strintzi, T. Tala, C. Giroud, T. Johnson, H. Leggate, E. Lerche, T. Loarer, a. Peeters, a. Salmi, S. Sharapov, D. Van Eester, P. de Vries, L. Zabeo, and K.-D. Zastrow. Experimental Study of the Ion Critical-Gradient Length and Stiffness Level and the Impact of Rotation in the JET Tokamak. *Physical Review Letters*, 102(17):175002, April 2009.

[230] J. C. Hillesheim, J. C. DeBoo, W. A. Peebles, T. A. Carter, G. Wang, T. L. Rhodes, L. Schmitz, G. R. McKee, Z. Yan, G. M. Staebler, K. H. Burrell, E. J. Doyle, C. Holland, C. C. Petty, S. P. Smith, A. E. White, and L. Zeng. Observation of a critical gradient threshold for electron temperature fluctuations in the diii-d tokamak. *Phys. Rev. Lett.*, 110:045003, Jan 2013.

[231] P Mantica, C Angioni, B Baiocchi, M Baruzzo, M N a Beurskens, J P S Bizarro, R V Budny, P Buratti, a Casati, C Challis, J Citrin, G Colyer, F Crisanti, a C a Figueiredo, L Frassinetti, C Giroud, N Hawkes,

J Hobirk, E Joffrin, T Johnson, E Lerche, P Migliano, V Naulin, a G Peeters, G Rewoldt, F Ryter, a Salmi, R Sartori, C Sozzi, G Staebler, D Strintzi, T Tala, M Tsalas, D Van Eester, T Versloot, P C DeVries, and J Weiland. Ion heat transport studies in JET. *Plasma Physics and Controlled Fusion*, 53(12):124033, December 2011.

[232] E. Buckingham. On physically similar systems; illustrations of the use of dimensional equations. *Phys. Rev.*, 4(4):345–376, Oct 1914.

[233] B.B. Kadomtsev. Tokamaks and dimensional analysis. *Soviet Journal of Plasma Physics*, 1(4):295, 1975.

[234] C.C. Petty. Sizing up plasmas using dimensionless parameters. *Physics of Plasmas*, 15(0):080501, 2008.

[235] T C Luce, C C Petty, and J G Cordey. Application of dimensionless parameter scaling techniques to the design and interpretation of magnetic fusion experiments. *Plasma Physics and Controlled Fusion*, 50(4):043001 (87pp), 2008.

[236] P. N. Yushmanov, T. Takizuka, K. S. Riedel, J. G. Cordey O. J. W. F. Kardaun, S. M. Kaye, and D. E. Post. Scalings for tokamak energy confinement. *Nuclear Fusion*, 30:8, 1990.

[237] S.M. Kaye and ITER Confinement Database working Group. Iter l mode confinement database. *Nuclear Fusion*, 37(9):1303–1328, 1997.

[238] J.G. Cordey, K. Thomsen, A. Chudnovskiy, O.J.W.F. Kardaun, T. Takizuka, J.A. Snipes, M. Greenwald, L. Sugiyama, F. Ryter, A. Kus, J. Stober, J.C. DeBoo, C.C. Petty, G. Bracco, M. Romanelli, Z. Cui, Y. Liu, D.C. McDonald, A. Meakins, Y. Miura, K. Shinohara, K. Tsuzuki, Y. Kamada, H. Urano, M. Valovic, R. Akers, C. Brickley, A. Sykes, M.J. Walsh, S.M. Kaye, C. Bush, D. Hogewei, Y. Martin, A. Cote, G. Pacher, J. Ongena, F. Imbeaux, G.T. Hoang, S. Lebedev, and V. Leonov. Scaling of the energy confinement time with beta and collisionality approaching iter conditions. *Nuclear Fusion*, 45(9):1078–1084, 2005.

[239] F. W. Perkins et ali. *Physics of Fluids B: Plasma Physics*, 5(2):477–498, 1993.

[240] C. C. Petty and T. C. Luce. Scaling of heat transport with collisionality. *Physics of Plasmas*, 6(3):909–921, 1999.

[241] J. G. Cordey. *Nuclear Fusion*, 49:052001, 2009.

[242] Gürcan, Ö. D., L. Vermare, P. Hennequin, and C. Bourdelle. *Nuclear Fusion*, 50:022003, 2010.

[243] C. Angioni, A. G. Peeters, F. Jenko, and T. Dannert. Collisionality dependence of density peaking in quasilinear gyrokinetic calculations. *Physics of Plasmas*, 12(11):112310, 2005.

[244] J. Candy and R. E. Waltz. Anomalous transport scaling in the diii-d tokamak matched by supercomputer simulation. *Phys. Rev. Lett.*, 91(4):045001, Jul 2003.

[245] T. Gerbaud. *Développement d'un réflectomètre micro-onde hétérodyne à balayage ultra rapide. Etude de l'influence de la turbulence du plasma sur la mesure des profils de densité électronique*. PhD thesis, Univ. Henri Poincaré Nancy I, France, 2008.

[246] T. Tala, K.-D. Zastrow, J. Ferreira, P. Mantica, V. Naulin, a. Peeters, G. Tardini, M. Brix, G. Corrigan, C. Giroud, and D. Strintzi. Evidence of Inward Toroidal Momentum Convection in the JET Tokamak. *Physical Review Letters*, 102(7):075001, February 2009.

[247] C. Bourdelle, C.F. Maggi, L. Chôné, P. Beyer, J. Citrin, N. Fedorczak, X. Garbet, A. Loarte, F. Millitello, M. Romanelli, Y. Sarazin, and JET EFDA Contributors. L to h mode transition: on the role of z eff. *Nuclear Fusion*, 54(2):022001, 2014.

[248] C. Bourdelle and et al. L to h mode transition: Parametric dependencies of the temperature threshold. *Submitted to Nuclear Fusion*, 2015.

[249] G. Dif-Pradalier and et al. Flux driven l mode edge investigation. *Transport Task Force meeting, USA*, 2013.

[250] L. Chôné, P. Beyer, Y. Sarazin, G. Fuhr, C. Bourdelle, and S. Benkadda. *Physics of Plasmas*, 21(7):070702, 2014.